



Peer Reviewed

Title:

The synergy of human arm and robotic system

Author:

[Li, Zhi](#)

Acceptance Date:

2014

Series:

[UC Santa Cruz Electronic Theses and Dissertations](#)

Degree:

Ph.D., [Computer Engineering](#)[UC Santa Cruz](#)

Advisor(s):

[Elkaim, Gabriel Hugh](#)

Committee:

[Rosen, Jacob](#), [Milutinovic, Dejan](#), [Elkaim, Gabriel Hugh](#), [Wiberg, Donald M.](#)

Permalink:

<https://escholarship.org/uc/item/0sb828pq>

Abstract:

Copyright Information:

All rights reserved unless otherwise indicated. Contact the author or original publisher for any necessary permissions. eScholarship is not the copyright owner for deposited works. Learn more at http://www.escholarship.org/help_copyright.html#reuse



eScholarship
University of California

eScholarship provides open access, scholarly publishing services to the University of California and delivers a dynamic research platform to scholars worldwide.

UNIVERSITY OF CALIFORNIA
SANTA CRUZ

THE SYNERGY OF HUMAN ARM AND ROBOTIC SYSTEM

A Dissertation Submitted in Partial Fulfillment of the
Requirements for the Degree of

DOCTOR OF PHILOSOPHY

in

COMPUTER ENGINEERING

by

Zhi Li
December 2014

This dissertation is approved by:

Professor Gabriel Hugh Elkaim, Chair

Professor Jacob Rosen

Associate Professor Dejan Milutinović

Professor Donald M. Wiberg

Dean Tyrus Miller
Vice Provost and Dean of Graduate Studies

Copyright © by
Zhi Li
2014

Contents

Table of Contents	iii
List of Tables	viii
List of Figures	ix
Abstract	xxiii
Dedication	xxvi
1 Introduction	1
1.1 Synergy of Human Limbs and Wearable Robot Systems	1
1.2 Motivation & Applications	2
1.2.1 Robot-assisted Stroke Rehabilitation	2
1.2.2 Surgical Robot System	10
1.3 Structure of the Dissertation	12
2 Literature Review	14
2.1 Upper Limb Exoskeleton	14
2.1.1 The Challenges in the Control of Upper Exoskeleton	15
2.1.2 Upper Limb Exoskeletons for Robot-assisted Stroke Rehabilitation	15
2.2 Surgical Robot Systems	16
2.2.1 The Human-Machine Interface of Surgical Robot Systems	17
2.2.2 Challenges in the Design of Multi-arm Surgical Robot Systems	19
2.3 Kinematically Redundancy Resolution Methods for Robotic Manipulator Control	20
2.3.1 Robotic Manipulators with Kinematic Redundancy	20
2.3.2 Redundancy Resolution at Different Levels	21

2.3.3	General Resolution to Inverse Kinematics	22
2.3.4	Task-based Redundancy Resolution	24
2.3.5	Performance-based Redundancy Resolution	25
2.4	Control Strategies of Human Arm Movements	33
2.4.1	Characteristics of human arm movements	33
2.4.2	Redundancy resolution based on performance optimization . .	37
2.5	Coordination of Macro- and Micro-structures in Human Arm Movements	41
2.5.1	Natural Separation of Macro- and Micro-structures in Human Arm	41
2.5.2	Separation of the Macro- and Micro-structures in Robotic Manipulators	44
2.6	Robot-assisted Bilateral Training for Stroke Rehabilitation	45
2.6.1	The Neural Mechanism of Bilateral Training	45
2.6.2	Bilateral Training Therapies	46
3	Method	47
3.1	Experiment	47
3.1.1	Devices	47
3.1.2	Protocols	48
4	Synthesized Control Criteria for the Redundancy Resolution of Human Arm Movements	53
4.1	Kinematics of the Upper Limb Exoskeleton EXO-UL7	54
4.1.1	Forward Kinematics	54
4.1.2	Inverse Kinematics	57
4.1.3	Jacobian matrix	62
4.2	Models of Human Arm	64
4.2.1	Kinematic Model	64
4.2.2	Dynamic Model	66
4.3	Criteria for Redundancy Resolution	66
4.3.1	Criterion 1: maximizing the motion efficiency	66
4.3.2	Criterion 2: maintaining the equilibrium posture	68
4.3.3	Criterion 3: minimizing joint angle change	69
4.3.4	Criterion 4: minimizing the change in kinetic energy	70
4.3.5	Criterion 5: minimizing the work in joint space	70

4.4	Methods of Inference of Criterion Contributions	71
4.4.1	The Least Squares Method	72
4.4.2	The Exponential method	73
4.4.3	Criterion Synthesization	74
4.5	Results	75
4.5.1	Prediction Performance of the Criteria	75
4.5.2	Characteristic Combinations of Motion Control Criteria	76
5	The Join Coordination in Reach-to-Grasp Movements	86
5.1	The Grasping-relevant Degrees of Freedom (GR-DOFs)	87
5.1.1	Data Analysis Method	88
5.1.2	Data Normalization and Component Separation	88
5.1.3	The Ratio of Active Motion Range	89
5.2	Results	89
5.2.1	The Reaching and Grasping Components.	89
5.2.2	The Task-relevance During the Movements	91
5.2.3	The Task-relevance at the End of the Movements	92
5.2.4	The Synergetic Coordination of Task-relevant GR-DOFs	93
6	Inter-arm Coupling in Bimanual Movements and the Efficacy of Bilateral Training for Stroke Recovery	100
6.1	Quantification of Movement Symmetry	101
6.1.1	Mapping Symmetry	101
6.1.2	Mapping Complexity	102
6.2	Statistical Data Analysis Method	104
6.3	Results	105
6.3.1	The Normalized and Averaged Joint Angles	105
6.3.2	Representative Mapping Plots	105
6.3.3	Results of Statistical Analysis	106
6.3.4	Summarized Results of Inter-mapping Comparisons	110
7	Discussion and Conclusions	115
7.1	The Spatial Map of Synthesized Criteria for the Redundancy Resolution of Human Arm Movements	115
7.1.1	Regional Motion Control Strategies in the Task Space	116
7.1.2	Methodology Contribution	117

7.2	Task-relevance of Grasping-related Degrees of Freedom in Reach-to-grasp Movements	118
7.2.1	The Task-dependent Coordination of GR-DOFs	119
7.2.2	On the Control of the Upper Limb Exoskeleton	120
7.3	The Effect of Inter-arm Coupling and the Efficacy of Bilateral Training	121
7.3.1	On the Inter-arm Mappings	121
7.3.2	On The Inter-mode Mappings	122
7.3.3	On the Control of Task-Relevant and Task-Irrelevant Joints .	123
7.3.4	On the Mapping Symmetry and Complexity Variables	123
7.3.5	Efficacy of the Bilateral Training	124
8	Appendix I: The Rotational Axis Approach for Resolving the Kinematic Redundancy of the Human Arm in Reaching Movements	125
8.1	Redundancy Resolution: the rotational axis method	125
8.2	The Equilibrium Posture of the Human Arm	126
8.3	Result of Data Analysis	127
9	Appendix II: the Maximum Entropy Principle and the Exponential Method for Criterion Synthesization	133
10	Appendix III: Manipulability Analysis of Multi-link Manipulators	136
10.1	Three-link Manipulator for Planar Task	136
10.1.1	Families of Configurations	137
10.1.2	Direct Kinematics	138
10.1.3	Inverse Kinematics for different families of configurations . .	140
10.2	Redundancy Resolution by Pseudo-inverse	144
10.2.1	Jacobian Matrix	144
10.2.2	Singular Value Decomposition of the Jacobian Matrix	145
10.2.3	Null Space of Jacobian Matrix	146
10.2.4	Pseudo-inverse of Jacobian	150
10.2.5	Initial Condition in Joint Space	152
10.2.6	Trajectories in Joint Space and Task Space	155
10.2.7	Discussion on Pseudo-inverse Solution	160
10.3	Redundancy Resolution by Optimizing Manipulability	162
10.3.1	Analytical derivation of manipulability performance indices .	162

10.3.2	Manipulability performance measured by w_n	173
10.3.3	Manipulability performance measured by C_n	179
10.3.4	Best manipulability performance by Link Length ratio	183
10.3.5	Analytical Derivation of Velocity & Force Ellipsoid	184
10.4	Entropy as the measurement of probabilistic reachability	188
10.4.1	Problem setup	188
10.4.2	Simulation results	194
11	Appendix IV: Design Optimization of a Multi-Arms Surgical Robotic System for Manipulation Dexterity	198
11.1	Introduction	198
11.2	Methodology	199
11.2.1	Direct Kinematics of the Raven IV Arms	199
11.2.2	Inverse Kinematics of the Raven IV Arms	201
11.2.3	The Common Workspace and the Reference Plane	206
11.2.4	Area-Circumference Ratio	207
11.2.5	Mechanism Isotropy	208
11.2.6	Cost Function	210
11.3	Results	212
11.3.1	Isotropy Performance	212
11.3.2	Robotic Mechanism Design - Link length	212
11.3.3	Robot Base Orientation	213
11.3.4	Ports Spacing	214
11.3.5	Full Optimization	215
11.4	Conclusion	216
Bibliography		222

List of Tables

Table 2.1 Performance Indices Used for Redundant Robotic Manipulator Control	25
Table 2.2 Proportional Percentages of the Limb Segments to the Body Weight [1]	42
Table 4.1 Base rotation of upper limb exoskeleton.	54
Table 4.2 Denavit-Hartenberg (DH) Parameters for upper limb exoskeleton.	56
Table 6.1 Results of two-way ANOVA on the inter-mapping comparisons A to H. Each analysis indicates a significant difference at the 95% confidence level with a “★”. Fig. 6.4b indicates which data are used in each comparison.	108
Table 6.2 Results of two-sample T-tests: inter-mapping comparisons on the means of each variable.	110
Table 10.1 Joint angle ranges for each family of configurations	138
Table 10.2 Reachable ranges of the end-effector when the manipulator takes initial configurations of different families.	156
Table 10.3 Link Length Measurement (mm) and Link Length Ratio for Man and Woman.	184
Table 11.1 Denavit-Hartenberg Parameters for Raven IV Arms (standard method).	201
Table 11.2 Parameter Ranges and preferred values for the optimization of the Raven IV surgical robot system.	218

List of Figures

Fig. 1.1	The synergy of human arms and wearable robot system comes from the evolution of the multi-disciplinary research on human-robot interaction.	2
Fig. 1.2	EXO-UL7, a dual arm exoskeleton with seven DOFs in each arm. This system exhibits kinematic redundancy identical to the human arm.	3
Fig. 1.3	Raven IV Surgical Robot System - CAD rendering of the four Raven arms interacting with the patient. The workspace is marked as transparent cones. Intersecting cones identify a shared workspace. Note that most of the actuators were removed from the base of each arm to expose to the rest of the arms and the shared workspace.	11
Fig. 1.4	Separation of macro and micro structure in a robotic manipulator.	12
Fig. 2.1	Classification of surgical robotic systems based on a Surgeon-Robot (S-R) interface (horizontal axis) defining the level of automation and a Robot-Patient (R-P) interface dictating the level of invasiveness (vertical axis).	17
Fig. 2.2	The limb segments with mass distribution: (a) the upper limb, (b) the lower limb.	41
(a)	41
(b)	41
Fig. 3.1	(a) and (b) show the top and front views of the spherical workspace, respectively. (c) A subject is performing the instructed reaching movements, with markers attached to her right arm and the torso for position tracking.	48
(a)	Top View.	48
(b)	Front View	48

(c)	Attached markers.	48
Fig. 3.2	In the experiment of point-to-point reaching movements, eight targets are selected among all the available targets (denoted by blue dots in circles).	49
Fig. 3.3	(a) Eight targets are involved in the reach-to-grasp experiment; (b) in the four reach-to-grasp sessions, the handles are oriented at 0° , 45° , 90° , 135° on the plane that the subject face to, with respect to the direction of gravity.	50
(a)	Targets positions.	50
(b)	Target orientations.	50
Fig. 3.4	Experimental setups: (a) passive reflective markers are attached to the arms and torso of the subjects for position tracking; (b) the targets corresponding to each hand are aligned on circles the centers which are aligned with the shoulder of the subject. . .	51
(a)	Experimental setup.	51
(b)	Targets in 3D workspace.	51
Fig. 4.1	The upper limb exoskeleton with seven DOFs, supporting 99% of the range of motion required to preform daily activities. . . .	55
Fig. 4.2	(a) Given a 3D wrist position, the arm plane formed by the positions of the shoulder (P_s), the elbow (P_e) and the wrist (P_w) can move around an axis that connects the shoulder and the wrist due to kinematic redundancy. (b) The redundant DOF can be represented by a swivel angle ϕ	65
(a)	65
(b)	65
Fig. 4.3	(a) Criterion 1 maximizes motion efficiency by maximizing the projection of the longest principle eigen-vector of the manipulability ellipsoid on the direction from the hand to the virtual target P_m . The corresponding elbow position falls on the plane formed by P_s , P_w and P_m . (b) Criterion 2 intends to maintain the arm posture close to the equilibrium arm posture by placing the elbow on the plane formed by the wrist position P_w and the direction of the equilibrium vector \vec{v}_e	67
(a)	67

(b)	67
Fig. 4.4	Swivel angle prediction performance for each candidate criterion. μ and σ denote the mean and the standard deviation of the prediction error.	79
(a)	Criterion 1.	79
(b)	Criterion 1.	79
(c)	Criterion 2.	79
(d)	Criterion 2.	79
(e)	Criterion 3.	79
(f)	Criterion 3.	79
(g)	Criterion 4.	79
(h)	Criterion 4.	79
(i)	Criterion 5.	79
(j)	Criterion 5.	79
Fig. 4.5	Swivel angle prediction performance of the synthesized criteria using (a) the least squares method and (b) the exponential method. μ and σ denote the mean and the standard deviation of the prediction error.	80
(a)	Least squares method (LSQ).	80
(b)	Exponential method (EXP).	80
Fig. 4.6	The swivel angle predictions of candidate criteria, as well as their inferred contributions. c_1 to c_5 refer to the candidate criteria. Est refers to the synthesized criteria. Exp refers to the swivel angle measurements.	81
(a)	Least squares method (LSQ).	81
(b)	Exponential method (EXP).	81
Fig. 4.7	The sum of the squared distances to the cluster centroid (s_N) is computed for increasing cluster number (N). When the ratio between s_N and s_1 is reduced to 5%, the clustering is stabilized, at $N = 9$	82
(a)	Clustering threshold.	82
(b)	Cluster distribution, $N = 9$	82

Fig. 4.8	Characteristic combinations of contribution coefficients are identified by K-means clustering. With respect to the threshold coefficient value 0.2, the dominant criteria are distinguished from the non-dominant ones.	83
(a)	Cluster 1.	83
(b)	Cluster 2.	83
(c)	Cluster 3.	83
(d)	Cluster 4.	83
(e)	Cluster 5.	83
(f)	Cluster 6.	83
(g)	Cluster 7.	83
(h)	Cluster 8.	83
(i)	Cluster 9.	83
Fig. 4.9	The clusters' frequencies in the task space for Cluster 1 to 6.	84
(a)	Cluster 1.	84
(b)	Cluster 2.	84
(c)	Cluster 3.	84
(d)	Cluster 4.	84
(e)	Cluster 5.	84
(f)	Cluster 6.	84
Fig. 4.10	The clusters' frequencies in the task space for Cluster 7 to 9. (d) compares the graphs for the nine clusters and illustrates the most-frequent combination of motion control criteria for each cell in the task space.	85
(a)	Cluster 7.	85
(b)	Cluster 8.	85
(c)	Cluster 9.	85
(d)	Color Map.	85
Fig. 5.1	(a) The anatomical arm model and (b) the swivel-angle arm model.	87
(a)	Anatomical arm model.	87
(b)	Swivel-angle arm model.	87
Fig. 5.2	The comparison between the two modeling methodologies.	88

Fig. 5.3	(a) The swivel angle trajectories are normalized with respect to the percentage of path length. (b) The averaged trajectories are found with their time-varying standard deviation. With reference to the averaged trajectory of the reaching movement, the reach-to-grasp movements can be separated into (c) the reaching component and (d) the grasping component.	90
	(a) Swivel angle normalized w.r.t the percentage of path length.	90
	(b) Averaged swivel angle and standard deviation.	90
	(c) The reaching component.	90
	(d) The grasping component.	90
Fig. 5.4	The reaching and grasping components of the swivel angle (ϕ), pronation-supination (θ_5), flexion-extension (θ_6) and radial deviation (θ_7).	95
	(a) The reaching components.	95
	(b) The grasping components.	95
Fig. 5.5	Second order derivative of the grasping component.	96
	(a)	96
	(b)	96
	(c)	96
	(d)	96
Fig. 5.6	The normalized R-ARM values across target position and orientation. (a) The mean R-AMR of the reaching component w.r.t the percentage of the path length; (b) the progression of R-AMR values of the grasping component during movement: across-target-position vs. across-target-orientation R-AMR for each GR-DOF starting from the bottom-left.	97
	(a) The reaching Component.	97
	(b) The grasping Component.	97
Fig. 5.7	Multiple comparison of the R-AMR values at the end of the movements (i.e., the $R-AMR_{100\%}$) between the reaching and grasping components.	97
	(a) The Swivel angle.	97
	(b) The Forearm supination.	97
	(c) The Wrist flexion.	97
	(d) The Radial deviation.	97

Fig. 5.8	Multiple comparison of R-AMR _{100%} values for reach-to-grasp tasks. GR-DOFs 1 to 4 refer to swivel angle, forearm supination, wrist flexion, and radial deviation respectively.	98
(a)	Across target position.	98
(b)	Across target orientation.	98
Fig. 5.9	Multiple comparison of across-target-position R-AMR _{100%} values among different target orientations.	98
(a)	The swivel angle.	98
(b)	The forearm supination.	98
(c)	The swivel angle.	98
(d)	The forearm supination.	98
Fig. 5.10	The averaged response of grasping component for (a) the swivel angle, (b) the pronation-supination and (c) the hand orientation. (d) $\sigma_\eta - (\sigma_\phi^2 + \sigma_{\theta_5}^2)^{1/2}$ is negative, indicating that the swivel angle and the pronation-supination exhibit synergy.	99
(a)	99
(b)	99
(c)	99
(d)	99
Fig. 6.1	The four joint angles extracted from the reaching movements are the shoulder abduction (θ_1), shoulder flexion (θ_2), shoulder rotation (θ_3) and elbow flexion (θ_4).	101
Fig. 6.2	The variables for measuring mapping symmetry. (a) Diverging trajectories result in different slopes. (b) Parallel trajectories result in different intersections. (c) Nonlinear deviations influence R^2	103
(a)	p_1 - Slope.	103
(b)	p_2 - Intersection.	103
(c)	R^2 - Coefficient of determination.	103
Fig. 6.3	Mapping complexity V.S. Fitting quality for a pair of movements at a single joint.	104
(a)	$R^2 > 0.90$	104
(b)	$R^2 > 0.95$	104
(c)	$R^2 > 0.99$	104

(d) R^2 Versus N	104
Fig. 6.4 (a)The flowchart for the methodology steps, and (b) the mappings (denoted by numbers) and the inter-mapping comparisons (denoted by letters).	105
(a)	105
(b)	105
Fig. 6.5 The normalized and averaged joint angle trajectories. “uni” and “bi” are for unimanual and bimanual modes, while “D” and “ND” are for dominant and non-dominant arms.	106
(a) θ_1 shoulder abduction.	106
(b) θ_2 shoulder flexion.	106
(c) θ_3 shoulder rotation.	106
(d) θ_4 elbow flexion.	106
Fig. 6.6 Examples of mapping plots: (a) healthy subject, inter-arm mapping; (b) stroke subject, inter-arm mapping; (c) healthy subject inter-mode mapping; (d) stroke subject, inter-mode mapping.	107
(a) From the dominant arm to the non-dominant arm.	107
(b) From the non-paretic arm to the paretic arm.	107
(c) From the unimanual mode to bimanual mode.	107
(d) From the unimanual mode to bimanual mode.	107
Fig. 6.7 Results of multi-comparison among joints. The inter-arm mappings are: (a) healthy subject, unimanual mode; (b) healthy subject, bimanual mode; (c) stroke subject, unimanual mode; (d) stroke subject, bimanual mode.	109
(a) Mapping 1.	109
(b) Mapping 2.	109
(c) Mapping 3.	109
(d) Mapping 4.	109
Fig. 6.8 Results of multi-comparison among joints. The inter-mode mappings are: (a) healthy subject, dominant arm; (b) healthy subject, non-dominant arm; (c) stroke subject, non-paretic arm; (d) stroke subject, paretic arm.	109
(a) Mapping 5.	109
(b) Mapping 6.	109
(c) Mapping 7.	109

(d) Mapping 8.	109
Fig. 6.9 Results of multi-comparison of the unimanual and bimanual modes in comparisons A and B.	111
(a) Comparison A, R^2 at θ_2	111
(b) Comparison A, R^2 at θ_4	111
(c) Comparison A, N_c at θ_4	111
(d) Comparison B, p_2 at θ_2	111
Fig. 6.10 Results of Multi-comparison the Unimanual and Bimanual Modes: Comparison D	112
(a) Comparison D, p_1 at θ_2	112
(b) Comparison D, p_2 at θ_2	112
(c) Comparison D, p_2 at θ_3	112
Fig. 6.11 Mapping 9: from the paretic arm in bimanual mode to the non-paretic arm in unimanual mode. (a) Results of multiple comparison among joints. (b) and (c) Significant differences in Comparison I (Mapping 3 V.S. Mapping 9).	113
(a) Multiple comparison among joints.	113
(b) p_2 at θ_2	113
(c) N_c at θ_3	113
Fig. 8.1 (a) Equilibrium posture directs the arm to its position of equilibrium of the periarticular muscles, and (b) brings the working hands in the range of stereoscopic visual control.	127
(a)	127
(b)	127
Fig. 8.2 The direction of the rotational axis can be specified by the flexion angle (α) and abduction angle (β). The direction of equilibrium posture of the upper arm is a possible candidate for the direction of the rotational axis.	128
Fig. 8.3 Performance comparison of two swivel angle estimation methods by the distributions of the mean and standard deviation of estimation error.	129
(a) Rotational axis method.	129
(b) Rotational axis method.	129
(c) Motion efficiency method.	129

(d)	Motion efficiency method.	129
Fig. 8.4	The directions of the rotational axis are estimated for each valid trial. A linear regression model describes the surface that constrains the axis direction when the right arm moves in its comfortable motion range.	130
(a)	Subject 1.	130
(b)	Subject 2.	130
(c)	Subject 3.	130
(d)	Subject 4.	130
(e)	Subject 5.	130
(f)	Subject 6.	130
Fig. 8.5	Continue Fig. 8.4.	131
(a)	Subject 7.	131
(b)	Subject 8.	131
(c)	Subject 9.	131
(d)	Subject 10.	131
Fig. 8.6	Targets in the reaching movement experiment. For the right arm, target 1, 2, 3, 5, 7 (in green circles) are within the comfortable arm motion range while target 4, 6, and 8 (in magenta circles) are close to the motion range boundary	132
Fig. 10.1	Modeling by simplification: from human arm to redundant manipulator. Left - Human arm with 7 or more DOFs, for spatial task; Right - Kinematical redundant manipulator with 3 DOFs for planar task.	137
(a)	137
(b)	137
Fig. 10.2	Families of configurations.	137
Fig. 10.3	Three-link mechanism.	140
Fig. 10.4	Availability of redundancy resolution for a three-link manipulator.	141
Fig. 10.5	Availability of redundancy resolution for a three-link manipulator, choosing θ_1 as free variable.	142
Fig. 10.6	Family 1: $\theta_1 > 0, \theta_2 > 0, \theta_3 > 0$	142
Fig. 10.7	Family 1: $\theta_1 > 0, \theta_2 < 0, \theta_3 > 0$	144
Fig. 10.8	Family 1: $\theta_1 > 0, \theta_2 > 0, \theta_3 < 0$	144

Fig. 10.9 Velocity Mapping from Joint Space to Task Space, by Jacobian Matrix.	146
Fig. 10.10 Many-to-one mapping from joint space to task space.	151
Fig. 10.11 Family 1: mapping from joint space to task space	152
Fig. 10.12 Family 2: mapping from joint space to task space.	153
Fig. 10.13 Family 3: mapping from joint space to task space.	154
Fig. 10.14 Problem setup: end-effector trajectory specified in task space. .	155
Fig. 10.15 The initial manipulator conditions for different families.	156
Fig. 10.16 Joint space profile for Family 1.	157
Fig. 10.17 Joint space profile for Family 2.	157
Fig. 10.18 Joint space profile for Family 3.	158
Fig. 10.19 Joint space profile for different families of manipulator configurations.	159
Fig. 10.20 Least-norm solution \mathbf{x}_{ln} has smaller norm than any other solution.	161
Fig. 10.21 w_n of Family 1 Configurations.	174
Fig. 10.22 w_n of Family 2 Configurations.	175
Fig. 10.23 Manipulability of Family 3 Configurations.	176
Fig. 10.24 Max w_n along the designed trajectory.	177
Fig. 10.25 Two-link manipulator: w_n for Different Link Length Ratio. la is the end-effector position in task space	178
(a)	178
(b)	178
(c)	178
(d)	178
Fig. 10.26 Two-link manipulator: w_n for Different Link Length Ratio, plotted by θ_2	179
(a)	179
(b)	179
(c)	179
(d)	179
Fig. 10.27 Best w_n profile, plotted by θ_1, θ_2 , and θ_3	180
(a)	180
(b)	180
(c)	180
(d)	180

Fig. 10.28 Two-link manipulator: C_n for Different Link Length Ratio. la is the end-effector position in task space	181
(a)	181
(b)	181
(c)	181
(d)	181
Fig. 10.29 Two-link manipulator: C_n for Different Link Length Ratio, plotted by θ_2	182
(a)	182
(b)	182
(c)	182
(d)	182
Fig. 10.30 Best C_n profile, plotted by θ_1, θ_2 , and θ_3	183
(a)	183
(b)	183
(c)	183
(d)	183
Fig. 10.31 Best Manipulability Performance (measured by w_n) for Different $0.1 \leq k_1 \leq 5$ and $k_2 = 1$	190
(a)	190
(b)	190
(c)	190
(d)	190
(e)	190
(f)	190
Fig. 10.32 Best Manipulability Performance (measured by w_n) for Different $k_1 = 1$ and $0.1 \leq k_2 \leq 5$	191
(a)	191
(b)	191
(c)	191
(d)	191
(e)	191
(f)	191

Fig. 10.33 Best Manipulability Performance (measured by w_n) for Different k_1 and k_2 around the Measurements of Human Arms (50 percentile).	192
(a)	192
(b)	192
(c)	192
(d)	192
(e)	192
(f)	192
Fig. 10.34 For a two-link Manipulator, generated from unit sphere $\dot{\theta}^T \dot{\theta} = 1$	193
Fig. 10.35 For a two-link Manipulator, generated from unit sphere $\tau^T \tau = 1$	193
Fig. 10.36 Relevant research.	194
Fig. 10.37 Relevant research.	195
Fig. 10.38 Relevant research.	195
Fig. 10.39 Relevant research.	196
Fig. 10.40 Relevant research.	196
Fig. 10.41 Relevant research.	197
 Fig. 11.1 Reference Frame of the Raven IV surgical robot system.	200
(a) Robot arm.	200
(b) Surgical tool.	200
Fig. 11.2 The common workspace projected onto the reference plane: (a) 3D view; (b) projection onto x-z plane. For each Raven IV arm, the gray bar represents its base. The magenta and the cyan bars represent the first and second link respectively.	206
(a)	206
(b)	206
Fig. 11.3 Example of two typical common workspaces of two Raven arms constructed from two different link lengths defined by α and β : (a) Two arm configuration defined by links length $\alpha = 65^\circ$, and $\beta = 15^\circ$, resulted with $\varsigma = 2.23$; (b) Two arm configuration defined by links length $\alpha = 65^\circ$, $\beta = 80^\circ$, resulted with $\varsigma = 4.48$	208
(a)	208
(b)	208
Fig. 11.4 Parameters for the optimization of the common workspace.	211

Fig. 11.5 Isotropy as a function of the first two joint angles for a specific arm configuration ($\alpha = 55^\circ, \beta = 40^\circ$) (a) Range of θ_2 as it is affected by different Iso_{\min} values marked by dashed vertical lines.	213
(b) Isotropy Iso as a function of the time dependent variable θ_1 (shoulder joint angle) θ_2 (elbow joint angle).	213
(a)	213
(b)	213
Fig. 11.6 Distribution of ς for different Iso_{\min} . (a)For $Iso_{\min} = 0$, $\varsigma_{\max} = 6.64$ when $\alpha = 80^\circ, \beta = 40^\circ$; (b) For $Iso_{\min} = 0.5$, $\varsigma_{\max} = 6.55$ when $\alpha = 70^\circ, \beta = 35^\circ$	214
(a)	214
(b)	214
Fig. 11.7 Best Performance of C_{\max} for different Iso_{\min}	215
Fig. 11.8 The cost function values C_{\max} as a function of the link length α and β plotted with a resolution of 10 degrees in a range of [0,90]. The cost function is maximized for $\alpha = 85^\circ$ and $\beta = 65^\circ$	216
Fig. 11.9 Effect of base orientation (ϕ_x, ϕ_y , and ϕ_z).	217
Fig. 11.10 Performance criterion C_{\max} is plotted as a function of various base orientation (ϕ_x, ϕ_y , and ϕ_z). In (a), (c) and (e), a color map is depicting the value of Performance criterion C_{\max} in pairs of two coordinates and the corresponding projection of the arms in two planes are depicted in (b) x-y plane, (d) x-z plane and (f) y-z plane of the world coordinate system. The gray bar represents the base of a Raven IV arm.	220
(a)	220
(b)	220
(c)	220
(d)	220
(e)	220
(f)	220
Fig. 11.11 Performance criteria C_{\max} as a function of port spacing along two orthogonal directions b_x and b_y	221
Fig. 11.12 Optimal configuration of the Raven IV surgical robot four arms following a brute force search (a) Relative position and orientation of the system bases (b) optimized workspace.	221

(a)	221
(b)	221

Synergy of Human Arm and Robotic System

Zhi Li

ABSTRACT

The synergy of human arm and wearable robot systems studies the compatibility of a wearable robot system and its operators. Ideally, the motion of a wearable robot system should be dynamically transparent to a healthy operator, sensitively responsible to the voluntary and involuntary motions of its operator. When used for robot-assisted stroke rehabilitation and/or power augmentation, a wearable robot system is expected to provide assist to the operator's motor skills and correct the abnormal movements resulted from motor disabilities. Inspired by the control strategies of human motor system, the robot systems can be more dexterous in manipulations and more adaptable to various tasks and uncertain environments.

The study on synergy of human arm and wearable robot systems intends to find out the motor control strategies that dominate human arm movements, in order to apply to the control of robotic systems, such as the upper limb exoskeletons and the surgical robot systems. This research experimentally investigated the arm movements in various tasks, to enhance the understanding of human motor control and to benefit the control robotic systems. With the data collected from point-to-point reaching movements, it proposed a redundancy resolution methodology based on multi-criterion performance optimization, which provides real-time predictions of arm postures with improved accuracy. Based on the comparison between reaching and reach-to-grasp movements, it further studied arm postures affected by grasping orientations and pointed out the control strategy that dominates the macro- and micro- structure coordination. From both healthy subjects and stroke patients, experimental data of unimanual and bimanual movements are recorded for identical tasks. The statistical analysis shows that motor function of the paretic arm can be improved when moving symmetrically with the non-paretic arm, which reveals the beneficial effects of the inter-arm coupling on stroke rehabilitation.

The dissertation contributed to answer the following three research questions:

- **How to predict the natural arm postures of reaching movement?**

The kinematic redundancy of the human arm enables the elbow position to

rotate about the axis going through the shoulder and wrist, which results in infinite possible arm postures when the arm reaches to a target in a 3-dimensional workspace. To infer the control strategy the human motor system uses to resolve redundancy in reaching movements, this research compares five redundancy resolution criteria and evaluates their arm posture prediction performance using data on healthy human motion. Two synthesized criteria are developed to provide better real-time arm posture prediction than the five individual criteria. Of these two, the criterion synthesized using an exponential method predicts the arm posture more accurately than that using a least squares approach, and therefore is preferable for inferring the contributions of the individual criteria to motor control during reaching movements. As a methodology contribution, this paper proposes a framework to compare and evaluate redundancy resolution criteria for arm motion control. A cluster analysis which associates criterion contributions with regions of the workspace provides a guideline for designing a real-time motion control system applicable to upper-limb exoskeletons for stroke rehabilitation.

- **How do the arm joints coordinate in reach-to-grasp movement?**

Reach-to-grasp movements are widely observed in activities of daily living, particularly in tool manipulations. In order to reduce the complexity in redundancy resolution and facilitate upper-limb exoskeleton control in reach-to-grasp tasks, we studied joint coordination in the human arm during such movements. Experimental data were collected on reach-to-grasp movements in a 3-dimensional (3D) workspace for cylinder targets of different positions and grasping orientations. For comparison, reaching movements toward the same targets are also recorded. In the kinematic analysis, the redundant degree of freedom in human arm is represented by the swivel angle. The four grasping-relevant degrees of freedom (GR-DOFs), including the swivel angle and the three wrist joints, behave differently in reach-to-grasp movements comparing to how they behave in reaching movements. The ratio of active motion range (R-AMR) is proposed for quantitatively comparison the task-relevance of the GR-DOFs. Analysis on the R-AMR values shows that the task-relevant GR-DOFs are more actively used, while the task-irrelevant joints are left uncontrolled and maintain their neutral positions. Among the task-relevant GR-DOFs, the smaller joints (micro-structure) are more actively used than the larger joints (macro-structure). The

coordination of the task-relevant GR-DOFs is shown to be synergistic. Analysis of the acceleration/deceleration at the GR-DOFs indicates different levels of voluntary control in three phases of the movements. The study of the characteristics of the joint coordination in reach-to-grasp movements provides guidelines for simplifying the control of the upper limb exoskeleton.

- **Can the bilateral training benefit the post-stroke stroke recovery?**

Bilateral training has been used for post-stroke rehabilitation of patients with paretic upper arms. This training method exploits the inter-arm coupling in bimanual movements which tends to synchronize the paretic arm with the non-paretic arm for motor function recovery. Different levels of motor function recovery have been reported in clinical studies, yet the efficacy of bilateral training is still not clear. As a result, this paper collected data on bimanual symmetric reaching movements in a 3-dimensional (3D) workspace from ten healthy subjects and eight chronic stroke patients, to investigate the effects of inter-arm coupling. In reaching experiments, identical tasks are also performed unimanually and recorded. Mapping variables are proposed to measure arm behavior changes and to quantify the similarity of the movements of the two arms. Among the four proposed mapping variables, mapping linearity and mapping complexity were found to reflect both the motion complexity and the task-relevance of a joint, while the other two variables captured changes in motion range and relative velocity. Statistical analysis shows that inter-arm coupling increases inter-arm symmetry more at task-relevant joints than at task-irrelevant joints. To achieve symmetric bimanual movement, the dominant arm of healthy subjects and the non-paretic arm of stroke patients deviate more from their unilateral behavior than the non-dominant/paretic arms. For stroke patients, the effect of inter-arm coupling on arm function depends on the task-relevance of a joint. During bimanual movement, joint behavior at task-irrelevant joints is different from behavior during unimanual movement, which implies that bimanual rehabilitation may help break abnormal movement patterns for these joints. For task-relevant joints, the average arm posture of the paretic arm is significantly higher in bimanual movement, which indicates the possible efficacy of bilateral rehabilitation.

DEDICATION & ACKNOWLEDGMENT

I would like to acknowledge the following persons, for their guidance, support, and inspiration.

I would like to extend my sincere appreciation and gratitude to my advisors, Professor Jacob Rosen and Professor Dejan , who have walked with me step by step during my PhD program, with patience and kindness. Thanks to my committee members, Professor Gabriel Elkaim and Professor Donlad Wiberg, for your warm support.

Many thanks to my colleagues and friends, Jay Ryan Roldan, Kierstin Gray, Kaitlyn Garifi, and Zachary Wells, for helping me with data collection and processing in the arm motion study experiment. Thanks to Daniel Glozman, who has setup the foundation of the work on the design optimization of the surgical robot system.

I dedicate this dissertation to my loving and supporting family, particular to my dear husband, Peter Andrew Mawhorter, my dear dear otter. I also want to express my deep thanks to Professor Jacob Rosen and Professor Daniela Contantinescu, my academic parents, who have planted and watered me in the academic field. It is a time to celebrate for their work and harvest.

But by the grace of God I am what I am:

And his grace which was bestowed upon me was not in vain.

Praise to the one that makes good things grow.

I dedicate myself to working hard,

Knowing that it is not I, but the grace of God which was, is, and will be with me.

Chapter 1

Introduction

1.1 Synergy of Human Limbs and Wearable Robot Systems

The synergy of human arm and wearable robot systems studies the compatibility of a wearable robot system and its operators. Ideally, the motion of a wearable robot system should be dynamically transparent to a healthy operator, sensitively responsible to the voluntary and involuntary motions of its operator. When used for robot-assisted stroke rehabilitation and/or power augmentation, a wearable robot system is expected to provide assist to the operator's motor skills and correct the abnormal movements resulted from motor disabilities. Inspired by the control strategies of human motor system, the robot systems can be more dexterous in manipulations and more adaptable to various tasks and uncertain environments.

The synergy of human arms and wearable robot system is a multi-disciplinary research topic. It requires research efforts both on the human motor control as well as on robotics. Previous researches on human motor control have explored the morphology, function and behavior of human limbs. The control strategies based on performance optimization have been proposed to predict the movements of healthy human limbs. Movements with and without sensory feedback have been compared, to studies the effects of perceptions on movement generation. The research effort on robotics proposed various methodology for redundancy resolution. Control strategies based on optimization of different performance indices have been implemented on various kinds of kinematical redundant manipulators, hoping to generate the natural motions of healthy human arms. The study on inter-arm coupling revealed the inter-

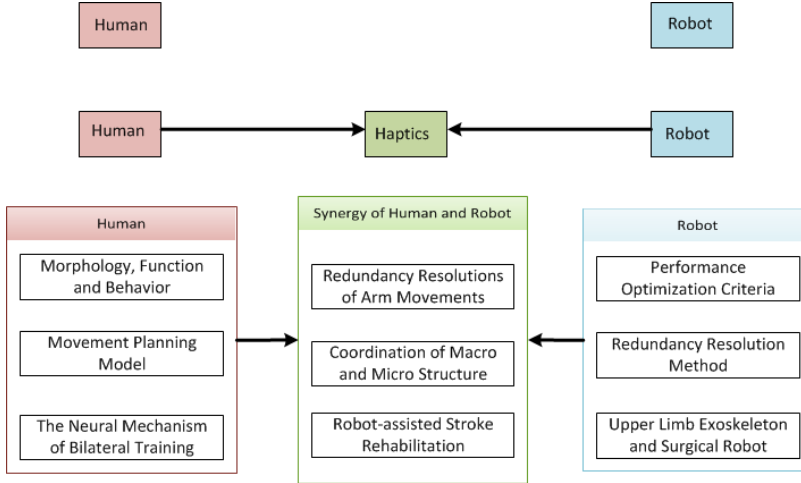


Figure 1.1: The synergy of human arms and wearable robot system comes from the evolution of the multi-disciplinary research on human-robot interaction.

ference between motor control of two hemispheres and implicates the possibility of stroke rehabilitation via bilateral training.

This research aims at enhancing the synergy of human arm and the wearable robot systems from the following three perspectives. It proposed a framework to compare and evaluate redundancy resolution criteria for arm motion control, which resulted in a redundancy resolution that enable the upper limb exoskeleton to render natural arm postures for reaching tasks. In addition, it investigated the hand-arm coordination in the reach-to-grasp movements and proposed a general control strategy for the joint coordination of a robotic manipulator with macro- and micro-structures. Furthermore, it compared the arm movements in unimanual and bimanual tasks and indicated the possible efficacy of bilateral training for stroke rehabilitation.

1.2 Motivation & Applications

1.2.1 Robot-assisted Stroke Rehabilitation

This research intends to contribute to stroke rehabilitation using dural arm exoskeleton. As shown in Fig. 4.1, EXO-UL7 is a dual arm exoskeleton with seven DOFs in each arm. This system exhibits kinematic redundancy identical to the human arm. Articulation of the exoskeleton is achieved by seven single-axis revolute joints which support 99% of the range of motion required to perform daily activities. Three rev-

olute joints are responsible for shoulder abduction-adduction, flexion-extension and internal-external rotation. A single rotational joint is employed at the elbow, creating elbow flexion-extension. Finally, the lower arm and hand are connected by a three-axis spherical joint resulting in wrist pronation-supination, flexion-extension, and radial-ulnar deviation. As a human-machine interface (HMI), four six-axis force/torque sensors (ATI Industrial Automation, model-Mini40) are attached to the upper arm, the lower arm, the hand and the tip of the exoskeleton. The force/torque sensor at the tip of the exoskeleton allows measurements of the interactions between the exoskeleton and the environment [2, 3, 4].



Figure 1.2: EXO-UL7, a dual arm exoskeleton with seven DOFs in each arm. This system exhibits kinematic redundancy identical to the human arm.

Existing researches have shown that the planning and executing bilateral movements post-stroke may facilitate cortical neural plasticity by increasing the usage of spared pathways in motor cortex. As a result, the resulting rehabilitation strategy, such as bilateral training, encourages the dysfunctional arm to move with the functional arm in a mirror image fashion. In robot-assisted stroke rehabilitation, the motions of the patient can be supported by the upper limb exoskeleton. The functional arm tele-operate the dysfunctional arm with bilateral or unilateral force feedback. By varying the coupling between the two wearable robotic arms between fully coupled mode to fully decoupled mode, the paretic arm of the stroke patient can move passively or independently. The interactions between human arms and upper

limb exoskeletons are expected to accelerate the recovery of the lost motor functions.

The proposed research intends to meet three challenges in the robot-assisted stroke rehabilitation. First of all, the upper limb exoskeleton is designed to assist self-initiated arm movements in unexpected tasks. Therefore, the redundancy resolution is required to provide real-time motion control rather than off-line planning. Second, the coordination of the hand and arm of the upper limb exoskeleton needs to be energy-efficient and is preferred to have low control complexity given the kinematic redundancy. Third, the coupling between the two robot arms should complement the effect the inter-arm coupling rather than substitute it. Less robotic assist should be provided at the joints of strong inter-arm coupling, to encourage the voluntary movement of the paretic arm, while more support should be provided to the joint with less inter-arm coupling.

The applications on robot-assisted stroke rehabilitation motivates research efforts on the following four topics:

- A Proposed Biological-based Arm Posture Prediction Method

The human arm is kinematically redundant with respect to reaching and grasping tasks in a 3-dimensional (3D) workspace. As a result, an upper limb exoskeleton designed for stroke rehabilitation requires a motion control strategy that can render natural arm postures. By analyzing the data collected from reaching movements, this research found out that the arm plane (defined by the shoulder, elbow and wrist position) rotates about an axis going through the shoulder position. For reaching movements in the comfortable motion range, the rotational axis directions are constrained to a surface, which can be parameterized by a linear model. For reaching movements close to the boundary of the motion range, the directions deviate from the surface most likely due to the blocking effect of the torso. As a result, a biological-based redundancy resolution based on the direction of the axis is proposed, which can predict the arm posture with a higher accuracy.

- Synthesizing Multiple Redundancy Resolutions for Human Arm Postures Prediction

To render natural arm postures with the EXO-UL7 upper limb exoskeleton, this research studies reaching movements to infer the motor control strategy used by the healthy human arm, compared different redundancy resolution criteria and

evaluates their arm posture prediction performance and propose a method of synthesizing multiple redundancy resolutions for accurate real-time arm posture prediction.

Conventionally, motion control has been viewed as a matter of the structure and function of the central nervous system. Studies from the perspective of neuroanatomy have focused on relating motor functions to different cortical, sub-cortical, and spinal subsystems [5, 6]. From the perspective of neurophysiology, Donders' law has been applied to arm postures in reaching movements, yet it is violated when pointing at a target with the elbow flexed [7]. On the other hand, the equilibrium-point (EP) hypothesis specifies physiological variables used by the central nervous system (CNS) as control variables, to address the redundancy problem (i.e., the behavior of the uncontrolled manifold) in the human motor system at the muscle level [8]. Unlike the neurophysiological perspective, a robotic viewpoint considers the human body, particularly the musculoskeletal system, as a mechanical system with kinematic and kinetic properties. The behaviors of this mechanical system are constrained by its physical structures and the laws of physics. The neural system does not so much to dictate the movement of this mechanical system as to enhance the compatibility of the system with the environment so that the task can be completed according to the requirements and with satisfactory performance [9, 10]. In this context, the redundancy of the human arm is resolved by control criteria which optimize performance variables used in mechanical engineering. Such criteria have been applied to human motor control processes such as motor planning, control, estimation, prediction and learning [11, 12].

When executing a movement plan on a robot with redundant degrees of freedom, it is necessary to resolve the ill-posed inverse kinematics and kinetics to determine the mapping from the planned trajectory to joint motions, and then to joint torques. The problem of controlling redundant degrees of freedom (DOFs), i.e., redundancy resolution, has been considered in the control of robot manipulators. Resolution methods utilize task dependent constraints [13, 14], or more commonly, performance criteria. The latter include manipulability [15, 16, 17, 18], energy consumption [7, 19], smoothness of movement [20, 21, 22, 23], task accuracy [24] and control complexity [25]. However, there is no general framework that compares and evaluates these criteria.

Redundancy resolution that synthesizes multiple movement control criteria has addressed the characteristics of movement behavior to a better extent. For instance, Miyamoto *et al.* studied reaching movements in a 2D workspace without end-point boundary conditions. By adding a signal dependent noise to the movement controls, a linear combination of criteria maximizing the task achievement and minimizing the energy consumption resulted in a good match to the experimentally-measured hand trajectories [26]. Biess *et al.* broke down the motion control task into independent spatial and temporal motor planning. A control criterion that restricts the arm dynamics to geodesic paths is combined with a control that minimizes the squared jerk along the selected end-effector path. The resulting reaching movements in a 3D workspace are close to those which minimize the change in joint torques and the peak value of kinematic energy [27]. Kim *et al.* studied the movements of reaching to a sequence of targets and predicted the arm postures in real-time by integrating a biological-based kinematic control criterion that maximizes the motion efficiency with a dynamic criterion that minimizes the work in joint space, showing that the kinematic criteria outperforms the dynamic one [28]. A study of the trade-off between minimizing the angular joint displacement and averaging limits of the shoulder joint range [29] showed that a 70% – 30% linear combination of arm posture predicted by these two criteria leads to a satisfactory redundancy resolution.

From the robotic perspective, this research proposes a general framework to compare and evaluate motion control strategies that predict arm posture in reaching movements. In this framework, the arm posture predictions of each candidate criterion are tested against experimental data collected from point-to-point reaching. By combining these candidate criteria according to their arm posture prediction accuracies, synthesized criteria are developed. The candidate criteria that better predict arm posture are assigned larger coefficients in the synthesized motion control criteria, and are therefore recognized as the ones that dominate the arm motion. For control of an upper limb exoskeleton in robot-assisted stroke rehabilitation, real-time motion control criteria are preferred, since unlike off-line motion control criteria (e.g., minimum jerk principle [21]), real-time criteria (e.g. bounded jerk criterion [30]) do not need to know about future states (e.g., the end position of the movement). Without the constraint of pre-planned movements, the upper limb exoskeleton can deal with unexpected

tasks and encourages self-initiated movements on the part of the stroke patients.

- The Control Strategy Underlying the Joint Coordination in Reach-to-grasp Movement

Reach-to-grasp movements are widely observed in activities of daily living, particularly in tool manipulations. It is critical to study joint coordination of a human arm in reach-to-grasp movements in order to reduce the complexity in redundancy resolution and facilitate control of the upper limb exoskeleton used to support such movements (see Fig. 4.1). Although efficient redundancy resolution methods have been proposed to determine the configurations of robotic manipulators [14, 31], yet these general methods are not capable of rendering the natural joint coordination in the human arm. Studies on reaching movements have resolved the kinematic redundancy in the human arm by performance optimizations [15, 16, 17, 18, 7, 19, 20, 21, 22, 23]. However, arm postures in reach-to-grasp movements are affected by the orientation of the grasp target, and these postures cannot be explained by the motor control strategies that have successfully addressed arm postures in reaching movements [32, 33].

Previous research has investigated the joint coordination in reach-to-grasp movements. Research has shown that hand-arm coordination is subject to both temporal [34] and spatial constraints [35]. While approaching a target, arm movement directs the thumb, preparing to match the hand orientation with the target [36, 37]. The rotation of the arm plane about the shoulder-wrist axis is coordinated with the supination of the forearm to achieve the desired hand orientation. If the target orientation is perturbed when the hand is moving to the target, the hand orientation begins to match the original target orientation and then adjusts to match the final target orientation [38]. This smooth adaptation to the perturbed target orientation implies that the reach-to-grasp movements may be a superposition of separate reaching and grasping components. Given arm postures predicted for reaching movements, arm postures for reach-to-grasp movements can be constructed based on grasping-related differences. Furthermore, human motor system prefers a joint coordination that minimizes the intervention when redundancy in control variables exists [25, 39]. The control emphasis is placed on task-relevant variables, while task-irrelevant variables are loosely monitored for tolerable variability [40, 41].

As a result, this research investigates the spatial and temporal characteristics

of the joint coordination in reach-to-grasp movements. Experimental data are collected on the reach-to-grasp movements in a 3-dimensional (3D) workspace, for cylinder targets of different positions and grasping orientations, in addition to the reaching movements toward the targets of the same positions. By kinematic analysis, the grasping-relevant degrees of freedom (GR-DOFs) in the human arm are distinguished from the grasping-irrelevant degrees of freedom (GI-DOFs). Since the kinematic redundancy for reaching movements has been resolved, this paper focuses on the difference between reach-to-grasp and reaching movements and their coordinated spatial and temporal responses to the changes in target position and orientation.

- The Effect of Inter-arm Coupling in Bimanual Movements and the Efficacy of Bilateral Training for Stroke Recovery

The bimanual movements of human arms are characterized by temporal and spatial coupling between the two arms. Due to the temporal and spatial symmetry constraint [42], healthy humans tend to move their arms in mirror-image symmetrical bimanual movements [43, 44, 45, 46, 47, 48, 49, 50]. Such arm movements are preformed either in-phase or anti-phase with identical frequencies [51, 46, 45, 52, 53] and with small differences in peak velocities [54, 55, 56, 57]. If a healthy human subject is instructed to move both arms while following two different non-symmetric trajectories repetitively, as the frequency of the motion increases the trajectories converge into contours of similar mirror-image symmetrical shapes followed with a similar frequency - a phenomenon known as the spatial magnetic effect [58, 59, 43, 45, 48, 55, 60, 61].

For healthy subjects, handedness limits the effects of inter-arm coupling on bimanual movements. The dominant and non-dominant arms have different trajectories when performing an identical reaching task unimanually [62, 63]. Differences in hand trajectories were demonstrated in symmetric bimanual circle drawing due to handedness [61]. One of the explanations provided to address these differences is the superior capability of the dominant arm in intersegmental coordination such as regulating interaction torque (INT) [64, 65, 66, 67, 63]. However there is a disagreement regarding the control architecture. One school of thoughts claims that identical control commands rendered by a centralized controller are simultaneously sent to homologous muscles of the two arms and the inter-arm differences in symmetric bimanual movements may be re-

lated to the different dynamics of two arms [43, 45, 68, 69, 70, 50]. Another school of thoughts argues that the two arms are more likely subjected to different controllers [61], and the symmetric constraints in the bimanual movements are due to the intra-hemispherical cross-talk that couples the two controllers [71, 72, 73, 74, 69]. As a consequence, the superior performance of dominant arm is due to both the differences in motor control and arm dynamics (e.g., muscle strength, length, mass, etc.). For healthy subjects, although similar neural distributed networks in both hemispheres are activated during symmetrical bilateral movements [75, 76, 77, 78, 79], significant differences in EMG patterns have been observed in the homologous muscles when the two arms are performing symmetrical bimanual movements [64] which may provide the experimental support for the existence of two separate controllers. Furthermore, it was hypothesized that the dominant arm depends more on feedforward control and therefore it is more proficient in response to unexpected changes of inertial loads and intersegmental dynamics [80, 81, 82].

For subjects with motor disability (i.e., hemiparesis) due to stroke, inter-arm coupling still confines bimanual movements despite the deteriorated motor functions as a result of brain damage [83]. Studies conducted with chronic stroke patients have shown that the peak velocities of the paretic arm were increased in symmetrical bilateral movements, at the expense of deteriorated performance of the non-paretic arm, such as longer movement time and lower peak velocity [84, 85]. This inter-arm coupling implies that the paretic arm may improve its motor function by moving with the non-paretic arm in effective bilateral training therapies. Improved motor function of paretic arms has been reported in therapy with symmetrical exercises (e.g., Bobath neuro-developmental approach), simultaneous and mirror upper-limb activities, and other bilateral training [86, 87, 88, 89, 90]. However, other research argues that bilateral training provided no more facilitation than alternative therapies [91, 92].

As a results, this study aims at investigating the effect of inter-arm coupling on the arm movement of healthy subjects and stroke patients. To evaluate the behavior differences between arms and the arm behavior change in unimanual and bimanual movements, this research introduces a method for quantifying the similarity between two recorded arm movements. The proposed quantitative approach is independent of the task and its associated kinematic and dynamic

variables (e.g., joint angles, velocities, forces, torques, etc.), and is applicable to both in-phase and anti-phase bimanual movements as well as unimanual movements. The inter-arm comparisons provide insight into motor control differences between arms with higher and lower motor function, particularly in chronic stroke patients.

1.2.2 Surgical Robot System

The control of the surgical robot system can also benefit from the proposed research. Raven IV is a new generation of surgical robotic systems that includes four articulated arms. consists of two pairs of surgical robotic arms. The pairs are mirror images of each other, which results in symmetric kinematics. Each arm has seven degrees of freedom (DOFs): six DOFs for positioning and orienting the end-effector and one for opening and closing the end-effector. As shown in Fig. 1.3, it allows two surgeons to collaborate using two surgical consoles that are located either next to the patient or at two remote locations. Raven IV is the second generation of Raven I [?]-[?]. The kinematic optimization of Raven I was based on the analysis of the workspace of a single arm [?, ?]. Several major structural changes were made to minimize the foot print of the individual robotic arm including the following: (1) All the actuators located on the base of the robot are mounted on top of the base allowing to move the base closer to the patient body; (2) the detention of actuation pack was reduced (3) The link length were change base on the reported results (4) the tensioning mechanisms of the cables were relocated in the base plate to provide better access and solid performances; (5) a universal tool interface was design to accept surgical robotics tools from different vendors (6) A unique tool with a dual wrist joints was designed an incorporated into the system.

The proposed research aims at improving the control of the surgical robot system from the following two perspectives:

- The Raven robot arm has a robotic joints and links of different sizes and weights. The first three links that are responsible for positioning in large motion range have large sizes and heavy weights and therefore are considered as the macro-structure. The rest links of the Raven arms that insert to body and operate in relatively smaller ranges are considered as the micro-structure, due to their small sizes and light weights. From the energy consumption perspective, the motion control strategy for the surgical robot arms is expected to move the

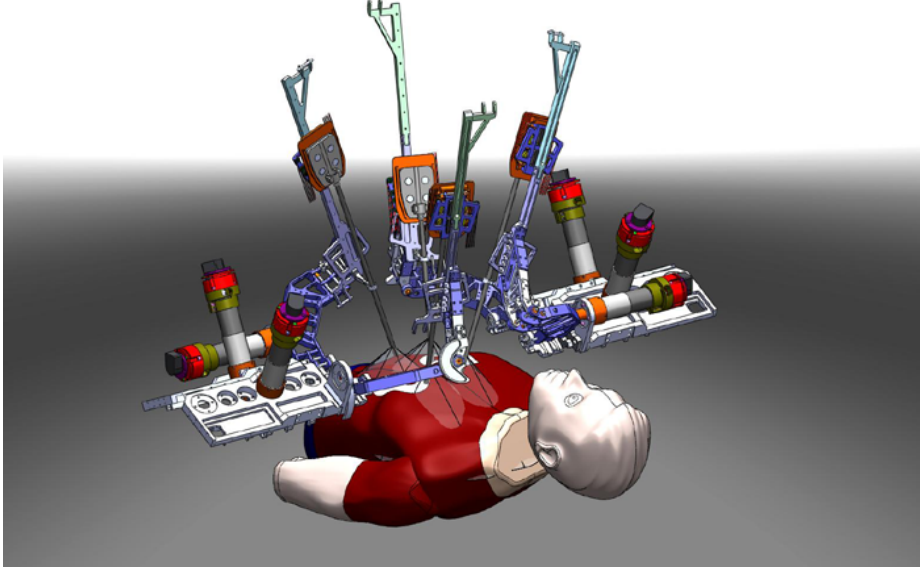


Figure 1.3: Raven IV Surgical Robot System - CAD rendering of the four Raven arms interacting with the patient. The workspace is marked as transparent cones. Intersecting cones identify a shared workspace. Note that most of the actuators were removed from the base of each arm to expose to the rest of the arms and the shared workspace.

macro-structure less on the premise that the task can be successfully complete with satisfactory performance. Regarding the dexterity of the end-effector, the macro-structure should be controlled so that the focus of the manipulation task have high probability to reside in the dexterous workspace of micro-structure (Fig. 1.4).

The motion control strategy for controlling robotic manipulator with macro- and micro-structure can be inspired by hand-arm coordination in reach-to-grasp movements. In the context of reach-to-grasp movements, one way to segment the macro/micro structures refers to the arm as a macro mechanism and the hand as a micro mechanism. As such, the arm as a gross positioner is manipulable to maximize the dexterity of the hand as the micro manipulator which is responsible for accomplishing the task [93, 94]. To adjust the hand orientation, since the motion of the upper arm (macro) and the pronation-supination angle of the forearm (micro) can serve the same purpose, it is more energy-efficient to adjust the pronation-supination angle of the forearm as opposed to

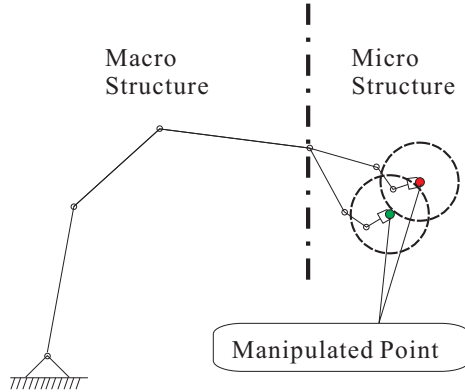


Figure 1.4: Separation of macro and micro structure in a robotic manipulator.

moving the shoulder joint for arm posture change if the target orientation is within the range of motion of the forearm. In this research, the analysis of the task-relevance of arm joints, which measures how much each joint contributes to satisfy the goal of the task, will reveal the control strategy of macro- and micro-structure coordination.

- Maximizing Dexterous Workspace and Optimal Port Placement of a Multi-Arm Surgical Robot.

This research effort aims to configure the link architecture of each robotic arm, along with the position and orientation of the four bases which dictates the port placement and configuration with respect to the patient body. The common workspace reachable by all four robotic arms is optimized given a total of 2.3×10^{10} possible system configurations resulted from seven different parameters. Based on the kinematic analysis of the Raven surgical robot arms, the common workspace is optimized by adjusting the link lengths, the port spacing and the base orientations within practical ranges of each parameter. The cost function of the optimization involves the mechanism isotropy and a proposed dexterity performance index (i.e. the Area-circumference ratio).

1.3 Structure of the Dissertation

In the rest of the dissertation, Chapter 2 will review the state of the art, including the control strategies of human arm movements and kinematic redundant manipulator. The research efforts on the human-machine interface of surgical robot systems and

the coordination of macro- and micro-structures of the robotic manipulators are also addressed, as well as the neural mechanism underlying the stroke rehabilitation using bilateral training therapy. After introducing the experimental data collection and data processing methods in Chapter 3, Chapter 4 to ?? will present the investigation regarding the four research questions. Chapter 4 proposed a method to synthesize multiple control criteria to provide real-time arm posture prediction with improved accuracy, and to evaluate the contribution of each component motion control criteria. Chapter 5 investigate the synergetic hand-arm coordination, which results in a control strategy that coordinates the macro- and micro-structures of a robotic manipulator based on the amount of usage of each degrees of freedom. Chapter 6 studies the effect of inter-arm coupling on the symmetric bimanual movements of healthy subject and stroke patients, which support the efficacy of bilateral training therapy on stroke rehabilitation. Discussion and conclusions on the four research topics are presented in Chapter 7. The appendix presents (1) a biological-based redundancy resolution method for arm posture prediction, which is one of five candidate arm posture prediction criteria (see Appendix I); (2) the detailed mathematics of the proposed exponential method, which is used to synthesize the five candidate arm posture prediction criteria and to infer the contribution of each component criterion (see Appendix II); (3) the fundamental work on analysis of the manipulability of multiple-link planner manipulators (see Appendix III); and (4) design optimization of multi-arm surgical robot system, which results in configuration parameters that maximize the manipulation dexterity (see Appendix IV).

Chapter 2

Literature Review

This chapter introduce the state of arts regarding the synergy of human arms and wearable robot systems. After introducing the research and design progress on the upper limb exoskeleton and the surgical robot systems, this chapter will present the existing research efforts on (1) the kinematically redundancy resolution method for robotic manipulator control, (2) the redundancy resolution criteria for arm posture prediction, (3) the control strategies for coordinating the macro- and micro-structures of robotic manipulators, as well as (4) the neural mechanism of bilateral training.

2.1 Upper Limb Exoskeleton

Integrated human-robotic systems are superior to any autonomous robotic systems in unstructured environments that demands significant adaptation. For power augmentation, the exoskeleton systems are designed for both the upper limb and lower limb [95].

The upper limb exoskeletons, which are also known as assist devices or human power extenders, are mainly built for power augmentation in the manipulations of heavy and bulky objects. They are mostly used for factory floors, warehouse, and distribution centers, and therefore are hung from overhead cranes. An upper limb exoskeleton can simulate the forces on a worker's arms and torso, which are usually much smaller than the forces needed to maneuver a load. When a worker uses an upper-extremity exoskeleton to move a load, the device bears the bulk of the weight by itself. The worker can sense a feedback which is scaled-down value of the load's actual weight and adjust manipulative movements accordingly. These assist devices

can filter out the forces that increase the difficulty of maneuvering and/or cause fatigue. In some cases, the exoskeletons are programmed to follow a pre-planned trajectory.

Existing upper limb exoskeletons are mostly designed based using compliance control schemes that relied on the measurement of interaction force between the human and the machine [96, 97, 98, 99]. Various experimental systems have been designed to verify the theories, such as a two-handed upper limb exoskeleton where artificially create friction forces between the load and the arms allow for grasping objects [100], and an one-handed upper limb exoskeleton where a gripper allow for grasping of heavy objects [101].

2.1.1 The Challenges in the Control of Upper Exoskeleton

The exoskeletons are expected to shadow the wearer's voluntary and involuntary movements without delay and hinderance. This requests a high level of sensitivity in response to all forces and torques on the exoskeleton, particularly the forces imposed by the operator, which is in conflict with the control of science's goal of minimizing system sensitivity in a closed-loop feedback system. The exoskeleton with a low sensitivity would not move freely with its operator, whereas an exoskeleton with high sensitivity will be much responsive to external forces and torques, instead of the operator's voluntary movements. In addition, the system with high sensitivity to external forces and torques are not robust to variations and therefore the precision of the system performance will be proportional to the precision of the exoskeleton dynamic model.

2.1.2 Upper Limb Exoskeletons for Robot-assisted Stroke Rehabilitation

Recently research results have demonstrated that robotic devices can deliver effective rehabilitation therapies to patients suffering from the chronic neuromuscular disorders [2, 3, 102]. MIT-MANUS is one of the successful rehabilitation robots which adopted back-drivable hardware and impedance control as a robot control system [103]. ARMin is a 7-DOF upper limb exoskeleton developed in ETH Zurich and the University of Zurich. This robot provides visual, acoustic and haptic interfaces together with cooperative control strategies to facilitate the patient's active participa-

tion in the game. The lengths of the upper arm, lower arm, hand and the height of the device are adjustable to accommodate patients of different sizes. The rehabilitation site and robotic system are wheelchair accessible. Pneu-WREX is a 6-DOF exoskeleton robot developed in UC Irvine. This robotic system adopted pneumatic actuators [104]. Although the pneumatic actuator is harder to control due to its non-linear characteristics, it produces relatively large forces with a low on-board weight [105]. The robot interacts with the virtual-reality game T-WREX based on a Java Therapy 2.0 software system [104, 104]. Arizona State University researchers developed a robotic arm, RUPERT (Robotic Upper Extremity Repetitive Therapy) targeting cost-effective and light-weight stroke patient rehabilitation [106, 107]. The device provides the patient with assistive force to facilitate fluid and natural arm movements essential for the activities of daily living. The controller for the pneumatic muscles can be programmed for each user to improve their arm and hand flexibility, as well as strength by providing a repetitive exercise pattern. In our previous work [108], the seven-DOF exoskeleton robot UL-EXO7 [109, 2, 110] was exploited as a core mechanical system for the long-term clinical trial of the bilateral and unilateral rehabilitation program. The controllers equipped in UL-EXO7 provided the assistive force to help patients make the natural arm posture based on the work in [18, 28]. For the objective and fine-scale rehabilitation assessment, a new assessment metric, an efficiency index, was introduced to tell the therapist how close the patient's arm movements are to the normal subject's arm movements.

2.2 Surgical Robot Systems

The recent introduction of surgical robotics into the operating room offers a significant breakthrough in the way surgery is conducted. It combines technological and clinical breakthroughs in developing new robotic systems and surgical techniques to improve the quality and outcome of surgery. The promise of surgical robotics is to deliver high levels of dexterity and vision to anatomical structures that cannot be approached by the surgeon's fingers and viewed directly by the surgeon's eyes, while simultaneously minimizing the impact and trauma to the tissue surrounding the surgical site. Making this technology available to surgeons has led to the development of new surgical techniques that would otherwise be impossible.

2.2.1 The Human-Machine Interface of Surgical Robot Systems

Two human-machine interfaces are established with the introduction of a surgical robotic system: the surgeon-robot interface (S-R) and the patient-robot interface (R-P). Each has a unique set of requirements that dictates its design capabilities and functions. These two interfaces may be used to classify the various surgical robotic systems as depicted in Fig. 2.1.

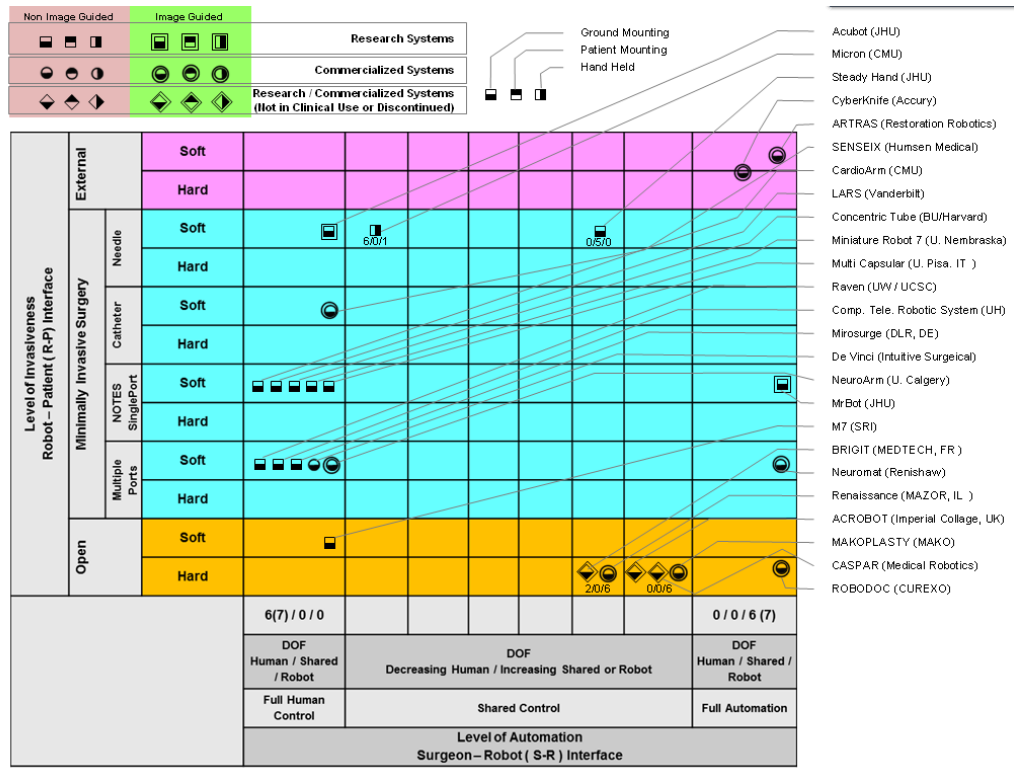


Figure 2.1: Classification of surgical robotic systems based on a Surgeon-Robot (S-R) interface (horizontal axis) defining the level of automation and a Robot-Patient (R-P) interface dictating the level of invasiveness (vertical axis).

The S-R interface is defined by a wide spectrum of control levels provided to the surgeon over the surgical robotic system (Figure 1 - horizontal axis). Assuming a certain level of control required to complete a task, this control level can be distributed between the human operator and the robotic system at different ratios. The distribution of the control level between the surgeon and the robotic system defines the level of automation allocated for the task. The level of automation is bounded by

two extreme scenarios. In a fully autonomous mode of operation, the surgical robot executes a predefined trajectory, maintaining full control over the execution of a plan that was predefined by the surgeon. The surgeon initiates the execution of the process and monitors its progress. Other than to terminate the procedure in case of emergency, the surgeon will not be able to change the preoperative planning during its execution. In a full surgeon control mode of operation any movement of the surgical robotic system is in direct response to a real time position command input provided by the surgeon. The system architecture used to enable this approach is teleoperation, utilizing a master/slave configuration. The master is defined as the surgical console and the slave serves as the surgical robot itself interacting with the patient's tissue through the surgical tools. The teleoperation architecture brings the surgeon back into the surgical scene to control and execute every motion of the surgical robot.

The level of automation incorporated into a robotic surgical procedure varies widely, and is defined by the how the surgical task is shared between the robotic system and the surgeon. At one end of the spectrum, the surgical procedure may be broken down into sub tasks and selected subtasks can be automated. At the other end of the spectrum, an effort is made to develop a control strategy in which both the surgeon and the robot hold a set of surgical tools simultaneously and collaborate during the surgical procedure.

The robot-patient (R-P) interface determines the level of invasiveness (see Fig. 2.1 - vertical axis). The level of invasiveness spectrum spans across a range of surgical approaches including (1) the invasive open-procedure approach, which requires a large incision to expose the targeted anatomy, (2) variations of minimally invasive surgical approaches with a gradual reduction of invasiveness, such as multiple tools inserted through ports, NOTES, catheters and needles and a noninvasive approach in which energy (radiation) is provided by an external source to a localized space to provide a localized therapy. As the level of invasiveness decreases, the level of manipulation also decreases and, as a result, the surgeon has fewer degrees of freedom to mechanically manipulate the tissues.

As depicted in Fig. 2.1, most of the systems are either fully tele-operated by the surgeon [add ref] or run autonomously executing preplanned trajectories [add ref]. The space between these two extreme scenarios in which the surgeon collaborate with the surgical robotic system and share control is lightly populated [add ref]. In general, some current research efforts in the field focused on operating the surgical robot in a collaborative fashion utilizing autonomy and supervisory control along with a parallel

efforts to reduce the size of the robot’s end effector and the foot print of the surgical robot as a whole.

2.2.2 Challenges in the Design of Multi-arm Surgical Robot Systems

Surgical procedures are traditionally performed by two or more surgeons, along with staff nurses. The collaborative effort of two or more surgeons is a derivative of the high cognitive and manual loads introduced by the surgical procedure itself. With the introduction of a surgical robot into the operating room, the dynamics between the primary and assisting surgeons changed significantly. The primary surgeon, who controls the surgical robot, is immersed in a surgical console and is physically removed from the surgical site itself, while the assistant is usually located next to the patient and holds another set of non robotic surgical tools. Reproducing the interaction of two surgeons with the surgical site using a surgical robotic system requires at least four robotics arms and two stereo cameras rendering the surgical site. Once multiple robotic arms were introduced several operational modes are available in which each pair of arms can be under full human control or under semi autonomous mode (supervisory control).

In spite of the advantages the introduction of multiple robotic arms into a relatively small space presents a challenge. From the operational perspective the need is to maximize the common workspace that is accessible by the end effectors of all four arms. This common workspace must overlap the surgical site dictated by the patient internal anatomy. Increasing the common workspace may lead to a larger robotic arms that may result in patient-robot or robot-robot collisions.

Other Previous research efforts mainly focused on the design of port placement for cardiac procedures while using several existing robotic arm architectures such as the Zeus [111, 112] or DaVinci [113, 114] or a similar four bar mechanism [115] inserted between the ribs. With the introduction of four robotic arms, a new optimization approach is required for designing the size and the shape of the common workspace of the four robotic arms while ensuring the kinematic performance of each robotic arm. The scope of this research effort is a kinematic optimization of the surgical robotic arms in terms of their structural configurations as well as their positions (port placement) and orientations with respect to the patient.

2.3 Kinematically Redundancy Resolution Methods for Robotic Manipulator Control

2.3.1 Robotic Manipulators with Kinematic Redundancy

A kinematically redundant robotic manipulator processes more degrees of freedom (DOFs) than those strictly required by its task. As a result, the redundancy of a manipulator is a task-based characteristics rather than an inherent property. Since only six DOFs are needed to fully specify the position and orientation of an object in a three-dimensional (3D) workspace, a robotic manipulator with seven DOFs are definitely kinematically redundant with respect to tasks in such a workspace.

The kinematic redundancy is a beneficial characteristics of a robotic manipulator. The fault tolerant properties of the kinematical redundancy [116] is an attractive characteristics for the robotic arms working at distant and/or hazardous locations [117, 118, 119]. Traditionally, robotic manipulators has been utilizing the kinematic redundancy to sustain in the presence of the joint failures such as free-swinging joint failures [120] or locked joint failures [121]. A redundant manipulator is able to compensate the failure of some of its joints with the extra degree of freedom, being affected by reduced manipulability in the workspace instead of losing the control of its end-effector [122].

Besides the advantage of failure tolerance, the kinematic redundancy enables the robotic manipulator with improved manipulability. The improved dexterity may help with avoiding singularities, joint limits, as well as obstacles in the workspace [123, 124], in addition to completing the main task. Moreover, the kinematic redundancy can be employed in controlling a manipulator's postures [125], the impulsive force and rebounded effects [126], and the joint torque [127], and optimizing the motions for proper performance indices.

The design and control of the redundant robotic manipulators have been inspired by the control of articulated biological limbs. A human-arm-like manipulator, or an upper limb exoskeleton that consists of seven degree of freedom can be controlled according to the control strategy of human arm movements. The hyper-redundant manipulators [128, 129] intend to imitate the morphology of various biological limbs swan's necks [130], snakes [131], elephant trunks [132] and tentacles [133]. The highly articulated structures that process a large or infinite number of degrees of freedom results in enhanced dexterity for operations in congested environments and there-

fore are capable to rendering highly sophisticated movements. Observations on the motions of the biological systems have shown that the hyper-redundancy perform relatively restricted movements, which can be described with simple parameters and be governed by simple control algorithms.

2.3.2 Redundancy Resolution at Different Levels

By resolving the inverse kinematics problem, a mathematically relation is derived between the joint-space configuration and the task-space specification of a redundant manipulator. Given the joint-space coordinate vector θ and the task-space coordinate vector x , the relation between the joint-space and task-space can be expressed by the different levels of kinematics.

- At the position level, the relation is expressed by the direct kinematics:

$$x = T(\theta) \quad (2.1)$$

where T is a nonlinear vector function.

- At the velocity level, the relation is expressed by the first-order differential kinematics:

$$\dot{x} = J(\theta)\dot{\theta} \quad (2.2)$$

Where \dot{x} is the task-space velocity vector, $\dot{\theta}$ is the joint space velocity vector, $J(\theta)$ is the $M \times N$ analytical Jacobian.

- At the acceleration level, the relation is expressed by the second-order differential kinematics:

$$\ddot{x} = J(\theta)\ddot{\theta} + \dot{J}(\theta)\dot{\theta}\dot{\theta} \quad (2.3)$$

Most of the inverse kinematics problems express the input in form of a reference velocity or acceleration. Therefore, the redundancy resolutions are mostly proposed

at the velocity or acceleration level. For a time-varying task, the inverse kinematics are preferred to be resolved analytically.

The redundancy resolutions at the velocity level are of two types: the exact and the approximate solutions. For an under-determined system described by Eq. (2.2), a least-squares solution that minimizes the Euclidian norm of joint velocity vector is an exact solution, while the damped least squares method provides an approximate solution. The computation of joint accelerations is required when controlling the dynamics of a robotic manipulator, such as in the case of compliant control. As a result, kinematic redundancy should be resolved at the acceleration level.

The exact and approximate redundancy resolution at the acceleration level can be derived in a similar way. The resulted redundancy resolutions minimize the norm of the joint acceleration vector \ddot{x} . Unlike the kinematic redundancy resolutions at velocity level, the redundancy resolutions at acceleration level may be internally instable [134], which is due to the instability of the zero dynamics given the formulation in Eq. (2.3). The pseudo-inverse solution at velocity level results in a minimum norm velocity solution, which does not have any null space component, while the pseudo-inverse solution at the acceleration level generates a minimum norm acceleration solution, which does not guarantee the elimination of the null space component of the velocity. This zero dynamics problem can be resolved by requiring the symbolic expression of the derivative of the pseudo-inverse of the Jacobian matrix at a cost of large amount of computation [135]. A alternative method combines the computational efficiency with stabilization of internal motion [39].

The kinematic redundancy can also be resolved in the framework of configuration control. In this framework, additional task requirement are integrated in the Jacobian matrix. The possible additional task requirements can reflect desirable kinematic characteristics of manipulator such as posture control, joint limiting, and obstacle avoidance, if the redundancy is resolved at velocity level. Similarly, dynamic task requirements (e.g., contact forces, inertia control, etc) can be introduced to the redundancy resolutions at acceleration level [136].

2.3.3 General Resolution to Inverse Kinematics

In general, the inverse kinematics formulated in Eq. (2.2) or Eq. (2.3) can be resolved using the pseudo-inverse method. the pseudo-inverse of the Jacobian matrix J , denoted by J^\dagger , satisfies the Moore-Penrose conditions described by Equations (10.71)

to (10.74).

$$JJ^\dagger J = J \quad (2.4)$$

$$J^\dagger JJ^\dagger = J^\dagger \quad (2.5)$$

$$(JJ^\dagger)^T = JJ^\dagger \quad (2.6)$$

$$(J^\dagger J)^T = J^\dagger J \quad (2.7)$$

For the low-rectangular and full-rank Jacobian, the pseudo-inverse can be computed as:

$$J^\dagger = J^T (JJ^T)^{-1} \quad (2.8)$$

The resulted general solution to Eq. (2.2) can be written as:

$$\dot{\theta} = J^\dagger \dot{x} + (I - J^\dagger J)\dot{\theta}_0 \quad (2.9)$$

Eq. (2.9) provides all the least square solution to the end-effector task constraint at velocity level. It minimizes $\|\dot{x} - J\dot{\theta}\|$. In other words, if J is low-rectangular and full-rank, all joint velocities given by Eq. (2.9) exactly realize the assigned task velocity. $I - J^\dagger J$ represents the orthogonal projection matrix in the null space of J , and $\dot{\theta}_0$ is an arbitrary joint space velocity. Indeed, the $(I - J^\dagger J)\dot{\theta}_0$ is the null-space velocity. By acting on $\dot{\theta}_0$, one can still obtain different joint velocities that give the same end-effector task velocity. Note that the particular solution obtained by $\dot{\theta}_0 = 0$ provides the least square solution of Eq. (2.9) and is known as pseudo-inverse solution. The least square solution quantifies the accuracy of the end-effector.

With regards to the second order kinematics in Eq. (2.3), the least square solution can be expressed as

$$\ddot{\theta} = J^\dagger (\ddot{x} - J\dot{\theta}) + (I - J^\dagger J)\ddot{\theta}_0 \quad (2.10)$$

where $\ddot{\theta}_0$ is an arbitrary joint space acceleration. The particular solution for $\ddot{\theta}_0 = 0$ gives the acceleration vector with minimized Euclidian norm.

Singular value decomposition (SVD) can be applied to the pseudo-inverse matrix

J^\dagger to investigate the singularity robustness of the pseudo-inverse solution. By singular value decomposition, J^\dagger can be expressed as:

$$J^\dagger = V\Sigma U^T = \sum_{i=1}^R \frac{1}{\sigma_i} v_i u_i^T \quad (2.11)$$

Where R is the rank of the Jacobian matrix, and $\sigma_1 \geq \sigma_2 \geq \dots \geq \sigma_R \geq 0$. Relating Eq. (2.11) with Eq. (2.9), it can be found that the task velocity is first decomposed along u_i and then reconstructed along v_i . A scaling factor of $\frac{1}{\sigma_i}$ is applied between decomposition and reconstruction. When a singularity is approached, the R -th singular value tends to zero and $\frac{1}{\sigma_R}$ tends to infinite. Therefore, excessive joint-space velocities are required in the neighborhood of singularity. Particularly at the singularity point, the joint space solution is discontinuous.

2.3.4 Task-based Redundancy Resolution

For given task, the Jacobian matrix consisting of the mechanical constraints can be augmented by the task-dependent constraints [137, 13, 14]. By extending the Jacobian matrix, the freedom of the under-determined system is reduced and the inverse kinematics may be resolved as controlling a non-redundant manipulator. Note that to fully eliminate the redundancy, the dimension of the additional task constraints should be equal to the degree of redundancy. The augmentation of Jacobian matrix may introduce artificial singularities in addition to the inherent singularity of the mechanical system. Since it is hard to analytically distinguish the artificial singularity introduced by the task-based augmentation from the inherent singularity, the solution based on the inverse of the augmented Jacobian may result in instability near a singular configuration. A singularity robust and task prioritized formulation was proposed, using the weighted damped least square method at the velocity level. Under the framework of configuration control, the solution is given by

$$\ddot{x} - J\dot{\theta} = J\ddot{\theta} \quad (2.12)$$

This method aims to minimize the cost function of $\dot{E}_e^T W_e \dot{E}_e + \dot{E}_c^T W_c \dot{E}_c + \dot{\theta}^T W_v \dot{\theta}$, where $W_e(m \times m)$, $W_c(k \times k)$ and $W_v(n \times n)$ are diagonal positive-definite weighting

matrices that assign priority between the main task, additional task and the singularity robustness task. $\dot{E}_e = \dot{x} - \dot{x}_d$ and $\dot{E}_c = \dot{z} - \dot{z}_d$ are the n-dimensional and k-dimensional vectors representing the residual velocity errors of the main task and the additional task. This method does not have the restrictions on the dimensions of the additional task, comparing to method of augmented Jacobian matrix,

2.3.5 Performance-based Redundancy Resolution

For kinematically redundant manipulators, the inverse kinematics problem admits an infinite number of solutions such that a criterion to select one of them is needed. Hence, the redundancy resolution can be considered from the perspective of optimization at the velocity level of kinematics and multiple performance indices are available to serve as the optimization criterion.

Performance indices	Formula	Comments
Determinant of Jacobian (1984)	$w_n = \sqrt{J J^T}$	Uniformity of the torque-velocity gain
Condition number (1982)	$\kappa = \frac{\sigma_{max}}{\sigma_{min}}$	Variance in velocity/force transmission
Isotropy (1987)	$Iso = \frac{\sigma_{min}}{\sigma_{max}}$	same as condition number
Min eigen-value of Jacobian (1987)	$Iso = \frac{\sigma_{min}}{\sigma_{max}}$	Efficiency of force/velocity transmission
Dynamic Manipulability (1985)	$G = J^{-T} M J^{-1}$	Uniformity of this torque-acceleration gain
Distance from singularity (1987)	$H = \prod_i^p \Delta_i ^{1/p}$	Related to manipulability by $w_n = \sqrt{\sum_i^p \Delta_i}$
Acceleration radius (1988)	$\tau = M(\ddot{\theta}) + C(\theta, \dot{\theta})\dot{\theta}$	acceleration capability of the end-effector
Force transmission ratio (1988)	$\alpha = [(u^T (J J^T) u)^{1/2}]$	Force gain along task-compatibility direction
Velocity transmission ratio (1988)	$\beta = [u^T (J J^T)^{-1} u]^{1/2}$	Velocity along task-compatibility direction
Min Jerk model (1984)	$\min\left(\frac{\partial^3 x}{\partial t^3}\right)$	Motion smoothness
Min (commanded) torque-change (1985,1989)	$\min\left(\frac{\partial \tau}{\partial x}\right)$	Motion smoothness
Min work model (1983)	$\min(W)$	Energy
Min variance model (1989)	$\min[\text{var}(x - x_d)]$	Task accuracy

Table 2.1: Performance Indices Used for Redundant Robotic Manipulator Control

Manipulability

The motivation to study manipulability of robots comes from the fact that, in order to perform an end-effector twist or to withstand a wrench acting on the end-effector, the velocities and the efforts at the actuators are, in general, greater at configurations close to singularities. At singular configuration, some twists cannot be executed and some wrenches can only be passively resisted by the manipulator. Therefore, maintaining a manipulator away from singularities is convenient to general task execution.

By defining the manipulability as the distance from the singularity, the Jacobian matrix J (or the matrices JJ^T when J is a low-rectangular matrix) has been the object of study to characterize manipulability, which implicitly indicate the proximity of a configuration to a singularity. Many performance indices have been proposed to characterize the manipulability performance, including the condition number, the isotropy, the minimum singular value of Jacobian, the minimum eigenvalue of the Jacobian and the determinant of Jacobian. Due to the fact that by normalization, the determinant of Jacobian is invariant with respect to changes of reference frame, which make this performance indices the most popular one as measurement of manipulability. Note that there are other proposed performance indices for the characterization of manipulability, on the premise of defining the manipulability as the manipulability as the properties of the forward kinematic map between joint space and task space. For example, [138] interpreted the manipulability as how closely the forward kinematic map of a manipulator approximates an isometry whereas [139] regarded the manipulability as the efficiency of the velocity and force transmission between the joint space and task space as certain configuration of the manipulator.

For robots with only one type of joints and for one type of tasks, the transformation of velocities (forces) can be characterized by a comparison of the end-effector velocity (wrench) produced by unit joint velocities (torques) [140]. Therefore, the manipulability can be analytically represented by velocity (force) ellipsoid.

Considering the joint velocities contained in the unit sphere of the joint velocity space, such that

$$\dot{\theta}^T \dot{\theta} \leq 1 \quad (2.13)$$

It can be shown that the corresponding velocities in the task space are defined by

$$\dot{x}^T (JJ^T)^{-1} \dot{x} \leq 1 \quad (2.14)$$

The velocity ellipsoid is useful for analyzing the velocity transmission performance of the robot. The principle axes of the ellipsoid are given by the vector of U_i , which are the eigen-vectors of JJ^T . The length of the principle axes are determined by the singular value σ_i of J . The optimum direction to generate velocity is along the major axis where the transmission ratio is maximized. Conversely, the velocity is most accurately controlled along the minor axis. The volume of the velocity ellipsoid of a robot gives a measurement of its capacity to generate velocity. Consequently,

According to the duality of the velocity and force transmission, the the capacity of force transmission can also be represented by the force ellipsoid. The principle axes of the force ellipsoid coincide those of the velocity ellipsoid. The length of a principle axis of the force ellipsoid is reciprocal of that of the velocity ellipsoid in the same direction.

- Determinant of Jacobian

Based on the construction of manipulability ellipsoid, the velocity manipulability of the robot can be defined as:

$$w_n(\theta) = \sqrt{\det[J(\theta)J^T(\theta)]} \quad (2.15)$$

Since the motion are caused by forces and torques acting on rigid body, it seems reasonable to formulate performance indices that takes into account the inertial properties of the mechanism. Asada [15] proposed the generalized-inertia ellipsoid (GIE), as the ellipsoid defined by

$$GIE = J^{-T} M J^{-1} \quad (2.16)$$

where M denotes the inertia matrix of the manipulator and J is the Jacobian matrix.

Based on the generalized-inertia ellipsoid, Yoshikawa [16] further defined a corresponding dynamic manipulability measure as

$$w_d(\theta) = \det[J M^{-1} (J M^{-1})^T] \quad (2.17)$$

Note that w_d measures the uniformity of this torque-acceleration gain, whereas GIE characterizes the inverse of this gain. If a human operator were holding the end-effector and attempting to move it about, the GIE would measure the resistance of the robot to this end-effector motion.

- Condition Number

Salisbury and Craig [141] introduced the concept of dexterity when working on the design of articulated hands. As demonstrated by the velocity/force ellipsoid, the Jacobian matrix distorts the velocity/force inputs that are uniformly applied towards all the directions joint space into an ellipsoidal outputs in the end-effector space. The condition number is used to describe the distortion in the velocity and force transmission. Along the direction of major semi-axis of the ellipsoid, disturbance in the joint space will result in larger error of end-effector in the task space. Therefore, the condition number also measures the ability of error propagation of a mechanism at some kinematical configuration.

The condition can be computed in more than one ways. One of the computation defined the condition number as the ratio of the largest singular value (σ_M) to the smallest singular value σ_m of the Jacobian. This definition of condition number implies intensive computation for all the singular values of the Jacobian matrix J and can not be conducted analytically.

$$\kappa_2 = \frac{\sigma_M}{\sigma_m} \quad (2.18)$$

The computation of condition number in Eq. (2.18) is applicable to both rectangular matrices and square matrices. Particularly for square matrices, the condition number can be defined in a more general way as

$$\kappa(A) = ||A|| \cdot ||A||^{-1} \quad (2.19)$$

where

$$||J|| = \begin{cases} \max_i (\sigma_i) & \text{for 2-norm} \\ \sqrt{\frac{1}{n} \text{tr}(JJ^T)} = \sqrt{\frac{1}{n} \text{tr}(J^T J)} & \text{for weighted matrix Frobenius norm} \end{cases} \quad (2.20)$$

Note that the computation of the weighted matrix Frobenius norm $||J||_F$ does not require the knowledge of all the singular values. It produces the root-mean-square (RMS) value of set of the singular values, regardless of the number of rows and columns of the Jacobian matrix. Based on the weighted matrix Frobenius norm, a Frobenius condition number can be defined as

$$\begin{aligned} \kappa_F(J) &= \frac{1}{n} \sqrt{\text{tr}(JJ^T)} \sqrt{\text{tr}[(JJ^T)^{-1}]} \\ &= \frac{1}{n} \sqrt{\text{tr}(J^T J)} \sqrt{\text{tr}[(J^T J)^{-1}]} \end{aligned} \quad (2.21)$$

which can be computed analytically.

The analytical computation of the condition number brings about great advantage in robotic design. The differentiable $K_f(\cdot)$ can be used in gradient-dependent optimization methods, which are much faster than direct methods based only on function evaluation. In robot control, real-time computation of $K_f(\cdot)$ can be conducted by matrix inversion. The computational burden of singular values are avoided.

- Isotropy

$$Iso = \frac{1}{\kappa(J)} \quad (2.22)$$

Kinematic isotropy Iso is defined by [142] as defined as the reciprocal of its min

condition number κ_J , which denotes the singular values of the Jacobian matrix are all identical and non zero at certain kinematically possible configuration. Similar to the condition number, the concept of isotropy is applicable to both the square Jacobian matrices and rectangular Jacobian matrices [143]. Robotic manipulators with serial [144] and parallel structure [145] can use the isotropy as a conditioning index for performance measurement, as well as the guideline of control and design.

- Task Compatibility

- Acceleration Radius

The acceleration radius is initially proposed to measure the minimum acceleration capability of the end-effector in arbitrary directions, for given torque bounds on the actuators [146]. Specifically, given the dynamic equations for a serial chain in the form

$$\tau = M(\ddot{\theta}) + C(\theta, \dot{\theta})\dot{\theta} \quad (2.23)$$

in which M is the inertia matrix and $C(\theta, \dot{\theta})$ is the matrix mapping the joint-rate vector to the vector of Coriolis and centrifugal in the joint space. Moreover, the actuator are assumed to have joint torque limits of the form

$$\tau_{min} \leq \tau \leq \tau_{max} \quad (2.24)$$

where the lower and upper limits τ_{min} and τ_{max} are constant or functions of the manipulator posture θ . The end-effector **twist rate**, denoted as \dot{t} , can be expressed as

$$\dot{t} = J(\theta)\ddot{\theta} + J(\theta, \dot{\theta})\dot{\theta} \quad (2.25)$$

where $J(\theta, \dot{\theta})$ is the Jacobian matrix time-derivative.

Under the assumption that $J(\theta)$ is nonsingular, one can write

$$\ddot{\theta} = J(\theta)^{-1}\dot{t} - J(\theta)J(\theta, t) \quad (2.26)$$

substituting the above expression into the Eq. (2.23) leads to

$$\tau(\theta, t, \dot{t}) = M'\dot{t} - C'(\theta, t) \quad (2.27)$$

where

$$M' = M(\theta)J(\theta)^{-1} \quad (2.28)$$

$$C' = [C(\theta, t) - M(\theta)J(\theta)^{-1}\dot{J}(\theta, t)]J^{-1}(\theta) \quad (2.29)$$

Hence for a given state $(\theta, \dot{\theta})$ and the limits of torques as Eq. (2.24), a polytope in the twist-rate space is defined.

In [146], the acceleration radius is defined as the largest sphere centered at the origin that is constrained in this polytope; the radius reflects the minimum guaranteed end-effector acceleration in arbitrary directions. This concept is applied to measure the end-effector acceleration radius. In [147], this concept is generalized to capture both the force and acceleration capabilities of the end-effector, with a view to quantifying the worst-case dynamic performance capability of a manipulator.

- Other Characterization of Manipulability

The various definitions of manipulability discussed above all refer to the same qualitative feature of the ability of a robot to move and apply force in arbitrary directions. A different viewpoint is taken in the work of Liegeois [148] and Klein and Huang [149], where dexterity is quantified in terms of joint range availability. The driving motivation here lies in that most robots have joint limits; therefore, one should minimize the possibility of a joint reaching a stop.

From a control perspective, Spong [150] shows that if the inertia matrix of

a manipulability has a vanishing Riemannian curvature, there exists a set of coordinates in which the equations of motion assume a particularly simple form. The curvature of the inertia matrix also reflects the sensitivity of the dynamics to certain robot parameters. Minimizing the curvature, therefore, is another possible criterion for dexterity.

- Global Manipulability Indices

Available manipulability indices are generally proposed as local measurement. They are useful for applications ranging from redundancy resolution to workspace positioning, but for design applications, a global measurement may be more desirable. One straightforward way of extending local measurements to global ones is to integrate them over the allowable joint space. In [151], Gosselin and Angeles integrate the Jacobian condition number over the workspace to define a global measurement, thereby producing a global conditioning index. For the simpler cases of planar positioning, and spherical manipulators, the global conditioning index was found to coincide with its local counterpart.

- Velocity ratio and mechanical advantage

Velocity ratio (VR) and mechanical advantage (MA) are performance measurement for single-input-single-output mechanisms. The velocity ratio is the ratio of the velocity applied to a mechanism to the acquired velocity that is motivated by this input. Similarly, the mechanical advantage is the ratio of the output force of a mechanism to the input force that motivates this output. As a performance measurement, the velocity ratio in a direction represents the mechanism's efficiency of moving in that direction, while the mechanical advantage in a direction describes the mechanism's ability of applying force in that direction. For an ideal mechanism, the velocity ratio equals to its mechanical advantage, indicating the fact that the input work equals to the output work and the mechanism has no energy dissipation.

The concept of the velocity ratio and mechanical advantage can be naturally extended to evaluate the performance of a multi-input-multi-output mechanical system. When applied to redundant manipulator, the velocity ratio can be defined as the ratio of the Euclidean norm of the end-effector velocity to the norm of joint velocity, while the mechanical advantage can be defined as the ratio of the end-effector force and moment vector norm to the joint torque vector

norm [152].

2.4 Control Strategies of Human Arm Movements

2.4.1 Characteristics of human arm movements

Research on the characterization of human arm movements falls into two categories: from the perspective of regularity, the movements of healthy human arms demonstrate significant similarity when completing daily-life tasks, within and across human individuals; from the perspective of variability, it has been observed that the arm movements of each human individual are not exactly the same even when repeating the same task. These characteristics, namely regularity and variability universally exist in human movement, including human arm movement. Both of them contribute to the higher performance of the human arm, compared to that of existing robotic arms.

Regularity in human arm movements

For decades, continuous research efforts on the regularity of human movements intended to reveal the control strategy of the healthy human motor system. Posture-based motion control strategies such as the Donders' law, the Fitts' law, the 2/3-power law have been experimentally tested, which resulted in a category of postured-based motion planning strategies.

- Donders' law

According to Donders' law, the central nervous system (CNS) chooses a unique eye orientation for each gaze direction. When applied to human arm movements, Donders' law predicts that every position of the hand in 3D space naturally corresponds to a unique posture of the arm, which can be parameterized by joint angles at the shoulder and elbow. The unique pointing direction of the human arm corresponding to a given hand position (denoted by \vec{r}) can be expressed by a rotation axis \vec{n} and a rotation angle α .

$$\vec{r} = \tan \frac{\alpha}{2} \vec{n} \quad (2.30)$$

However, there have been experimental results that contradicted Donders' law. The law is obeyed more strictly for pointing movements with straight arms than for pointing movements with less restriction. According to Soechting *et al* [32], the arm posture corresponding to a given hand location is not independent of its previous posture. Furthermore, it has been confirmed that Donders's law is violated in some 3D space tasks [153]. The upper arm torsion varies widely when the pointing target is specified, yet the variation of torsion can be reduced by specifying the elbow angle. Note that while Donders's law is partially valid for reaching/pointing movements, it is generally invalidated by grasping experiments [32, 33]. Due to the limited motion range at the wrist, the posture of the upper arm is strongly affected by hand orientation and therefore the violation of Donders's law is significant. Without restricting the precise orientation of the hand, Donders' law might still be applicable to the arm motions [154].

- Fitts' law

The Fitts' law pointed out that the faster the pointing motion is conducted, the less accurate the pointing could be [155]. It predicts that the time required to rapidly move to a target area is a function of the distance to and the size of the target. By extending the Shannons theorem, the Fitts' law can be mathematically formulated as:

$$T_M = a + b \log_2\left(\frac{2A}{W} + c\right) \quad (2.31)$$

where T_M is the movement time; A is distance between the initial position and the target position; W is the width of the target, reflecting the accuracy of the motion; a and b are device dependent constants; c is constant which takes 0, 0.5 or 1 for different variation of the Fitts law [156].

The Fitts' law originates from the physical touching of the object with a hand or a finger and is generally applicable to motion of feet, head-mounted sights, eye gaze, as well as to human motion in virtual environments. The formulation of Fitts' law can be more complicated for better data fitting, yet models of less complexity is preferred according to the philosophy of Occam's razor [37]. Essentially, all variations of Fitts' law are about the trade-off between the motion speed and motion accuracy.

- The 2/3 Power Law

The 2/3 power law presents the invariant features of human motion by describing the relation between motion trajectories and motion velocity. Primitive study on handwriting and drawing motion reveals the existence of the systematic relationship between the velocity of the end-effector and the geometric path of the motion [157, 158]. This relationship was further quantified as 2/3 power law, saying the angular velocity of the end-effector $\omega(t)$ is proportional to the curvature of the end-effector trajectory $k(t)$ such that

$$\omega(t) = C_1 k^{\frac{2}{3}}(t) \quad (2.32)$$

Where C_1 is constant. Given the fact that the radius $r(t)$ is reciprocal of the curvature $k(t)$, the 2/3 power law can also be expressed as a function of the linear velocity of the end-effector as:

$$v(t) = C_2 k^{\frac{1}{3}}(t) \quad (2.33)$$

where C_2 is constant. The alternative expression of 2/3 power law is based on the fact that the linear velocity of the end-effector $v(t)$ is equal to the product of angular velocity $\omega(t)$ and the radius $r(t)$, i.e.,

$$v(t) = \omega(t)r(t) \quad (2.34)$$

The definition of the 2/3 power law implies that the data points on a natural human motion trajectory should fall on a straight line of slope 2/3, if the angular velocity $\omega(t)$ and the curvature of trajectory $k(t)$ are both plotted in their logarithms. The test of the 2/3 power law are straightforward. The validity of this power law has been generally supported, with small derivations at the exponent index and at the constant coefficient. Experimental results demonstrates that the 1/3 at the exponent of Eq. (2.33) is more complied by the motion with small amplitude. It is also noticed that the proportional co-

efficient C_1 in Eq. (2.32) may change discontinuously with each new segment motion is introduced, which results in the hypothesis that drawing movements in 3D can be decomposed into piecewise planar end-effector trajectory. Further derivations from the 2/3 power law depend on the change of curvatures along a trajectory. In the experiments of tracking moving targets, The linear velocity is slower than the prediction of 2/3 power during the path segments of high curvature and faster than the prediction during the path segments of low curvature [159].

Several hypotheses have been proposed to reveal the underlying mechanisms that account for the 2/3 power law. One of the explanation suggests that the velocity-curvature might result from the coupling of two independent harmonic oscillators. Indeed, it can be shown that 2/3 power law is applicable to any movement consisting of two orthogonal harmonic oscillation components. An alternative explanation proposed that the 2/3 power law is due to the smoothness of the motion. The 2/3 power law might be the side effect of jerk minimization in the motion control. To summarize, the 2/3 power law that is consistent with other control strategies tends to be a converging phenomena instead of underlying principle.

The posture consistency in reaching movements of the human arm revealed by the above arm motion laws results in a category of posture-based movement planning strategies. These movement planning strategies assume that there exists an optimal final posture for each target position at the end of the trajectory. This assumption contradicts the prediction of trajectory-based movement planning strategies, which may lead to various arm postures at the end of the trajectory. It was proposed that posture-based strategies plan the movements at a kinematic level, while trajectory-based strategies plan the movements at a dynamic level [160]. Other approaches of combining movement planning at kinematic and dynamic levels with the posture at the end of the trajectory are described in [161, 162]. The predictions of available hypothesis, working individually or collaboratively, are not fully complied with the natural motions generated by human arms, which implies necessity of hypothesis on new motion strategies and on the way that multiple motion strategies are integrated.

Variability in human arm movements

Variability is another universal characteristic of the motor control of human arm movements [163, 164]. Early experimental studies (e.g. recording of hammering movements by Bernstein [165]) in human motor control find that human movements do not repeat in exactly the same way for the same task, even with intention. It has been found that this variability can be used as a signature to distinguish skilled from unskilled task performance. A lower level of the variability may indicate the existence of control, while its absence may indicate diseases [166]. The redundancy in the human motor system may contribute to the variability of human movements, though it is not necessarily the source of the variability [167, 168, 25].

2.4.2 Redundancy resolution based on performance optimization

By controlling redundant degrees of freedom, the resolution of inverse kinematics or inverse dynamics can satisfy additional task-based constraints and/or achieve an optimized performance. Existing research has considered performance optimization from the perspectives of manipulability, energy consumption, smoothness of movement, task accuracy and control complexity. Task-based redundancy resolutions are more straightforward since the control of the extra DOFs can be generally achieved by integrating the task-dependent constraints into an augmented Jacobian matrix [137, 13, 14]. The redundancy resolutions based on performance optimization tend to be more flexible, given that there are many performance indices in consideration.

Manipulability performance

At a singular configuration, a manipulator can only execute motion and/or resist wrenches in limited directions. Keeping the manipulator away from its singularities is convenient for task operation in general, and this can be achieved either by mechanical design and/or motion planning.

Manipulability was originally defined either as the distance from the singularity [?], or as the efficiency of velocity/force transmission [139]. The Jacobian matrix, denoted as \mathbf{J} (or the matrix \mathbf{JJ}^T if \mathbf{J} is a lower-rectangular matrix), has been used to quantify manipulability. Singular value decomposition (SVD) can be applied to

the Jacobian matrix of manipulators, in order to construct the manipulability ellipsoid [140]. Possible manipulability indices for performance optimization are mostly based on the measures of the manipulability ellipsoid. The radii of the manipulability ellipsoid are frequently considered, either for the maximum/minimum singular values, or for their ratio (e.g., condition number [15], isotropy [142]). The determinant of the Jacobian matrix or dynamic Jacobian is also considered, resulting in performance indices such as manipulability and dynamic manipulability [16, 17].

The directions of the principle axes of the manipulability ellipsoid have rarely been considered as manipulability performance indices. It is worth noting that the direction of the principle axes indicate the movement efficiency of a manipulator configuration. For a given uniform effort (measured by joint velocity) in all the applicable directions in the joint space, the most efficient movement in task space is in the direction of the major principle axis of the manipulability ellipsoid, while the least efficient movement in task space is in the direction of the minor principle axis. With regards to global manipulability, indices such as condition number, isotropy can be integrated for the measurements of the workspace [151, 169].

Energy performance

Minimization of energy, either in joint space or task space, implies that the final arm posture depends on both the initial arm posture and the trajectory. As a consequence, the arm postures for a given 3D hand position are not unique. It has been shown that energy minimization can not account for the average behavior of the arm movement [170], of eye movements [171] and of some full-body movements (e.g., standing up from a chair [172]). However, the consideration of energy performance can not be ruled out given the effects of dynamics. Instead, it should be integrated into other performance considerations such as the smoothness of motion, which reduces energy consumption by penalizing joint torque [22, 23], muscle forces [172], or time-derivatives of end-effector acceleration (i.e. jerk) [20, 21, 173, 37].

Smoothness of movement

The idea of optimization for the smoothness of movement was first introduced as the minimization of jerk [20, 21], to account for the straight path and bell-shaped velocity of task-space trajectories in reaching movements, as well as for trajectories of "via-point" tasks, in which the hand is instructed to pass a sequence of positions. For

arbitrary arm movements, minimizing the jerk along the trajectory accurately predict the speed profile of the trajectory [173] compared to the 2/3 power law [157, 158, 159]. The minimization of jerk has been also extended to account for movements in grasping tasks [37]. An alternative of jerk minimization in task space is to minimize the jerk in the joint space [23].

Performance optimization for the smoothness of motion can also be achieved at a dynamic level by minimizing the time-derivative of joint torque [22, 23]. This minimization also accounts for the slight asymmetry observed in some via-point tasks, which cannot be addressed by kinematic motion strategies that ignore the nonlinear arm dynamics.

Task accuracy

Motor noise is considered to contribute to the variance of end-effector position across repetitions of the same task. It is known that motor noise is dependent on control, with its magnitude proportional to muscle activations [25, 174, 175]. As a consequence, the choice of control signals will affect the variability of a movement.

Within an open-loop control framework, the control strategy of minimizing the variance intends to optimize a sequence of muscle activations, for reduced variances in the end-effector positions and improved task accuracy [171]. The minimum variance model produces an accurate prediction of eye movements at the level of muscle activations, yet its prediction accuracy is not clear for human arm movements. Movements with longer durations can not be addressed by minimum-variance control, since the movement variability is strongly affected by sensory feedback, which is not considered in open-loop control [176].

However, considering the universal existence of the motor noise in biological systems, it makes sense to assume that there exists a general control strategy so that the relation between a trajectory and its velocity profile can be addressed.

Control complexity

Control strategies yield different performance in the presence of noise, even if the averaged behavior is the same [?]. Optimal feedback controllers can resolve the redundancy in real-time according to the minimum intervention principle: make no effort to correct deviations away from the average behavior unless the task performance is affected.

As demonstrated in [25], the minimal intervention principle pushes the state vector orthogonally to the redundant direction, in which performance is maintained and corresponding states are equivalent to each other. In the redundant direction, which has been quantified as an "uncontrolled manifold", the probability distribution of observed states scatters in a wider range, compared to the non-redundant direction. A wide range of behaviors [25, 165, 40, 177, 178] have provided evidence of the minimal intervention principle.

Integrating multiple criteria for better arm posture prediction

Existing hypotheses, either working collaboratively or individually, have not been able to fully predict the natural movements of human arms. However, the integration of multiple hypotheses for better prediction can help in understanding the control strategy of natural human arm movements. In this case, the challenge of formulating a cost function is that performance indices have different units, and therefore it is not trivial to combine them in a single criterion. Having this in mind, an appropriately chosen intermediate variable may help the integration of different indices into a single criterion. As shown in [28], the swivel angle is chosen as the intermediate variable, to merge two performance indices of different units (manipulability and energy). However, the chosen intermediate variable may have different levels of sensitivity to changes in different performance indices.

The optimization of a comprehensive cost function that integrates various types of performance indices cannot be simply extended from the optimization of a single performance index, particularly with the presence of noise and disturbance in the implementation of the movement plan [179, 21]. The optimization of a single performance index along a deterministic trajectory can be constrained by task-dependent constraints, such as end-effector position, velocity and acceleration specified for the beginning or ending state. Such constraints are not valid for stochastic problems, in which the final state is affected by noise.

2.5 Coordination of Macro- and Micro-structures in Human Arm Movements

2.5.1 Natural Separation of Macro- and Micro-structures in Human Arm

The natural separation of macro- and micro-structures exist in upper and lower human limbs. The separation results from the evolution of the limb morphology and is based on the functions and behaviors of limb segments. The macro- and micro-structures human limbs inspires the robotic manipulators integrating arm and finger, as well as the anthropometric wearable robot system consisting arm exoskeleton and hand/finger exoskeleton.

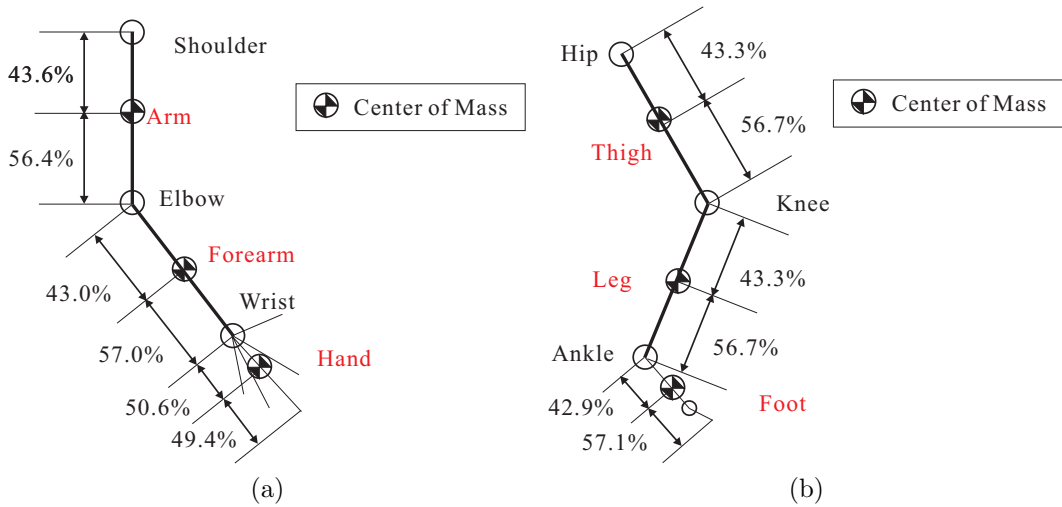


Figure 2.2: The limb segments with mass distribution: (a) the upper limb, (b) the lower limb.

In human anatomy, the upper limb consists of the shoulder, the arm, the elbow, the forearm, the wrist and the hand. The lower limb of human consists of the hip, the thigh, the knee, the leg, the ankle, and the foot. The lower limb constitutes a 15.6% of the total body weight), comparing to the much lighter upper limb which takes only 4.8% of the total body weight.(refer to Table 2.2). The center of gravity of the upper and lower limb segments are distributed as Fig. 2.2.

Human upper limbs are adapted to various tasks of object manipulation in time-varying environments, which requires the integration of two independent processes:

Table 2.2: Proportional Percentages of the Limb Segments to the Body Weight [1]

Limb Segments	Percentages of Total Body Weight (%)	Limb Segments	Percentages of Total Body Weight (%)
Arm	2.7	Thigh	9.7
Forearm	1.5	Leg	4.5
Hand	0.6	Foot	1.4
Total Upper Limb	4.8	Total Lower Limb	15.6

reaching and grasping [180]. The reaching process transport the hand toward the target, while the grasping concerned shaping the hand in accordance with the object. As observed in object manipulations, a successful object manipulation requires the sequencing and timing of reaching and grasping. In order to achieve a stable grasp, the relative timing of the wrist displacement and of the finger closure has to obey very strict constraints. Records clearly shows that the wrist velocity falls to zero at the time of contact of the fingers with object. If the hand displacement had not come to a stop at the time when the fingers closed, the object would be pushed forwards along the direction of reach. If the fingers had closed before contact, the object would be bumped and the grasp would fail; Conversely, if the finger closed too late, the contact with the object would be made with the palm of the hand, resulting in an awkward palmar grasp which indeed what may happen in pathological conditions.

The natural separation of the macro- and micro-structures in the upper limbs is at the wrist. The macro structure consists of the shoulder, the arm, the elbow, the forearm, and the wrist, which are mainly used for reaching. In the reaching movements, the shoulder allows the hands to be placed in all directions around the body, as well as turning the forearm inwards and outwards. The muscles arranged around the shoulder anchor the upper limb to the trunk. The weight of the upper limb are well supported during movements and are steadily hold in static postures for precise manipulation. The movements of the elbow bring a hand towards the head and the trunk. Particularly, the elbow flexion that can bring the hand to mouth is intensively used in daily activities such as eating, drinking and washing. The extension of the elbow allows for pushing against resistance. The elbow extension can also be used to assist body supporting and to compensate the lower limbs with power weakness.

The micro structure in the upper limbs is the hand, which involves palm and fingers. In object manipulation, the hand can conduct two kinds of grasping movements: (1) the power grasping and (2) the precise grasping. In the power grasp, all the fingers are flexed around the object. The thumb flexed in the opposite direction to the other four fingers for forcible press. The power grasp enable firm hold such that the manipulated objects can be efficiently moved by the macro structure of the upper limb, i.e. the motion at shoulder and elbow. The precise grasp hold the manipulated object with the thumb and no more than three of the other fingers. Precise grasp insists in the manipulation accuracy and requires better coordination among fingers. Actually, precision grasps are usually involved in two hand cooperation, with one hand conducting the precise manipulation and the other hand holding and stabilizing the manipulated object.

The two kinds of grasping movements differ in their motor behavior, particularly in their motor development. The power grasp is the most primitive grasping movements. The finger flexion in response to touching the palm is one of the primary reflexes of the newborn baby. Children of six months can perform palmar grasping, with the thumb properly placed in opposition. By the fifth year, children can perform power grasping individually with each hand. In contrast, the precise grasp is a more advance manipulation movements that requires independent control of each fingers [181]. After about ten months of age in children development, the index finger and the thumb can be isolated from the other fingers, in order to pick up small objects with precision. Before three years old, children have the difficulty of performing isolated finger movements, such as opposing the fingers to the thumb in sequence. Over the age from six to ten years old, the inter-dependency of fingers decreases with age. Children of ten years old have comparable performance to adults in independency of finger flexion. The independency of finger extension require even more time for fully development [182].

The coordination of micro-and macro-structures of the upper limbs results in the flexibility, stability and accuracy of human hand in object manipulation. The flexibility of hand motion is mainly attributed to the coordination of high degrees of freedom and the independent control of each fingers; while the stability hand motion is enhanced by the powerful thumb placed opposite to the other fingers. The accuracy of hand motions comes from the macro-structure, which directs the hand to comfortable posture and provides stable base during the precise manipulation [183].

2.5.2 Separation of the Macro- and Micro-structures in Robotic Manipulators

The human upper limb processes a high degree of freedom (DOF) and its redundant structures permits greater flexibility in various dexterous manipulations. The simplest structure of a multi-fingered robot arm is constructed by fixing a robot finger on the end-effector of a robot arm. A robot with such a structure is also called a macro-micro manipulator [184, 185]. Similar to the human upper limb, the finger arm robot exhibits a high redundancy. To emulate the movement of the human hand-arm system, resolution redundancy should be resolved properly.

Kinematic redundancy resolution has been a fundamental problem in the field of robotics. Avoidance control of kinematics singularity [186, 187], and obstacle collision avoidance [188, 116, 189, 190, 191] by using kinematically redundant DOFs has been mostly investigated. The null space [192] has been used for secondary task or optimization on specific criterion functions [193]. Despite of kinematical redundancy, it is inappropriate to directly apply the redundancy resolution strategies developed for the redundant manipulators in general to the finger-arm robots.

The finger-arm robot is a special redundant manipulators. A finger-arm robot involves a micro structure of small link size and light weight and a macro structure of large link size and range of motion. This micro-macro structure design coincides the hard-arm system of human. The human hand has limited range of motion. It is lighter, smaller and more sensible to environmental stimuli, and therefore is actively used in delicate and dexterous motions. The arm tends to assist the motion of hands. It transports the hand with smoothness and efficiency to the locations for comfortable manipulations. It also provide stable support during the hand's manipulation. The hand-arm coordination is well organized by the central nervous system so as to generate a natural movements. Therefore, in order to emulate the natural movements of a human upper limb, redundancy resolution strategies of the finger-arm robot should be based on the coordination between the macro and micro structures.

The coordination between the macro and micro structures has been investigated. [93, 194] proposed that the lightweight finger should be actively moved whereas the arm cooperate the movement of the finger, in order to achieve the dexterity like the human hand-arm system. [94] proposed that the arm should move to cooperate with the finger's motion such that the manipulability of the finger can be maintained at desired level [195, 196]. Complemented by the steepest ascent method, manipu-

lability of the finger can be immediately increased when it dropped below a given reference level. Further integration of impedance control enables the controlled finger to complete constrained tasks [184, 197].

2.6 Robot-assisted Bilateral Training for Stroke Rehabilitation

2.6.1 The Neural Mechanism of Bilateral Training

The efficacy of bilateral training therapy is based on several neural mechanisms of human motor control (for comprehensive review see [198]). First, post-stroke recovery is related to an increase in the use of ipsilateral pathway, which can be enhanced by bilateral training of symmetrical movements due to the symmetry constraints between the two arms [42, 199, 200, 201]. Second, bilateral training increases the involvement and activity of the healthy hemisphere, which may lead to improvements in post-stroke motor function [202, 88]. Third, following a stroke, the transcallosal inhibition from the stroke-impacted hemisphere to the healthy hemisphere is reduced, while the inhibition in the opposite direction is increased. The balance of inhibition and disinhibition can be recovered better by bilateral training [203, 204, 203].

Post stroke bilateral rehabilitation treatment was previously proposed based on neural recovery mechanisms [205]. Such a treatment protocol is based, in part, on the fact that activities of daily living (ADL) involve coordinated movements of both arms. From a functional perspective, it is appropriate to recover bilateral movements of the arm by bilateral training rather than by the unilateral training of the paretic arm or by relying on compensation from the non-paretic arm. As shown by ample neurophysiological evidence, the motor control mechanisms activated for controlling the arm are different when identical tasks are performed unimanually compared to bimanually. Neuron activities related to bimanual movements but not to the uni-manual movements are observed in the supplementary motor area, M1, and other cortical areas, which may compose a distributed network within the two hemispheres of the brain responsible for the control of bimanual movements [206]. Furthermore, previous results indicate that in addition to the recovery of bimanual motor skill, bilateral training can also improve unimanual task performance. In particular, bilateral priming, an approach that mechanically couples the two arms to practice symmet-

ric bilateral movements before conducting unimanual or bimanual tasks, resulted in increased excitability and reduced intracortical inhibition in the ipsilesional M1. Bilateral priming normalizes the transcallosal inhibition from the ipsilesional part of the brain to the contralateral part such that the improvement on behavioral measures continues during a follow-up period [203]. Studies on short-term bilateral training found an improvement in unimanual task performance shortly after bilateral training, which confirms the possible contribution of bilateral training to the recovery of unimanual functions [207].

2.6.2 Bilateral Training Therapies

In bilateral training, the two arms are usually coupled together so that the paretic arm is forced to move in response to the non-paretic arm. Depending on the severity of the stroke, the paretic arm can either move by itself (e.g., the bilateral isokinematic training [87, 89]), or assisted by various (robotic) devices [208]. Comparing to the low-tech devices, the computer-controlled robotic devices are more suitable to the practice of repetitive/rhythmic movements, providing varying levels of support and demanding less involvement of the therapists. The bilateral movements designed for training can be in-phase (symmetrical) or anti-phase (asymmetrical). The additional therapies (e.g. the mirror therapy [209, 210]) are augmented to the bilateral training for further improvements.

In bilateral training therapies, the inter-arm coupling enhances the symmetry of arm movements in healthy subjects, and changes the behaviors of both the dominant and non-dominant arms. With stroke patients, the inter-arm coupling synchronizes the paretic arm with the non-paretic arm, leading to possible recovery of stroke-impacted motor function. Previous research efforts studied symmetry in bimanual movements by either comparing the kinematic and dynamic variables of the two arms (e.g., movement timing, direction, amplitude, hand trajectory, velocity, joint angles & torques, muscle activity, etc.), or by task-dependent performance indexes (e.g., the aspect ratio for circle drawing tasks) [54, 53, 79, 72, 64, 65, 66, 67, 61]. There are no previously published methods for quantifying the similarity between arm movements, however.

Chapter 3

Method

Experiments are conducted to investigate the control strategies of human arm movements. This chapter presents the experiments for the studies on (1) reaching movements, (2) reach-to-grasp movements, as well as (3) the unimanual and bimanual arm movements. Since data analysis methods used for the three studies are different and will be presented in their own chapters.

3.1 Experiment

3.1.1 Devices

During the experiment, the subject sits in a chair with a straight back. The chair is placed such that the subject can point at the targets with comfort and with his/her elbow naturally flexed. The height of the workspace center is adjustable and is always aligned with the right shoulder of the subject. The subject's right arm is free for reaching movements, but the body of the subject is set against the chair back to minimize shoulder displacement. During the reaching movements, subjects keep the pointing fingers in line with the forearm to minimize wrist flexion.

Subjects are asked to perform the instructed movements at their comfortable pace. After receiving a “start” command, the subject moves his/her index finger from the start target to the end target. A motion capture system records a single file for each trial at a sampling rate of 100 Hz. As shown in Fig. 3.1c, passive reflective markers are attached to the torso and the right arm of the subject. The recording starts from the time when the subject points the index finger to the start target and ends after the index finger tip becomes steady at the end target. To minimize the effect of

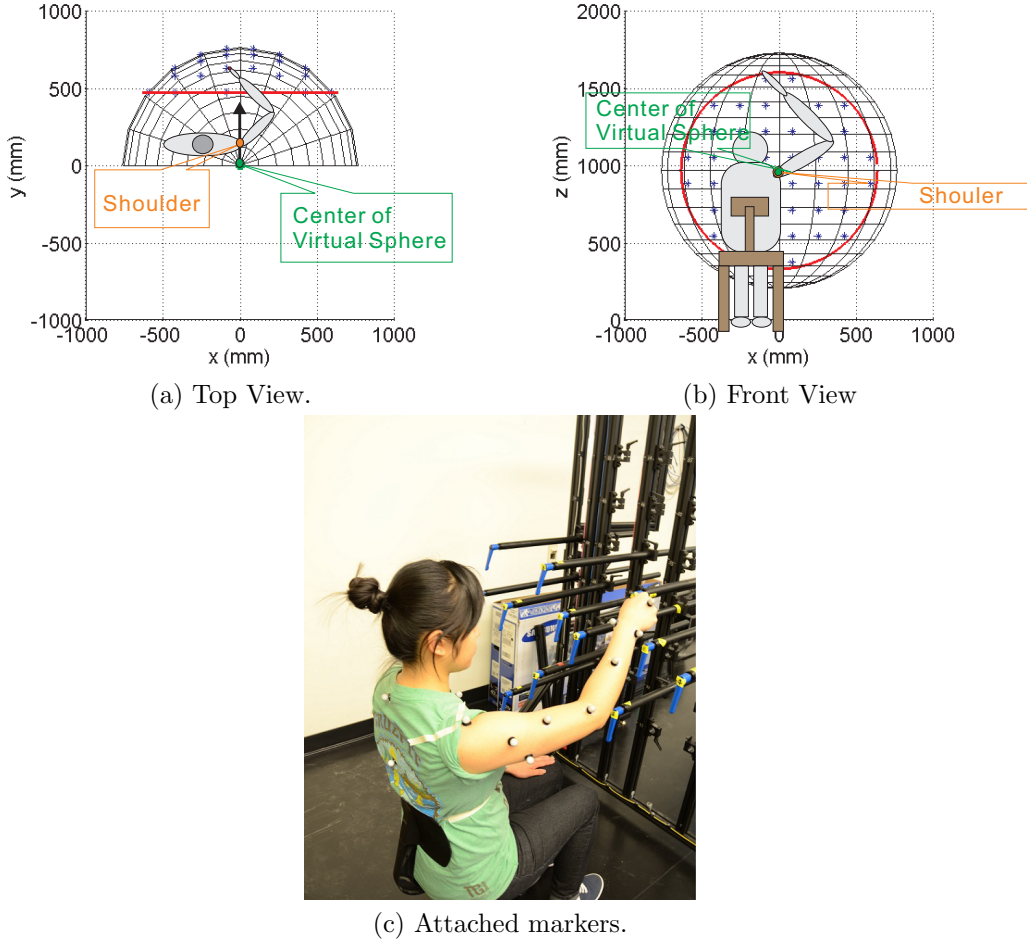


Figure 3.1: (a) and (b) show the top and front views of the spherical workspace, respectively. (c) A subject is performing the instructed reaching movements, with markers attached to her right arm and the torso for position tracking.

fatigue, subjects take a rest after completing each session. With the recorded data of shoulder, elbow and wrist positions, the swivel angles profiles are extracted for each trial.

3.1.2 Protocols

Reaching Movements

Experimental data are collected on point-to-point reaching movements. In this experiment, ten healthy subjects (six males and four females) are instructed to conduct

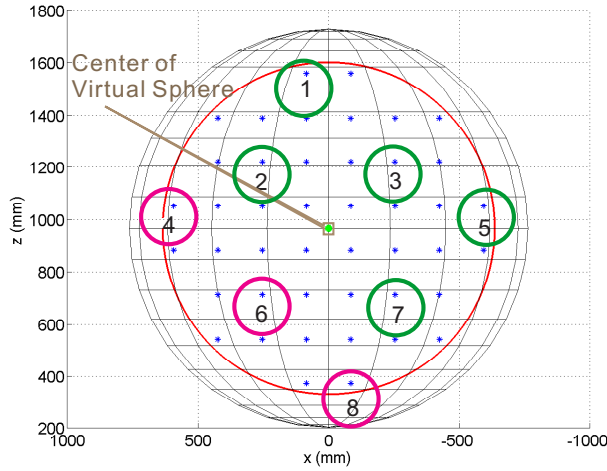


Figure 3.2: In the experiment of point-to-point reaching movements, eight targets are selected among all the available targets (denoted by blue dots in circles).

reaching movements with their right arms to each of the eight targets specified in the spherical workspace (Fig. 3.2). Each subject performs eight reaching movement sessions, one for each target. The reaching movements in each session start from one of the remaining seven targets. A complete session consists of five repetitions of seven different movements. The total number of trials for each subject is $8 \times 7 \times 5 = 280$. During the experiments, subjects are asked to point with the index finger tip at a comfortable pace. At the beginning of each trial, the subject is informed of the targets that the trajectory starts with and ends at, i.e., the start and end targets.

Reach-to-grasp Movements

The experimental protocol aimed to compare reach-to-grasp movements with reaching movements. Nine subjects (three males and six females) were instructed to conduct movements with their right arms. Each subject conducted four sessions of reach-to-grasp movements and one session of reaching movements. Each session consisted of five repetitions of eight different movements. Each subject completed a total of $5 \times 8 \times 5 = 200$ trials.

The target positions are shown in Fig. 3.3a. In each reaching session, after a “start” command, the subjects pointed from the start point (see Figures 3.1a and 3.1b) to the instructed target, with their index finger in line with the forearm. In the reach-to-grasp sessions, the subjects started by pointing to the start point and reached

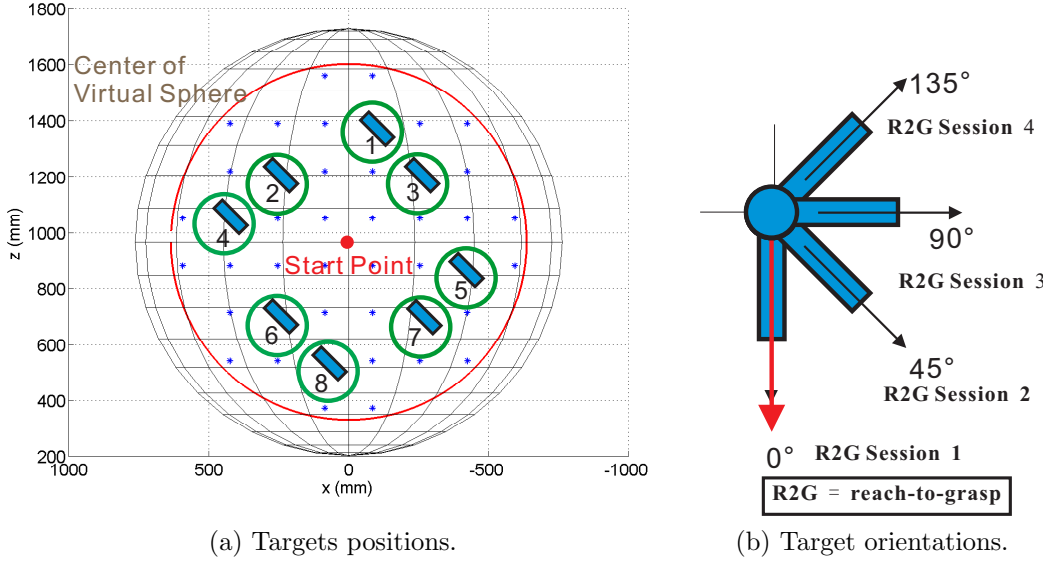


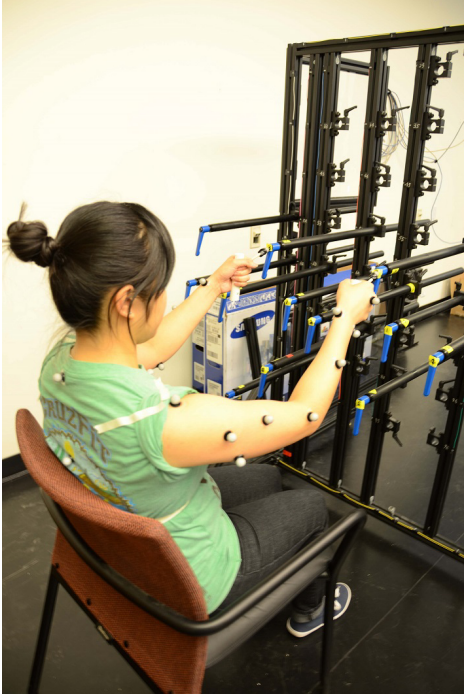
Figure 3.3: (a) Eight targets are involved in the reach-to-grasp experiment; (b) in the four reach-to-grasp sessions, the handles are oriented at 0° , 45° , 90° , 135° on the plane that the subject face to, with respect to the direction of gravity.

to grasp the handle at the instructed target, the orientation of which varied in the plane that the subjects faced (see Fig. 3.3b). The subjects were asked to grasp the target with a firm power grasp. To avoid fatigue, subjects took a rest after each session.

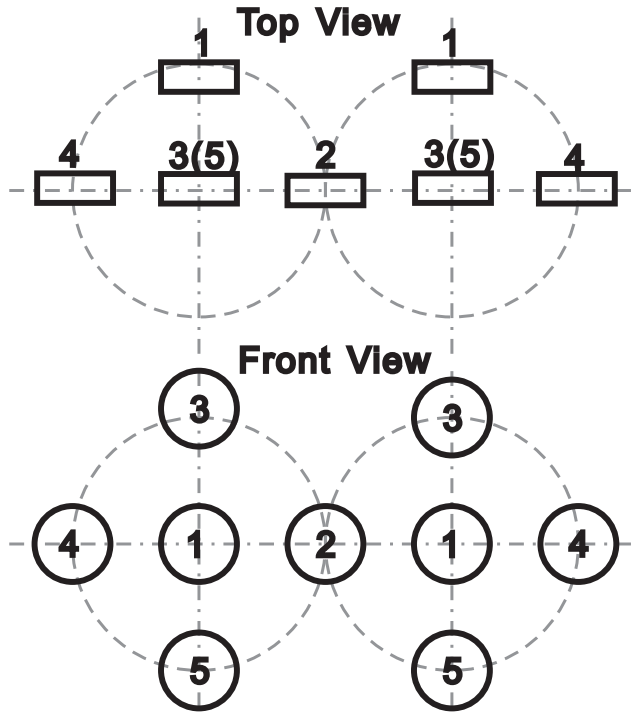
Reach-to-grasp Movements

The data for this study were collected from ten healthy subjects and eight chronic stroke patients. The healthy subjects ranged in age from 20 to 29 years old (average 22.6 ± 3.0). Among the ten subjects, seven were right-handed and three were left-handed. The chronic stroke subjects ranged in age from 53 to 72 years old (average 60.4 ± 7.2). Among the eight subjects, six were impacted on the right arm and two on the left arm. Subjects scored between 20 and 27 on the upper limb volitional movement portions of the Fugl-Meyer assessment, out of a total score of 30.

Fig. 3.4a depicts the setup of the experiment. As shown in Fig. 3.4b, the left/right targets are arranged on the surfaces of spheres corresponding to the left/right hand of the subject. The center and radius of the two spheres are adjusted according to the shoulder width and height of the subject to align Target 1 in each sphere with



(a) Experimental setup.



(b) Targets in 3D workspace.

Figure 3.4: Experimental setups: (a) passive reflective markers are attached to the arms and torso of the subjects for position tracking; (b) the targets corresponding to each hand are aligned on circles the centers which are aligned with the shoulder of the subject.

the corresponding shoulder. The distance between the subject and the workspace is adjusted such that the subject can reach each target comfortably. During the experiment, the subject starts from resting their arms on the handle of the chair, with consistent wrist positions. At a “go” command, the subject starts reaching for the instructed target, touching the target with the tip of the tool held in hand (the stroke subjects usually have difficulty extending their index fingers for pointing, so both healthy and stroke subjects are asked to point with the tool tip for experimental consistency). The experiment consists of two unimanual sessions and one bimanual session. In the unimanual session, the subjects reach with their left/right hand to the five targets corresponding to that hand. In the bimanual session, the subjects reach for both the left and right targets symmetrically. Each session consists of 25 individual trials (5 targets \times 5 repetitions). A motion capture system records the trials at sampling rate of 100 Hz, tracking the positions of the passive reflective

markers attached to the arms and torso of the subject. To minimize the effect of fatigue, subjects take a rest after completing each session.

Chapter 4

Synthesized Control Criteria for the Redundancy Resolution of Human Arm Movements

From the robotic perspective, this research proposes a general framework to compare and evaluate motion control strategies that predict arm posture in reaching movements. In this framework, the arm posture predictions of each candidate criterion are tested against experimental data collected from point-to-point reaching. By combining these candidate criteria according to their arm posture prediction accuracies, synthesized criteria are developed. The candidate criteria that better predict arm posture are assigned larger coefficients in the synthesized motion control criteria, and are therefore recognized as the ones that dominate the arm motion. This synthesized redundancy resolution is proposed for real-time control of the upper limb exoskeleton used for robot-assisted stroke rehabilitation.

The rest of this chapter first presents the forward and inverse kinematics of the upper limb exoskeleton EXO-UL7 in Section 4.1. Section 4.1.2 further describes a human arm model compatible with the EXO-UL7 upper limb exoskeleton. After introducing the real-time redundancy resolution criteria in Section 4.3, the methods used for criterion contribution inference and the experimental protocol for data collection are presented in Section 4.4 and Section 3.1.2, respectively. The data analysis results in Section 4.5 infers the contribution of each criterion to the control of arm motion and further presents a map that associates the dominant motion control strategy with different task space regions.

4.1 Kinematics of the Upper Limb Exoskeleton EXO-UL7

The upper limb exoskeleton EXO-UL7 is designed to support human arm movements during activities of daily living (ADL) (see Fig. 4.1) [2, 211]. Articulation of the exoskeleton is achieved by seven single-axis revolute joints which support 99% of the range of motion required to perform daily activities [2]. Three revolute joints are responsible for shoulder abduction-adduction, flexion-extension and internal-external rotation. A single rotational joint is employed at the elbow, creating elbow flexion-extension. Finally, the lower arm and hand are connected by a three-axis spherical joint resulting in wrist pronation-supination, flexion-extension, and radial-ulnar deviation. As a human-machine interface (HMI), four six-axis force/torque sensors (ATI Industrial Automation, model-Mini40) are attached to the upper arm, the lower arm, the hand and the tip of the exoskeleton [4]. The force/torque sensor at the tip of the exoskeleton allows measurement of interactions between the exoskeleton and the environment.

4.1.1 Forward Kinematics

This section derives the forward kinematics for the upper limb exoskeleton.

Base rotation for singularity avoidance

The bases of the two robotic arms of the upper limb exoskeleton are rotated according to Table 4.1, in order to move the singularity out of the range of the daily movements of the human arm.

Table 4.1: Base rotation of upper limb exoskeleton.

	about X-axis (θ_X)	about Y-axis (θ_Y)	about Z-axis (θ_Z)
Left arm	132.5°	45°	90°
Right arm	132.5°	-45°	90°

The transformation matrix for base rotation can be represented as Eq. (4.1). Note that $\sin \theta_i$ is denoted as s_i , $\cos \theta_i$ is denoted as c_i , $\sin \alpha_i$ is denoted as $s\alpha_i$, $\cos \alpha_i$ is



Figure 4.1: The upper limb exoskeleton with seven DOFs, supporting 99% of the range of motion required to preform daily activities.

denoted as $c\alpha_i$.

$$\begin{aligned}
 T_{base} &= \text{Rot}_x(\theta_X) \text{Rot}_z(\theta_Y) \text{Rot}_z(\theta_Z) \\
 &= \begin{bmatrix} 1 & 0 & 0 & 0 \\ 0 & c\theta_X & -s\theta_X & 1 \\ 0 & s\theta_X & c\theta_X & 1 \\ 0 & 0 & 0 & 1 \end{bmatrix} \begin{bmatrix} c\theta_Y & 0 & s\theta_Y & 1 \\ 0 & 1 & 0 & 0 \\ -s\theta_Y & 0 & c\theta_Y & 1 \\ 0 & 0 & 0 & 1 \end{bmatrix} \begin{bmatrix} c\theta_Z & -s\theta_Z & 0 & 1 \\ s\theta_Z & c\theta_Z & 0 & 1 \\ 0 & 0 & 1 & 0 \\ 0 & 0 & 0 & 1 \end{bmatrix} \quad (4.1)
 \end{aligned}$$

For the left arm,

$$T_{base} = \begin{bmatrix} 0.0000 & -0.7071 & 0.7071 & 0 \\ -0.6756 & -0.5213 & -0.5213 & 0 \\ 0.7373 & -0.4777 & -0.4777 & 0 \\ 0 & 0 & 0 & 1.0000 \end{bmatrix} \quad (4.2)$$

,

for the right arm,

$$T_{base} = \begin{bmatrix} 0.0000 & -0.7071 & -0.7071 & 0 \\ -0.6756 & 0.5213 & -0.5213 & 0 \\ 0.7373 & 0.4777 & -0.4777 & 0 \\ 0 & 0 & 0 & 1.0000 \end{bmatrix} \quad (4.3)$$

Denavit-Hartenberg (DH) parameters

The Denavit-Hartenberg (DH) parameters of the upper limb exoskeleton (shown in Table 4.2) are derived in the standard method defined by [212].

Table 4.2: Denavit-Hartenberg (DH) Parameters for upper limb exoskeleton.

Robot	$i - 1$	i	α_i	a_i	d_i	θ_i
Left Arm	0	1	$\pi/2$	0	0	$\theta_1 + \pi - 32.94^\circ$
	1	2	$\pi/2$	0	0	$\theta_2 + \pi/2 - 28.54^\circ$
	2	3	$\pi/2$	0	0	$\theta_3 + \pi - 53.6^\circ$
	3	4	$\pi/2$	0	L_1	θ_4
	4	5	$-\pi/2$	0	0	$\theta_5 - \pi/2$
	5	6	$-\pi/2$	0	L_2	$\theta_6 + \pi/2$
Right Arm	6	7	$\pi/2$	0	0	$\theta_7 + \pi$
	0	1	$\pi/2$	0	0	$\theta_1 - 32.94^\circ$
	1	2	$\pi/2$	0	0	$\theta_2 - \pi/2 - 28.54^\circ$
	2	3	$-\pi/2$	0	0	$\theta_3 - \pi - 53.6^\circ$
	3	4	$-\pi/2$	0	$-L_1$	θ_4
	4	5	$\pi/2$	0	0	$\theta_5 + \pi/2$
	5	6	$-\pi/2$	0	$-L_2$	$\theta_6 + \pi/2$
	6	7	$\pi/2$	0	0	$\theta_7 + \pi$

Note that L_1 and L_2 are the length of the upper and lower arms, respectively.

By direct kinematics, we can derive the transformation matrix 0T_7 , which includes the position and the orientation of the wrist of the exoskeleton with respect to the

base frame:

$${}_{\text{7}}^{\text{base}}T = T_{\text{base}} \cdot {}_1^0T \cdot {}_2^1T \cdot {}_3^2T \cdot {}_4^3T \cdot {}_5^4T \cdot {}_6^5T \cdot {}_7^6T = \begin{bmatrix} r_{11} & r_{12} & r_{13} & P_{wx} \\ r_{21} & r_{22} & r_{23} & P_{wy} \\ r_{31} & r_{32} & r_{33} & P_{wz} \\ 0 & 0 & 0 & 1 \end{bmatrix} \quad (4.4)$$

For reaching movements, the three DOFs at the wrist are not considered. Therefore, the forward kinematics that involves four DOFs of the human arm (three DOFs at the shoulder and one DOF at the elbow) becomes:

$${}_{\text{7}}^{\text{base}}T = T_{\text{base}} \cdot {}_1^0T \cdot {}_2^1T \cdot {}_3^2T \cdot {}_4^3T \cdot {}_5^4T \quad (4.5)$$

4.1.2 Inverse Kinematics

With the specification of the transformation matrix ${}_{\text{7}}^0T$, the inverse kinematics of the exoskeleton can be derived for the left and the right arms, respectively. The redundant DOF of the human arm can be constrained by specifying the elbow position ($P_e = [P_{e_x}, P_{e_y}, P_{e_z}]^T$).

Based on shoulder position P_s , elbow position P_e , and wrist position P_w , θ_4 can be derived as:

$$W = \|P_w - P_s\| \quad (4.6)$$

$$c_4 = \frac{L_1^2 + L_2^2 - W^2}{2L_1L_2} \quad (4.7)$$

$$s_4 = \sqrt{1 - c_4^2} \quad (4.8)$$

$$\theta_4 = \pi - \text{Atan2}(s_4, c_4) \quad (4.9)$$

The transformation matrix ${}_{\text{4}}^3T$ and its inverse ${}_{\text{4}}^3T^{-1}$ can be found based on θ_4 .

The transformation matrix without the base rotation, denoted ${}_{\text{7}}^0T$, can be found by:

$${}_{\text{7}}^0T = T_0^{-1} \cdot {}_{\text{7}}^{\text{base}}T = \begin{bmatrix} r'_{11} & r'_{12} & r'_{13} & {}_0^7P_{wx} \\ r'_{21} & r'_{22} & r'_{23} & {}_0^7P_{wy} \\ r'_{31} & r'_{32} & r'_{33} & {}_0^7P_{wz} \\ 0 & 0 & 0 & 1 \end{bmatrix} \quad (4.10)$$

Thus, the wrist position with respect to the rotated base is ${}^0P_w = [{}^0P_{wx}, {}^0P_{wy}, {}^0P_{wz}]^T$.

Similarly, the elbow position with respect to the rotated base, denoted by ${}^0P_e = [{}^0P_{ex}, {}^0P_{ey}, {}^0P_{ez}]^T$, is:

$$\begin{bmatrix} {}^0P_{ex} \\ {}^0P_{ey} \\ {}^0P_{ez} \\ 1 \end{bmatrix} = T_0^{-1} \cdot \begin{bmatrix} {}^{base}P_{ex} \\ {}^{base}P_{ey} \\ {}^{base}P_{ez} \\ 1 \end{bmatrix} \quad (4.11)$$

Note that ${}^0P_e = {}^4P_e$ and

$${}^0T = {}^0T \cdot {}^1T \cdot {}^2T \cdot {}^3T \cdot {}^4T = \begin{bmatrix} {}^0R & {}^0P_{ex} \\ 0 & 1 \end{bmatrix} = \begin{bmatrix} {}^0R & L_1c_1s_2 \\ 0 & 1 \end{bmatrix} \quad (4.12)$$

For the both arms,

$$c_2 = \frac{{}^0P_{ey}}{L_1} \quad (4.13)$$

For the left arm,

$$s_2 = \sqrt{(1 - c_2^2)} \quad (4.14)$$

for the right arm,

$$s_2 = -\sqrt{(1 - c_2^2)} \quad (4.15)$$

Thus, θ_2 can be resolved as:

$$\theta_2 = Atan2(s_2, c_2) - (\pi/2 - 28.54^\circ) \quad (4.16)$$

To resolve θ_1 , for the both arms,

$$c_1 = \frac{{}^0P_{ex}}{L_1s_2} \quad (4.17)$$

$$s_1 = \frac{{}^0P_{ez}}{L_1s_2} \quad (4.18)$$

Thus, for the left arm,

$$\theta_1 = \text{Atan2}(s_1, c_1) - (\pi - 32.94^\circ) \quad (4.19)$$

for the right arm,

$$\theta_1 = \text{Atan2}(s_1, c_1) + 32.94^\circ \quad (4.20)$$

The transformation matrices ${}_1^0T$ and ${}_2^1T$ and their inverses ${}_1^0T^{-1}$ and ${}_2^1T^{-1}$ can be found accordingly.

Thus, the wrist position with respect to Frame 2, denoted ${}_7^2P_w = [{}_7^2P_{wx}, {}_7^2P_{wy}, {}_7^2P_{wz}]^T$, can be found:

$${}_7^2T = {}_2^1T^{-1} \cdot {}_1^0T^{-1} \cdot {}_7^0T = \begin{bmatrix} & & {}_7^2P_{wx} \\ & {}_7^2R & {}_7^2P_{wy} \\ 0 & 0 & {}_7^2P_{wz} \\ & & 1 \end{bmatrix} \quad (4.21)$$

For the left arm,

$${}_7^2P_w = \begin{bmatrix} -L_2c_3s_4 \\ -L_1 - L_2c_4 \\ -L_2s_3s_4 \end{bmatrix} \quad (4.22)$$

for the right arm,

$${}_7^2P_w = \begin{bmatrix} -L_2c_3s_4 \\ -L_1 - L_2c_4 \\ L_2s_3s_4 \end{bmatrix} \quad (4.23)$$

To resolve θ_3 , for the both arms,

$$c_3 = \frac{{}_7^2P_{wx}}{-L_2s_4} \quad (4.24)$$

For the left arm,

$$s_3 = \frac{\frac{2}{7}P_{wz}}{L_2 s_4} \quad (4.25)$$

$$\theta_3 = Atan2(s_3, c_3) - (\pi - 53.6^\circ) - 2\pi \quad (4.26)$$

for the left arm,

$$s_3 = \frac{\frac{2}{7}P_{wz}}{-L_2 s_4} \theta_3 = Atan2(s_3, c_3) + (\pi + 53.6^\circ) \quad (4.27)$$

The transformation matrix ${}_3^2T$ and its inverse ${}_3^2T^{-1}$ can be found accordingly.

θ_5 , θ_6 and θ_7 can be derived from the transformation matrices from Frame 4 to Frame 7 ${}_7^4T$.

$${}_7^4T = {}_4T^{-1} \cdot {}_3^2T^{-1} \cdot {}_2^1T^{-1} \cdot {}_1^0T^{-1} \cdot {}_7^0T = \begin{bmatrix} \frac{4}{7}r_{11} & \frac{4}{7}r_{12} & \frac{4}{7}r_{13} & \frac{4}{7}P_{wx} \\ \frac{4}{7}r_{21} & \frac{4}{7}r_{22} & \frac{4}{7}r_{23} & \frac{4}{7}P_{wy} \\ \frac{4}{7}r_{31} & \frac{4}{7}r_{32} & \frac{4}{7}r_{33} & \frac{4}{7}P_{wz} \\ 0 & 0 & 0 & 1 \end{bmatrix} \quad (4.28)$$

For the left arm,

$$\begin{aligned} {}_7^4T &= {}_4T^{-1} \cdot {}_3^2T^{-1} \cdot {}_2^1T^{-1} \cdot {}_1^0T^{-1} \cdot {}_7^0T \\ &= \begin{bmatrix} c_5c_6c_7 - s_5s_7 & -c_7s_5 - c_5c_6s_7 & c_5s_6 & 0 \\ -c_7s_6 & s_6s_7 & c_6 & L_2 \\ -c_5s_7 - c_6c_7s_5 & c_5c_7 - c_6s_5s_7 & -s_5s_6 & 0 \\ 0 & 0 & 0 & 1 \end{bmatrix} \end{aligned} \quad (4.29)$$

for the right arm,

$$\begin{aligned} {}_7^4T &= {}_4T^{-1} \cdot {}_3^2T^{-1} \cdot {}_2^1T^{-1} \cdot {}_1^0T^{-1} \cdot {}_7^0T \\ &= \begin{bmatrix} c_5c_6c_7 - s_5s_7 & -c_7s_5 - c_5c_6s_7 & c_5s_6 & 0 \\ c_7s_6 & -s_6s_7 & -c_6 & L_2 \\ c_5s_7 + c_6c_7s_5 & c_5c_7 - c_6s_5s_7 & s_5s_6 & 0 \\ 0 & 0 & 0 & 1 \end{bmatrix} \end{aligned} \quad (4.30)$$

Thus, for the left arm,

$$c_6 = \frac{4}{7}r_{23} \quad (4.31)$$

$$s_6 = \sqrt{1 - c_6^2} \quad (4.32)$$

$$c_5 = \frac{\frac{4}{7}r_{13}}{s_6} \quad (4.33)$$

$$s_5 = -\frac{\frac{4}{7}r_{33}}{s_6} \quad (4.34)$$

$$c_7 = -\frac{\frac{4}{7}r_{21}}{s_6} \quad (4.35)$$

$$s_7 = \frac{\frac{4}{7}r_{22}}{s_6} \quad (4.36)$$

for the right arm,

$$c_6 = -\frac{4}{7}r_{23} \quad (4.37)$$

$$s_6 = \sqrt{1 - c_6^2} \quad (4.38)$$

$$c_5 = -\frac{\frac{4}{7}r_{13}}{s_6} \quad (4.39)$$

$$s_5 = -\frac{\frac{4}{7}r_{33}}{s_6} \quad (4.40)$$

$$c_7 = -\frac{\frac{4}{7}r_{21}}{s_6} \quad (4.41)$$

$$s_7 = -\frac{\frac{4}{7}r_{22}}{s_6} \quad (4.42)$$

For the left arm,

$$\theta_5 = Atan2(s_5, c_5) + \pi/2 \quad (4.43)$$

$$\theta_6 = Atan2(s_6, c_6) - \pi/2 \quad (4.44)$$

$$\theta_7 = Atan2(s_7, c_7) - \pi + 2\pi \quad (4.45)$$

for the right arm,

$$\theta_5 = Atan2(s_5, c_5) - \pi/2 \quad (4.46)$$

$$\theta_6 = Atan2(s_6, c_6) - \pi/2 \quad (4.47)$$

$$\theta_7 = Atan2(s_7, c_7) - \pi + 2\pi \quad (4.48)$$

For reaching movements, the four DOFs in consideration (three DOFs at the shoulder and one DOF at the elbow) can be resolved based on the wrist position P_w and the elbow position P_e : θ_4 is resolved according to Eq. (4.9); θ_1 and θ_2 are resolved according to Equations (4.12) to (4.20). With regards to θ_3 ,

For the left arm,

$${}^2_5 P_w = \begin{bmatrix} -L_2 c_3 s_4 \\ -L_1 - L_2 c_4 \\ -L_2 s_3 s_4 \end{bmatrix} \quad (4.49)$$

for the right arm,

$${}^2_5 P_w = \begin{bmatrix} -L_2 c_3 s_4 \\ -L_1 - L_2 c_4 \\ L_2 s_3 s_4 \end{bmatrix} \quad (4.50)$$

Therefore, θ_3 can be resolved as Equations (4.24) to (4.27).

4.1.3 Jacobian matrix

The Jacobian matrix denotes the mapping from joint space to task space at the velocity level.

$$\dot{P}_w = J\dot{\theta} \quad (4.51)$$

For the seven-DOF arm model involving wrist orientation,

$$\dot{P}_w = J_{3 \times 7} \dot{\theta} \quad (4.52)$$

where $\theta = [\theta_1, \theta_2, \theta_3, \theta_4, \theta_5, \theta_6, \theta_7]^T$, and

$$J_{3 \times 7} = \begin{bmatrix} J_1 & J_2 & J_3 & J_4 & \mathbf{0} & \mathbf{0} & \mathbf{0} \end{bmatrix} \quad (4.53)$$

The arm model for reaching movements only involves four DOFs and therefore

$$\dot{P}_w = J_{3 \times 4} \dot{\theta} \quad (4.54)$$

where $\theta = [\theta_1, \theta_2, \theta_3, \theta_4]^T$ and

$$J_{4 \times 7} = \begin{bmatrix} J_1 & J_2 & J_3 & J_4 \end{bmatrix} \quad (4.55)$$

For the right arm, given that

$$P_w = \begin{bmatrix} L_2(s_4(s_1s_3 - c_1c_2c_3) + c_1c_4s_2) + L_1c_1s_2 \\ L_1c_2 + L_2(c_2c_4 + c_3s_2s_4) \\ L_1s_1s_2 - L_2(s_4(c_1s_3 + c_2c_3s_1) - c_4s_1s_2) \end{bmatrix} \quad (4.56)$$

we have

$$J_1 = \begin{bmatrix} L_2(s_4(c_1s_3 + c_2c_3s_1) - c_4s_1s_2) - L_1s_1s_2 \\ L_1c_2 + L_2(c_2c_4 + c_3s_2s_4) \\ L_2(s_4(s_1s_3 - c_1c_2c_3) + c_1c_4s_2) + L_1c_1s_2 \end{bmatrix} \quad (4.57)$$

$$J_2 = \begin{bmatrix} L_2(s_4(s_1s_3 + c_1c_3s_2) + c_1c_2c_4) + L_1c_1c_2 \\ -L_1s_2 - L_2(c_4s_2 - c_2c_3s_4) \\ L_1c_2s_1 - L_2(s_4(c_1s_3 - c_3s_1s_2) - c_2c_4s_1) \end{bmatrix} \quad (4.58)$$

$$J_3 = \begin{bmatrix} L_2(s_4(c_3s_1 + c_1c_2s_3) + c_1c_4s_2) + L_1c_1s_2 \\ L_1c_2 + L_2(c_2c_4 - s_2s_3s_4) \\ L_1s_1s_2 - L_2(s_4(c_1c_3 - c_2s_1s_3) - c_4s_1s_2) \end{bmatrix} \quad (4.59)$$

$$J_4 = \begin{bmatrix} L_2(c_4(s_1s_3 - c_1c_2c_3) - c_1s_2s_4) + L_1c_1s_2 \\ L_1c_2 - L_2(c_2s_4 - c_3c_4s_2) \\ L_1s_1s_2 - L_2(c_4(c_1s_3 + c_2c_3s_1) + s_1s_2s_4) \end{bmatrix} \quad (4.60)$$

For the left arm, given that

$$P_w = \begin{bmatrix} L_2(s_4(s_1s_3 - c_1c_2c_3) + c_1c_4s_2) + L_1c_1s_2 \\ L_1c_2 + L_2(c_2c_4 + c_3s_2s_4) \\ L_1s_1s_2 - L_2(s_4(c_1s_3 + c_2c_3s_1) - c_4s_1s_2) \end{bmatrix} \quad (4.61)$$

we have

$$J_1 = \begin{bmatrix} -L_2(s_4(c_1s_3 - c_2c_3s_1) + c_4s_1s_2) - L_1s_1s_2 \\ L_1c_2 + L_2(c_2c_4 + c_3s_2s_4) \\ L_1c_1s_2 - L_2(s_4(s_1s_3 + c_1c_2c_3) - c_1c_4s_2) \end{bmatrix} \quad (4.62)$$

$$J_2 = \begin{bmatrix} L_1c_1c_2 - L_2(s_4(s_1s_3 - c_1c_3s_2) - c_1c_2c_4) \\ -L_1s_2 - L_2(c_4s_2 - c_2c_3s_4) \\ L_2(s_4(c_1s_3 + c_3s_1s_2) + c_2c_4s_1) + L_1c_2s_1 \end{bmatrix} \quad (4.63)$$

$$J_3 = \begin{bmatrix} L_1c_1s_2 - L_2(s_4(c_3s_1 - c_1c_2s_3) - c_1c_4s_2) \\ L_1c_2 + L_2(c_2c_4 - s_2s_3s_4) \\ L_2(s_4(c_1c_3 + c_2s_1s_3) + c_4s_1s_2) + L_1s_1s_2 \end{bmatrix} \quad (4.64)$$

$$J_4 = \begin{bmatrix} L_1c_1s_2 - L_2(c_4(s_1s_3 + c_1c_2c_3) + c_1s_2s_4) \\ L_1c_2 - L_2(c_2s_4 - c_3c_4s_2) \\ L_2(c_4(c_1s_3 - c_2c_3s_1) - s_1s_2s_4) + L_1s_1s_2 \end{bmatrix} \quad (4.65)$$

4.2 Models of Human Arm

4.2.1 Kinematic Model

The kinematic model of human arm has seven DOFs (three DOFs for the shoulder, three DOFs for the wrist and one DOF for the elbow motion). The forward kinematics, including the Denavit-Hartenberg (DH) parameters, is described in [213]. The three shoulder joint and one elbow joint are actively involved in reaching movements. As a result, the orientation of the hand in the arm model is pre-specified by locking the three DOFs at the wrist joint.

Given the wrist position in 3D workspace, the human arm has one redundant DOF which allows the elbow to move around an axis that goes through the center of the shoulder and the wrist joints. This redundant DOF can be represented by a swivel angle ϕ (see Fig. 4.3). Given a fixed wrist position in a 3D workspace, the arm plane formed by the positions of the shoulder (P_s), the elbow (P_e) and the wrist (P_w) can move around an axis that connects the shoulder and the wrist due to the kinematic

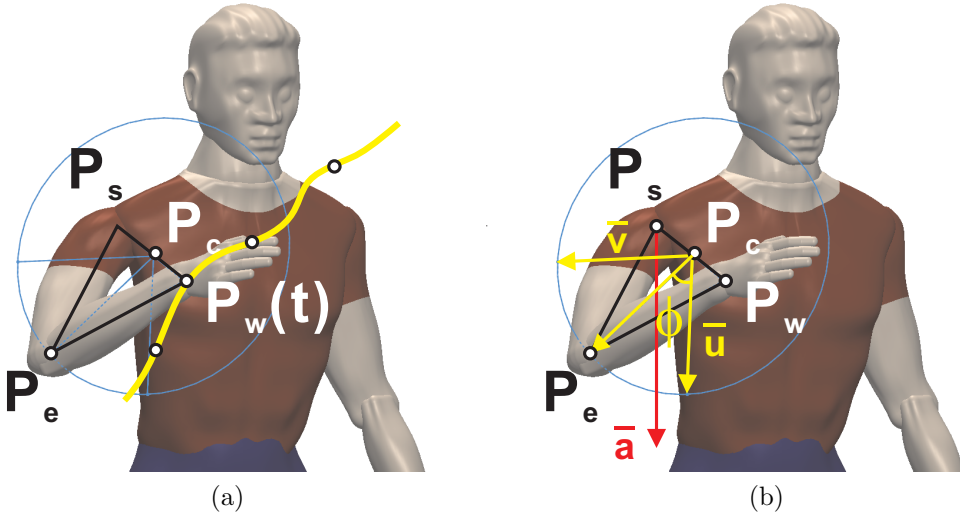


Figure 4.2: (a) Given a 3D wrist position, the arm plane formed by the positions of the shoulder (P_s), the elbow (P_e) and the wrist (P_w) can move around an axis that connects the shoulder and the wrist due to kinematic redundancy. (b) The redundant DOF can be represented by a swivel angle ϕ .

redundancy. The direction of the elbow pivot axis (denoted by \vec{n}) is defined as:

$$\vec{n} = \frac{\vec{P}_w - \vec{P}_s}{\|\vec{P}_w - \vec{P}_s\|} \quad (4.66)$$

A plane orthogonal to \vec{n} can be determined given the position of P_e . The point of intersection between the orthogonal plane and the vector $\overrightarrow{P_w - P_s}$ is P_c . $\overrightarrow{P_e - P_c}$ is the projection of the upper arm ($\overrightarrow{P_e - P_s}$) on the orthogonal plane. \vec{u} is the projection of a normalized reference vector \vec{a} onto the orthogonal plane, which can be calculated as:

$$\vec{u} = \frac{\vec{a} - (\vec{a} \cdot \vec{n})\vec{n}}{\|\vec{a} - (\vec{a} \cdot \vec{n})\vec{n}\|} \quad (4.67)$$

The swivel angle ϕ , representing the arm posture, is defined by the angle between the vector $\overrightarrow{P_e - P_c}$ and \vec{u} . If the reference vector \vec{a} is $[0, 0, -1]^T$, then the swivel angle $\phi = 0^\circ$ when the elbow is at its lowest possible point [214].

4.2.2 Dynamic Model

The dynamic models of the left and right human arms are rendered via the Autolev software package [215]. The motion equations generated by Kane's method [216] integrate the estimates of mass, the center of mass and the moment of inertia with the kinematic model of the arm. Given the initial arm condition, the dynamic model can respond to external forces (such as gravity) and provide an analytical calculation of the joint space variables (i.e., joint angles, velocities and accelerations), as well as the kinetic energy and potential energy. When customizing the dynamic model for each individual subject, the center of mass is estimated according to the distribution of the center of mass (COM) in [1]. On average, the arm contributes 4.8% of the total body weight. The mass of arm segments and their inertia matrices are calculated based on the weight of subjects according to the regression in [217].

4.3 Criteria for Redundancy Resolution

The EXO-UL7 exoskeleton is designed to assist self-initiated arm movements in unexpected tasks. Therefore, it requires real-time motion control rather than pre-planned motion control, and thus redundancy resolution based on local (instead of global) optimization. In this section, three kinematic and two dynamic motion control criteria are presented, which have been successful in resolving the kinematic redundancy of the human arm in reaching movements [18, 218, 7, 20, 21, 219, 19]. The criteria designed for pre-planned motion control are modified as in [19] to provide real-time arm posture prediction.

4.3.1 Criterion 1: maximizing the motion efficiency

Criterion 1 provides real-time arm posture prediction by maximizing the motion efficiency of self-feeding movements. Given the role of the head as a cluster of sensing organs and the importance of arm manipulation to deliver food to the mouth, the arm postures are determined by the human motor control system for efficiently retracting the hand to the head region. Proposed in [18], Criterion 1 determines the swivel angle by maximizing the motion efficiency to a virtual target in the head. A good candidate for the position of the virtual target is the position of the mouth, which is supported by intra-cortical stimulation experiments [220, 221]. When evoking coordinated fore-limb movements in conscious primates, each stimulation site produced a stereotyped

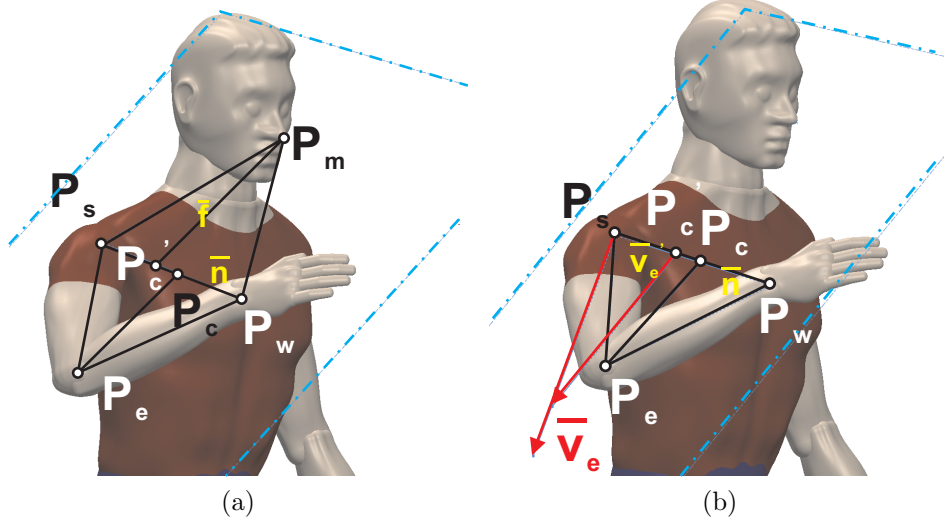


Figure 4.3: (a) Criterion 1 maximizes motion efficiency by maximizing the projection of the longest principle eigen-vector of the manipulability ellipsoid on the direction from the hand to the virtual target P_m . The corresponding elbow position falls on the plane formed by P_s , P_w and P_m . (b) Criterion 2 intends to maintain the arm posture close to the equilibrium arm posture by placing the elbow on the plane formed by the wrist position P_w and the direction of the equilibrium vector \vec{v}_e .

posture by which the arm moved to the same final position regardless of its posture in the initial stimulation. In the most complex example, a monkey formed a frozen pose with its hand in a grasping position in front of its open mouth, which implies that during the arm movement toward an actual target, the virtual target point at the head can be set so that the potential retraction of the hand to the mouth can be efficient.

Criterion 1 specifies a unique arm posture for each wrist position P_w in a 3D workspace. As shown in Fig. 4.3a, when the elbow falls on the plane formed by the positions of the shoulder P_s , the wrist P_w and the virtual target P_m , the projection of the longest principle eigen-vector of the manipulability ellipsoid on the direction from the hand to the virtual target P_m is maximized. In the direction of the longest principle axis of the manipulability ellipsoid, the efficiency of the velocity-force transmission between the joint space and the task space is maximized. The end-effector of the manipulator can move fastest in this direction given the velocity inputs in the joint space. If the position of P_m is set to be the position of mouth, the designated arm postures can be the most efficient ones for self-feeding.

4.3.2 Criterion 2: maintaining the equilibrium posture

Criterion 2, the rotational axis method proposed in [218], prefers equilibrium postures at which periarticular shoulder muscle actuation is minimized. At such postures, the upper arm is aligned with the equilibrium vector, which points out from the center of the shoulder along the axis of the circumduction cone. Criterion 2 stipulates that the axis of rotation of the arm plane (i.e., the plane formed by the positions of the shoulder, elbow, and wrist) should be the equilibrium vector. The wrist position and axis of rotation determine the arm plane which fixes the elbow position.

The direction of the equilibrium vector for the upper arm has been experimentally investigated by NASA [222]. In microgravity, the estimated shoulder flexion is about 36° and the shoulder abduction is about 50° . Given the direction of this axis, the position of the elbow always falls on the plane formed by the rotational axis \vec{v}_e and the wrist position P_w . As shown in Fig. 4.3b, \vec{v}'_e is the vector component of the rotational axis direction \vec{v}_e perpendicular to \vec{n} , i.e, the vector rejection of \vec{v}_e from \vec{n} . Given that \vec{v}'_e is parallel with the vector $P_e - P_c$, the swivel angle is:

$$\phi = \arctan2(\vec{n} \cdot (\vec{v}'_e \times \vec{u}), \vec{v}'_e \cdot \vec{u}) \quad (4.68)$$

The rotational axis method is an important contribution of this research. By analyzing the experimental data collected for the point-to-point reaching movements, this research has found out that the arm plane (defined by the shoulder, elbow and wrist position) rotates about an axis going through the shoulder position. For reaching movements in the comfortable motion range, the rotational axis directions are constrained to a surface, which can be parameterized by a linear model. For reaching movements close to the boundary of the motion range, the directions deviate from the surface most likely due to the blocking effect of the torso.

The existence of the rotational axis and the constraining surface may reveal a relationship between path planning and redundancy resolution from another perspective. It is possible that knowing the start and end points, human motor control system influences a preferred direction of the axis so that by rotating about the axis, the human arm can easily bring the hand from the start point to its destination. Further research will be conducted to find out how to specify the direction of the rotational axis on the constraining surface, given the start and end points in the workspace, and to integrate the path planning and redundancy resolution in a general algorithm.

For the details of the rotational axis method, as well as its arm posture prediction performance, please refer to Appendix I.

4.3.3 Criterion 3: minimizing joint angle change

The human motor system prefers motion smoothness. Kinematic criteria that minimize the jerk in joint space and task space were proposed to account for the straight paths and bell-shaped velocity profiles observed in reaching movements [20, 21, 219], while dynamic criteria that minimize the change in joint torque [22, 23] further explained the mild curvature in the roughly straight task space trajectories. However, these available control strategies for motion smoothness are mostly designed for off-line motion control. Therefore, this paper proposes to a real-time motion control strategy based on local optimization.

Similar to T. Kang's minimization of the work in joint space [19], Criterion 3 determines the arm postures in the following way: given the expected positions of the wrist $P_w(k+1)$ and the shoulder $P_s(k+1)$, Criterion 3 explores the possible swivel angles for the next time step $\phi'(k+1)$ and selects the one that minimizes the norm of the change in the joint angle vector. Experimental data from [19] as well as data collected in this research show that the swivel angle never changes more than 0.5° per 0.01 sec. Given the current swivel angle $\phi(k)$, Criterion 3 searches within the range of $[\phi(k) - 0.5^\circ, \phi(k) + 0.5^\circ]$ with a step of $\delta\phi = 0.1^\circ$, and the swivel angle for the next time step $\phi(k+1)$ is:

$$\begin{aligned}\phi(k+1) &= \arg \min_{\phi'(k+1)} |\vec{\theta}(k) - \vec{\theta}'(k+1)| \\ &= \arg \min_{\phi'(k+1)} \sqrt{\sum_{i=1}^4 (\theta_i(k) - \theta'_i(k+1))^2}\end{aligned}\quad (4.69)$$

In Eq. (4.69), $\vec{\theta}(k) = [\theta_1(k), \theta_2(k), \theta_3(k), \theta_4(k)]^T$ is the joint angle vector for current time step. $\vec{\theta}'(k+1)$ is the joint angle vector for the next time step computed from a possible $\phi'(k+1)$ value. Since this algorithm is generally applicable to local optimization of various performance indices, in Section 4.3.4 it is also used to generate real-time control criteria that minimize kinetic energy.

4.3.4 Criterion 4: minimizing the change in kinetic energy

Energy-efficiency is another possible consideration. Since activities of daily living are well adapted to gravity, unless the dynamics of the human body are under additional load, the human motor system may be more concerned with the kinetic energy than potential energy. Regarding arm motion control, J.F. Soechting *et al.* suggested predicting the arm posture in reaching movements by minimizing peak kinetic energy [7]. Alternatively, A. Biess *et al.* minimized kinetic energy by looking for a geodesic path in the Riemannian configuration space. The resulting joint space trajectories demand less muscular effort since the sum of all configuration-speed-dependent torques vanishes along this path [27].

The aforementioned methods are for pre-planned motion control. For real-time applications, Criterion 4 determines the arm posture by local minimization of kinetic energy. With the dynamic model, kinetic energy (Ke) for each time step is computed given the states of the arm. The algorithm described in Eq. (4.70) is similar to that of Criterion 3: given the kinetic energy for the current time step $Ke(k)$, Criterion 4 explores the possible swivel angles for the next time step $\phi'(k+1)$ within the range of $[\phi(k) - 0.5^\circ, \phi(k) + 0.5^\circ]$ by the step of $\delta\phi = 0.1^\circ$. The expected kinetic energy demanded at the next time step $Ke'(k+1)$ is extracted from the dynamic arm model. The swivel angle that minimizes the change in kinetic energy will be selected as the swivel angle prediction for the next time step ($\phi(k+1)$).

$$\phi(k+1) = \arg \min_{\phi'(k+1)} |Ke(k) - Ke'(k+1)| \quad (4.70)$$

4.3.5 Criterion 5: minimizing the work in joint space

Minimizing the work in joint space is proposed by T. Kang as a real-time dynamic control criterion [19]. The work in the joint space at each time step depends on (1) the joint torques and (2) the difference in joint angles, which can be extracted from the dynamic model given the states of the arm. As Eq. (4.71), Criterion 5 explores in the neighborhood of the current swivel angle $\phi(k)$ and determines the swivel angle $\phi(k+1)$ for next time step to be the one that demands the least work in joint space.

$$\begin{aligned}
\phi(k+1) &= \arg \min_{\phi'(k+1)} |W_i|_{t_k, t_{k+1}} \\
&= \arg \min_{\phi'(k+1)} \sum_{i=1}^4 |W_i|_{t_k, t_{k+1}}
\end{aligned} \tag{4.71}$$

In Eq. (4.71), $|W_i|_{t_k, t_{k+1}}$ denotes the work to be done by the i-th joint.

4.4 Methods of Inference of Criterion Contributions

The five arm motion control criteria presented in Section 4.3 account for different performance considerations, including motion efficiency, muscle actuation efficiency, motion smoothness, and energy consumption. Their prediction performance has been tested against data collected from different experimental setups, but not against a common baseline. As a result, comparing their performance is difficult, and the relative contributions of these criteria to arm motion control have not been evaluated.

Individual contributions of different criteria inferred from experimental data provide an important guideline to coefficient assignment when combining multiple control criteria. However, methods of inferring criterion contributions have not been well explored. Kashi *et al.* inferred criterion contributions using brute-force search within a limited number of coefficient combinations [29]. This inference is neither precise enough to distinguish the behavior of different subjects, nor efficient enough to compare more control criteria within the same scale. Kim *et al.* applied least squares regression to infer the criterion contribution of the two control criteria in comparison. The inferred criterion contributions for each recorded movement are constant, which reflects behavior differences between subjects, but not how criterion contributions change during movement. In order to provide real-time inference of criterion contributions, this paper proposes (1) a modified least squares method and (2) an exponential method, both of which can compare and evaluate large numbers of criteria efficiently.

4.4.1 The Least Squares Method

The least squares method infers criterion contributions during a period. Considering the five candidate criteria presented in Section 4.3, given the individual swivel angle prediction of each criterion for a time step (denoted by $\phi_i(k)$, $i = 1, \dots, 5$), the prediction of swivel angle for that time step (denoted by $\phi(k)$) is:

$$\phi(k) = \sum_1^5 c_i(k) \phi_i(k) \quad (4.72)$$

c_i ($i = 1, \dots, 5$) is the criterion contribution inferred for the i th criterion. Using recent swivel angle measurements (twenty continuous time steps in measurement history before and including the current time step), the criterion contribution of each criterion for the next time step are computed by:

$$\mathbf{C}(\mathbf{k} + \mathbf{1})_{5 \times 1} = A^{-1} \cdot b \quad (4.73)$$

where A is the prediction history from the five criteria (as Eq. (4.74)),

$$A = \begin{bmatrix} \phi_{c1}(k-19) & \cdots & \phi_{c5}(k-19) \\ \vdots & \ddots & \vdots \\ \phi_{c1}(k) & \cdots & \phi_{c5}(k) \end{bmatrix}_{20 \times 5} \quad (4.74)$$

b is the measurement history (as Eq. (4.75)),

$$b = \begin{bmatrix} \phi_{exp}(k-19) \\ \vdots \\ \phi_{exp}(k) \end{bmatrix}_{20 \times 1} \quad (4.75)$$

and A^{-1} is the pseudo-inverse of matrix A using the least squares method.

The coefficients that indicate the contributions are further normalized as:

$$c(k+1)_i = \frac{C(k+1)_i}{\sum_{i=1}^5 C(k+1)_i} \quad (4.76)$$

With reference to Eq. (4.72), these coefficients will be used to generate the $k+1$ -th swivel angle prediction.

Note that for the least squares method, the more criteria being evaluated the more measurements the least squares method requires to render the estimation for current time step. The precision of the inference can be improved by involving more measurements from previous time steps. However, as the older measurements are involved, the inferred contributions become less sensitive to the temporal variation of the criterion contributions. As a result of this tradeoff, this paper tentatively proposes using the last twenty measurements when inferring the contributions by the least squares method. In experimental data, a typical trial in the reaching movement experiments lasts for 150 to 250 time steps at the sampling rate of 100 Hz.

4.4.2 The Exponential method

An alternative method of inferring contribution is the exponential method [223]. This method evaluates the contribution coefficient of a criterion based on the difference between the experimentally recorded swivel angle $\phi_{exp}(k)$ and the swivel angle predicted by this criterion. At time step k , each of the five candidate criteria ($i = 1, 2, \dots, 5$) provides an individual swivel angle prediction, denoted by $\phi_i(k)$. The norm of the prediction error for each criterion is computed as:

$$\varepsilon_i(k) = |\phi_{exp}(k) - \phi_i(k)| \quad (4.77)$$

Based on the five prediction errors, the standard deviation among the prediction errors (denoted by $\hat{\sigma}(k)$) can be computed.

According to the principle of maximum entropy, the probability of the criterion i can be expressed as:

$$p_i = c \cdot \exp(-\lambda \varepsilon_i^2) \quad (4.78)$$

Since the maximum entropy principle does not result in the probability distribution providing bias towards any model, the experimental outcomes from all the models are assumed possible. Therefore, the standard deviation of the prediction errors $\hat{\sigma}$ is the property shared among the models, which results in the criterion contribution

$c(k+1)_i$ computed as:

$$C_i(k+1) = \exp\left[-\frac{\varepsilon_i^2(k)}{\hat{\sigma}^2(k)}\right] \quad (4.79)$$

The criterion contributions are then normalized:

$$c(k+1)_i = \frac{C_i(k+1)}{\sum_{i=1}^5 C_i(k+1)} \quad (4.80)$$

which will be used to generate the swivel angle prediction at time step $k+1$.

Because it does not rely on as much history, the exponential method is expected to outperform the least squares method for real-time contribution inference, particularly when the contributions of various criteria change during movement. Furthermore, the exponential method has no limit on number of the criteria it can process in parallel. The detail of the exponential method can be found in Appendix II.

4.4.3 Criterion Synthesization

The two proposed methods infer criterion contributions in real-time, which can be used to compare the candidate criteria. These inferred contributions can also be used as coefficients for criterion synthesis to improve arm posture prediction accuracy, because no individual control criterion can fully account for arm postures in reaching movements.

Arm motion control is adapted to various environmental constraints and is therefore subject more than one performance consideration. Synthesizing multiple control criteria takes this complexity into account. The contribution-inference/criterion-synthesis methods presented here are not limited to the five candidate criteria presented in Section 4.3. Instead, these methods are proposed as general frameworks for control criteria comparison and evaluation. By inferring the contributions of different control criteria, a limited number of “major” components that are significant to the motor control strategy will be distinguished from the “minor” components that are less prominent considerations in arm motion control. The synthesized arm motion control criteria aim to capture the important factors that influence the motor control system, rather than generate good arm posture predictions by over-fitting the experimental data with too many variables.

4.5 Results

This section presents the results of the arm posture prediction performance of the five candidate criteria, as well as the performance of the synthesized criteria using the least squares and exponential methods. The comparison shows that the least squares method results in prediction performance comparable to the candidate criteria with good prediction performance, while the exponential method infers the criteria contribution more accurately and therefore generates much better arm posture predictions. Further data analysis clusters the computed coefficients to identify characteristic combinations of motion control criteria. The dominant regions of each characteristic combination are presented in a map that associates the clusters with wrist positions in task space.

4.5.1 Prediction Performance of the Criteria

Fig. 4.4 and Fig. 4.5 show the means (μ) and standard deviations (σ) of the prediction errors for all the valid trails (2674 out of 2800) conducted by ten subjects. Fig. 4.4 shows the prediction performance of the five candidate criteria. Fig. 4.5 shows the prediction quality of the synthesized criteria using the least squares method and the exponential method, respectively. Comparison between Fig. 4.5 and Fig. 4.4 shows that the predictions of the synthesized criteria using least squares is more accurate than Criterion 1 and 2, comparable to Criterion 3 and 4, and worse than Criterion 5, while the synthesized criteria using the exponential method is much more accurate than any candidate criterion. For the exponential method, 79.32% of the trials have both $\mu_{EXP} \leq 5^\circ$ and $\sigma_{EXP} \leq 5^\circ$, and only 3.37% trials have either $\mu_{EXP} \geq 10^\circ$ or $\sigma_{EXP} \geq 10^\circ$. For the least squares method, 15.78% of the trials have both $\mu_{LSQ} \leq 5^\circ$ and $\sigma_{LSQ} \leq 5^\circ$. 71.20% trials have either $\mu_{LSQ} \geq 10^\circ$ or $\sigma_{LSQ} \geq 10^\circ$.

The exponential method infers the variance of the criterion contributions better than the least squares method. As shown in Fig. 4.6, the contribution coefficients assigned by the exponential method vary more than those assigned by the least squares method. In Fig. 4.6, the swivel angle and the coefficients were normalized relative to the percentage of the path length traversed by the hand (instead of time), since in the reaching experiments each subject moved at his/her own pace. The coefficients corresponding to the candidate criteria are denoted by c_i , where $i = 1, 2, 3, 4, 5$. “Exp” denotes the measured (experimental) swivel angle profiles, and “Est” denotes the swivel angle predicted (estimated) by the synthesized criteria. Although both

methods for inferring criteria contribution coefficients result in the predictions that follow trends of the measured swivel angle, the prediction errors of the exponential method are much smaller. This may be because the exponential method uses the most recent data sample, while the least square method depends on the last 20 data samples. Comparison of the coefficient profiles shows that the criteria with large prediction errors are suppressed efficiently by the exponential method, which result in a bigger spread of coefficient c_i values.

4.5.2 Characteristic Combinations of Motion Control Criteria

The previous subsection has shown that healthy reaching movements can be best explained by synthesizing multiple criteria using the exponential method. The coefficient assigned to each criterion indicates the time-varying contribution of that criterion. In the following section, K-means clustering will be applied to the contribution coefficients inferred by the exponential method to identify the characteristic combinations of motion control criteria, which can be further mapped to task space the wrist positions.

K-means Clustering of Coefficient Vectors

For each step during the movement, the exponential method has inferred the criterion contribution coefficients, which forms coefficient vectors $v = [c_1, \dots, c_5]^T$. Regardless of the sequences of consecutive steps, each coefficient vector is considered as an individual data point in the K-means clustering. In order to decide the number of clusters, the sum of the squared distances from each point to the center of its cluster (denoted by s_N) is computed. This sum s_N decreases as the number of clusters increases. Fig. 4.7 shows the normalized s_N with respect to s_1 for $N = 1, 2, \dots, 20$. At $N = 9$, the ratio between s_N and s_1 is reduced to 5%, which is appropriate for clustering. The percentages of vector coefficients in each cluster for $N = 9$ is shown in Fig. 4.7b. Cluster 1 has about 30% of the coefficient vectors, while the population in every other cluster is less than 15%.

Results of K-means Clustering

Shown in Figures 4.8a to 4.8i , the K-means clustering of the coefficient vectors has identified characteristic combinations of contribution coefficients. With five candidate criteria, a threshold coefficient value of 0.2 is set to distinguish between the dominant and non-dominant criteria. As a result, the characteristic combination of coefficients can be encoded a five digit binary string. For instance, the characteristics of movements in Cluster 1 (see Fig. 4.8a) can be encoded as 00111, indicating that Criteria 3, 4, and 5 are the dominant criteria, whereas Criteria 1 and 2 make no significant contribution.

In Fig. 4.8, the clusters are ordered by point populations. Clusters 1, 2, 3 and 6, which in total have about 70% of the point population, are dominated by multiple criteria, while each of the remaining five clusters has only one dominant criterion. This explains the higher performance of the synthesized criteria: most of the data can only be predicted using multiple criteria. It also explains how individual criteria can have good prediction performance in some cases: some parts of the data are best explained by a single criterion.

Associating Clusters with Task Space Wrist Positions

The clusters of coefficient vectors, which indicate the characteristic combinations of motion control criteria, can be mapped to wrist position in the task space. As shown in Figures 4.9a to 4.10c , the 3D task space is divided into cells with a $50 \times 50\text{mm}$ grid on the plane the subject is facing (i.e., the x-z plane). Every data point (i.e., coefficient vector) falls into a cell according to its associated wrist position. The frequency of a cluster in a cell is the ratio between the number of points from that cluster within that cell and the total number of points in that cell. Given a specific cluster that represents a characteristic combination of criteria, arm postures are more accurately predicted by that cluster in the regions where it has higher frequency.

Clusters 1, 2, 3 and 6 correspond to characteristic combinations with multiple dominant criteria. For instance, the dominant criteria of Cluster 1 minimize the joint angle change, the kinetic energy and the work in joint space. In Fig. 4.9a, Cluster 1 has high frequency in the lower half of the task space, and in the top-right corner. Cluster 2 is like Cluster 1 except that it does not minimize kinetic energy. It only has high frequency in the lower-right of the task space. Both Clusters 3 and 6 are dominated by the rotational axis criterion. Cluster 3 also minimizes the joint angle

change and works best in the top-left of the task space, while Cluster 6 also minimizes the work in joint space and works best when the wrist is on the left side of the task space.

The remaining clusters correspond to the combinations dominated by single criteria. As a result, their frequency graphs indicate the task space regions in which individual criteria have good arm posture prediction. Cluster 4 minimizes the change in joint angle and works best for the right side of the task space. Cluster 5 minimizes the kinetic energy and works well in the lower left of the task space. Cluster 7 emphasizes Criterion 1 and has high performance predicting arm posture when the hand reaches the leftmost edge of the task space or moves around the top-right of the task space. Cluster 8 is dominated by only the rotational axis method and works well for the top half of the task space. Cluster 9 minimizes the work in joint space and works best for the top-right and bottom-left regions.

Fig. 4.10d is a combination of the individual frequency graphs. In Fig. 4.10d, each cell in the task space is filled with the color of the cluster with the highest frequency in that region. This colored map reflects the most frequent combinations of criteria in different regions of the task space.

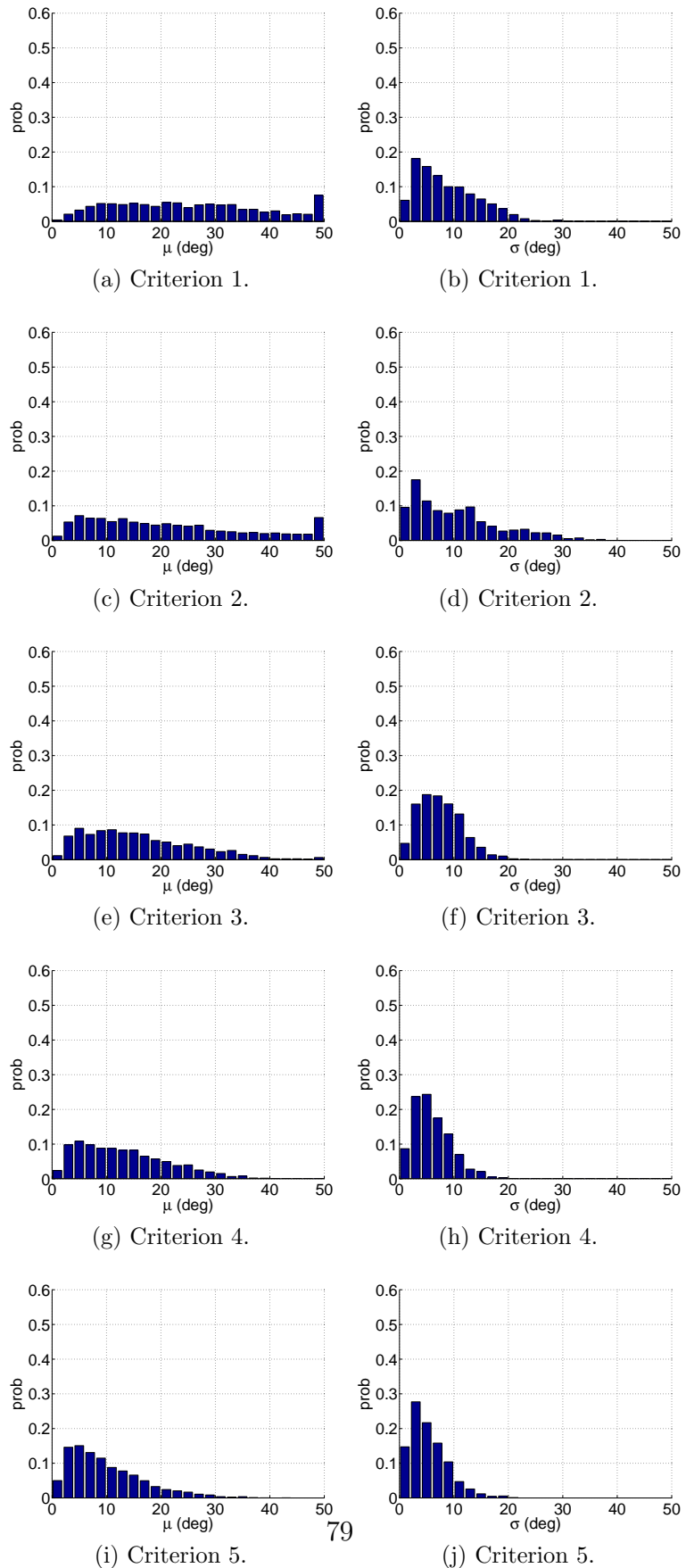


Figure 4.4: Swivel angle prediction performance for each candidate criterion. μ and σ denote the mean and the standard deviation of the prediction.

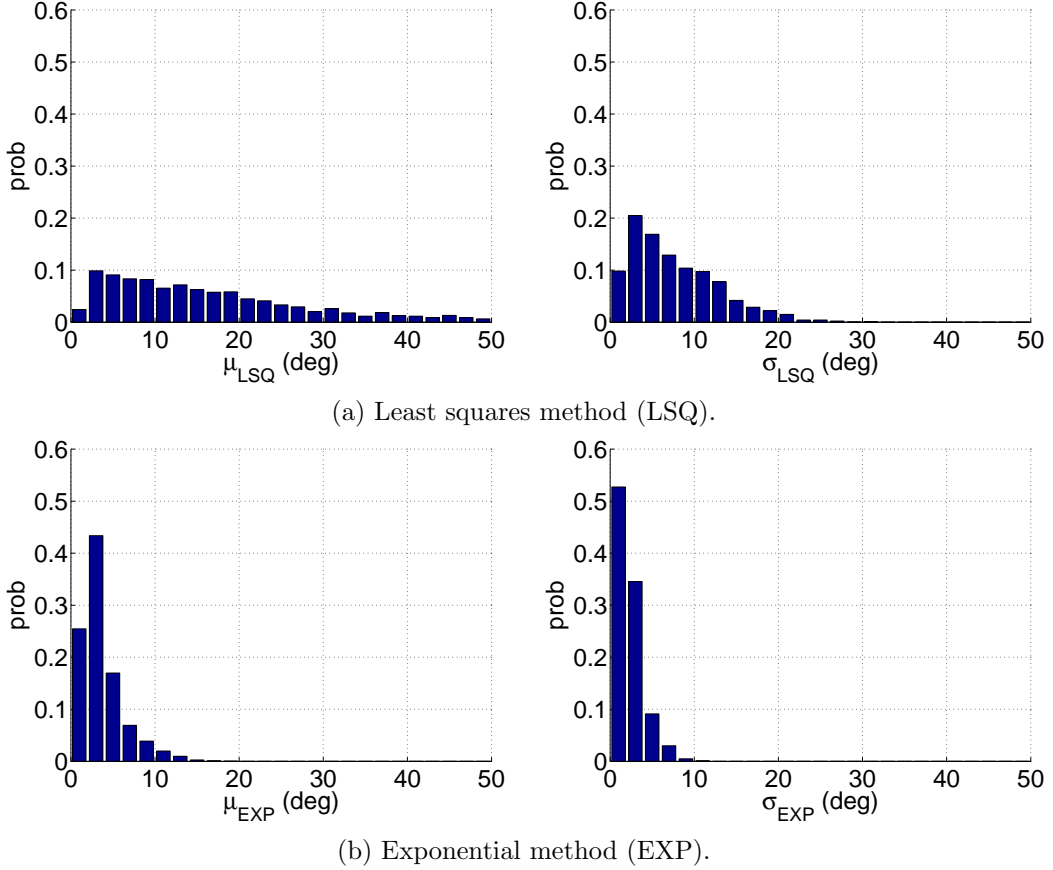
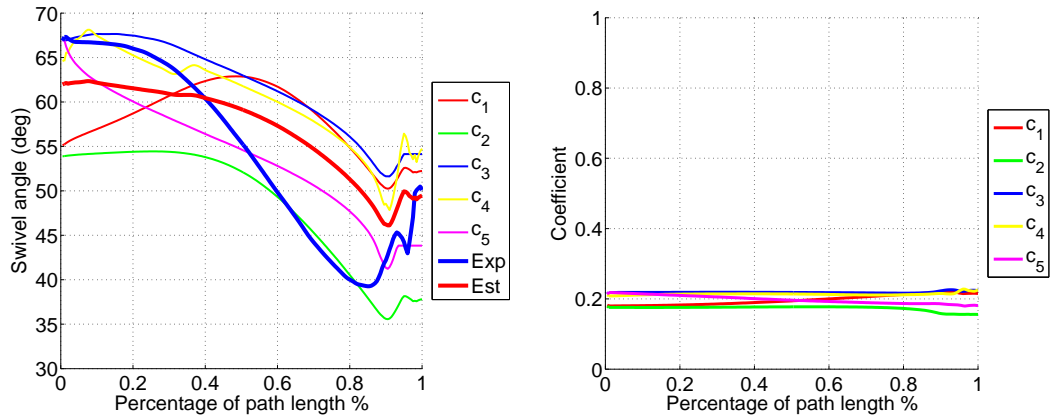
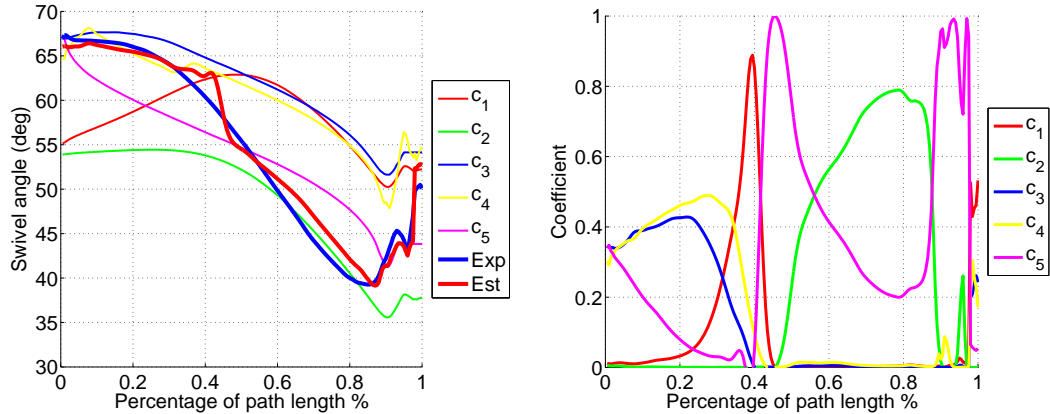


Figure 4.5: Swivel angle prediction performance of the synthesized criteria using (a) the least squares method and (b) the exponential method. μ and σ denote the mean and the standard deviation of the prediction error.



(a) Least squares method (LSQ).



(b) Exponential method (EXP).

Figure 4.6: The swivel angle predictions of candidate criteria, as well as their inferred contributions. c_1 to c_5 refer to the candidate criteria. Est refers to the synthesized criteria. Exp refers to the swivel angle measurements.

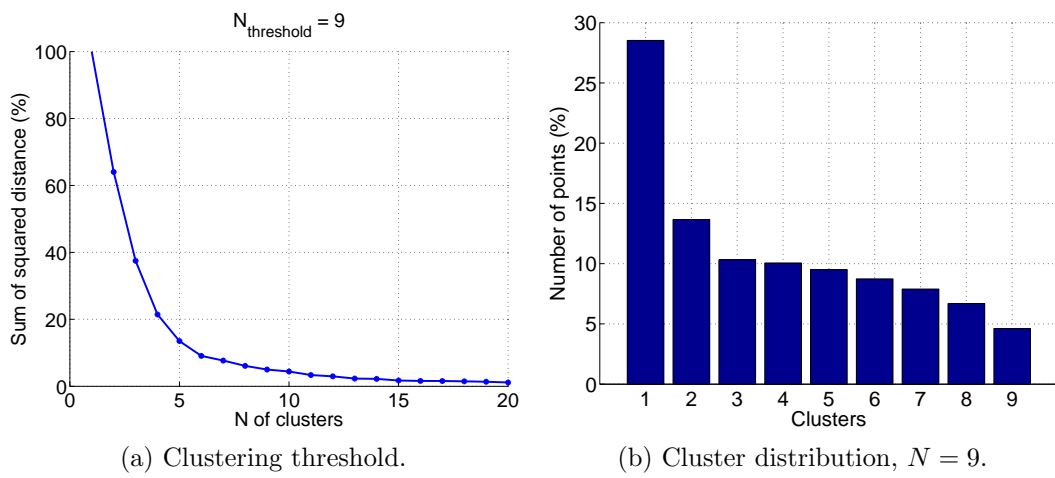


Figure 4.7: The sum of the squared distances to the cluster centroid (s_N) is computed for increasing cluster number (N). When the ratio between s_N and s_1 is reduced to 5%, the clustering is stabilized, at $N = 9$.

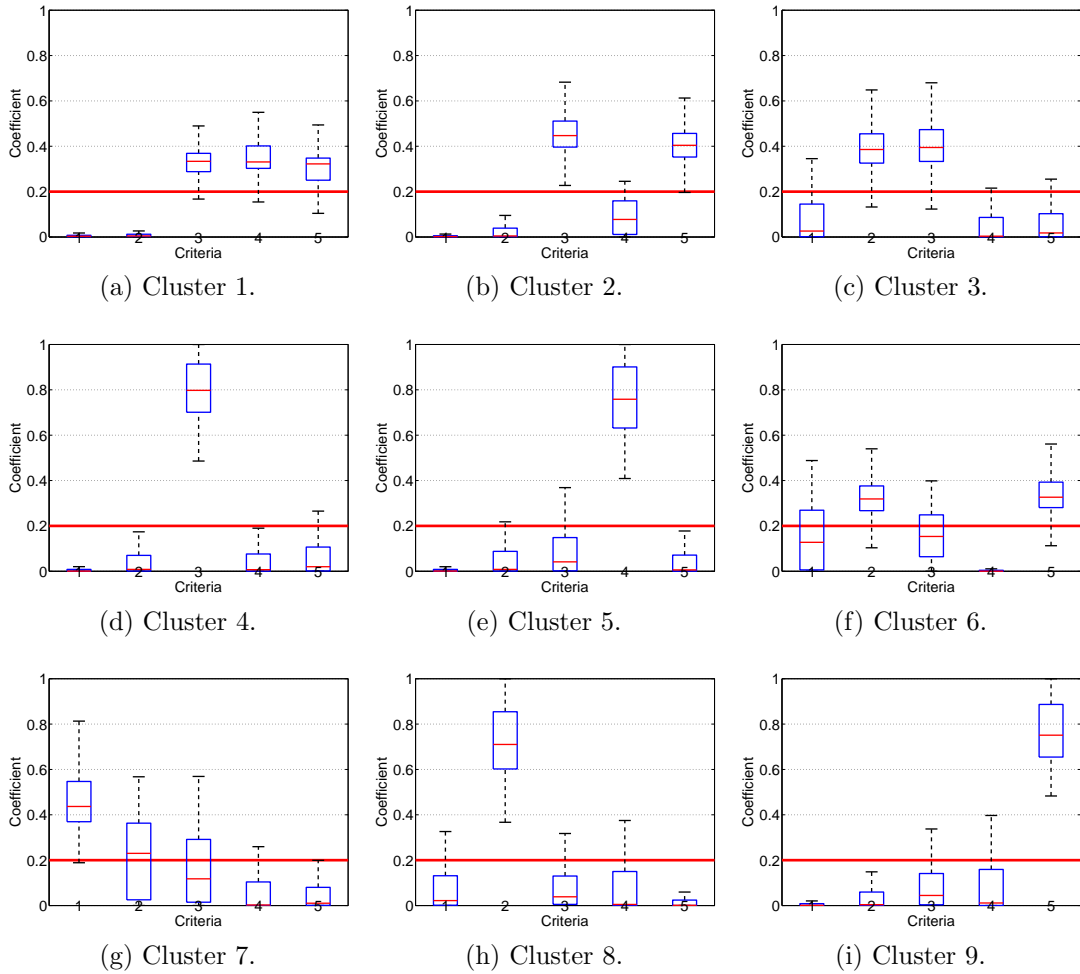


Figure 4.8: Characteristic combinations of contribution coefficients are identified by K-means clustering. With respect to the threshold coefficient value 0.2, the dominant criteria are distinguished from the non-dominant ones.

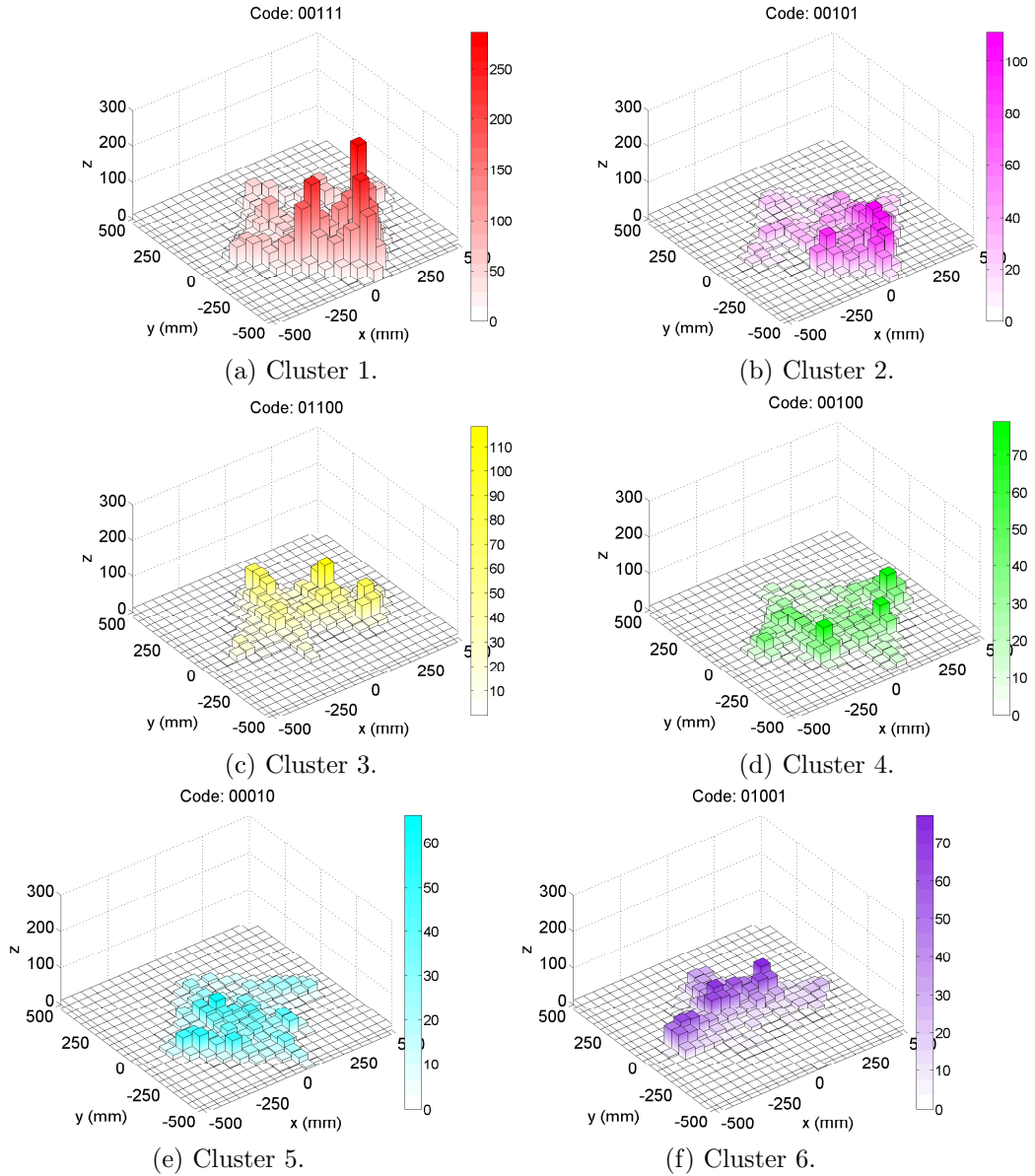


Figure 4.9: The clusters' frequencies in the task space for Cluster 1 to 6.

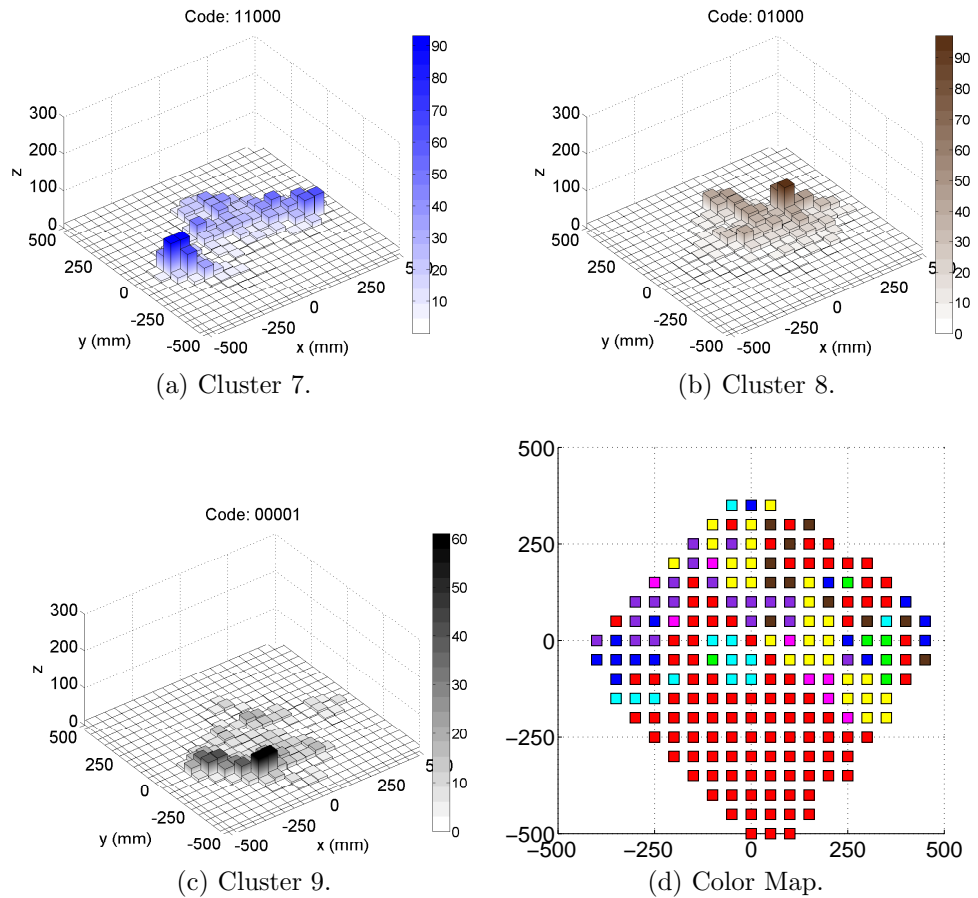


Figure 4.10: The clusters' frequencies in the task space for Cluster 7 to 9. (d) compares the graphs for the nine clusters and illustrates the most-frequent combination of motion control criteria for each cell in the task space.

Chapter 5

The Joint Coordination in Reach-to-Grasp Movements

This study investigates the spatial and temporal characteristics of the joint coordination in reach-to-grasp movements. Experimental data are collected on the reach-to-grasp movements in a 3-dimensional (3D) workspace, for cylinder targets of different positions and grasping orientations, in addition to the reaching movements toward the targets of the same positions. The proposed kinematic model enables the separation between the grasping-relevant degrees of freedom (GR-DOFs) and the grasping-irrelevant degrees of freedom (GI-DOFs). The four grasping-relevant degrees of freedom (GR-DOFs), including the swivel angle and the three wrist joints, behave differently in reach-to-grasp movements comparing reaching movements and therefore becomes the focus of the research.

Given the kinematic redundancy of the human arm, the arm posture can be affected by hand orientation when grasping. The coordination of grasping-related degrees of freedom (GR-DOFs), including swivel angle, forearm supination, wrist flexion and radial deviation, depends on their task-relevance, which can be quantified by the ratio of a joint's active motion range to its total motion range (R-AMR). The R-AMR values are computed across the target position and orientation to compare the task-relevance of the GR-DOFs. Statistical analysis of R-AMR values at the end of reach-to-grasp movements shows that among the GR-DOFs, radial deviation is most sensitive to changes in target position, while forearm supination is most sensitive to changes in target orientation. The forearm supination and swivel angle coordinate for energy-efficiency such that the swivel angle, which adjusts the posture of the whole

arm, is largely unused until the forearm supination approaches its joint limit. The results further the understanding of the human motor control system in arm motion control and may benefit the design of the control algorithm for the upper limb exoskeleton.

5.1 The Grasping-relevant Degrees of Freedom (GR-DOFs)

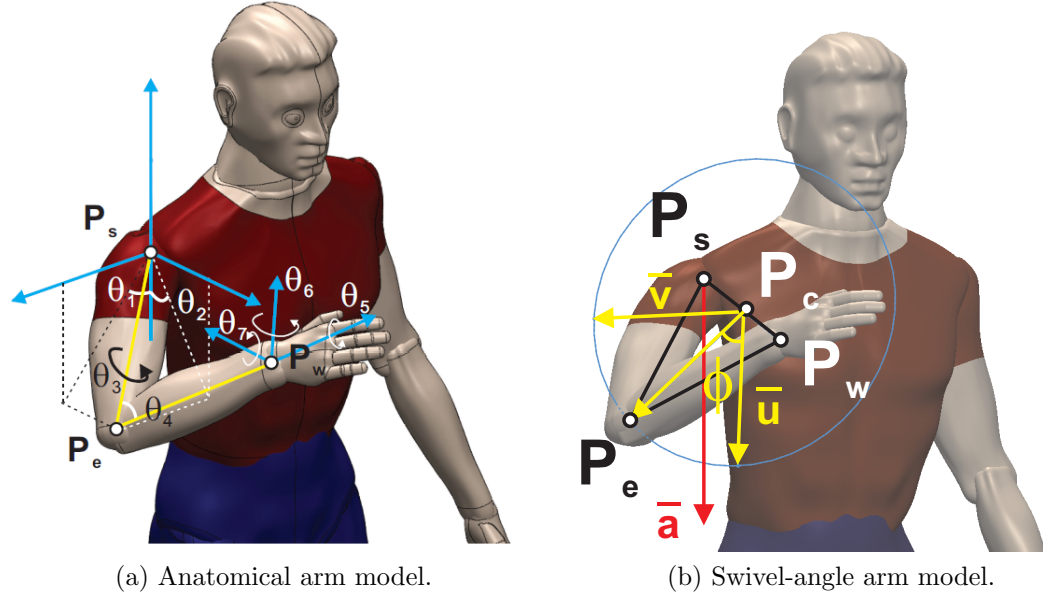


Figure 5.1: (a) The anatomical arm model and (b) the swivel-angle arm model.

Traditionally, the joint coordination in reach-to-grasp movement is based on the kinematic model in accordance with the anatomical joints. As shown in Fig. 5.1, the seven degrees of freedom (DOFs) are: shoulder abduction θ_1 , shoulder flexion θ_2 , shoulder rotation θ_3 , elbow flexion θ_4 , supination θ_5 , wrist flexion θ_6 and radial deviation θ_7 . According to this kinematic model, all the seven DOFs of human arm are subject to the hand grasping orientation. To reduce the analysis complexity, this research propose to perform the motion analysis based on the kinematic model described in Chapter 4, which can identify the DOFs that are not affected by grasping orientation.

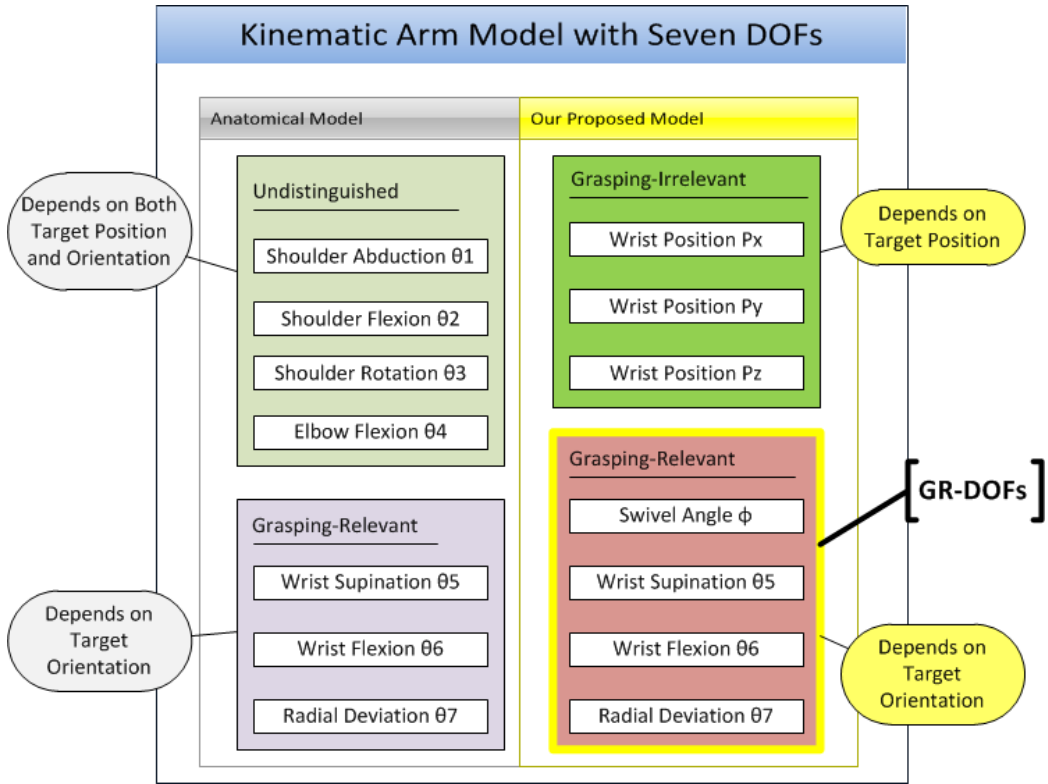


Figure 5.2: The comparison between the two modeling methodologies.

As shown in Fig. 5.1b, the seven DOFs of the kinematic model are: three DOFs for the wrist position, one DOF for the swivel angle, and three DOFs for the wrist orientation. In the reaching and reach-to-grasp movements towards the same target, the hand paths are not quite different. The arm postures are changed mostly due to the effect of target orientation on the four grasping-relevant DOFs, including the swivel angle and three wrist angles. Fig. 5.2 compares the DOFs in the two kinematic models. By representing the kinematic redundancy using the swivel angle, the four grasping-related DOFs are identified, which significantly reduce the analysis complexity.

5.1.1 Data Analysis Method

5.1.2 Data Normalization and Component Separation

During the experiments, the trajectories of the markers are recorded and the trajectories of the four GR-DOFs are computed by inverse kinematics. These trajectories

were normalized relative to the percentage of the path length traversed by the hand (instead of time) and averaged based on five repetitions of the same movement. With reference to the reaching movements, grasping-related differences are computed so that the reaching component can be separated from the grasping component. This component separation is applied to the four GR-DOFs, including the swivel angle and the three wrist DOFs.

5.1.3 The Ratio of Active Motion Range

In joint coordination, the joints that are actively used respond more to the changes in task specifications than the joints not actively involved in the movements. The **ratio of the active motion range** (R-AMR) for each GR-DOF is computed to evaluate the responses of the grasping component of the GR-DOFs to the changes in target position and orientation. At the end of the movements, we computed the standard deviation of the value of the grasping component for each GR-DOF across different movements. The R-AMR is then defined as the ratio between this standard deviation and half of the motion range of this GR-DOF. Note that the R-AMR can be computed across different movement sets, including movements to targets at a particular position or in a particular orientation. For a movement set, a large R-AMR value indicates that that particular DOF is sensitive to the task parameters that vary within that movement set. For example, the R-AMR of a DOF across reach-to-grasp movements towards a particular target position with different orientations indicates the sensitivity of that DOF to target orientation. Likewise, the R-AMR of a DOF across movements to different targets that share the same orientation indicates sensitivity to target position.

5.2 Results

5.2.1 The Reaching and Grasping Components.

This section presents results from the analysis of the grasping components of the reach-to-grasp movements. Prior to computing the R-AMR values for each GR-DOF, the data collected on reach-to-grasp movements were processed by data normalization and component separation. Fig. 5.3 shows an example of data normalization of the swivel angle in the trials collected from a representative subject. In Fig. 5.3a, swivel

angle trajectories regarding to the same individual target are normalized with respect to hand path length. The averaged trajectory of five repetitions of each movement is shown in Fig. 5.3b. With reference to the reaching movement, each reach-to-grasp movement to the same target is separated into a reaching component (Fig. 5.3c) and a grasping component (Fig. 5.3d). A grasping component is computed as the difference between the reaching movement and the reach-to-grasp movement to the same target but of different grasping orientation.

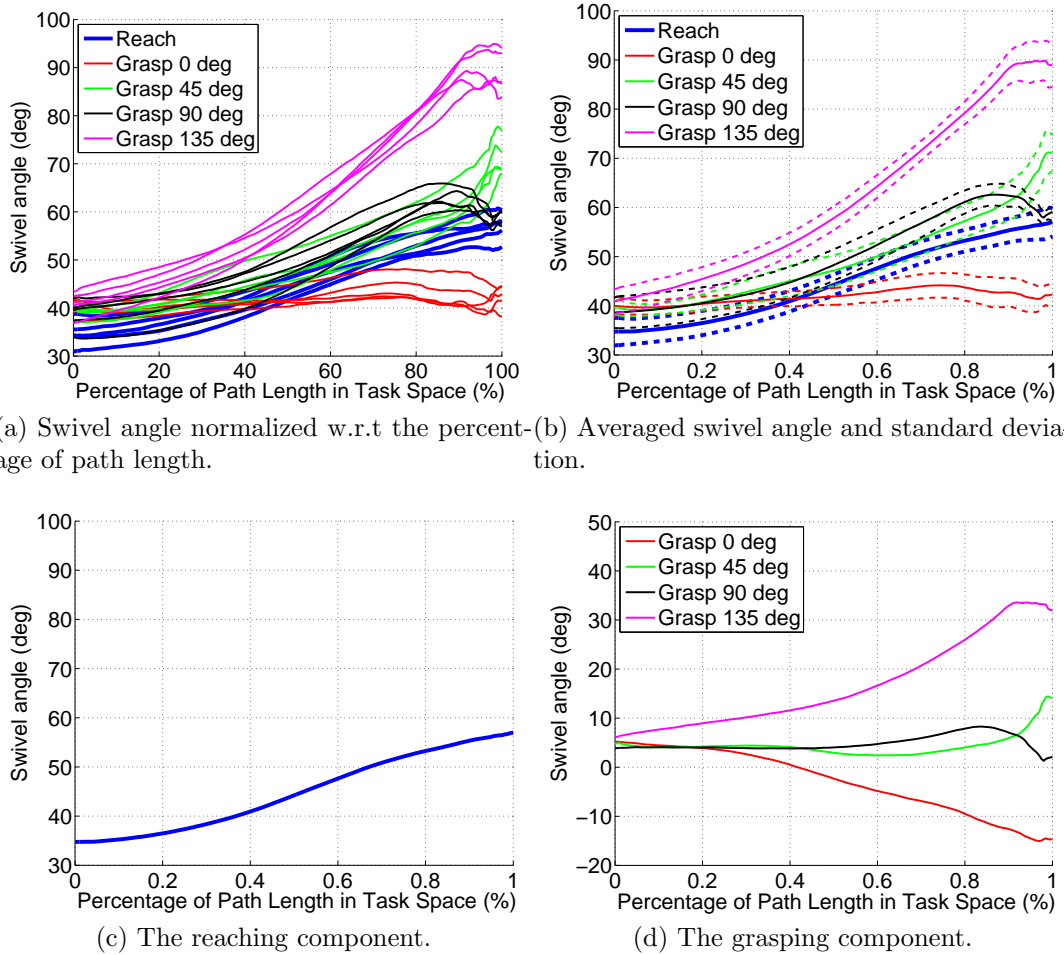


Figure 5.3: (a) The swivel angle trajectories are normalized with respect to the percentage of path length. (b) The averaged trajectories are found with their time-varying standard deviation. With reference to the averaged trajectory of the reaching movement, the reach-to-grasp movements can be separated into (c) the reaching component and (d) the grasping component.

In Fig. 5.4, component separation is applied to the data from a representative

subject for each GR-DOF. The reaching components of all the GR-DOFs are approximately linear with respect to the percentage of the hand path length. The reaching components of the swivel angle vary for different targets, while the reaching components of the other GR-DOFs are mostly constant. In reaching movements, the index finger is aligned with the forearm, which results in little movement of forearm pronation-supination. With regard to the grasping components, the swivel angle and the forearm pronation-supination is linear for most of the path length percentages. The flexion-extension and radial deviation at the wrist are nonlinear. The nonlinear flexion-extension during the movement is possibly due to opening and closing of the hand aperture preparing for grasping.

Fig. 5.5 shows the second derivative of the grasping components of the four GR-DOFs. During the reach-to-grasp movements, each GR-DOF experiences three distinguishable phases with different amounts of acceleration/deceleration. The first 10% – 20% of the movement is the “pre-match” phase. Knowing the designated target orientation, subjects coordinate the four grasping variables for matching the hand orientation with the target orientation. After the pre-match phase, there is a period during which there is no significant change in the acceleration of the variables. After 60% – 80% of the path length, the hand has been transported close enough to the target such that the four variables are adjusted for closing the hand and for matching the hand with the target more precisely. The second phase is called the “transportation phase” and the third phase is called the “match phase”. Regarding the temporal responses of the GR-DOFs, the three distinguishable amounts of acceleration/deceleration indicate different levels of voluntary control in different phases of motion.

5.2.2 The Task-relevance During the Movements

This section presents the results of the statistical analysis on the R-AMR values during reach-to-grasp movements. Foremost, different GR-DOFs are not used to the same extent: although arm postures start to match the target orientation early in a movement, the wrist joint, which is responsible for final adjustment, is not actively used until the hand is close to the target. As the use of a GR-DOF increases during a reach-to-grasp movement, its variance (with respect to task parameters such as target position and orientation) increases accordingly, reflected in an increased R-AMR value. To investigate task-relevance during movement, the R-AMR values were

computed with increment of 0.5% of the hand path. For reaching components, R-AMR values are computed based on the standard deviations across different target positions. Fig. 5.6a shows the mean R-AMR values of the reaching component during movement. The mean R-AMR of the swivel angle quickly becomes much larger than that of the other DOFs. For the grasping component, R-AMR values are computed based on the standard deviation across target position and across target orientation, respectively. Fig. 5.6 plots the mean of the across-target-orientation R-AMR against the mean of the across-target-position R-AMR. Comparing the slopes of the four profiles, the slopes of the swivel angle and forearm supination are greater than one while the other GR-DOFs are less than one. This implies that the swivel angle and forearm supination are more sensitive to changes in target orientation than to changes in target position, while the other GR-DOFs are the opposite. It is notable that the profile for wrist flexion is nonlinear, corresponding to the opening and closing of the hand during movement in preparation for grasping the target, while for the other three GR-DOFs, the across-target-orientation R-AMR increases roughly linearly with the across-target-position R-AMR. Note also that wrist flexion near the end of the task falls on the reference line indicating equal sensitivity to both target position and orientation.

5.2.3 The Task-relevance at the End of the Movements

The $R\text{-AMR}_{100\%}$ value for a set of movements is the R-AMR computed at the end of the task. Fig. 5.7 computes $R\text{-AMR}_{100\%}$ values for reaching and grasping components separately for each subject, and compares them using multiple comparison. For all of the GR-DOFs, the $R\text{-AMR}_{100\%}$ of the grasping component is significantly larger than that of the reaching component. The swivel angle, which has the largest reaching-component $R\text{-AMR}_{100\%}$, exhibits the smallest difference between the reaching and grasping components. Among the grasping components, the forearm supination and radial deviation are much higher than the other two GR-DOFs. The wrist flexion has the lowest $R\text{-AMR}_{100\%}$ for both the reaching and grasping components, which coincides with its limited motion due to the wrist tension in power grasps.

In Fig. 5.8, across-target-position and across-target-orientation $R\text{-AMR}_{100\%}$ values are computed without component separation. In Fig. 5.8a, the radial deviation has significantly higher $R\text{-AMR}_{100\%}$ across the target positions than other GR-DOFs, which implies high task-relevance to the changes in target position. Fig. 5.8b shows

that forearm supination is the GR-DOF most relevant to changes in target orientation, while wrist flexion is least relevant. The swivel angle, which adjusts hand orientation by moving the whole arm, has much lower task-relevance than forearm supination.

Fig. 5.9 compares the swivel angle and the forearm supination by their end values and across-target-position grasping-component R-AMR_{100%} values at different target orientations. Comparing Figures 5.9a and 5.9b , the end values of the swivel angle increase significantly when the target orientation changes from 90° to 135°, while the changes in the forearm supination is small. Before the target orientation reaches 90°, the forearm supination changes more with the target orientation than the swivel angle. Comparing Figures 5.9c and 5.9d , the R-AMR_{100%} values of the swivel angle are consistently low for different target orientations, while the R-AMR_{100%} of the forearm supination is significantly reduced as the target orientation increases and settles down when the target orientation reaches 90°.

5.2.4 The Synergetic Coordination of Task-relevant GR-DOFs

Section ?? has shown that the GR-DOFs of higher task-relevance are more actively used, which inspires a study of their coordination. During the experiment, the target orientation only changes in the plane that the subject faces. As a result, hand orientation is cooperatively adjusted by the swivel angle and pronation-supination. When the target orientation is greater than 90°, the swivel angle is largely used to provide comfortable grasping postures. To investigate this task-dependent coordination of the GR-DOFs, for each subject, we computed the average of the end values of the grasping components of a GR-DOF across all target positions for the same target orientation. The average end values corresponding to different target orientations form the response of a GR-DOF to the change in target orientation. In Figures 5.10a and 5.10b , each solid blue line represents the response of a subject to target orientations. The associated dashed blue lines are the third-order spline regressions. The averaged response of all subject is represented by a solid red line, bounded by two red dash lines that represent the standard deviation. While Figures 5.10a and 5.10b describe the responses at the swivel angle and the pronation-supination, Fig. 5.10c shows the changes of hand orientation resulting from their task-dependent coordination. Denoting the target orientation by φ and the hand orientation by η , the coordination of the nonlinear responses of the swivel angle and pronation-supination results in an approximately linear response in hand orientation (see Equations (5.1)

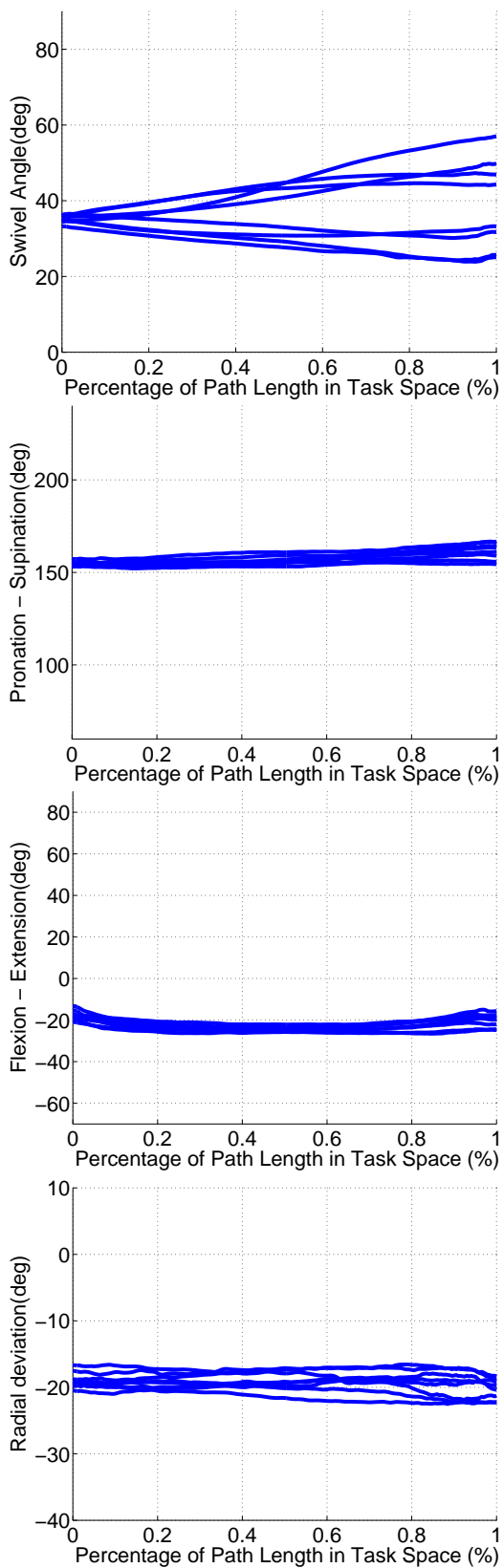
and (5.2)).

$$\phi = 0.0015\varphi^2 + 0.0502\varphi - 7.9475 \quad (5.1)$$

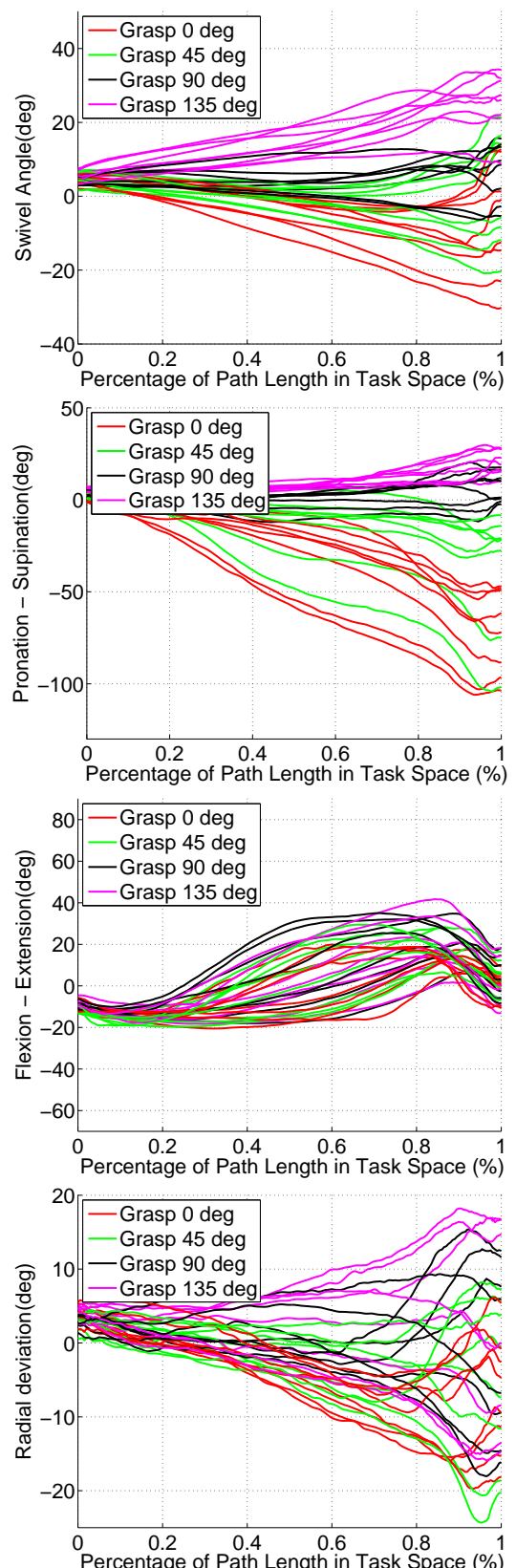
$$\theta_5 = -0.0043\varphi^2 + 1.1630\varphi - 56.3191 \quad (5.2)$$

$$\eta = 0.8658\varphi - 62.4985 \quad (5.3)$$

For each subject, we computed the standard deviations across the target position for the end values of the swivel angle, the pronation-supination and the hand orientation, denoted by σ_ϕ , σ_{θ_5} and σ_η , respectively. The standard deviations are computed based on the regression of variable responses and cover the target orientation range from 0 to 135° . To analyze the variance of the coordinated joints and their resulted hand orientation, we compute $(\sigma_\phi^2 + \sigma_{\theta_5}^2)^{1/2}$ and compare it to σ_η . Fig. 5.10d shows $\sigma_\eta - (\sigma_\phi^2 + \sigma_{\theta_5}^2)^{1/2}$ values are mostly negative for all the nine subjects, which indicates that the coordination of swivel angle and the pronation-supination is synergetic [8].



(a) The reaching components.



(b) The grasping components.

Figure 5.4: The reaching and grasping components of the swivel angle (ϕ), pronation-supination (θ_5), flexion-extension (θ_6) and radial deviation (θ_7). 95

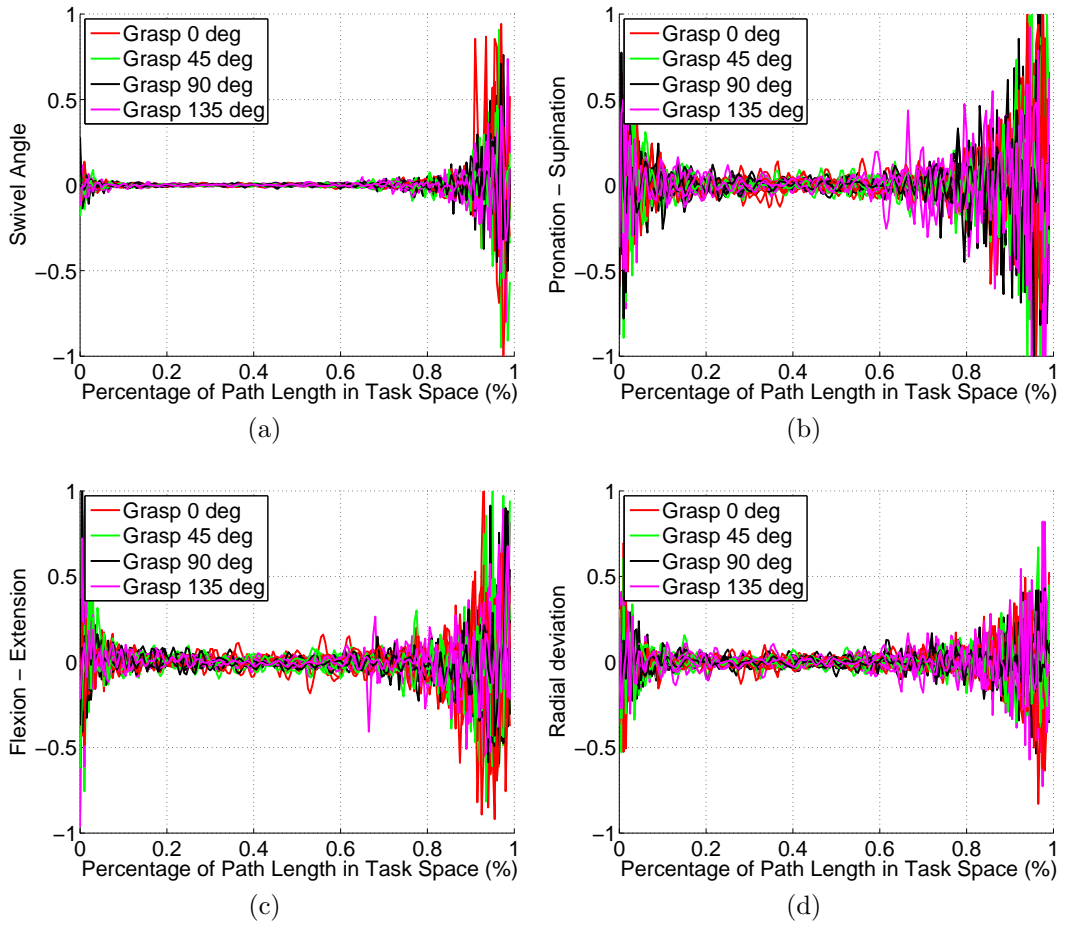


Figure 5.5: Second order derivative of the grasping component.

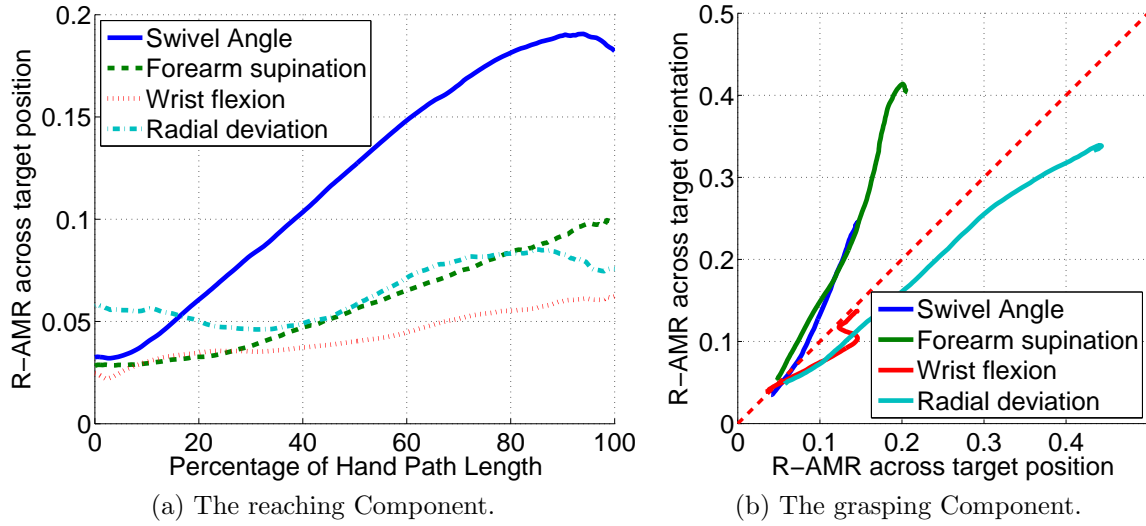


Figure 5.6: The normalized R-AMR values across target position and orientation.
 (a) The mean R-AMR of the reaching component w.r.t the percentage of the path length; (b) the progression of R-AMR values of the grasping component during movement: across-target-position vs. across-target-orientation R-AMR for each GR-DOF starting from the bottom-left.

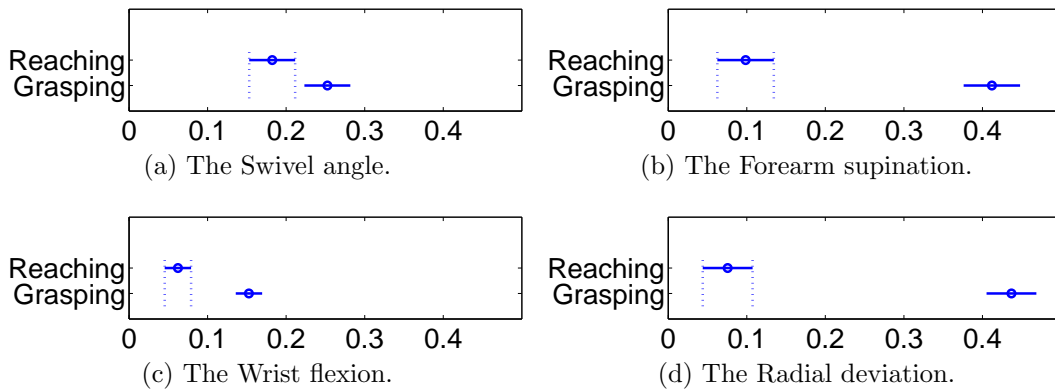


Figure 5.7: Multiple comparison of the R-AMR values at the end of the movements (i.e., the R-AMR_{100%}) between the reaching and grasping components.

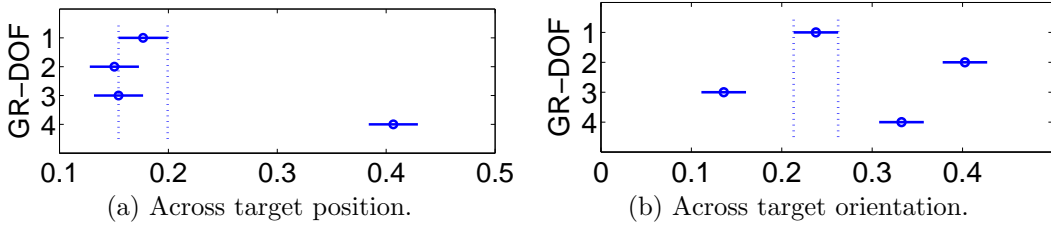


Figure 5.8: Multiple comparison of $R\text{-AMR}_{100\%}$ values for reach-to-grasp tasks. GR-DOFs 1 to 4 refer to swivel angle, forearm supination, wrist flexion, and radial deviation respectively.

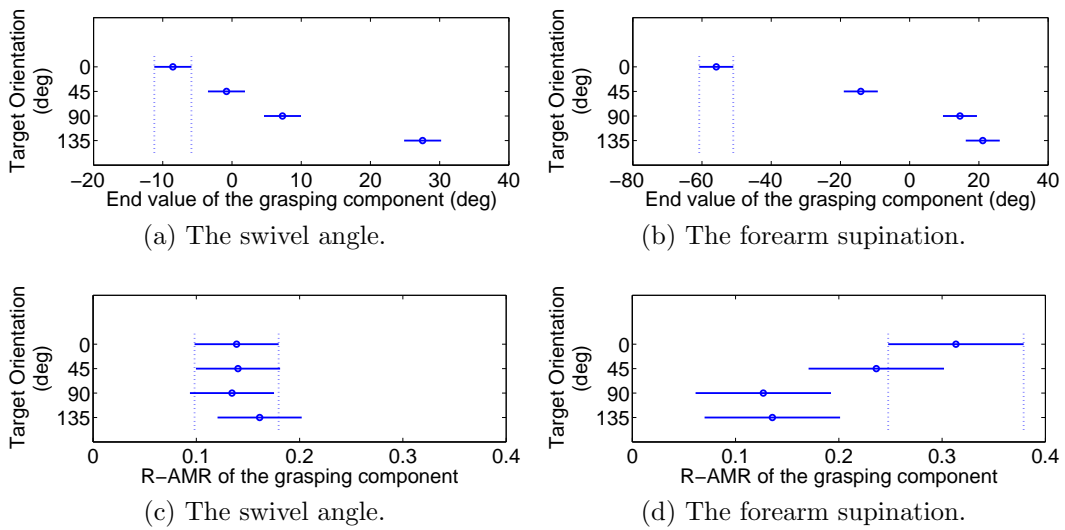


Figure 5.9: Multiple comparison of across-target-position $R\text{-AMR}_{100\%}$ values among different target orientations.

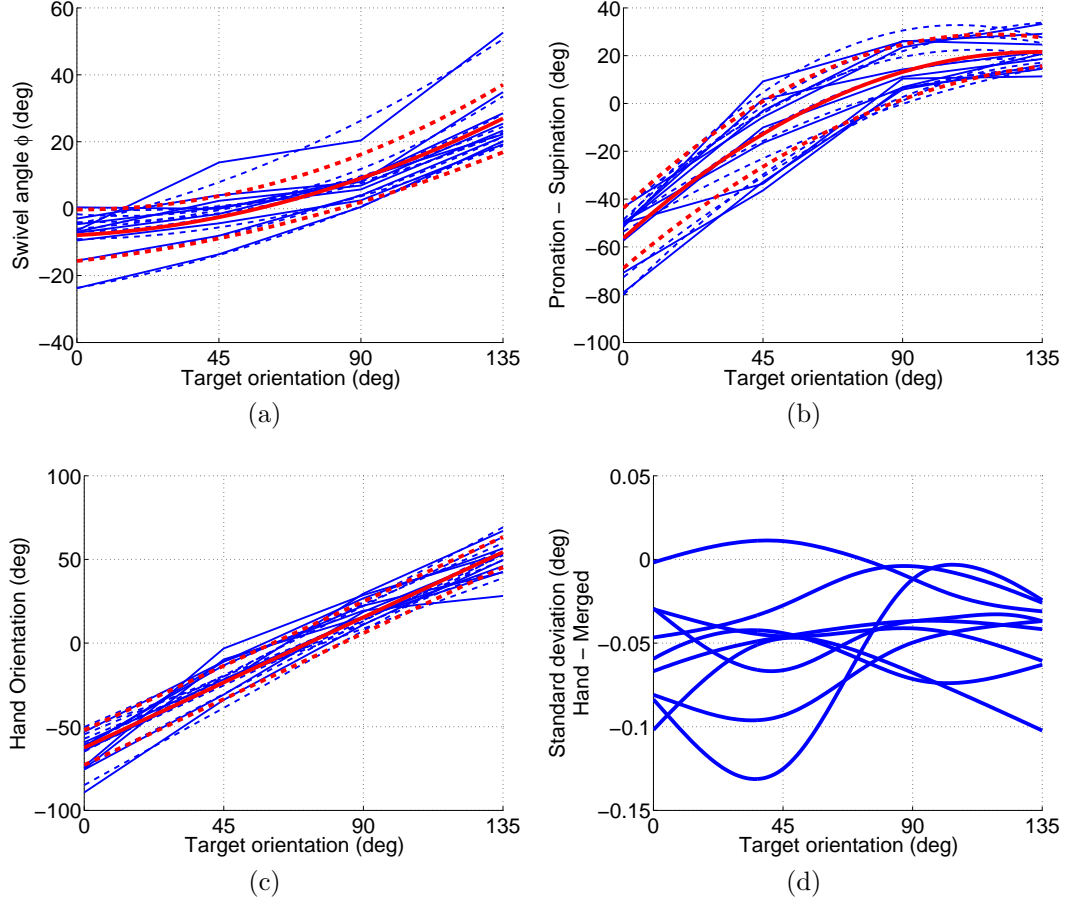


Figure 5.10: The averaged response of grasping component for (a) the swivel angle, (b) the pronation-supination and (c) the hand orientation. (d) $\sigma_\eta - (\sigma_\phi^2 + \sigma_{\theta_5}^2)^{1/2}$ is negative, indicating that the swivel angle and the pronation-supination exhibit synergy.

Chapter 6

Inter-arm Coupling in Bimanual Movements and the Efficacy of Bilateral Training for Stroke Recovery

Bilateral training has been used for post-stroke rehabilitation of patients with paretic upper arms. This training method exploits the inter-arm coupling in bimanual movements which tends to synchronize the paretic arm with the non-paretic arm for motor function recovery. Different levels of motor function recovery have been reported in clinical studies, yet the efficacy of bilateral training is still not clear. As a result, this paper collected data on bimanual symmetric reaching movements in a 3-dimensional (3D) workspace from ten healthy subjects and eight chronic stroke patients, to investigate the effects of inter-arm coupling.

In reaching experiments, identical tasks are also performed unimanually and recorded. This chapter will introduce a method for quantifying the similarity between two recorded arm movements, to measure arm behavior changes and to quantify the similarity of the movements of the two arms. The proposed method provides a quantitative approach which is independent of the task and its associated kinematic and dynamic variables. It is applicable to both in-phase and anti-phase bimanual movements as well as unimanual movements. The inter-arm comparisons provide insight into motor control differences between arms with higher and lower motor function, particularly in chronic stroke patients.

6.1 Quantification of Movement Symmetry

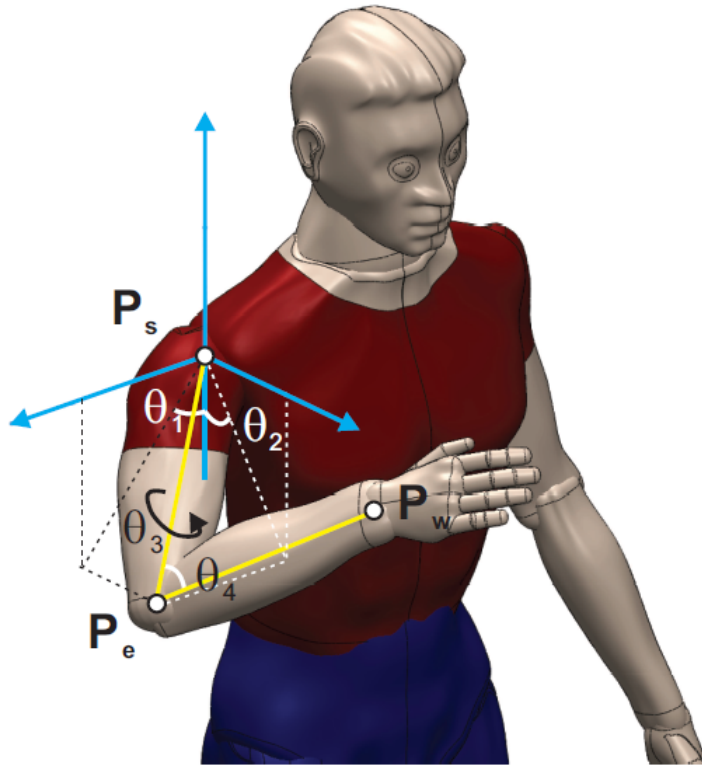


Figure 6.1: The four joint angles extracted from the reaching movements are the shoulder abduction (θ_1), shoulder flexion (θ_2), shoulder rotation (θ_3) and elbow flexion (θ_4).

In reaching experiments, time sequences of shoulder, elbow and wrist positions (denoted by P_s , P_e and P_w respectively; see Fig. 6.1) are recorded and the joint angles are computed by inverse kinematics. Since each subject conducted the reaching movements at their own comfortable pace, the time sequences from each trial are aligned with respect to the percentage of the path length that the wrist has covered as a normalization step. Each mean trajectory is averaged from the five repetitions of the same movement.

6.1.1 Mapping Symmetry

Three mapping symmetry variables can be used to quantify the similarity of two movements. As shown in Fig. 6.2, the normalized and averaged joint angles of one movement (denoted by θ_i) are plotted against the corresponding joint angles from the

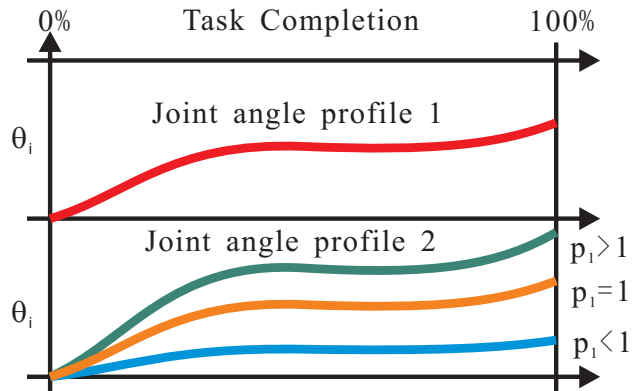
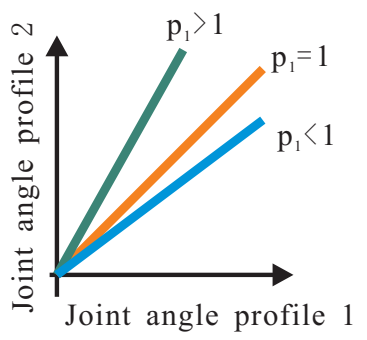
other movement (denoted by θ'_i). A mapping plot based on the movements of the two arms is an inter-arm mapping, while the movements of an identical task performed by the same arm in unimanual and bimanual modes results in an inter-mode mapping. Linear regression is used to find the slope p_1 and the intersection p_2 for a mapping (i.e., $\theta'_i = p_1\theta_i + p_2$). The coefficient of determination R^2 is computed and referred as the mapping linearity. For ideally symmetric movements, the mapping plots are straight line segments with $p_1 = 1$, $p_2 = 0$ and $R^2 = 1$. Any deviation from ideal symmetry is reflected by changes in the three mapping symmetry variables.

As shown in Fig. 6.2 p_1 indicates which motion traverses more of the joint space. Differences between the average postures of two movements result in a non-zero p_2 , while nonlinear deviations lead to an R^2 value less than 1. For inter-arm mappings, the mapping symmetry variables measure inter-arm differences (which reflect both differences in motor control between the hemispheres and differences in arm dynamics). For inter-mode mappings, the mapping symmetry variables measure behavior changes of an individual arm and reflect the effects of inter-arm coupling.

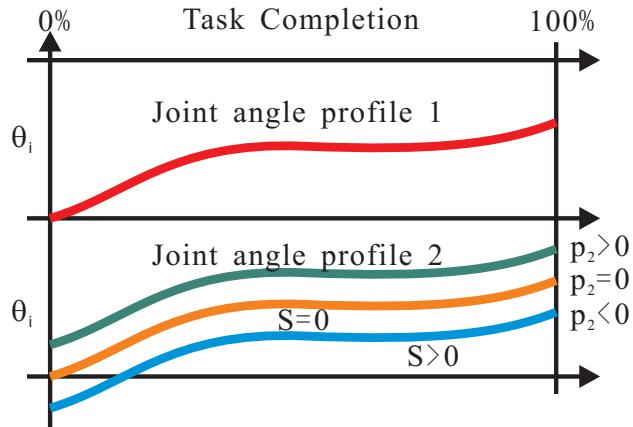
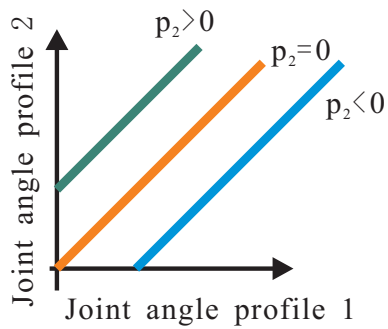
6.1.2 Mapping Complexity

In addition to the mapping symmetry variables, the similarity of two movements can be quantified by their mapping complexity. Identical movements (in-phase or anti-phase) can be mapped to each other using a single line segment, but for movements that differ, an approximate mapping must use multiple line segments to achieve tolerable accuracy (measured by R^2). Using piecewise linear fitting, a mapping plot can be approximated by a sequence of connected line segments, and the number of segments used can be increased until a desired quality of fitting is achieved. Fig. 6.3 shows an example of piecewise linear regression applied to an inter-arm mapping at the elbow flexion θ_4 of a stroke patient.

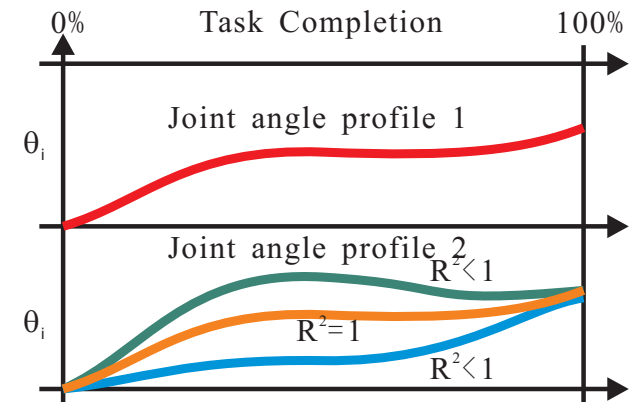
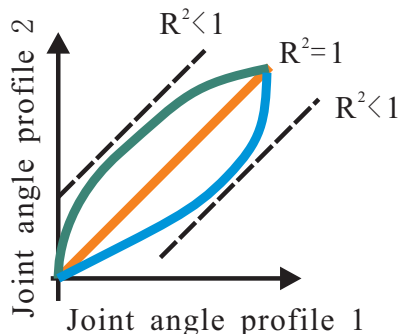
As the number of the approximation line segments (denoted by N) goes up, the coefficient of determination R^2 increases and stabilizes for large N . To represent the shape of a mapping plot without overemphasizing negligible turning points, the mapping complexity N_c is defined as the smallest N such that $R^2 > 0.95$. The mapping complexity of two movements reflects the difficulty in generating one movement given the knowledge of the other. It is similar to the mapping linearity variable R^2 , since the mismatching of two movements usually results in more turning points in the mapping plot and therefore more approximation segments. However, the mapping



(a) p_1 - Slope.



(b) p_2 - Intersection.



(c) R^2 - Coefficient of determination.

Figure 6.2: The variables for measuring mapping symmetry. (a) Diverging trajectories result in different slopes. (b) Parallel trajectories result in different intersections. (c) Nonlinear deviations influence R^2 .

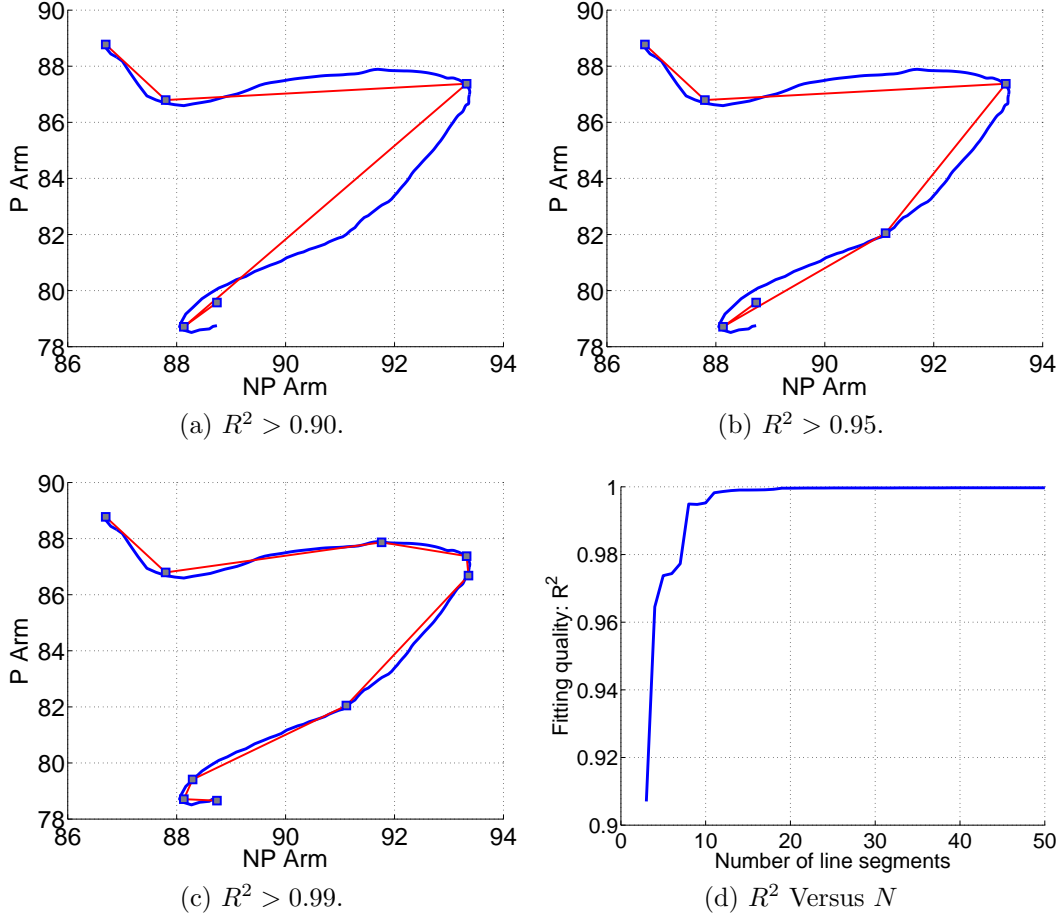


Figure 6.3: Mapping complexity V.S. Fitting quality for a pair of movements at a single joint.

linearity and complexity are not the same. A mapping plot that consists of a few largely non-collinear segments may have large R^2 but low mapping complexity.

6.2 Statistical Data Analysis Method

Fig. 6.4a summarizes the steps of the methodology in a flowchart. As shown in Fig. 6.4b, the data for both arms on both unimanual and bimanual movements are collected from healthy and chronic stroke subjects. Mapping symmetry and complexity variables are extracted for inter-arm and inter-mode mappings, and statistical tests are used to compare the distribution of the variables (1) among the joint angles, and (2) between different experimental cases, including unimanual/bimanual modes and

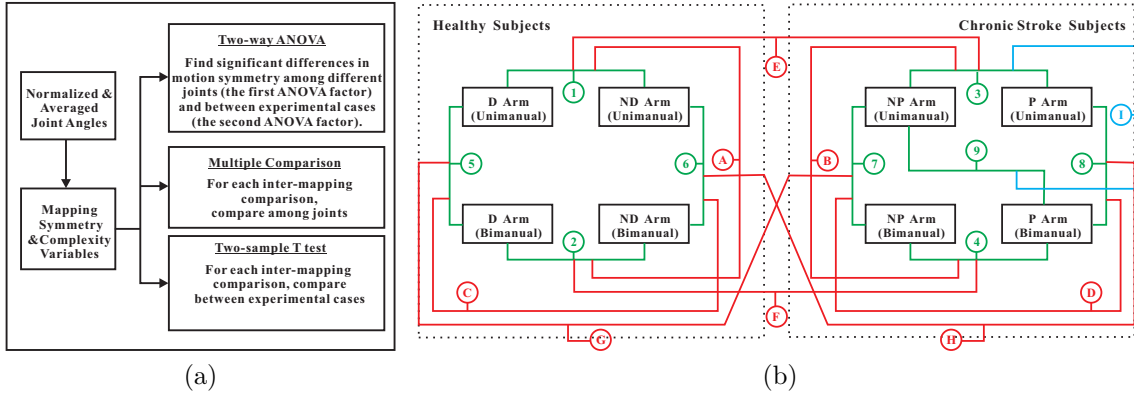


Figure 6.4: (a)The flowchart for the methodology steps, and (b) the mappings (denoted by numbers) and the inter-mapping comparisons (denoted by letters).

healthy/stroke subject categories.

6.3 Results

6.3.1 The Normalized and Averaged Joint Angles

Fig. 6.5 shows an example of normalized and averaged joint angle profiles from a healthy subject. Each bundle consists of five trajectories, each corresponding to the mean trajectory (over five trials) towards a single target. The difference in color/pattern distinguishes movements performed by different arms in different modes.

6.3.2 Representative Mapping Plots

Fig. 6.6 shows the representative mapping plots for the inter-arm mappings and the inter-mode mappings. In each graph, two movements are plotted against each other. These mappings are more nonlinear for stroke subjects than for healthy subjects. Among the joint angles, shoulder flexion θ_2 has the best mapping linearity, while elbow flexion θ_4 is the most nonlinear. The mapping symmetry and complexity indicate the similarity of the two movements being compared.

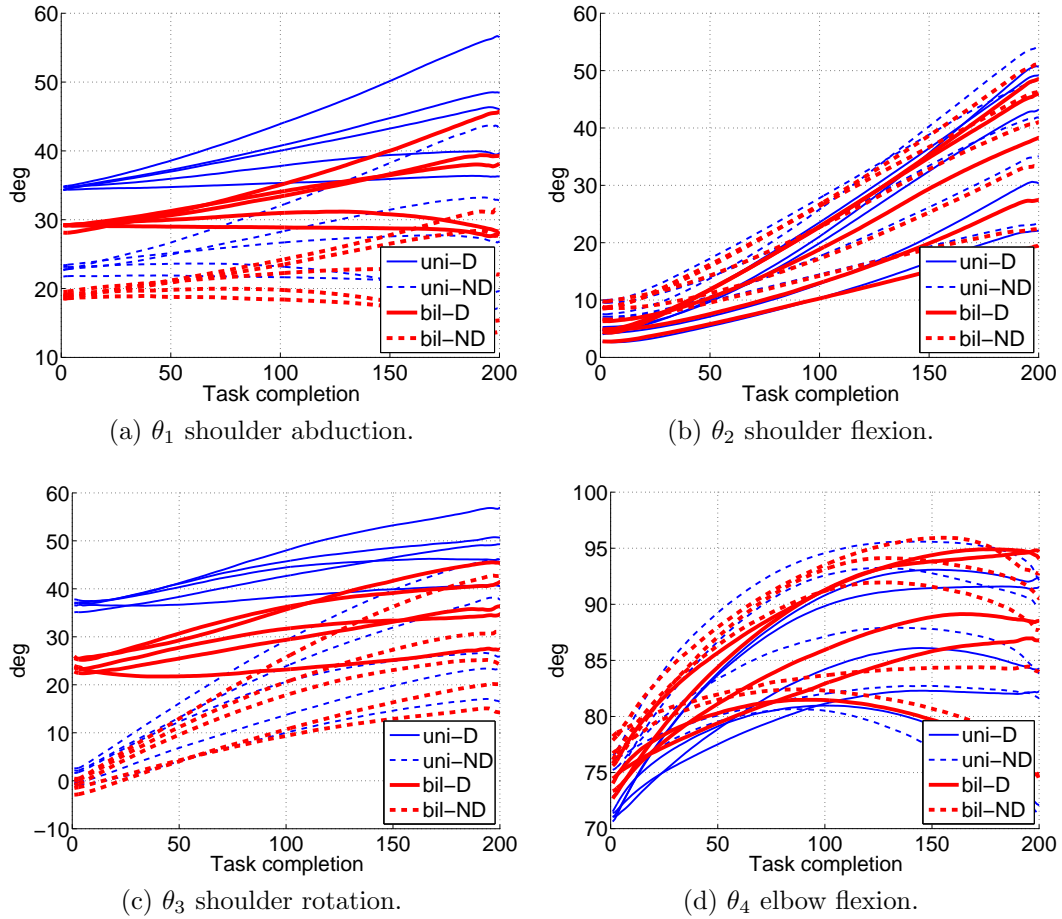
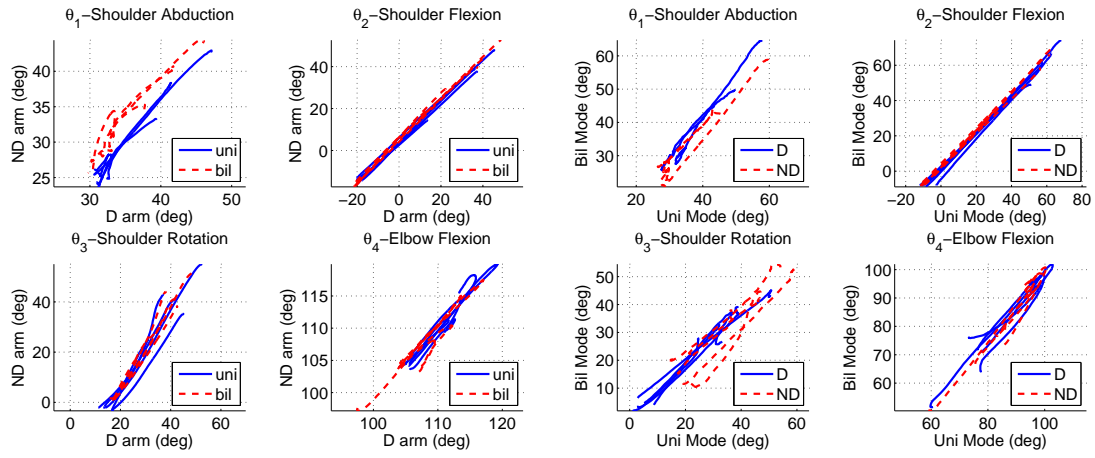


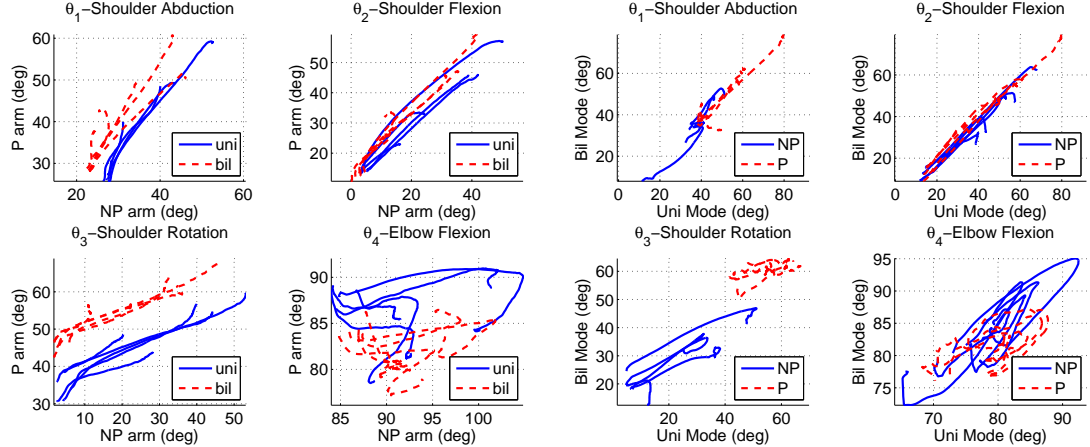
Figure 6.5: The normalized and averaged joint angle trajectories. “uni” and “bi” are for unimanual and bimanual modes, while “D” and “ND” are for dominant and non-dominant arms.

6.3.3 Results of Statistical Analysis

This section presents the results of statistical analysis. First of all, two-way ANOVA is applied to find out the significant differences (1) among joints and (2) between experimental cases (including unimanual/bimanual modes, healthy/stroke subjects, etc.). The significant differences found by two-way ANOVA are further investigated: significant differences among joints are illustrated by multi-comparison, while significant differences between experimental cases are confirmed by two-sample T-test. The summarized results of inter-mapping comparisons presented in Section 6.3.4 first refer to Table 6.1 for significant differences in general. For significant differences among joints it refers to Figures 6.7 and 6.8 , and for significant differences between

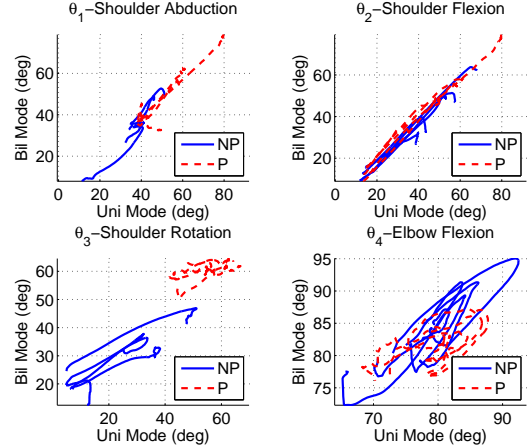


(a) From the dominant arm to the non-dominant arm.



(b) From the non-paretic arm to the paretic arm.

(c) From the unimanual mode to bimanual mode.



(d) From the unimanual mode to bimanual mode.

Figure 6.6: Examples of mapping plots: (a) healthy subject, inter-arm mapping; (b) stroke subject, inter-arm mapping; (c) healthy subject inter-mode mapping; (d) stroke subject, inter-mode mapping.

experimental cases it refers to Table 6.2.

Results of Two-Way ANOVA

Table 6.1 shows the results of two-way ANOVA on comparisons A to H. Each comparison uses a pair of mappings to find differences in motion symmetry among different joints (the first ANOVA factor) and between experimental cases (the second ANOVA factor). The second factor is mode (unimanual/bimanual) for comparisons A and

	Comparison A			Comparison B		
	θ_i	Uni/Bi	Interaction	θ_i	Uni/Bi	Interaction
p_1	★			★		
p_2	★			★		
R^2	★	★		★		
N_c	★	★		★		
	Comparison C			Comparison D		
	θ_i	D/ND	Interaction	θ_i	NP/P	Interaction
p_1	★			★		
p_2	★			★	★	
R^2	★			★		
N_c	★			★		
	Comparison E			Comparison F		
	θ_i	H/S	Interaction	θ_i	H/S	Interaction
p_1		★	★	★	★	★
p_2	★	★	★	★	★	★
R^2	★	★	★	★	★	★
N_c	★	★		★	★	★
	Comparison G			Comparison H		
	θ_i	H/S	Interaction	θ_i	H/S	Interaction
p_1	★		★	★	★	
p_2	★			★	★	★
R^2	★			★	★	★
N_c	★	★		★	★	

Table 6.1: Results of two-way ANOVA on the inter-mapping comparisons A to H. Each analysis indicates a significant difference at the 95% confidence level with a “★”. Fig. 6.4b indicates which data are used in each comparison.

B, arm dominance/paresis for comparisons C and D, and subject category (“H” for healthy and “S” for stroke) for comparisons E, F, G, and H. Where a significant difference is found with a confidence level of 95%, a “★” is shown.

For the first factor (joint), all the comparisons show significant differences, except for the p_1 variable for comparison E. For the second factor, a few significant differences are found for the comparisons within subject categories (comparisons A, B, C, and D), including (1) the coefficient of determination R^2 and mapping complexity N_c for comparison A, and (2) posture difference p_2 in comparison D. The comparisons between healthy and stroke subjects reveal more significant differences.

Multiple Comparison Among Joints

Based on the two-way ANOVA results, a post hoc comparison is applied to find joints with outstanding behavior. The significant differences in the θ_i column of Table 6.1 are further illustrated by Figures 6.7 and 6.8.

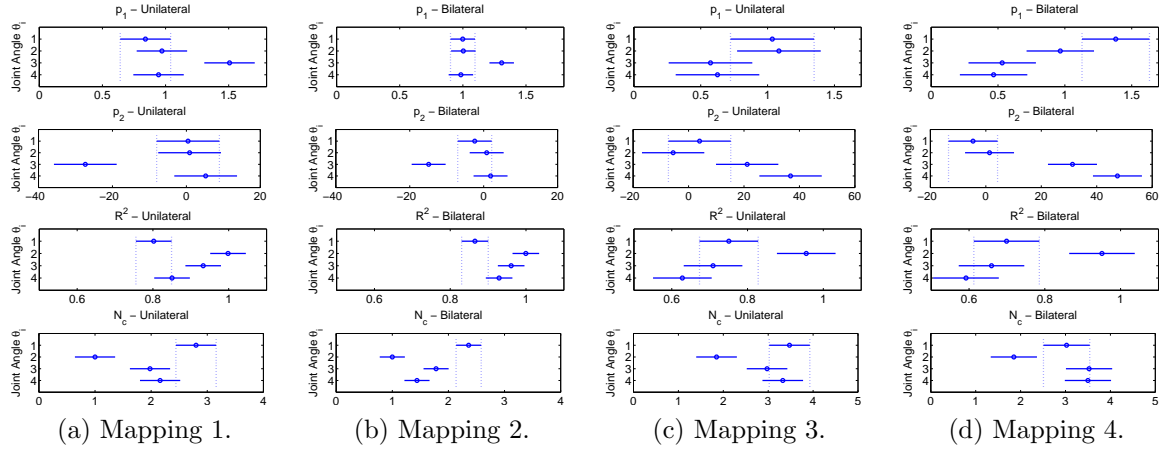


Figure 6.7: Results of multi-comparison among joints. The inter-arm mappings are: (a) healthy subject, unimanual mode; (b) healthy subject, bimanual mode; (c) stroke subject, unimanual mode; (d) stroke subject, bimanual mode.

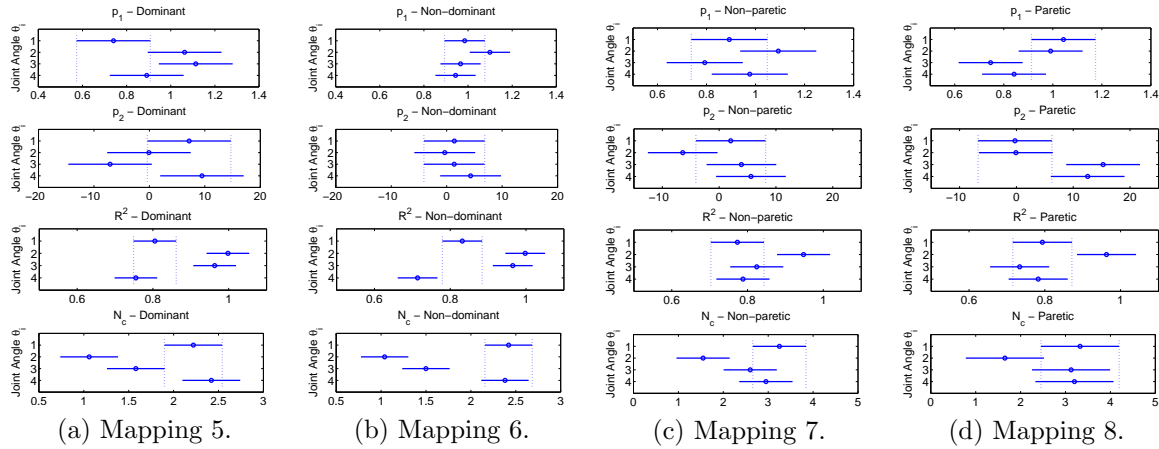


Figure 6.8: Results of multi-comparison among joints. The inter-mode mappings are: (a) healthy subject, dominant arm; (b) healthy subject, non-dominant arm; (c) stroke subject, non-paretic arm; (d) stroke subject, paretic arm.

Results of Two-sample T-tests

	Comparison A				Comparison B				Comparison C				Comparison D			
	θ_1	θ_2	θ_3	θ_4												
p_1															-	
p_2					+								+	+		
R^2	+		+													
N_c			-													
	Comparison E				Comparison F				Comparison G				Comparison H			
	θ_1	θ_2	θ_3	θ_4												
p_1			-	-			-	-						-	-	
p_2	-	+	+			+	+		-					+		
R^2	-	-	-	-	-	-	-	-	-	-	-	-	-	-	-	-
N_c	+	+	+	+		+	+	+	+	+	+	+		+	+	+

Table 6.2: Results of two-sample T-tests: inter-mapping comparisons on the means of each variable.

Table 6.2 shows the results of two-sample T-tests on the distribution of the variables extracted from each of the two mappings corresponding to the same joint. The two-sample T test is used to compare the means of the two populations. At the 95% confidence level, a significant increase is marked by “+” and a significant decrease by “-”. The details of the significant differences will be elaborated for each comparison.

6.3.4 Summarized Results of Inter-mapping Comparisons

Comparison A

Mappings 1 and 2 are the inter-arm mappings of healthy subjects in unimanual and bimanual modes. As shown in Figures 6.7a and 6.7b , in both unimanual and bi-manual modes, θ_3 stands out in both p_1 and p_2 , indicating that the non-dominant arm traverses more of the joint space (largest positive p_1) but is lower in average arm posture (smallest negative p_2) than the dominant arm. R^2 indicates significant differences between θ_2 and θ_1 , which is more pronounced in their N_c . Particularly, θ_2 is close to ideally symmetric for p_1 , p_2 , and R^2 , in addition to having the lowest N_c .

Table 6.1 shows the significant differences in R^2 and N_c between the inter-arm mappings in unimanual and bimanual modes. Referring to Table 6.2, in bimanual mode, (1) R^2 is increased at θ_2 and θ_4 (see Figures 6.9a and 6.9b), and (2) N_c

is reduced at θ_4 (see Fig. 6.9c). As expected, these differences indicate that the bimanual mode exhibits increased symmetry in arm movement, presumably due to interarm coupling.

Comparison B

Mappings 3 and 4 are the inter-arm mappings of the chronic stroke subjects in unimanual and bimanual modes. As shown in Figures 6.7c and 6.7d, in both unimanual and bimanual modes, at both shoulder rotation θ_3 and elbow flexion θ_4 , the paretic arm traverses less of the joint space ($p_1 < 1$) and has higher average arm posture (large positive p_2) than the non-paretic arm. Shoulder flexion θ_2 has the highest R^2 and the lowest N_c of the joints, while the R^2 and N_c of shoulder abduction θ_1 are comparable to those of θ_3 and θ_4 , which indicates that shoulder flexion is the most symmetric joint in stroke patients.

According to Table 6.2, the shoulder flexion θ_2 of the paretic arm has lower average arm posture than the non-paretic arm in unimanual mode, while in bimanual mode, the two arms have about the same posture. As shown in Fig. 6.9d, p_2 is increased at θ_2 , while its mean is close to zero.

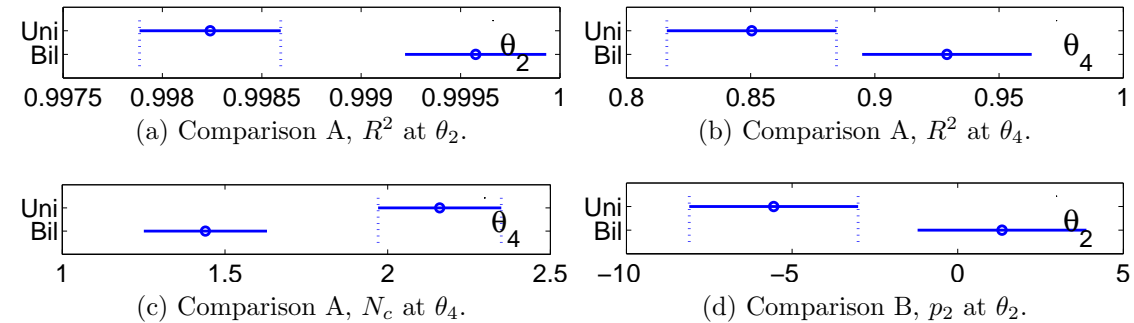


Figure 6.9: Results of multi-comparison of the unimanual and bimanual modes in comparisons A and B.

Comparison C

Figures 6.8a and 6.8b compares the inter-mode mappings of the dominant and non-dominant arms of the healthy subjects. For both of the two arms, θ_2 and θ_3 have larger R^2 and lower N_c . Comparing among the joints, for the dominant arm, p_1 at θ_1 is much less than 1; p_2 at θ_1 and θ_4 is greater than zero, while at θ_3 , p_2 is less than

zero (see Fig. 6.8a). On the other hand, p_1 and p_2 of the non-dominant arm deviate less from ideal symmetry (see Fig. 6.8b). Table 6.1 confirms the significant differences among joints but shows no significant differences between the two arms.

Comparison D

Figures 6.8c and 6.8d compares the inter-mode mappings of paretic and non-paretic arms of the chronic stroke patients. For the non-paretic arm, the mapping is most nonlinear at θ_4 (largest R^2). The posture of the paretic arm raised was higher at θ_3 and θ_4 in bimanual mode. For both of the two arms, θ_2 is outstanding for highest R^2 and lowest N_c .

Table 6.1 reports the significant differences in p_2 and R^2 between the inter-mode mappings of the two arm. With reference to Table 6.2, we find the following significant differences between the paretic and non-paretic arms: (1) at θ_2 , the paretic arm traverses about the same distance in joint space (p_1 is about 1) and maintains about the same average arm posture (p_2 is about zero) for different modes, while the non-paretic arm traverses more of the joint space (p_1 is about 1.1) and reduces the average arm posture ($p_2 < 0$) in bimanual mode (see Figures 6.10a to 6.10b); (2) at θ_3 , the increase of arm posture is more pronounced in the paretic arm than the non-paretic arm (see Fig. 6.10c).

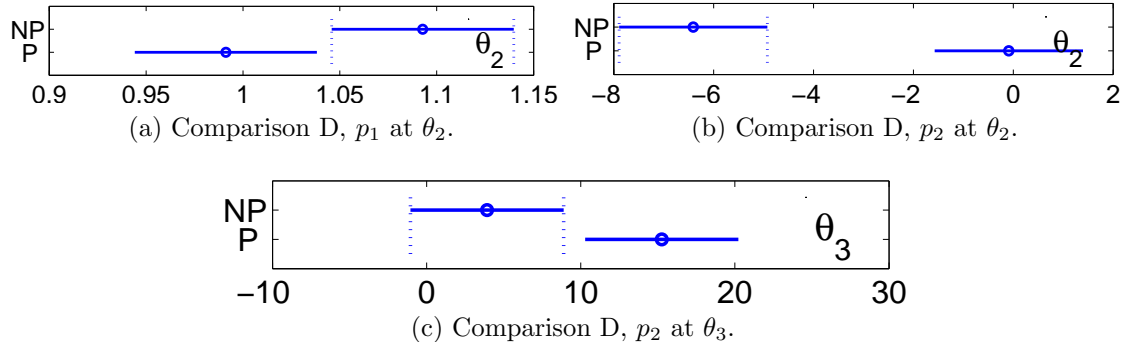


Figure 6.10: Results of Multi-comparison the Unimanual and Bimanual Modes: Comparison D

Comparison Between Healthy and Stroke Subject (Comparison E to H)

Comparison E to H are the comparisons between the mappings of the healthy and stroke subjects. Referring to the significant differences listed in Table 6.1 and 6.2, the stroke subjects have higher mapping nonlinearity (R^2) and mapping complexity (N_c) than the healthy subjects, where a significant difference exists. In general, the mappings with significantly higher nonlinearity also have higher mapping complexity. However, the mapping linearity R^2 and the mapping complexity N_c do not report significant differences consistently all the time. Referring to the p values, when R^2 reports a significant difference, the p -value of N_c is very close to the level of significance (i.e., $p = 0.05$). On the other hand, when N_c reports a significant difference, the p -value of R^2 is much larger than the level of significance.

Comparison I (Changes in the Paretic Arm w.r.t the Non-paretic Arm)

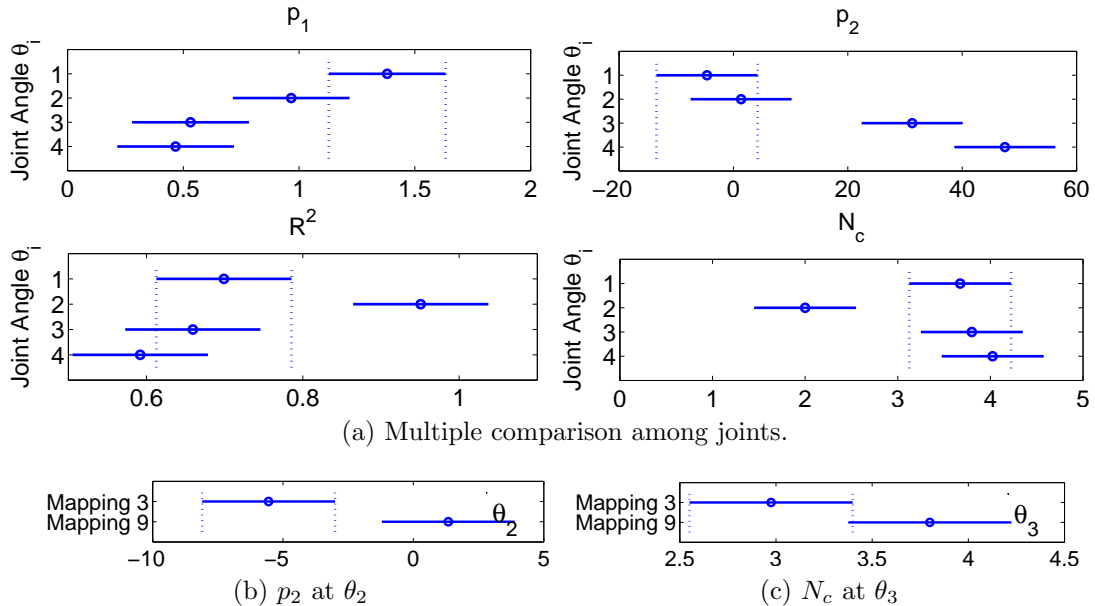


Figure 6.11: Mapping 9: from the paretic arm in bimanual mode to the non-paretic arm in unimanual mode. (a) Results of multiple comparison among joints. (b) and (c) Significant differences in Comparison I (Mapping 3 V.S. Mapping 9).

To investigate changes in the paretic arm when inter-arm coupling takes effect, we compare the inter-arm mappings from the unimanual and bimanual movements of the paretic arm to the unimanual movements of the non-paretic arm. The mapping

symmetry and complexity variables are extracted from mapping 9 and compared with mapping 3. According to the comparison among joints (see Fig. 6.11a), the higher average arm posture of the paretic arm is more pronounced at shoulder rotation θ_3 and elbow flexion θ_4 ; the mapping complexity is the lowest at shoulder flexion θ_2 . As shown in Fig. 6.11c, the significant differences between mapping 3 and 9 show that: (1) the shoulder flexion θ_2 of the paretic arm is higher in bimanual mode with respect to the non-paretic arm in unimanual mode, and (2) the mapping complexity N_c is increased at the shoulder rotation θ_3 .

Chapter 7

Discussion and Conclusions

This chapter presents the discussions and conclusions based on the researches in Chapter 4 to 5.

7.1 The Spatial Map of Synthesized Criteria for the Redundancy Resolution of Human Arm Movements

This research has analyzed recorded data from reaching movements and inferred the contributions of various criteria to arm motion control. Five criteria (three kinematic and two dynamic) are investigated, and are compared by their the swivel angle prediction performance. Inference based on synthesized criteria using the exponential method predicts the arm postures more accurately than inference using the least squares method. Using the exponential method, among 2674 valid trials collected from ten healthy subjects, the mean and standard deviation of the prediction errors during movement was less than 5° for 79% of the trials, and only 3% of trials had either a mean or standard deviation of the prediction error of more than 10° .

Using K-means clustering, the contribution coefficient vectors are grouped into nine clusters with distinguishable coefficient value distributions, which indicate the characteristic combinations of motion control criteria. The clusters are mapped to wrist positions in the 3D workspace, and their high-frequency regions are presented in a colored map. Based on the results presented in Chapter 4, this section will provide further discussion that highlights the new findings regarding the strategies of healthy

arm motion control. Both the methodology contribution (i.e., the general framework that synthesizes, evaluates and compares motion control criteria that resolve the kinematic redundancy of human arm) and its application to the real-time control of an upper limb exoskeleton will be addressed.

7.1.1 Regional Motion Control Strategies in the Task Space

The data analysis has shown by synthesizing a limited number of control criteria that address different aspects of motion characteristics, the kinematic redundancy of the human arm can be resolved to render natural human arm postures in reaching movements. The redundancy resolution according to the combined control criteria outperforms all of its individual components. The method used to combine the criteria is critical to getting good estimations of arm posture. The arm postures are not well-predicted by the least squares method, which assigns the contribution coefficients based on the overall prediction performance within a relatively long history. The higher performance of the exponential method, which assigns contribution coefficients only based on the prediction of the last time step indicates that the contribution of each individual criterion is time-sensitive. Indeed, the contribution coefficient assigned to each individual criterion varies during the reaching movement, instead of maintaining a constant value for the whole movement. In previous research, Kashi *et al.* integrated two kinematic control criteria and suggested constant partial contributions to combine these two criteria: 70% for the criterion that minimized angular displacement and 30% for the criterion that averaged the limits of the shoulder joint range [29]. Kim *et al.* combined a criterion that maximized motion efficiency (Criteria 1) with one that minimized the work in joint space (Criteria 5) using least squares and claimed that the contribution of the dynamic criterion is negligible compared with the kinematic criterion [18]. Biess *et al.* suggested a global path planning method that defines the temporal properties of the movement by minimizing the squared jerk along the selected end-effector path, and the spatial properties of the movements by finding the geodesic path in joint space [27]. According to this method, there exists a single control criterion that dictates the spatiotemporal properties of reaching movements. These results are all challenged by our findings that (1) the contribution coefficients of combined criteria should be time-varying instead of constant, and (2) no single control criterion can accurately model arm movements from the beginning to the end.

Clustering the contribution coefficient vectors showed the spatial dependence of the criterion contributions in addition to its temporal dependence. A combined map of cluster frequency (Fig. 4.10d) shows that the lower part of the workspace is dominated by cluster 1 (represented by red). Cluster 1 is significantly affected by criteria 3, 4 and 5: the kinematic criterion that minimizes the joint angle change, as well as the two dynamic criteria that minimize the change in kinetic energy and the work done in joint space. A possible explanation for the high frequency of Cluster 1 in this region is that when reaching for targets in the lower part of the workspace, the arm is far away from the center of the stereoscopic visual range. Without seeing the movements of the whole arm, motion control may be more dependent on proprioceptive feedback. Low elbow postures in accordance with the direction of gravity do not block the view for reaching movement in this region, and therefore may be preferred for less energy consumption. In addition, when reaching to the lower-left part of the workspace, these energy-saving elbow postures may be preferred since the arm motion range is constrained by the torso.

In the upper-right part of the workspace, Cluster 3 is the most frequent (represented by yellow in Fig. 4.10d). According to Fig. 4.8c, the control strategy of cluster 3 is strongly affected by two kinematic criteria: maintaining the equilibrium posture (criterion 2) and minimizing the joint angle change (criterion 3). With the shoulder position aligned with the center of the workspace, the upper part of the workspace is about even with eye-level. The equilibrium posture may be preferred since it naturally brings the hand into the stereoscopic visual range, and results in less work for the periarticular muscles. Note that the dynamic model used simulates the human arm as linked rigid bodies. Without simulating muscular forces, dynamic criteria are less useful than the equilibrium posture criterion in predicting motions in this area. The criterion that minimizes the joint angle change demonstrates a strong impact in Clusters 1 to 4. Considering the fraction of the coefficient vectors in these four clusters (62.56%) and the area of the workspace where they have high frequency (see Figures 4.9a to 4.9d), this criterion that emphasizes smoothness of motion is generally applicable to the whole workspace.

7.1.2 Methodology Contribution

As a methodology contribution, this paper proposes: (1) a general framework for the comparison of real-time motion control criteria and (2) methods for criterion syn-

thesis and contribution inference. By synthesizing a highly-accurate motion control criterion out of several candidate criteria, the method followed here is able to infer the contribution of each candidate criterion to arm motion control, and the temporal and spatial variation of its contribution. Clustering is used to determine which criteria are related, and find characteristic combinations of criteria that best explain arm motion in different areas of the task space. This allows for high-fidelity analysis of the criterion contributions, and a computationally efficient cost function which ignores criteria with negligible contributions could be constructed as a result. This framework could also be used to evaluate more candidate criteria besides those presented in this paper.

Within the proposed general framework, the least squares and the exponential methods are investigated. Section 4.5.1 presents the prediction quality of the synthesized criteria using these methods, as well as the prediction quality of each candidate criterion. Compared to the least squares method, the proposed exponential method is preferable for criterion synthesis and contribution inference: it predicts the arm posture more accurately than all of the individual candidate criteria, while the least squares method predicts no better than the criterion with the best individual performance. The main difference between the two synthesis methods is that the least squares method considers the last 20 steps of history and tries to find a set of constant coefficients which maximize prediction accuracy during that period, whereas the exponential method only considers prediction error in the last step and adjusts the coefficients at each step accordingly. The least squares method would be able to predict arm posture accurately if the contribution of each candidate criterion were relatively constant, but the more accurate prediction rendered by the exponential method shows that the contributions of candidate criteria are not constant. As shown in Figures 4.6 to 4.10d , the contribution coefficients vary in time and space.

7.2 Task-relevance of Grasping-related Degrees of Freedom in Reach-to-grasp Movements

In reach-to-grasp movements, arm posture is significantly affected by grasp orientation. The kinematic analysis on human arm has indicated that compared to joint coordination in reaching movements, human arm only behaves differently at the four grasping-relevant degrees of freedom (GR-DOFs), including the swivel angle, the

pronation-supination, the wrist flexion and the radial deviation. As a result, this research focused on the four GR-DOFs and separated their grasping components from their reaching components.

7.2.1 The Task-dependent Coordination of GR-DOFs

Investigations of the grasping components of the GR-DOFs have indicated that the coordination of the GR-DOFs are task-dependent. Comparing their ratios of active motion range (R-AMR), the task-relevant GR-DOFs are more actively used, while the task-irrelevant joints are left uncontrolled. In the reach-to-grasp experiments, the target orientation varies in the plane that the subject faces, which demands the cooperative responses of the swivel angle and the pronation-supination. The wrist flexion is least useful for matching hand orientation to target orientation and therefore its joint angle does not vary much for different target positions and orientations. To minimize the control effort, such task-irrelevant joints are preferably maintained at their neutral positions [39].

The analysis on the R-AMR values further pointed out that among the task-relevant GR-DOFs, the smaller joints are more actively used than the larger joints. In the control of robotic manipulator, the macro and micro joints has been assigned with different control priorities in the trajectory tracking task. In [224], a flexible macro-structure that moves quickly over a wide range of motion is mainly responsible for the task, while a rigid micro-structure compensates for tracking errors. In the context of reach-to-grasp movements, one way to segment the macro/micro structures refers to the arm as a macro mechanism and the hand as a micro mechanism. As such, the arm as a gross positioner is manipulable to maximize the dexterity of the hand as the micro manipulator which is responsible for accomplishing the task [93, 94]. To adjust the hand orientation, since the swivel angle (macro) and the pronation-supination angle of the forearm (micro) can serve the same purpose, it is more energy-efficient to adjust the pronation-supination angle of the forearm as opposed to the swivel angle if the target orientation is within the range of motion of the forearm.

The coordination of the task-relevant GR-DOFs has been analyzed by their responses to the changes in target orientation. As shown in Fig. 5.10d, the total variance of the swivel angle and the pronation-supination is less than the variance in their resulted hand orientation, which indicates that the coordination of the task-relevant GR-DOFs is in synergy. Studies on the variability of human motion have pointed

out that motor synergy reduces the computational complexity of motor control. It is generally applicable to different levels of motor activities (neural, muscular, dynamic, kinematic, etc.), and appropriate for coordinating the numerous degrees of freedom in the body [165]. In previous research, the motor synergy has been found in the two-finger force production task [8]. As an original contribution, this paper provides a method to measure the task-relevance of the GR-DOFs and provides further evidence of the motor synergy of the task-relevant GR-DOFs in multiple joint coordination.

7.2.2 On the Control of the Upper Limb Exoskeleton

Studies on the joint coordination in reach-to-grasp movements provide useful guidelines for the control of the upper limb exoskeleton. The separation of the reaching and grasping components shows that the redundancy resolution of the reach-to-grasp movements can take advantage of existing redundancy resolution methods for reaching movements. During the movements, the grasping components of the swivel angle and pronation-supination are mostly linear with respect to the percentage of the hand path length. In response to the changes in the target orientation, the end values of these two synergistically coordinated GR-DOFs may follow the proposed regression (see Equations (5.1) to (5.3)). For reach-to-grasp tasks similar to the experiments described in this paper, the end values of the radial deviation varies more across target position than across target orientation. At the end of the movements, the flexion-extension can be constrained to its neutral position to reduce the control complexity. Regarding the temporal responses of the GR-DOFs, the analysis of acceleration/deceleration shows that the reach-to-grasp movement has three distinguishable phases with different levels of voluntary control. As a result, this research suggests that feed-forward control be used during the first 80% of the path length and feedback control for precisely matching the hand orientation with the target orientation.

7.3 The Effect of Inter-arm Coupling and the Efficacy of Bilateral Training

7.3.1 On the Inter-arm Mappings

The inter-arm mappings in unimanual mode imply a general similarity of individual motor control for each arm. The comparisons of the inter-arm mapping between unimanual and bimanual modes reveal the effects of inter-arm coupling. According to the multiple comparisons among joints, for the healthy subjects, shoulder flexion θ_2 of the two arms has the most similar movements among all the joints in both unimanual and bimanual modes, indicated by its close-to-ideal symmetry and minimal mapping complexity. Shoulder rotation θ_3 is the least symmetric joint in terms of motion range in joint space and arm posture, while shoulder abduction θ_1 is outstanding for having the most nonlinearity (lowest R^2) and highest mapping complexity (highest N_c). For the stroke subjects, although there are not as many significant differences among the joints, shoulder flexion θ_2 still has the lowest mapping complexity. Shoulder rotation θ_3 and elbow flexion θ_4 are outstandingly non-symmetric in motion range and arm posture. The mapping linearity and complexity of the shoulder abduction θ_1 is comparable to those of the shoulder rotation θ_3 and elbow flexion θ_4 .

As shown in comparisons A and B, for both the healthy and stroke subjects, shoulder flexion θ_2 demonstrates improved mapping symmetry in bimanual mode; the mapping symmetry is improved at the elbow flexion θ_4 for the healthy subjects but not for the stroke subjects. It is possible that the symmetry effects of inter-arm coupling are task-dependent: in this reaching experiment, the subjects are asked to reach forward to touch the targets, which demands more movement in terms of the shoulder flexion θ_2 and elbow flexion θ_4 than at the shoulder abduction θ_1 and rotation θ_3 . In the unimanual mode, the two arms have more similar individual control at the task-relevant joints; in bimanual mode, the similarity is emphasized by the inter-arm coupling. Between the two task-relevant joints, the movements at the shoulder flexion θ_2 are simpler than those of the elbow flexion θ_4 in the reaching-forward task. Since controlling the elbow flexion in bimanual mode is challenging to the stroke subjects, the effects of inter-arm coupling are overshadowed, resulting in no significant improvement in mapping symmetry.

7.3.2 On The Inter-mode Mappings

The comparisons between the inter-mode mappings reveal the contributions of the two arms to movement symmetry. As shown in comparison C, there is no significant difference between the inter-modes mappings of the dominant and non-dominant arms. However, comparing the linearity of the joints, the inter-mode mapping of the dominant arm deviates further from ideal symmetry than the non-dominant arm. Note that the inter-mode mapping indicates the deviation of bimanual movements from unimanual movements of the same arm. Therefore the dominant arm, which has higher motor function than the non-dominant arm, is more affected by inter-arm coupling and contributes more to the inter-arm mapping symmetry. For the stroke subjects, comparison B shows that the two arms have improved symmetry at the shoulder flexion θ_2 in bimanual mode. Comparison D further shows that the paretic arm prefers to stick to its unimanual behavior, while the non-paretic arm changes significantly in bimanual mode. The non-paretic arm exhibits increased motion range and reducing posture at the shoulder flexion θ_2 , thus it contributes more to the improved inter-arm mapping symmetry. The inter-mode mapping at the elbow flexion θ_4 is more nonlinear for the non-paretic arm, which indicates a large deviation from its unimanual behavior.

According to the multiple comparison among joints for mapping 8, it is worth noting that the paretic arm has higher posture in bimanual mode than in unimanual mode at the shoulder rotation θ_3 and elbow flexion θ_4 . These changes do not result in significant improvement in inter-arm mapping symmetry, yet they indicate that inter-arm coupling has an effect on the abnormal behavior of the paretic arm. In comparison D, the increased arm posture at the shoulder rotation θ_3 is significantly larger in the paretic arm than in the non-paretic arm (see Fig. 6.10c). At the same time, at the shoulder flexion θ_2 , the paretic arm maintains its posture in bimanual mode, while the non-paretic arm significantly reduces its posture (see Fig. 6.10b). For the paretic arm, shoulder rotation θ_3 increases in order to compensate for the limited motion range in shoulder flexion θ_2 . Through inter-arm coupling, the paretic arm affects the non-paretic arm by suppressing shoulder flexion and encouraging shoulder rotation. It is hypothesized that for the stroke patients, the inter-arm coupling, although not strong enough to improve the symmetry of the two arms, tries to synchronize the movement tendency.

7.3.3 On the Control of Task-Relevant and Task-Irrelevant Joints

The results on the inter-arm and inter-mode mappings reveal the effects of inter-arm coupling on task-relevant and task-irrelevant joints. In reaching-forward tasks, the shoulder flexion θ_2 and elbow flexion θ_4 are more task-relevant than the other two joints. Considering the increased inter-arm mapping symmetry at shoulder flexion θ_2 and elbow flexion θ_4 of the healthy subjects, it is hypothesized that as a motor control constraint, inter-arm coupling affects the task-relevant joint(s) more strongly than it affects the task-irrelevant joint(s). However, for two joints of the same task-relevance, if the motion at one joint is more complicated than the other, the regulation effort of inter-arm coupling may not result in the same mapping symmetry and complexity. Referring to the mapping plots of different joints (see Fig. 6.6), the elbow flexion θ_4 first increases and then decreases in reaching-forward movements, while the other joints only increased. A more complicated motion at a joint implies higher control complexity.

The mapping linearity and complexity depend on both the task-relevance and the control complexity. The more task-relevant joints demand more control effort which results in increased mapping symmetry. On the other hand, at joints with higher control complexity, inter-arm coupling may not be able to fully synchronize their movements. For instance, the low mapping complexity at the shoulder flexion θ_2 results from its high task-relevance and its low control complexity. On the other hand, the mapping complexity at the elbow flexion θ_4 (a task-relevant joint) is as high as the shoulder rotation θ_3 (a task-irrelevant joint), since the motion at the elbow flexion θ_4 is more complicated than the shoulder flexion θ_2 in the reaching-forward task and therefore demands more control effort.

7.3.4 On the Mapping Symmetry and Complexity Variables

To measure the similarity on the movements, we have proposed four mapping symmetry and complexity variables. The three mapping symmetry variables are based on a linear regression of the mapping plot, while the mapping complexity is based on a piecewise linear fitting. In the statistical analysis, the four variables capture the effects of inter-arm coupling from different perspectives: the mapping symmetry variables p_1 and p_2 represent the motion range in joint space and the average posture respectively, while R^2 and N_c indicate the total effect of the control effort and control

complexity respectively. In general, R^2 and N_c behave consistently. In comparisons between healthy and stroke subjects, differences between R^2 and N_c show that N_c is more sensitive. N_c is more sensitive because it captures the significant changes in the paretic arm with respect to the unimanual movement of the non-paretic arm (see comparison I), which indicates the subtle but important inter-arm coupling effect, i.e., the effect of a stroke on joint coordination. At task-relevant joints, inter-arm coupling is strong enough to fight against the persistent individual planning of the paretic arm. The non-paretic arm, which is more adaptive and therefore more sensitive to the inter-arm coupling effect, is forced to behave like the paretic arm. At task-irrelevant joints, the control effort from individual planning is not as much as at task-relevant joints. As a result, the inter-arm coupling is overwhelmed such that it is necessary to use a sensitive variable to measure the subtle improvement from the bilateral training.

7.3.5 Efficacy of the Bilateral Training

What benefits can we get from bilateral training? According to comparison I, with respect to the unimanual movements of the non-paretic arm, the the paretic arm raised higher at shoulder flexion in bimanual mode than in the unimanual mode, which indicates an increase in average posture. Furthermore, the mapping complexity is increased at the shoulder rotation, which implies an effect on the abnormal joint co-ordination. When the motion range at shoulder flexion is limited, the stroke patients tend to increase the use of shoulder rotation, either due to voluntary compensation or involuntary abnormal joint coordination. In stroke rehabilitation, the recovery of healthy coordination among the joints requires encouraging task-relevant motions and suppressing the movement at task-irrelevant joints, including involuntary joint coupling and voluntary compensation. For joints with low control complexity, bilateral training has perturbs the abnormal joint behavior at the task-irrelevant joint, in addition to improving motor function at task-relevant joints.

Chapter 8

Appendix I: The Rotational Axis Approach for Resolving the Kinematic Redundancy of the Human Arm in Reaching Movements

In this appendix we presents the study on a biological-based redundancy resolution for arm posture prediction. Experiments performed on ten healthy subjects have shown that when reaching from one point to another, the human arm rotates around an axis going through the shoulder. The proposed redundancy resolution based on the direction of the axis can predict the arm posture with a higher accuracy comparing to a redundancy resolution that maximizes the motion efficiency. It is also shown that for reaching movements in the comfortable arm motion range, the directions of the axis are constrained by a linear model.

8.1 Redundancy Resolution: the rotational axis method

Our proposed redundancy resolution focuses on reaching movements between two points in a 3D workspace. It is based on the observation that during the reaching movement, the arm plane (i.e., the plane formed by the positions of the shoulder, the

elbow and the wrist) rotates about an axis that goes through the shoulder position. Given the direction of the axis, the position of the elbow always falls on the plane formed by the rotational axis and the wrist position.

In Fig. ??, \vec{v}_e' is the vector component of the rotational axis direction \vec{v}_e perpendicular to \vec{n} , i.e., the vector rejection of \vec{v}_e from \vec{n} . Given that \vec{v}_e' is parallel with the vector $P_e - P_c$, the swivel angle can be estimated as:

$$\phi = \arctan2(\vec{n} \cdot (\vec{v}_e' \times \vec{u}), \vec{v}_e' \cdot \vec{u}) \quad (8.1)$$

8.2 The Equilibrium Posture of the Human Arm

While it is possible that the rotational axis varies depending on the region in which the human arm performs a task, a good candidate for the rotational axis is the direction of the equilibrium vector. It is known that when the human arm rests in the equilibrium posture, the periarticular muscles are in the position of minimal muscle actuation. In the equilibrium posture, a human arm with fractures of the shoulder and of the upper arm can be rested in the position of immobilization for proper recovery. The arm postures that are derived from the equilibrium arm posture may be naturally preferred for redundancy resolution.

In Fig. 8.1a, the red arrow pointing from the center of the shoulder denotes the axis of the circumduction cone, which corresponds to the motion range of a healthy human arm. When the upper arm is aligned in the direction of the red arrow, the human arm is in the position of equilibrium of the periarticular muscles. As shown in Fig. 8.1b, the equilibrium arm posture naturally directs the upper arm so that the working hands lie in the sector of preferential accessibility and stay in the visual control [225].

Fig. 8.1b illustrates that for the equilibrium posture the range of accessible points in the task space overlaps with the stereoscopic visual range. This coincidence is likely a result of interactions between morphology (e.g., structures and arrangements of joint and muscles), actuation (e.g., the way that muscles actuate joints) and sensory feedback (e.g., visual feedback) in evolutionary development. It strongly affects the control strategies of human motor system, e.g., the way that human arm moves given its kinematic redundancy.

The neutral body posture (NBP), including the direction of the equilibrium vec-

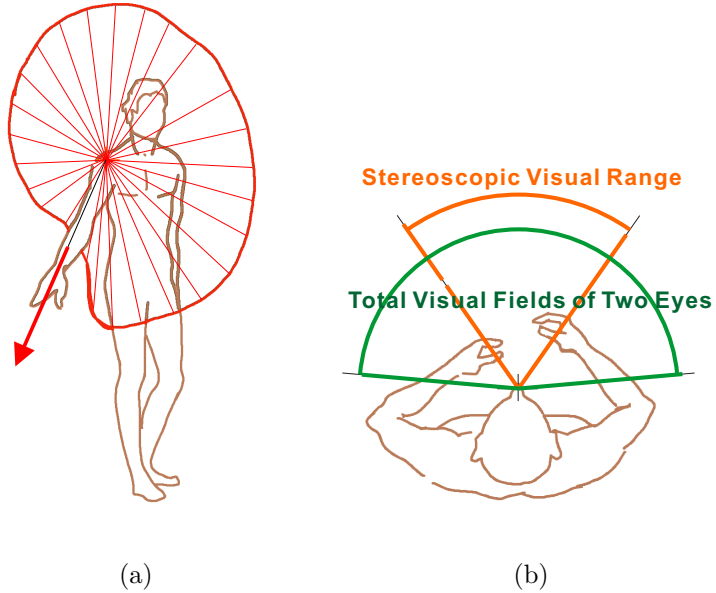


Figure 8.1: (a) Equilibrium posture directs the arm to its position of equilibrium of the periarticular muscles, and (b) brings the working hands in the range of stereoscopic visual control.

tor for the upper arm, has been experimentally investigated by NASA [222]. In the microgravity condition, the estimated shoulder flexion is about 36° and the shoulder abduction is about 50° . As shown in Fig. 8.2, the angles of flexion α and abduction β are measured from the projection of the equilibrium direction on the sagittal plane and coronal plane, respectively. Studies in Skylab collected static measurements from 12 subjects. Due to a small sample size and possible imprecision, further investigation took the general anthropometric body measurements from all six STS-57 crew members. The results showed that the NBP differed for different subjects within a wide range.

8.3 Result of Data Analysis

This section analyzes the data collected from the point-to-point reaching movements and confirms that when the human arm reach from one target to another, the plane of the arm rotates about an axis. The direction of the rotational axis varies for reaching movements between different targets, however it is constrained to a surface for the

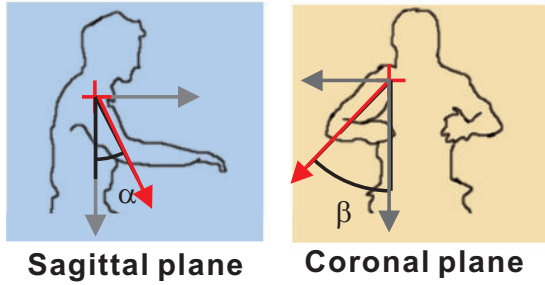


Figure 8.2: The direction of the rotational axis can be specified by the flexion angle (α) and abduction angle (β). The direction of equilibrium posture of the upper arm is a possible candidate for the direction of the rotational axis.

reaching movements within a comfortable motion range, where the subjects do not need to stretch their arms to the joint limits to reach the targets. The rotational axis will deviate from the constraining surface due to the blocking effect of the torso, when the reaching movements are close to the boundary of the arm motion range.

Fig. 8.3 shows the statistics of the prediction error for all the valid trials (2680 out of 2800) conducted by ten subjects. The swivel angle prediction based on the rotational axis method (RAM) and by the motion efficiency method (MEM) proposed by [18] are calculated for comparison. The mean and standard deviations of the prediction error are denoted by μ_{RAM} , μ_{MEM} , and σ_{RAM} , σ_{MEM} respectively.

Based on RAM, 79.59% of the trials have both $\mu_{RAM} \leq 5^\circ$ and $\sigma_{RAM} \leq 5^\circ$. 3.92% trials have either $\mu_{RAM} \geq 10^\circ$ or $\sigma_{RAM} \geq 10^\circ$. Therefore, with respect to the mean value and the variance, RAM predictions outperform MEM predictions (see Fig. 8.3). The direction of the axis can be estimated for each trial based on the measured shoulder, elbow and wrist position.

Figures 8.4 and 8.5 shows the estimated direction of the rotational axis in each of the movements. The vector of the rotational axis always points from the shoulder position and its direction is measured by the abduction and flexion angles. The yellow dots represent the estimated directions of the rotational axis for each trial. Some of the yellow dots are highlighted by either green circles or magenta circles, corresponding to the movements between target 1, 2, 3, 5 and 7, and the movements between target 4, 6 and 8, respectively. As shown in Fig. 8.6 for the right arm, target 1, 2, 3, 5, 7 are within the comfortable arm motion range while target 4, 6, and 8 are close to the motion range boundary.

A linear data fit is performed to summarize the relation between the abduction and

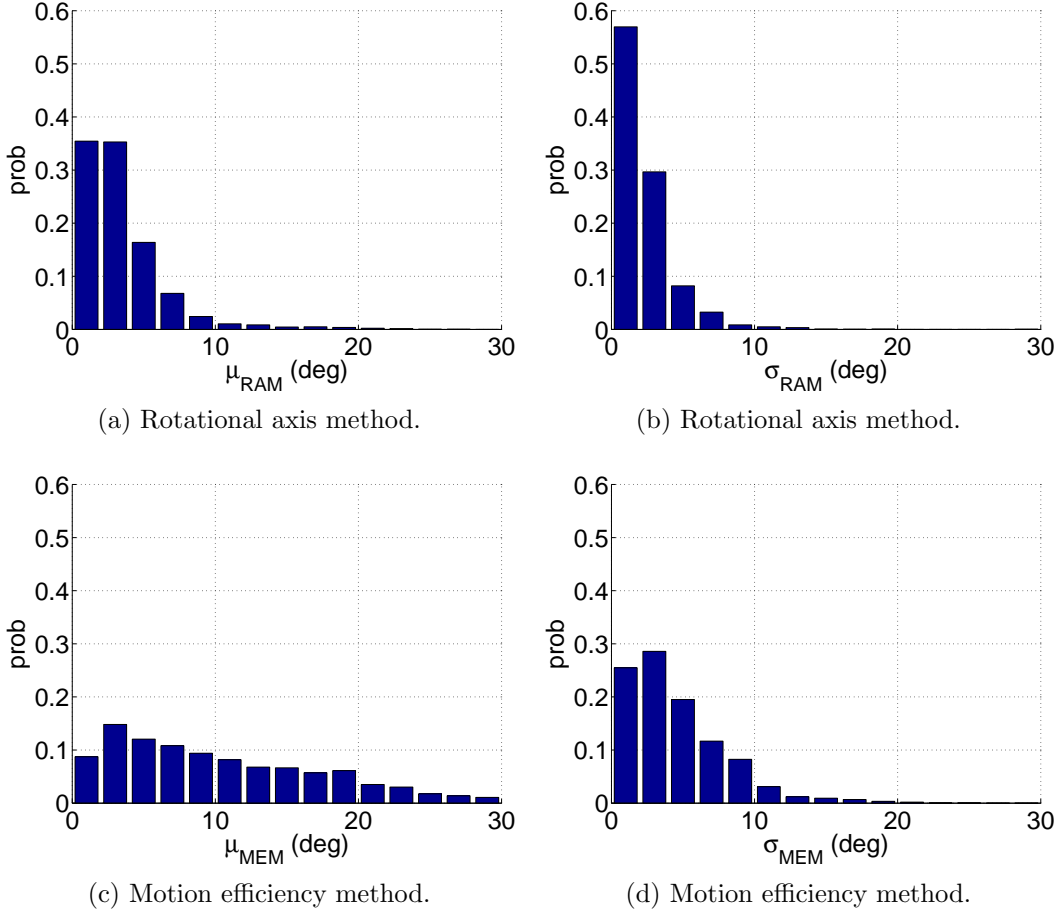


Figure 8.3: Performance comparison of two swivel angle estimation methods by the distributions of the mean and standard deviation of estimation error.

flexion of a rotational axis (see Fig. 8.4). The regression method iteratively re-weights least squares with the bi-square weighting function so that the effect of outliers can be reduced [226]. The line describes a surface constraining the rotational axis when the right arm moves within the comfortable motion range. For the movements close to the boundary of arm motion range (i.e., between target 4, 6 and 8), the estimated directions of the rotational axis strongly deviate from the line. The blue dot in Fig. 8.4 represents the direction of the equilibrium vector measured in microgravity condition by NASA [222]. It is close to our linear relation and therefore is one possible directions of the rotational axis when the arm moves between the targets in the comfortable motion range.

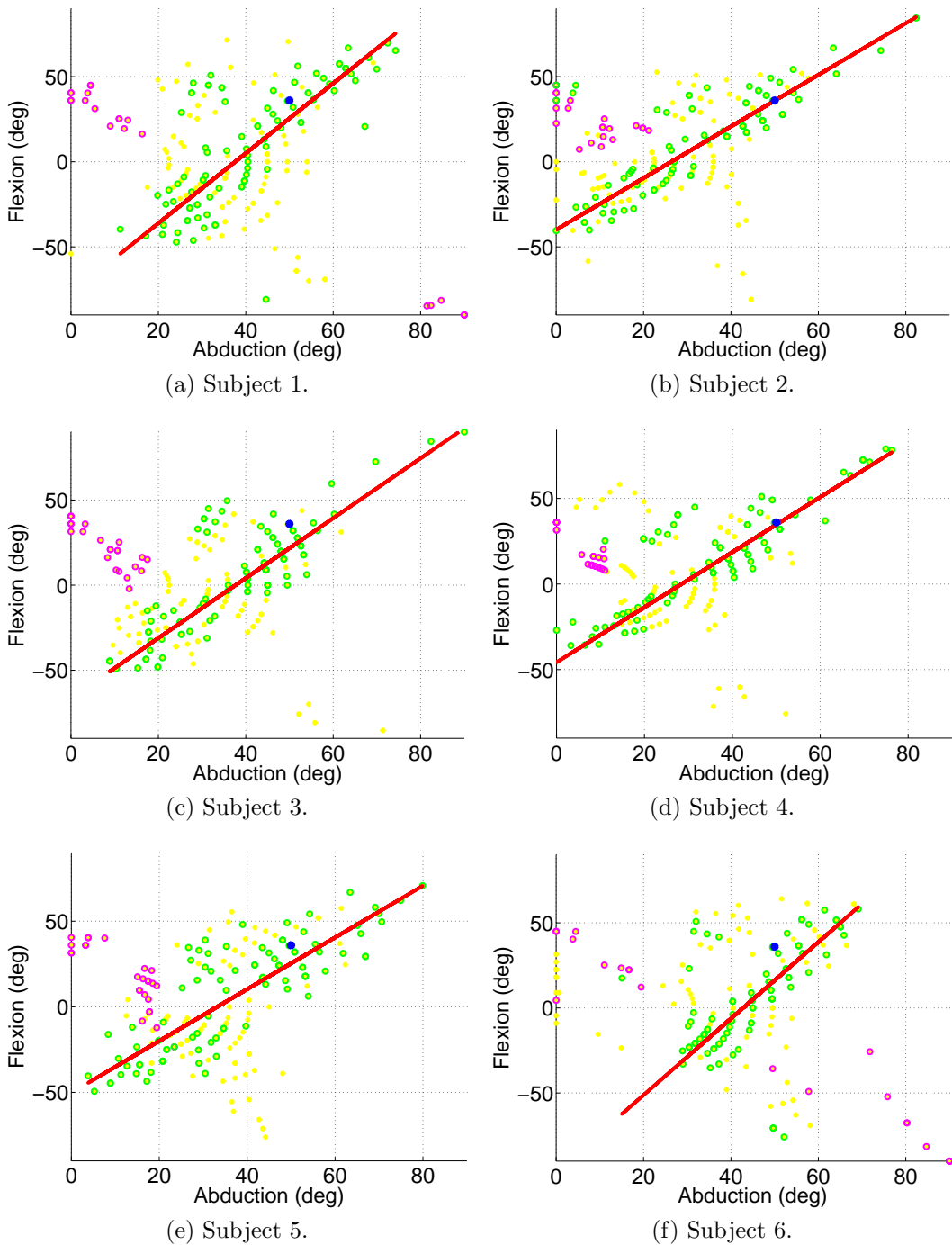


Figure 8.4: The directions of the rotational axis are estimated for each valid trial. A linear regression model describes the surface that constrains the axis direction when the right arm moves in its comfortable motion range.

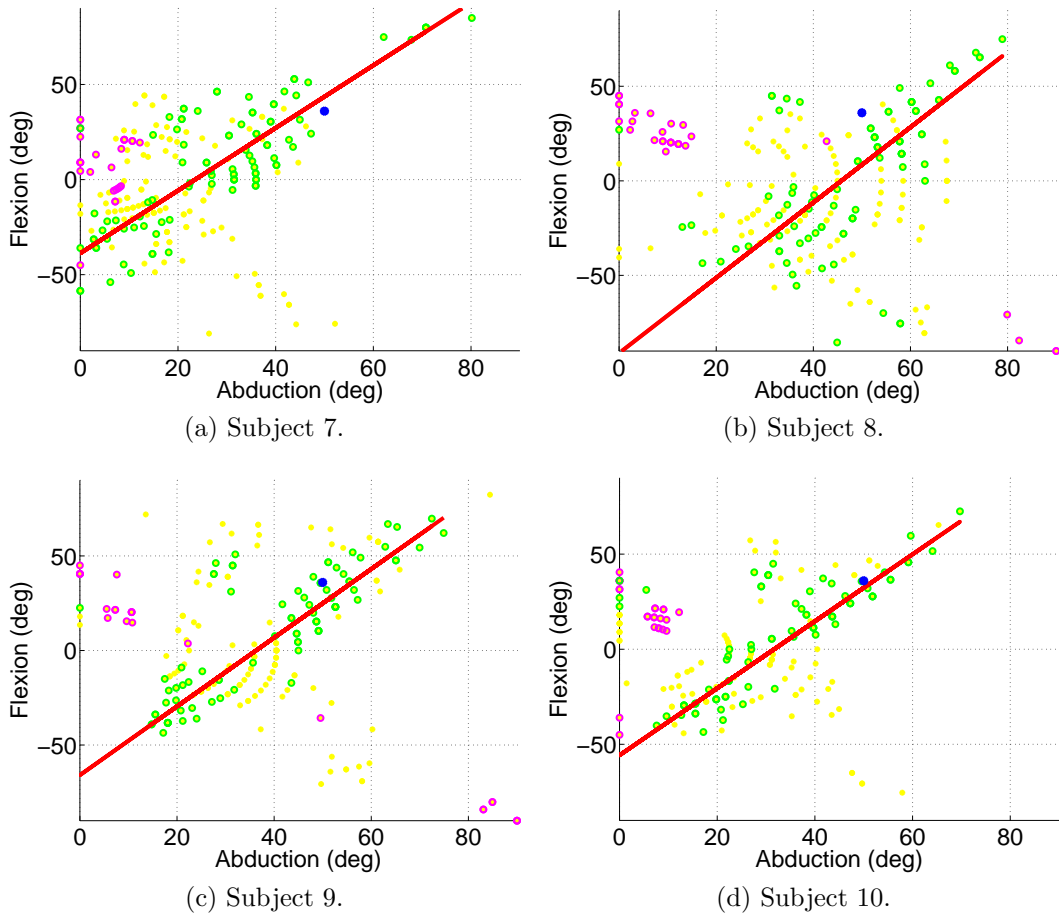


Figure 8.5: Continue Fig. 8.4.

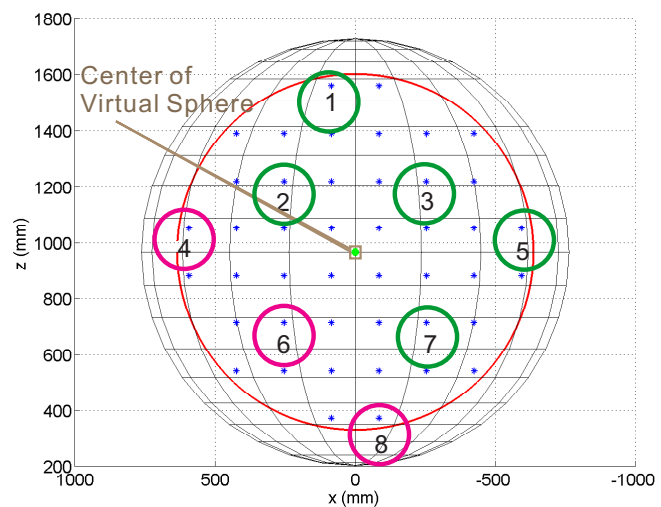


Figure 8.6: Targets in the reaching movement experiment. For the right arm, target 1, 2, 3, 5, 7 (in green circles) are within the comfortable arm motion range while target 4, 6, and 8 (in magenta circles) are close to the motion range boundary

Chapter 9

Appendix II: the Maximum Entropy Principle and the Exponential Method for Criterion Synthesization

The entropy $H(k)$ of the discrete probability distribution $p_i(k)$ ($i = 1, 2, \dots, N$) at the time step k is:

$$H(k) = \sum_{i=1}^N p_i(k) \ln p_i(k) \quad (9.1)$$

The distribution satisfies the constraint

$$\sum_{i=1}^N p_i(k) = 1 \quad (9.2)$$

Furthermore, based on the observed quantities, the variance of the distribution should be equal to the experimentally observed variance, that is:

$$\sum_{i=1}^N \varepsilon_i^2(k) p_i(k) = \hat{\sigma}^2 \quad (9.3)$$

According to the maximum entropy principle [223], the least informative prior

distribution is defined by the set of values $p_i(k)$ that maximize the entropy (Eq. (9.1)) under the above two constraints. This maximization problem can be solved using Lagrange multipliers λ_1 and λ_2 as an unconstrained maximization problem of the cost function J :

$$\begin{aligned} J &= \sum_{i=1}^N p_i(k) \ln p_i(k) - \lambda_1 \left(\sum_{i=1}^N \varepsilon_i^2(k) p_i(k) - \hat{\sigma}^2 \right) \\ &\quad - \lambda_2 \left(\sum_{i=1}^N p_i(k) - 1 \right) \end{aligned} \quad (9.4)$$

The maximum is defined by $\partial J/p_i(k) = 0$ for $i = 1, \dots, N$ and $\partial J/\lambda_j(k) = 0$ for $j = 1, 2$, which yields:

$$\ln p_i(k) + 1 - \lambda_1 \varepsilon_i^2(k) - \lambda_2 = 0 \quad (9.5)$$

and the resulted probability $p_i(k)$ is computed as:

$$p_i(k) = \exp(-1 + \lambda_1 \varepsilon_i^2(k) + \lambda_2) = c_0 \cdot \exp(\lambda_1 \varepsilon_i^2(k)) \quad (9.6)$$

According to the constraint on the sum of the probability, the probability $p_i(k)$ needs to be normalized as Eq. (9.7) such that the constant c_0 can be canceled.

$$p_i'(k) = \frac{\exp(\lambda_1 \varepsilon_i^2(k))}{\sum_{i=1}^N \exp(\lambda_1 \varepsilon_i^2(k))} \quad (9.7)$$

Given the prediction error based on the criterion i ($i = 1, 2, \dots, N$), λ_1 is a common property of $p(\varepsilon_i^2|i)$, which is the probability density function of ε_i^2 . These probability density functions satisfy

$$\int_0^\infty p(\varepsilon_i^2|i) d(\varepsilon_i^2) = 1 \quad (9.8)$$

such that: (1) $p(\varepsilon_i^2|i)$ is the exponential distribution and (2) it is independent of the criterion and therefore is the same for all i . Since $\lambda_1 = -1/\sigma_1^2$, we can set $\sigma_1^2 = \hat{\sigma}^2$ to obtain:

$$p(\varepsilon_i^2 | i) = \frac{1}{\hat{\sigma}^2} \exp \left(-\frac{\varepsilon_i^2}{\hat{\sigma}^2} \right) \quad (9.9)$$

Chapter 10

Appendix III: Manipulability Analysis of Multi-link Manipulators

This chapter presents preliminary work on the kinematical redundancy resolution of human arm movements. By simplification, biological arms are modeled as three-link redundant manipulators with various link-lengthes and joint limits. The configurations of the three-link manipulators are classified into four families, which shares the same forward kinematics and process different inverse kinematics. The redundancy resolution for the three-link manipulator in planar task are conducted based on pseudo-inverse method, which implicitly minimize the norm of joint velocity vector. Preparing for the redundancy resolution based on optimization of manipulability, this preliminary work studies the Jacobian matrix for two-link, three-link and four-link manipulator. Manipulability indices such as condition number, isotropy and determinant of Jacobian are derived analytically. Simulations are conducted to find the joint space profile for best manipulability performance, measured by condition number and determinant of Jacobian.

10.1 Three-link Manipulator for Planar Task

A three-link manipulator for planar task can serve as a simplified model in the primitive study of the kinematics of a biological arm.

Fig. 10.1a shows a three-link manipulator on x-y plane, with parameters as: (1)

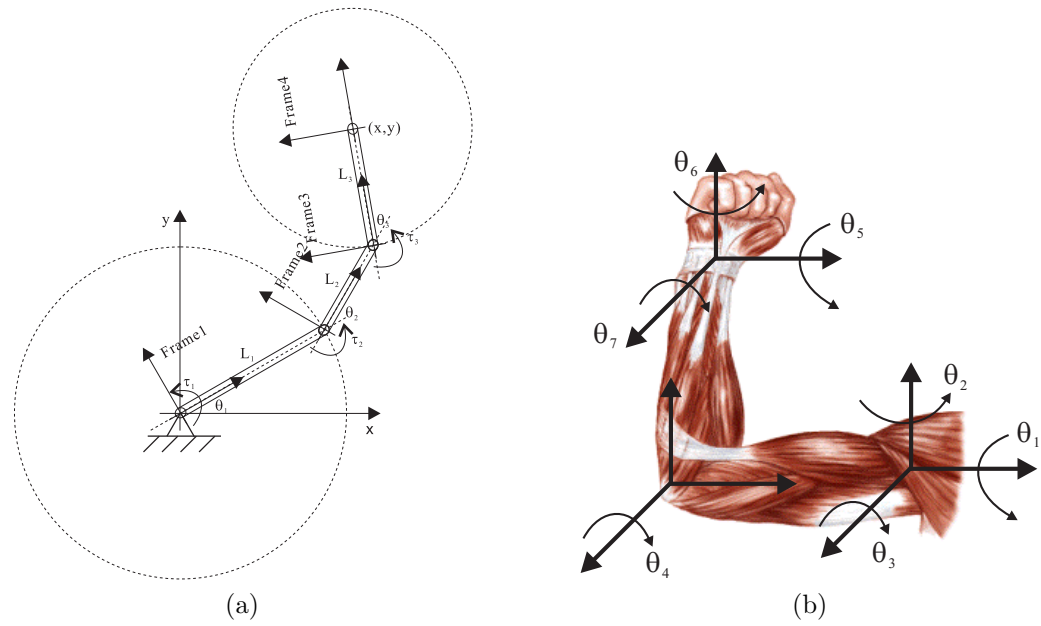


Figure 10.1: Modeling by simplification: from human arm to redundant manipulator. Left - Human arm with 7 or more DOFs, for spatial task; Right - Kinematical redundant manipulator with 3 DOFs for planar task.

L_i is length of the link i , (2) θ_i is the angular displacement of the $Frame_i$ relative to the $Frame_{i-1}$. (x, y) is The position of the end-effector of the three-link mechanism. The position of the origin is $(0, 0)$.

10.1.1 Families of Configurations

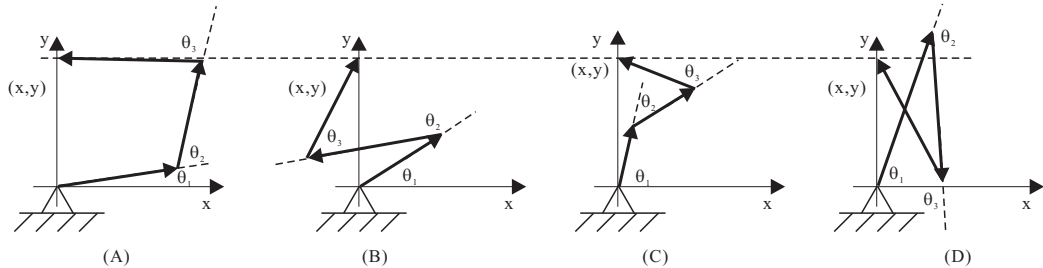


Figure 10.2: Families of configurations.

The three-link manipulator in Fig. 10.1a has a planar workspace and therefore it has one degree of redundancy. Its end effector can reach any point WITHIN the workspace with multiple orientations. In other words, more than one manipulator

configurations, denoted by the vector $q = [\theta_1, \theta_2, \theta_3]^T$, map to the same (x, y) location in task space. By the range of joint angles, the manipulator configurations can be grouped in the families illustrated in Fig. 10.2.

Given that $0 \leq \theta_1 \leq \frac{\pi}{2}$, θ_2 and θ_3 can take either positive values $[0, \pi]$ or negative values $[-\pi, 0]$, which leads to four possible families of configurations shown in Fig. 10.2. By symmetry, these four families also exist for $-\pi \leq \theta_1 \leq 0$. Table lists the details of each family of configurations. Note that manipulator configurations in Family 4 is not used in practice.

Families	Range of joint angles, $\theta_1 \in [0, \frac{\pi}{2}]$, $\theta_2 \in [-\pi, \pi]$, $\theta_3 \in [-\pi, \pi]$	Available in practice
Family 1 (Fig. 10.2.A)	$\theta_1 > 0, \theta_2 > 0, \theta_3 > 0$	yes
Family 2 (Fig. 10.2.B)	$\theta_1 > 0, \theta_2 > 0, \theta_3 < 0$	yes
Family 3 (Fig. 10.2.C)	$\theta_1 > 0, \theta_2 < 0, \theta_3 > 0$	yes
Family 4 (Fig. 10.2.D)	$\theta_1 > 0, \theta_2 < 0, \theta_3 < 0$	no

Table 10.1: Joint angle ranges for each family of configurations

Section 10.1.2 will derive the direct kinematics for all the four families of configurations with two approaches, while Section 10.1.3 will resolve the inverse kinematics for each of the four families of configurations.

10.1.2 Direct Kinematics

This section will derive the direct kinematics for all the families of configurations with two methods. The transformation that relates the frame of the end-effector (i.e. $Frame_4$) and the base frame (i.e. $Frame_0$) in the three-link manipulator is as:

$${}^4T = {}_0^1T {}_1^2T {}_2^3T {}_3^4T \quad (10.1)$$

$${}_0^1T = \begin{pmatrix} \cos\theta_1 & -\sin\theta_1 & 0 \\ \sin\theta_1 & \cos\theta_1 & 0 \\ 0 & 0 & 1 \end{pmatrix} \quad (10.2)$$

$${}_1^2T = \begin{pmatrix} \cos\theta_2 & -\sin\theta_2 & L_1 \\ \sin\theta_2 & \cos\theta_2 & 0 \\ 0 & 0 & 1 \end{pmatrix} \quad (10.3)$$

$${}^3_2 T = \begin{pmatrix} \cos\theta_3 & -\sin\theta_3 & L_2 \\ \sin\theta_3 & \cos\theta_3 & 0 \\ 0 & 0 & 1 \end{pmatrix} \quad (10.4)$$

$${}^4_3 T = \begin{pmatrix} 1 & 0 & L_3 \\ 0 & 1 & 0 \\ 0 & 0 & 1 \end{pmatrix} \quad (10.5)$$

$${}^4_0 T = {}^4_0 T(\theta_1, \theta_2, \theta_3) = \begin{pmatrix} c_{123} & -s_{123} & L_1 c_1 + L_2 c_{12} + L_3 c_{123} \\ s_{123} & c_{123} & L_1 s_1 + L_2 s_{12} + L_3 s_{123} \\ 0 & 0 & 1 \end{pmatrix} \quad (10.6)$$

which uses the shorthand notation for trigonometric function, e.g. $c_{12} = \cos(\theta_1 + \theta_2)$.

$$\begin{pmatrix} x \\ y \\ 1 \end{pmatrix} = {}^4_0 T \begin{pmatrix} 0 \\ 0 \\ 1 \end{pmatrix} \quad (10.7)$$

Hence, the direct kinematics of the three-link manipulator can be expressed as:

$$x = L_1 \cos\theta_1 + L_2 \cos(\theta_1 + \theta_2) + L_3 \cos(\theta_1 + \theta_2 + \theta_3) \quad (10.8)$$

$$y = L_1 \sin\theta_1 + L_2 \sin(\theta_1 + \theta_2) + L_3 \sin(\theta_1 + \theta_2 + \theta_3) \quad (10.9)$$

Another way of deriving the direct kinematics of the three-link manipulator is to use vector addition. Define the vector corresponding to link i to be \mathbf{r}_i as Fig. 10.3, we have:

- For link 1:

$$\mathbf{r}_1 = L_1 [\cos\theta_1, \sin\theta_1] \quad (10.10)$$

- For link 2:

$$\mathbf{r}_2 = L_2 [\cos(\theta_1 + \theta_2), \sin(\theta_1 + \theta_2)] \quad (10.11)$$

- For link 3:

$$\mathbf{r}_3 = L_3 [\cos(\theta_1 + \theta_2 + \theta_3), \sin(\theta_1 + \theta_2 + \theta_3)] \quad (10.12)$$

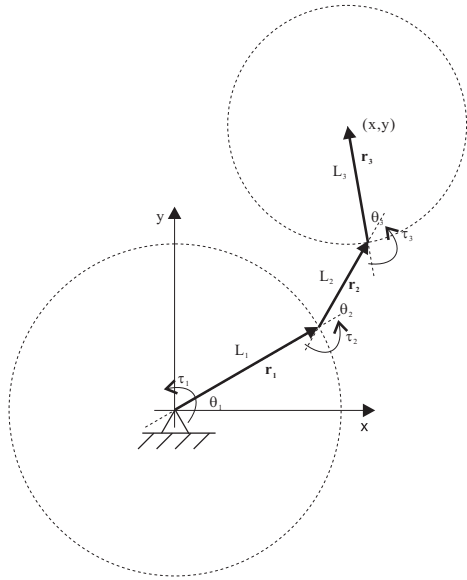


Figure 10.3: Three-link mechanism.

Thus, the position of the end-effector (x, y) is derived as:

$$x = L_1 \cos \theta_1 + L_2 \cos(\theta_1 + \theta_2) + L_3 \cos(\theta_1 + \theta_2 + \theta_3) \quad (10.13)$$

$$y = L_1 \sin \theta_1 + L_2 \sin(\theta_1 + \theta_2) + L_3 \sin(\theta_1 + \theta_2 + \theta_3) \quad (10.14)$$

10.1.3 Inverse Kinematics for different families of configurations

This section will resolve the inverse kinematics for different families of configurations via geometric approach. For simplicity, assume that $L_1 = L_2 = L_3 = l/3$

Availability of solutions

Given a point on the plane, the inverse kinematics of the given three-link manipulator may have no solution, unique solution and infinite number of solutions. As shown in Fig. 10.4, the workspace of the three-link manipulator forms a circle, with the radius R as sum of all the link length, i.e. $R = L_1 + L_2 + L_3$. For any point within the workspace, the inverse kinematics of the manipulator has infinite numbers of solutions. When the manipulator is fully extended to reach the boundary of the workspace, the

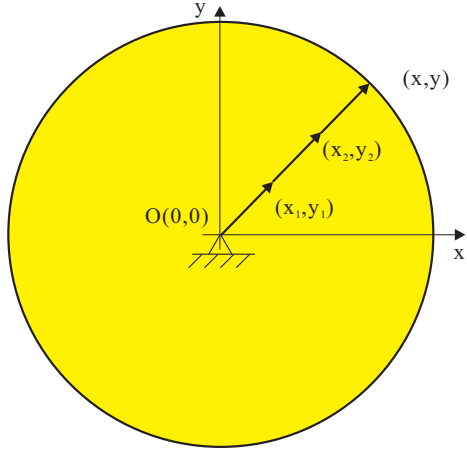


Figure 10.4: Availability of redundancy resolution for a three-link manipulator.

inverse kinematics has unique solution at singularity configuration. Points out of the workspace are not reachable for the manipulator. Therefore, no solutions available for the inverse kinematics of the given manipulator.

The availability of the solutions can be tested by comparing distance between target point and the origin of the manipulator DIS with the total link length R . Given the point (x, y) in task space coordinates, the $DIS - R$ can be positive, zero or negative, which corresponds to different availability of inverse kinematic solutions Eq. (10.15).

$$DIS - R = \sqrt{x^2 + y^2} - (L_1 + L_2 + L_3) \begin{cases} > 0 & \text{no solutions} \\ = 0 & \text{unique solutions} \\ < 0 & \text{infinite number of solutions} \end{cases} \quad (10.15)$$

For that case of infinite number of solutions, the inverse kinematics of the redundant manipulator can be represented choosing one of the joint angle as free variable. Note that given the range of θ_2 and θ_3 , the solution of the inverse kinematics, if there is any, can be uniquely represented using the free variable θ_1 . The representation of solutions exists only if the desired end-effector position (x, y) falls into the circle with the origin at the end of link 1 (x_1, y_1) and the radius of $r = L_2 + L_3$ (Fig. 10.5). Therefore, the availability of representation of solutions can be found out by comparing r with the distance between target position and the end of link 1 (as Eq. (10.16)).

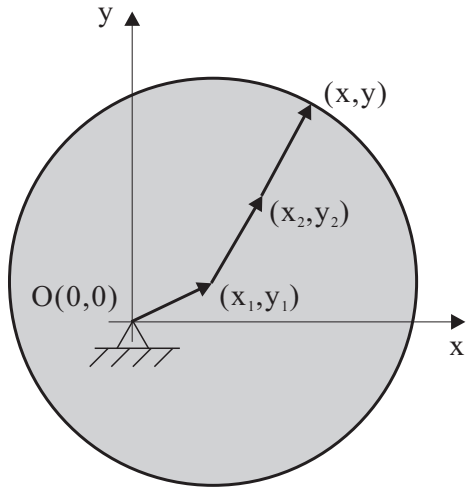


Figure 10.5: Availability of redundancy resolution for a three-link manipulator, choosing θ_1 as free variable.

$$dis - r = \sqrt{(x - x_1)^2 + (y - y_1)^2} - (L_2 + L_3) \begin{cases} > 0 & \text{no solutions} \\ = 0 & \text{unique representation at singularity} \\ < 0 & \text{unique representation} \end{cases} \quad (10.16)$$

Section 10.1.3 to Section 10.1.3 will resolve the inverse kinematics analytically, choosing joint angle θ_1 as the free variable. The resolution proceeds after testing the availability of the unique representation of solutions with Eq. (10.16).

Family 1

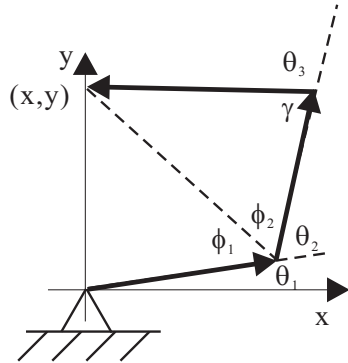


Figure 10.6: Family 1: $\theta_1 > 0, \theta_2 > 0, \theta_3 > 0$.

Assume that unique representation of solutions of inverse kinematics exist and the

configuration fall into Family 1. Choosing θ_1 as free variable, the position of the end of link 1 can be represented as:

$$x_1 = L_1 \cos \theta_1 \quad (10.17)$$

$$y_1 = L_1 \sin \theta_1 \quad (10.18)$$

Given $0 \leq \theta_3 \leq 180^\circ$, θ_3 can be resolved as:

$$\cos \gamma = \frac{L_2^2 + L_3^2 - (x - x_1)^2 - (y - y_1)^2}{2L_2 L_3} \quad (10.19)$$

$$\sin \gamma = \sqrt{1 - \cos^2 \gamma} \quad (10.20)$$

$$\gamma = \text{Atan2}(\sin \gamma, \cos \gamma) \quad (10.21)$$

$$\theta_3 = 180^\circ - \gamma \quad (10.22)$$

Given $0 \leq \theta_2 \leq 180^\circ$, configurations in Family 1 have $0 \leq \phi_1 \leq 180^\circ$ and $0 \leq \phi_2 \leq 180^\circ$. Thus, ϕ_1 and ϕ_2 can be resolved as: in Fig. 10.6

$$\cos \phi_1 = \frac{L_1^2 + (x - x_1)^2 + (y - y_1)^2 - x^2 - y^2}{2L_1[(x - x_1)^2 + (y - y_1)^2]} \quad (10.23)$$

$$\sin \phi_1 = \sqrt{1 - \cos^2 \phi_1} \quad (10.24)$$

$$\phi_1 = \text{Atan2}(\sin \phi_1, \cos \phi_1) \quad (10.25)$$

$$\cos \phi_2 = \frac{(x - x_1)^2 + (y - y_1)^2 + L_2^2 - L_3^2}{2L_2[(x - x_1)^2 + (y - y_1)^2]} \quad (10.26)$$

$$\sin \phi_2 = \sqrt{1 - \cos^2 \phi_2} \quad (10.27)$$

$$\phi_2 = \text{Atan2}(\sin \phi_2, \cos \phi_2) \quad (10.28)$$

which leads to:

$$\theta_2 = 180^\circ - (\phi_1 + \phi_2) \quad (10.29)$$

Family 2

For Family 2 as Fig. 10.7, after determining (x_1, y_1) by Equations (10.17) to (10.18), γ can be resolved as Equations (10.19) to (10.21), which results in θ_3 as Eq. (10.30). Given that $0 \leq \phi_1 \leq 180^\circ$ and $0 \leq \phi_2 \leq 180^\circ$, ϕ_1 and ϕ_2 can be resolved by Equations (10.23) to (10.28). Note that $-180^\circ \leq \theta_2 \leq 0$, which leads to θ_2 as:

$$\theta_3 = -(180^\circ - \gamma) \quad (10.30)$$

$$\theta_2 = 180^\circ - (\phi_1 - \phi_2) \quad (10.31)$$

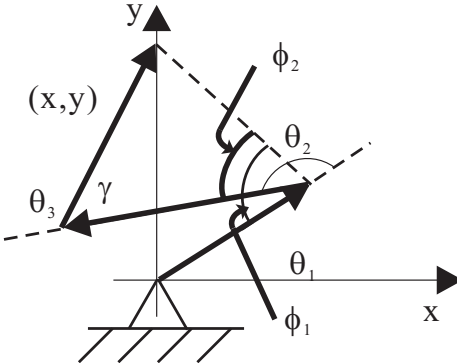


Figure 10.7: Family 1: $\theta_1 > 0, \theta_2 < 0, \theta_3 > 0$.

Family 3

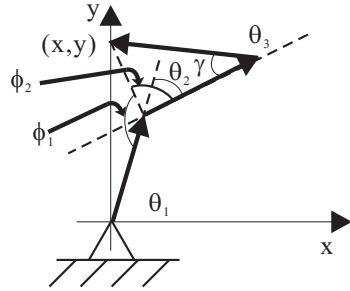


Figure 10.8: Family 1: $\theta_1 > 0, \theta_2 > 0, \theta_3 < 0$.

For Family 3 as Fig. 10.8, after determining (x_1, y_1) by Equations (10.17) to (10.18), θ_3 can be resolved as Equations (10.19) to (10.22). Resolve ϕ_1 and ϕ_2 by Equations (10.23) to (10.28). θ_2 can be found as Eq. (10.32).

$$\theta_2 = -[(\phi_1 + \phi_2) - 180^\circ] = 180^\circ - (\phi_1 + \phi_2) \quad (10.32)$$

Note that Family 3 are using the same computational algorithm as Family 1, for different angle ranges.

10.2 Redundancy Resolution by Pseudo-inverse

10.2.1 Jacobian Matrix

Redundancy resolution at velocity level intends to find the relation between joint space and task space constrained by

$$\dot{x} = \mathbf{J}(\theta)\dot{\theta} \quad (10.33)$$

Jacobian matrix, also called task Jacobian matrix or analytical Jacobian, represents the linear mapping of the joint space velocities into the task space velocities [227]. Given the joint space velocities as $\dot{\mathbf{q}} = (\dot{\theta}_1, \dot{\theta}_2, \dot{\theta}_3)$ and the space velocities as $\dot{\mathbf{x}} = (\dot{x}, \dot{y})^T$, this mapping can be represented as:

$$\dot{\mathbf{x}} = \begin{pmatrix} \dot{x} \\ \dot{y} \end{pmatrix} = \mathbf{J}\dot{\mathbf{q}} = \mathbf{J} \begin{pmatrix} \dot{\theta}_1 \\ \dot{\theta}_2 \\ \dot{\theta}_3 \end{pmatrix} \quad (10.34)$$

Given the dimension of $\dot{\mathbf{x}}$ as m and the dimension of $\dot{\mathbf{q}}$ as n , the Jacobian matrix is a $m \times n$ matrix. Thus, the Jacobian matrix here is as eqeq:Jacobian, with $m = 2$ and $n = 3$.

$$\mathbf{J}_{m \times n} = \mathbf{J}_{2 \times 3} = \begin{bmatrix} -L_1 s_1 - L_2 s_{12} - L_3 s_{123} & -L_2 s_{12} - L_3 s_{123} & -L_3 s_{123} \\ L_1 s_1 + L_2 c_{12} + L_3 c_{123} & L_2 c_{12} + L_3 c_{123} & L_3 c_{123} \end{bmatrix} \quad (10.35)$$

10.2.2 Singular Value Decomposition of the Jacobian Matrix

According to the singular value decomposition (SVD) theory, for any $m \times n$ matrix \mathbf{J} of rank r , there exists orthogonal matrices $\mathbf{U}_{m \times m}$ and $\mathbf{V}_{n \times n}$ such that:

$$\begin{aligned} \mathbf{J}_{m \times n} &= \mathbf{U}_{m \times m} \Sigma_{m \times n} \mathbf{V}^T_{n \times n} \\ &= \begin{bmatrix} \mathbf{U}_1_{m \times r} & \mathbf{U}_2_{m \times (m-r)} \end{bmatrix} \begin{bmatrix} \Sigma_1_{r \times r} & \mathbf{0}_{r \times (n-r)} \\ \mathbf{0}_{(m-r) \times r} & \mathbf{0}_{(m-r) \times (n-r)} \end{bmatrix} \begin{bmatrix} \mathbf{V}^T_1_{r \times n} \\ \mathbf{V}^T_2_{(n-r) \times n} \end{bmatrix} \end{aligned} \quad (10.36)$$

In Eq. (10.36) [227],

- The row vectors in $\mathbf{V}^T_1_{r \times n}$, i.e. $v_1^T, v_2^T, \dots, v_r^T$ are the orthogonal basis for the subspace of $\dot{\mathbf{q}}$ that generate non-zero task space velocities.
- The row vectors in $\mathbf{V}^T_2_{(n-r) \times n}$, i.e. $v_{r+1}^T, v_{r+2}^T, \dots, v_n^T$ are the orthogonal basis for the subspace of $\dot{\mathbf{q}}$ that gives task space $\dot{\mathbf{X}} = 0$. It corresponds the null space of \mathbf{J} , denoted by $\mathbb{N}(\mathbf{J})$.
- The column vectors in $\mathbf{U}^T_1_{m \times r}$, i.e. u_1, u_2, \dots, u_r are the orthogonal basis for the subspace of achievable task space velocity $\dot{\mathbf{X}}$. It corresponds the range of \mathbf{J} , denoted by $\mathbb{R}(\mathbf{J})$.

- The column vectors in $\mathbf{U}_{2_{m \times (m-r)}}$, i.e. $u_{r+1}, u_{r+2}, \dots, u_m$ are the orthogonal basis for the subspace of task space velocities $\dot{\mathbf{X}}$ that can not be generated by the robots. It corresponds to the complement of the range space \mathbf{J} , denoted by $\mathfrak{R}(\mathbf{J})^\perp$.
- The diagonal elements of $\Sigma_{1_{r \times r}}$, i.e. $\sigma_1, \sigma_2, \dots, \sigma_r$ are the velocity transmission ratio from the joint space to the task space.

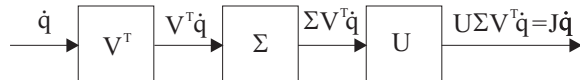


Figure 10.9: Velocity Mapping from Joint Space to Task Space, by Jacobian Matrix.

Indeed, the velocity mapping from joint space to task space by Jacobian matrix can be represented as Fig. 10.9. Given that (Eq. (10.37))

$$\mathbf{J}_{m \times n} = \mathbf{U} \Sigma \mathbf{V}^T = \sum_{i=1}^r \sigma_i u_i v_i^T \quad (10.37)$$

The mapping procedure can be interpreted as following steps:

- Compute coefficients of joint space velocity $\dot{\mathbf{q}}$ along the directions of $v_1^T, v_2^T, \dots, v_r^T$.
- Scale the computed coefficients of joint space velocity by σ_i .
- Reconstitute the task space velocity along the directions of u_1, u_2, \dots, u_r

10.2.3 Null Space of Jacobian Matrix

The null space of \mathbf{J} can be defined as the columns of $(\mathbf{I} - \mathbf{J}^\dagger \mathbf{J})$.

For \mathbf{J} as Eq. (10.35), the transpose of \mathbf{J} , denoted by \mathbf{J}^T is:

$$\mathbf{J}_{n \times m}^T = \mathbf{J}_{3 \times 2}^T = \begin{bmatrix} -L_1 s_1 - L_2 s_{12} - L_3 s_{123} & L_1 s_1 + L_2 c_{12} + L_3 c_{123} \\ -L_2 s_{12} - L_3 s_{123} & L_2 c_{12} + L_3 c_{123} \\ -L_3 s_{123} & L_3 c_{123} \end{bmatrix} \quad (10.38)$$

Since \mathbf{J} is fat (i.e. $m < n$), use $\mathbf{J}\mathbf{J}^T$ to find eigen-values λ_i and eigen-vectors of v_i :

$$\mathbf{J}\mathbf{J}^T = \begin{bmatrix} J_{11} & J_{12} \\ J_{21} & J_{22} \end{bmatrix} \quad (10.39)$$

where:

$$\begin{aligned}
J_{11} &= (-L_1 s_1 - L_2 s_{12} - L_3 \times s_{123})^2 \\
&+ (-L_2 s_{12} - L_3 s_{123})^2 \\
&+ (L_3 s_{123})^2 \\
&= L_1^2 s_1^2 + L_2^2 s_{12}^2 + L_3^2 s_{123}^2 + 2L_1 L_2 s_1 s_{12} + 2L_2 L_3 s_{12} s_{123} + 2L_1 L_3 s_1 s_{123} \\
&+ L_2^2 s_{12}^2 + L_3^2 s_{123}^2 + 2L_2 L_3 s_{12} s_{123} \\
&+ L_3^2 s_{123}^2
\end{aligned} \tag{10.40}$$

$$\begin{aligned}
J_{12} = J_{21} &= (-L_1 s_1 - L_2 s_{12} - L_3 s_{123})(L_1 c_1 + L_2 c_{12} + L_3 c_{123}) \\
&+ (-L_2 s_{12} - L_3 s_{123})(L_2 c_{12} + L_3 c_{123}) \\
&- L_3^2 s_{123} c_{123} \\
&= -L_1^2 s_1 c_1 - L_2^2 s_{12} c_{12} - L_3^2 s_{123} c_{123} \\
&- (L_1 L_2 s_1 c_{12} + L_2 L_1 s_{12} c_1) \\
&- (L_1 L_3 s_1 c_{123} + L_3 L_1 s_{123} c_1) - (L_2 L_3 s_{12} c_{123} + L_3 L_2 s_{123} c_{12}) \\
&- L_2^2 s_{12} c_{12} - L_3^2 s_{123} c_{123} - (L_2 L_3 s_{12} c_{123} + L_3 L_2 s_{123} c_{12}) \\
&- L_3^2 s_{123} c_{123}
\end{aligned} \tag{10.41}$$

$$\begin{aligned}
J_{22} &= (L_1 c_1 + L_2 c_{12} + L_3 c_{123})^2 \\
&+ (L_2 c_{12} + L_3 c_{123})^2 \\
&+ L_3^2 c_{123}^2 \\
&= L_1^2 c_1^2 + L_2^2 c_{12}^2 + L_3^2 c_{123}^2 + 2L_1 L_2 c_1 c_{12} + 2L_2 L_3 c_{12} c_{123} + 2L_1 L_3 c_1 c_{123} \\
&+ L_2^2 c_{12}^2 + L_3^2 c_{123}^2 + 2L_2 L_3 c_{12} c_{123} \\
&+ L_3^2 c_{123}^2
\end{aligned} \tag{10.42}$$

(10.43)

For simplicity, let $L_1 = L_2 = L_3 = 1/3$, then:

$$\begin{aligned}
J_{11} &= \frac{1}{9}[s_1^2 + s_{12}^2 + s_{123}^2 + 2s_1 s_{12} + 2s_{12} s_{123} + 2s_1 s_{123} \\
&+ s_{12}^2 + s_{123}^2 + 2s_{12} s_{123} \\
&+ s_{123}^2]
\end{aligned} \tag{10.44}$$

$$\begin{aligned}
J_{12} = J_{21} &= -\frac{1}{9}[s_1 c_1 + s_{12} c_{12} + s_{123} c_{123} \\
&+ (s_1 c_{12} + s_{12} c_1) + (s_1 c_{123} + s_{123} c_1) + (s_{12} c_{123} + s_{123} c_{12}) \\
&+ s_{12} c_{12} + s_{123} c_{123} + (s_{12} c_{123} + s_{123} c_{12}) \\
&- s_{123} c_{123}]
\end{aligned} \tag{10.45}$$

$$\begin{aligned} J_{22} &= \frac{1}{9}[c_1^2 + c_{12}^2 + c_{123}^2 + 2c_1c_{12} + 2c_{12}c_{123} + 2c_1c_{123} \\ &+ c_{12}^2 + c_{123}^2 + 2c_{12}c_{123} \\ &+ c_{123}^2] \end{aligned} \quad (10.46)$$

(10.47)

Thus, $(\mathbf{J}\mathbf{J}^T)^{-1}$ is:

$$(\mathbf{J}\mathbf{J}^T)^{-1} = \frac{1}{J_{11}J_{22} - J_{12}J_{21}} \begin{bmatrix} J_{22} & -J_{21} \\ -J_{12} & J_{11} \end{bmatrix} \quad (10.48)$$

where:

$$\begin{aligned} &J_{11}J_{22} - J_{12}J_{21} \\ &= 2s_{123}^2c_1c_{12} + 2s_{12}s_{123}c_{12}^2 + 2s_1s_{12}c_{123}^2 + 2s_1^2c_{12}c_{123} \\ &- 2s_1s_{12}c_1c_{12} - 2s_1s_{12}c_1c_{123} - 2s_1s_{123}c_1c_{12} \\ &- 4s_1s_{123}c_1c_{123} - 2s_1s_{123}c_{12}c_{123} - 2s_{12}s_{123}c_1c_{123} - 4s_{12}s_{123}c_{12}c_{123} \\ &+ s_1^2c_{12}^2 + 2s_1^2c_{123}^2 + s_{12}^2c_1^2 + 2s_{12}^2c_{123}^2 + 2s_{123}^2c_1^2 + 2s_{123}^2c_{12}^2 \end{aligned} \quad (10.49)$$

Therefore, the pseudo-inverse (\mathbf{J}^\dagger) is:

$$\mathbf{J}_{n \times m}^\dagger = \mathbf{J}_{3 \times 2}^\dagger = \mathbf{J}^T (\mathbf{J}\mathbf{J}^T)^{-1} = \frac{1}{J_{11}J_{22} - J_{12}J_{21}} \begin{bmatrix} J_{11}^\dagger & J_{12}^\dagger \\ J_{21}^\dagger & J_{22}^\dagger \\ J_{31}^\dagger & J_{32}^\dagger \end{bmatrix} \quad (10.50)$$

where:

$$\begin{aligned} J_{11}^\dagger &= -2s_1c_{12}c_{123} + s_{123}c_1c_{12} + s_{12}c_1c_{12} + s_{12}c_1c_{123} \\ &+ 2s_{123}c_1c_{123} + s_{123}c_{12}c_{123} - s_1c_{12}^2 - 2s_1c_{123}^2 - s_{12}c_{123}^2 \end{aligned} \quad (10.51)$$

$$\begin{aligned} J_{12}^\dagger &= 2s_{12}s_{123}c_1 - s_1s_{12}c_{12} - s_1s_{12}c_{123} - s_1s_{123}c_{12} \\ &- 2s_1s_{123}c_{123} - s_{12}s_{123}c_{123} + s_{12}^2c_1 + 2s_{123}^2c_1 + s_{123}^2c_{12} \end{aligned} \quad (10.52)$$

$$\begin{aligned} J_{21}^\dagger &= 2s_1c_{12}c_{123} - s_{123}c_1c_{12} - s_{12}c_1c_{12} - s_{12}c_1c_{123} \\ &+ s_1c_1c_{12} - s_{123}c_1c_{123} + s_1c_1c_{123} + s_{123}c_{12}c_{123} \\ &+ s_1c_{12}^2 + s_1c_{123}^2 - s_{12}c_1^2 - s_{12}c_{123}^2 - s_{123}c_1^2 \end{aligned} \quad (10.53)$$

$$\begin{aligned}
J_{22}^\dagger = & -2s_{12}s_{123}c_1 - s_1s_{12}c_1 + s_1s_{12}c_{12} + s_1s_{12}c_{123} \\
& - s_1s_{123}c_1 + s_1s_{123}c_{12} + s_1s_{123}c_{123} - s_{12}s_{123}c_{123} \\
& + s_1^2c_{12} + s_1^2c_{123} - s_{12}^2c_1 - s_{123}^2c_1 + s_{123}^2c_{12}
\end{aligned} \tag{10.54}$$

$$\begin{aligned}
J_{31}^\dagger = & -s_{123}c_1^2 - 2s_{123}c_1c_{12} - s_{123}c_1c_{123} - 2s_{123}c_{12}^2 - 2s_{123}c_{12}c_{123} \\
& + s_1c_1c_{123} + s_1c_{12}c_{123} + s_1c_{123}^2 + s_{12}c_1c_{123} + 2s_{12}c_{12}c_{123} + 2s_{12}c_{123}^2
\end{aligned} \tag{10.55}$$

$$\begin{aligned}
J_{32}^\dagger = & -s_1s_{123}c_1 - s_1s_{123}c_{12} + s_1s_{123}c_{123} - s_{12}s_{123}c_1 - 2s_{12}s_{123}c_{12} \\
& + 2s_{12}s_{123}c_{123} - s_{123}^2c_1 - 2s_{123}^2c_{12} + s_{123}^2c_{123} + 2s_1s_{12}c_{123} + 2s_{12}^2c_{123}
\end{aligned} \tag{10.56}$$

The null space of \mathbf{J} can be defined as the columns of $(\mathbf{I} - \mathbf{J}^\dagger \mathbf{J})$, in which:

$$(\mathbf{J}^\dagger \mathbf{J})_{n \times n} = (\mathbf{J}^\dagger \mathbf{J})_{3 \times 3} = \begin{bmatrix} a_{11} & a_{12} & a_{13} \\ a_{21} & a_{22} & a_{23} \\ a_{31} & a_{32} & a_{33} \end{bmatrix} \tag{10.57}$$

Specifically,

$$\begin{aligned}
a_{11} = & 2s_1^2c_{12}c_{123} + 2s_1s_{12}c_{123}^2 + 2s_{123}^2c_1c_{12} + 2s_{12}s_{123}c_1^2 \\
& - 2s_1s_{12}c_1c_{12} - 2s_1s_{12}c_1c_{123} - 2s_1s_{123}c_1c_{12} - 4s_1s_{123}c_1c_{123} \\
& - 2s_1s_{123}c_{12}c_{123} - 2s_{12}s_{123}c_1c_{123} - 2s_{12}s_{123}c_{12}c_{123} \\
& + s_1^2c_{12}^2 + 2s_1^2c_{123}^2 + s_{12}^2c_1^2 + s_{12}^2c_{123}^2 + 2s_{123}^2c_1^2 + s_{123}^2c_{12}^2
\end{aligned} \tag{10.58}$$

$$\begin{aligned}
a_{12} = & s_1s_{12}c_{123}^2 + s_{123}^2c_1c_{12} - s_1s_{123}c_{12}c_{123} - s_{12}s_{123}c_1c_{123} \\
& - 2s_{12}s_{123}c_{12}c_{123} + s_{12}^2c_{123}^2 + s_{123}^2c_{12}^2
\end{aligned} \tag{10.59}$$

$$\begin{aligned}
a_{13} = & s_1s_{123}c_{12}^2 + s_{12}^2c_1c_{123} - s_1s_{12}c_{123}^2 - s_{123}^2c_1c_{12} - s_1s_{12}c_{12}c_{123} \\
& + s_1s_{123}c_{12}c_{123} - s_{12}s_{123}c_1c_{12} + s_{12}s_{123}c_1c_{123}
\end{aligned} \tag{10.60}$$

$$\begin{aligned}
a_{21} = & s_1s_{12}c_{123}^2 + s_{123}^2c_1c_{12} - s_1s_{123}c_{12}c_{123} - s_{12}s_{123}c_1c_{123} \\
& - 2s_{12}s_{123}c_{12}c_{123} + s_{12}^2c_{123}^2 + s_{123}^2c_{12}^2
\end{aligned} \tag{10.61}$$

$$\begin{aligned}
a_{22} = & 2s_1^2 c_{12} c_{123} + 2s_{12} s_{123} c_1^2 - 2s_1 s_{12} c_1 c_{12} - 2s_1 s_{12} c_1 c_{123} \\
& - 2s_1 s_{123} c_1 c_{12} - 2s_1 s_{123} c_1 c_{123} - 2s_{12} s_{123} c_{12} c_{123} + s_1^2 c_{12}^2 \\
& + s_1^2 c_{123}^2 + s_{12}^2 c_1^2 + s_{12}^2 c_{123}^2 + s_{123}^2 c_1^2 + s_{123}^2 c_{12}^2
\end{aligned} \tag{10.62}$$

$$\begin{aligned}
a_{23} = & s_1^2 c_{12} c_{123} - s_1 s_{123} c_{12}^2 - s_{12}^2 c_1 c_{123} + s_1 s_{12} c_{123}^2 \\
& + s_{123}^2 c_1 c_{12} + s_{12} s_{123} c_1^2 - s_1 s_{12} c_1 c_{123} + s_1 s_{12} c_{12} c_{123} \\
& - s_1 s_{123} c_1 c_{12} - 2s_1 s_{123} c_1 c_{123} - s_1 s_{123} c_{12} c_{123} \\
& + s_{12} s_{123} c_1 c_{12} - s_{12} s_{123} c_1 c_{123} + s_1^2 c_{123}^2 + s_{123}^2 c_1^2
\end{aligned} \tag{10.63}$$

$$\begin{aligned}
a_{31} = & s_1 s_{123} c_{12}^2 + s_{12}^2 c_1 c_{123} - s_1 s_{12} c_{123}^2 - s_{123}^2 c_1 c_{12} \\
& - s_1 s_{12} c_{12} c_{123} + s_1 s_{123} c_{12} c_{123} - s_{12} s_{123} c_1 c_{12} + s_{12} s_{123} c_1 c_{123}
\end{aligned} \tag{10.64}$$

$$\begin{aligned}
a_{32} = & s_1^2 c_{12} c_{123} - s_1 s_{123} c_{12}^2 - s_{12}^2 c_1 c_{123} + s_1 s_{12} c_{123}^2 \\
& + s_{123}^2 c_1 c_{12} + s_{12} s_{123} c_1^2 - s_1 s_{12} c_1 c_{123} + s_1 s_{12} c_{12} c_{123} \\
& - s_1 s_{123} c_1 c_{12} - 2s_1 s_{123} c_1 c_{123} - s_1 s_{123} c_{12} c_{123} + s_{12} s_{123} c_1 c_{12} \\
& - s_{12} s_{123} c_1 c_{123} + s_1^2 c_{123}^2 + s_{123}^2 c_1^2
\end{aligned} \tag{10.65}$$

$$\begin{aligned}
a_{33} = & s_{123}^2 c_1^2 + 2s_{123}^2 c_1 c_{12} + 2s_{123}^2 c_{12}^2 - 2s_1 s_{123} c_1 c_{123} \\
& - 2s_1 s_{123} c_{12} c_{123} - 2s_{12} s_{123} c_1 c_{123} - 4s_{12} s_{123} c_{12} c_{123} \\
& + s_1^2 c_{123}^2 + 2s_1 s_{12} c_{123}^2 + 2s_{12}^2 c_{123}^2
\end{aligned} \tag{10.66}$$

10.2.4 Pseudo-inverse of Jacobian

The Jacobian matrix of a redundant manipulators is not square and therefore have to be inverted by pseudo-inverse. By definition, the pseudo-inverse of Jacobian matrix J , denoted by J^\dagger , should satisfy the following following properties:

$$JJ^\dagger J = J \tag{10.67}$$

$$J^\dagger J J^\dagger = J^\dagger \tag{10.68}$$

$$(JJ^\dagger)^T = JJ^\dagger \tag{10.69}$$

$$(J^\dagger J)^T = J^\dagger J \tag{10.70}$$

Which correspond to the properties of the inverse a square matrix A as:

$$JJ^{-1}J = J \quad (10.71)$$

$$J^{-1}JJ^{-1} = J^{-1} \quad (10.72)$$

$$(JJ^{-1})^T = JJ^{-1} \quad (10.73)$$

$$(J^{-1}J)^T = J^{-1}J \quad (10.74)$$

In addition, the pseudo-inverse \mathbf{J}^\dagger should two more condition to satisfy, which are:

$$(\mathbf{J}^\dagger)^\dagger = \mathbf{J} \quad (10.75)$$

$$(\mathbf{J}^T)^\dagger = (\mathbf{J}^\dagger)^T \quad (10.76)$$

The computation of pseudo-inverse of a Jacobian matrix $J_{n \times m}^\dagger$ varies depends on the structure of $J_{m \times n}$.

$$\mathbf{J}_{n \times m}^\dagger = \begin{cases} \mathbf{J}^T(\mathbf{J}\mathbf{J}^T)^{-1} & m < n \\ \mathbf{J}^{-1} & m = n \\ (\mathbf{J}\mathbf{J}^T)^{-1}\mathbf{J}^T & m > n \end{cases} \quad (10.77)$$

Note that with $m < n$, \mathbf{J} is a fat matrix; with $m > n$, \mathbf{J} is a skinny matrix.

By applying pseudo-inverse to Jacobian matrix, a unique solution to the inverse kinematics of a redundant manipulator can be determined as "least-norm solution". The least-norm solution minimizes $\frac{1}{2}\dot{\theta}^T\dot{\theta}$.

This section intends to study the motion of a redundant manipulator moving along a trajectory of a straight line segment with constant end-effector velocity.

Given the constant end-effector velocity, as well as the starting and ending point of the trajectory, joint angle θ can be computed by integrating the joint angle velocities $\dot{\theta}$ referring to time t . At each time step, a unique $\dot{\theta}$ can be determined by current joint angle θ , according to the pseudo-inverse of Jacobian matrix.

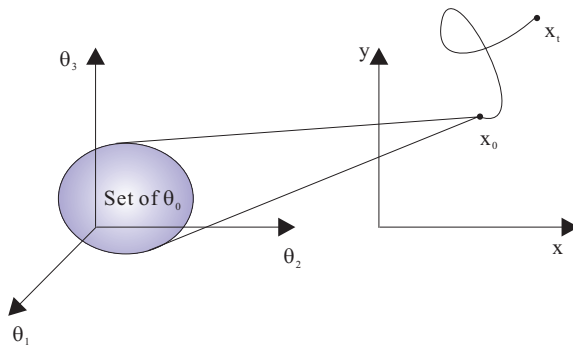


Figure 10.10: Many-to-one mapping from joint space to task space.

In addition to the kinematic equation, the evolution of a linear algebraic system also depends on the initial condition of the system. For a redundant manipulator, a starting point in task space, denoted by \mathbf{x}_0 , corresponds to a set of initial manipulator configurations in joint space, each of which can be denoted by θ_0 (Fig. 10.10). Therefore, the motion of manipulator starting the end-effector from the will evolve differently for different θ_0 corresponding to the same \mathbf{x}_0 , though the inverse kinematics can be resolved uniquely by pseudo-inverse of Jacobian matrix.

The following section will find out all the manipulator configurations corresponding to the same end-effector position in task space. In this way, a starting point in task space can be mapped to the initial manipulator configurations in joint space. After settling down the initial conditions, we can plot multiple trajectories in joint space corresponding to the same trajectory in task space, along which the end-effector moves with constant task space velocity.

10.2.5 Initial Condition in Joint Space

For a redundant manipulator, a end-effector position specified in task space corresponds to multiple manipulator configurations in joint space. The manipulator configurations corresponding the same end-effector position can be classified based on their families.

- Family 1

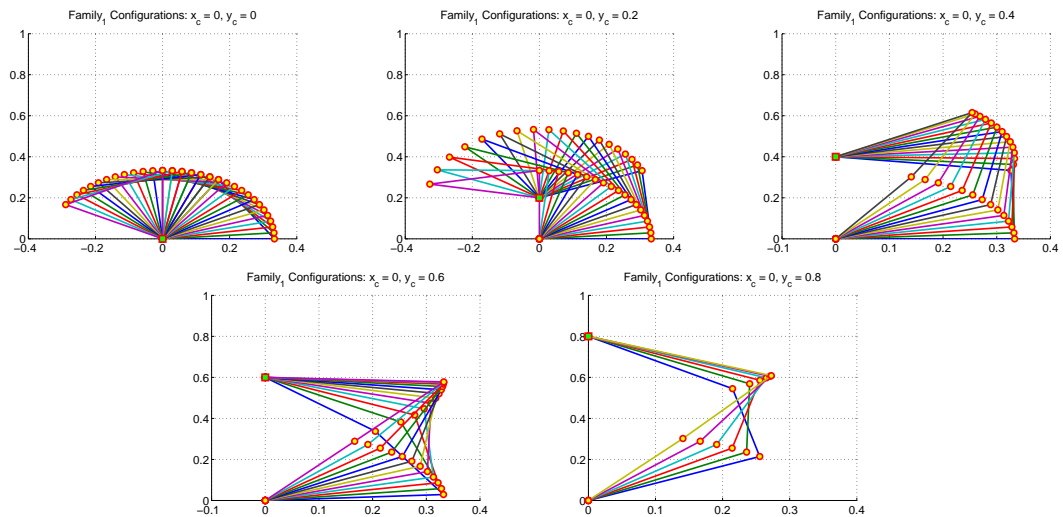


Figure 10.11: Family 1: mapping from joint space to task space

- Family 2 Some of Family 2 configurations are shown as(Fig. 10.12). Note that For Family 2, the end-effector can not reach all the points between $[0, 1]$ along y axis.

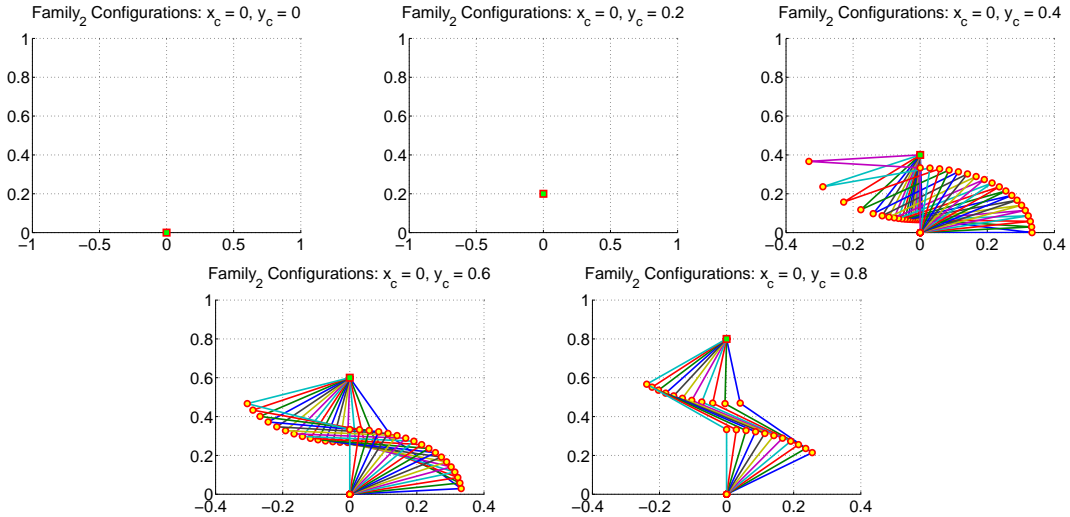


Figure 10.12: Family 2: mapping from joint space to task space.

- Configurations of Family 3

Some of Family 3 configurations are shown as(Fig. 10.13). Note that For Family 3, the end-effector can not reach all the points between $[0, 1]$ along y axis.

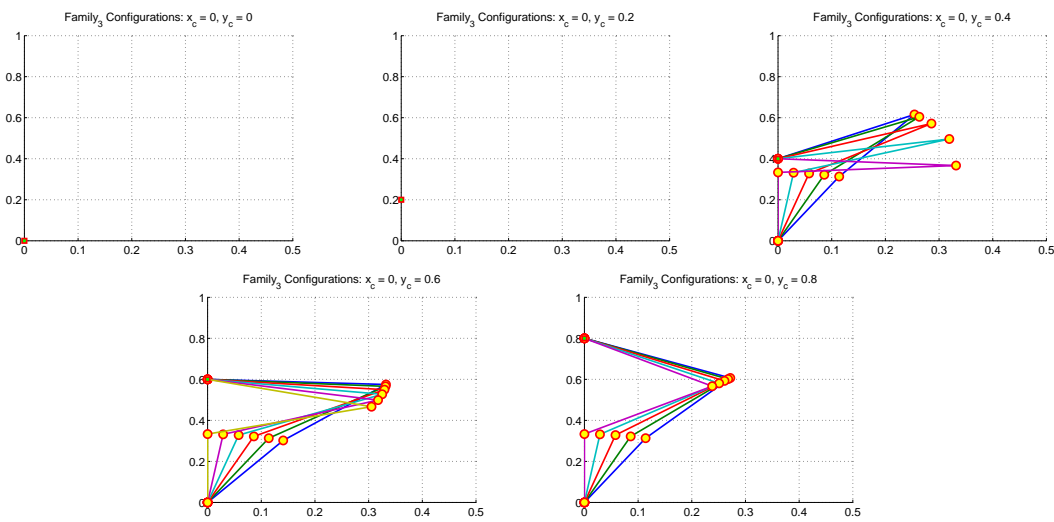


Figure 10.13: Family 3: mapping from joint space to task space.

10.2.6 Trajectories in Joint Space and Task Space

As the joint angles of a manipulator evolving in the joint space, the end-effector will render a unique trajectory in the task space. However, given the trajectory of the end-effector in task space, the evolution of joint angle of a redundant manipulator has many possible trajectories to follow. Assume that the inverse kinematics of the redundant manipulator is resolved by the pseudo-inverse of the Jacobian matrix. Therefore, the variation of the trajectories in joints space is due to the existence of multiple manipulator configurations corresponding to the same point in task space.

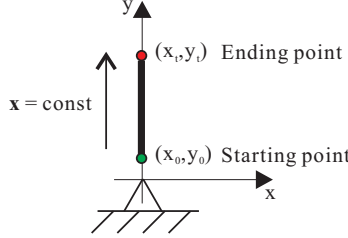


Figure 10.14: Problem setup: end-effector trajectory specified in task space.

This section studies the evolution of the joint angles of a redundant manipulator in the joint space, given a deterministic end-effector trajectory in task space and a specified moving velocity of the end-effector. As in Fig. 10.14, the end-effector of the three-link manipulator will move along a segment on y axis with constant speed of $\dot{\mathbf{x}} = [0, 1]^T$. Resolve the inverse kinematics by pseudo-inverse of Jacobian matrix as Equations (10.50) and (10.56), the evolution of joint space velocity can be found as Eq. (10.78):

$$\dot{\theta} = \mathbf{J}^\dagger \dot{\mathbf{x}} = \frac{1}{J_{11}J_{22} - J_{12}J_{21}} \begin{bmatrix} J_{11}^\dagger & J_{12}^\dagger \\ J_{21}^\dagger & J_{22}^\dagger \\ J_{31}^\dagger & J_{32}^\dagger \end{bmatrix} \begin{pmatrix} 0 \\ 1 \end{pmatrix} = \frac{1}{J_{11}J_{22} - J_{12}J_{21}} \begin{bmatrix} J_{12}^\dagger \\ J_{22}^\dagger \\ J_{32}^\dagger \end{bmatrix} \quad (10.78)$$

Given a initial manipulator configuration θ_0 , the continuous-time evolution of the joint angles θ from can be determined by:

$$\theta_t = \theta_0 + \int_0^t \dot{\theta} dt \quad (10.79)$$

In discrete-time, the evolution of the joint angles θ from can be approximated as:

$$\theta(k+1) = \theta(k) + \dot{\theta}(k)\Delta T \quad (10.80)$$

where ΔT is the sampling time.

Simulations are conducted to demonstrate the evolutions of the joint angles in discrete-time. Manipulator configurations from different families are chosen to be θ_0 . Note that reachable ranges of the end-effector vary when the manipulator takes initial configurations of different families. For each family of manipulator configurations, the limitation of reachable ranges of the end-effector is due to the specified range of joint angle in the family definition, in addition to the length limitation and the singularity. The reachable ranges for different families are approximately found by simulations (results in Table 10.2). For the convenience of comparison, further simulations will be conducted along a trajectory within the common reachable range of all the families, which is [0.4, 0.9] on y axis.

Families	Range of joint angles	Reachable range (along y axis)
Family 1 (Fig. 10.2.A)	$\theta_1 > 0, \theta_2 > 0, \theta_3 > 0$	(0,1)
Family 2 (Fig. 10.2.B)	$\theta_1 > 0, \theta_2 > 0, \theta_3 < 0$	(0.3,1)
Family 3 (Fig. 10.2.C)	$\theta_1 > 0, \theta_2 < 0, \theta_3 > 0$	(0.3,1)

Table 10.2: Reachable ranges of the end-effector when the manipulator takes initial configurations of different families.

For illustration, some of the initial manipulator in each family are shown in Fig. 10.15:

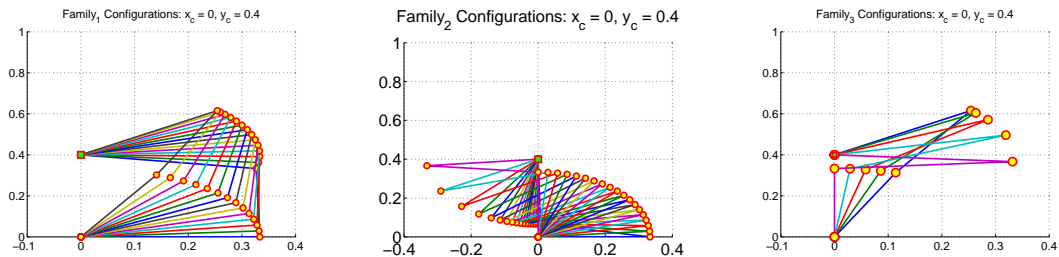


Figure 10.15: The initial manipulator conditions for different families.

- Joint space profile for Family 1 (Fig. 10.16)
- Joint space profile for Family 2 (Fig. 10.17)

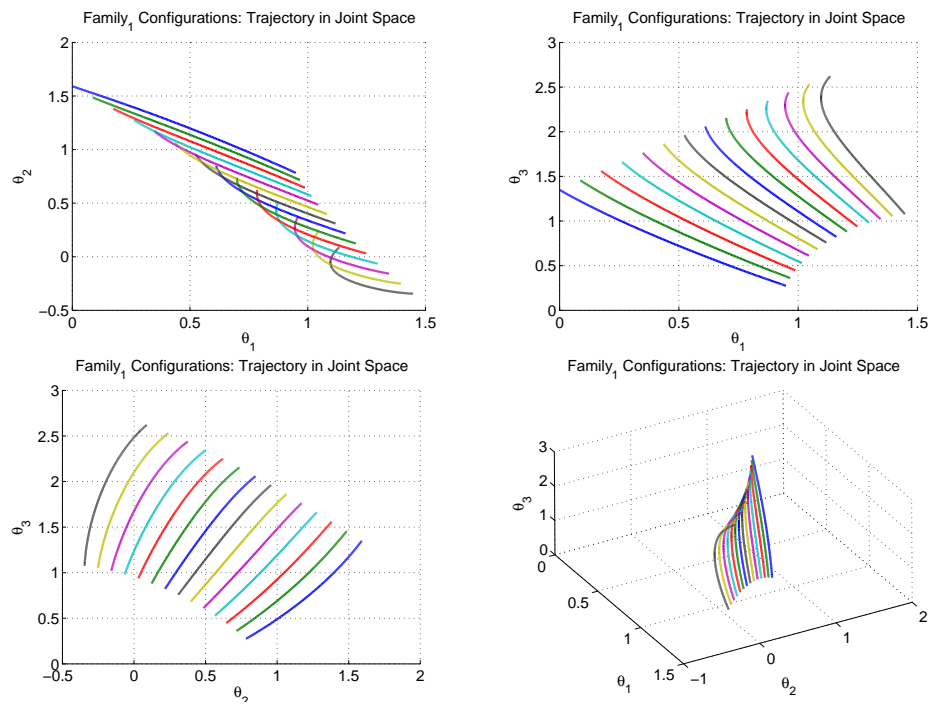


Figure 10.16: Joint space profile for Family 1.

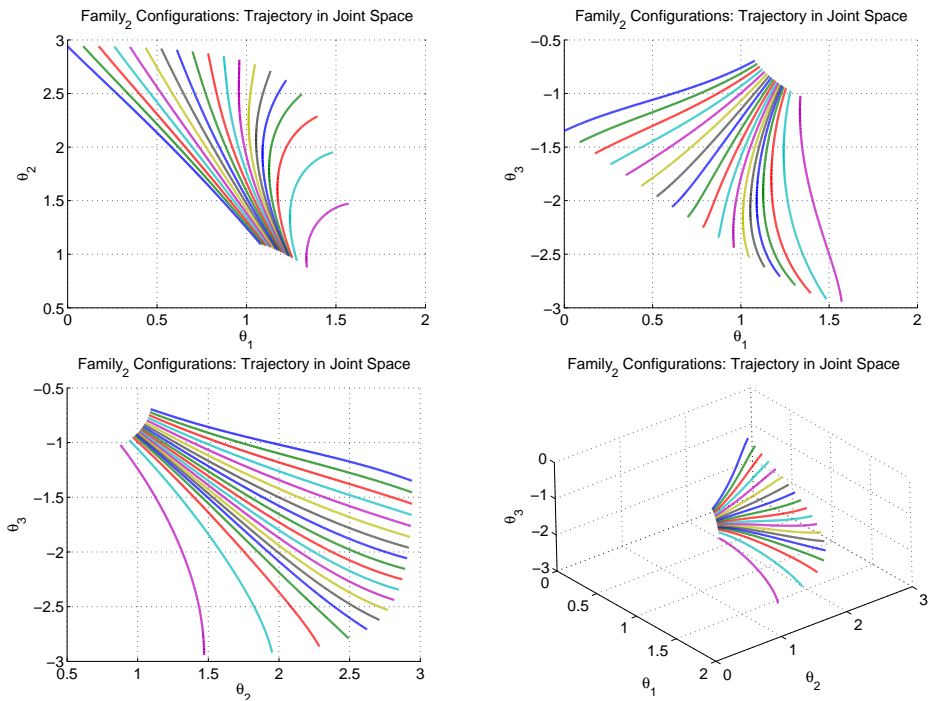


Figure 10.17: Joint space profile for Family 2.

- Joint space profile for Family 3 (Fig. 10.18)

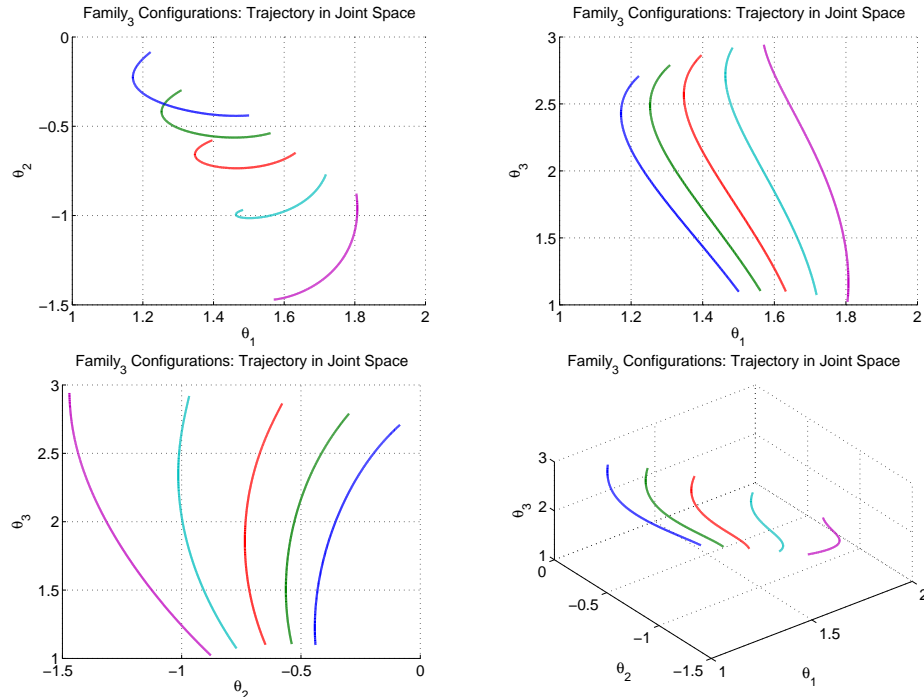


Figure 10.18: Joint space profile for Family 3.

Fig. 10.19 gets together all the evolutions of joint angles from different families: approximately, evolutions of Family 1 and Family 3 fall on the the same surface, while evolutions of Family 2 fall onto another. It is possible that these two surfaces can merge into a continuous one.

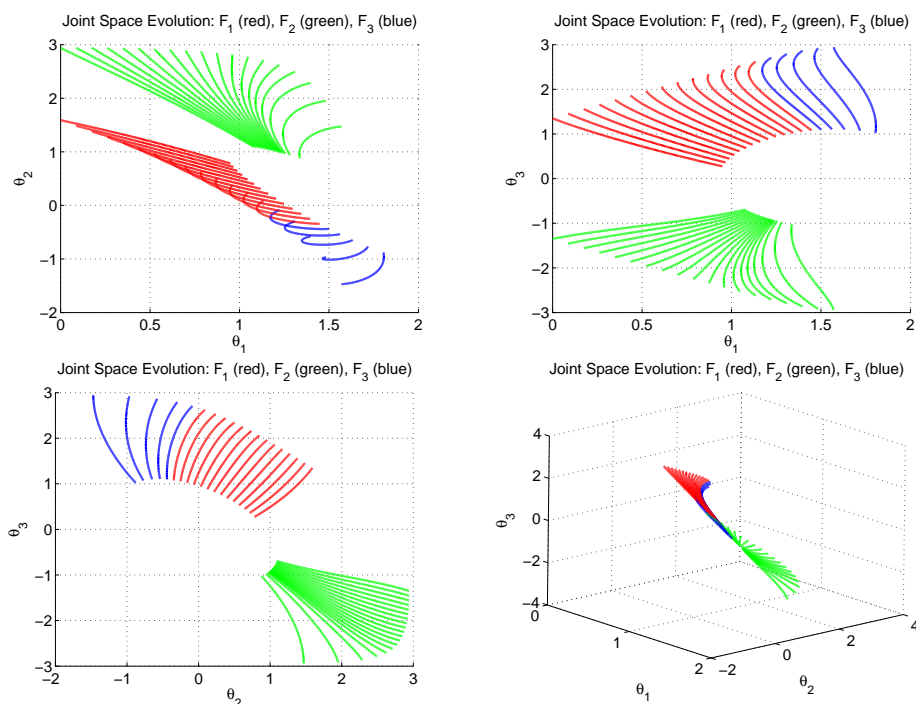


Figure 10.19: Joint space profile for different families of manipulator configurations.

10.2.7 Discussion on Pseudo-inverse Solution

Redundancy resolution by pseudo-inverse of Jacobian implicitly minimize the norm of the joint space velocity, i.e., $\min(\dot{\theta}^T \dot{\theta})$. Consider the redundant manipulator as a under-determined system, the pseudo-inverse intends to find the least square solution of the system.

Under-determined linear System

An under-determined linear system can be defined as $\mathbf{x} = A\mathbf{y}$, where $A \in \mathbf{R}^{m \times n}$ is fat, i.e. $m < n$. An under-determined linear system has more variables than equations, which makes \mathbf{x} under-specified, i.e, many choices of \mathbf{x} can result in the same \mathbf{y} .

Assume that A has full rank, for each $\mathbf{y} \in \mathbf{R}^m$, there is a solution set formed as Eq. (10.81).

$$\{\mathbf{x} | A\mathbf{x} = \mathbf{y}\} = \{\mathbf{x}_p + \mathbf{z} | \mathbf{z} \in N(A)\} \quad (10.81)$$

where $\mathbf{x}_p \in \mathbf{R}^m$ can be any particular solution that satisfies $A\mathbf{x}_p = \mathbf{y}$, $\mathbf{z} \in \mathbf{R}^{n-m}$ can be any solution that makes $A\mathbf{z} = 0$.

Least-norm Solution

An under-determined linear system can be optimized by minimizing $\|\mathbf{x}\|^2 = \mathbf{x}^T \mathbf{x}$ under the condition of $A\mathbf{x} = \mathbf{y}$. The least-norm solution that resolves the optimization problem can be derived via Lagrange multipliers. Define the Lagrange Multiplier L as Eq. (10.82),

$$L(x, \lambda) = \mathbf{x}^T \mathbf{x} + \lambda^T (A\mathbf{x} - \mathbf{y}) \quad (10.82)$$

Therefore, the optimal conditions are:

$$\frac{\partial L}{\partial \mathbf{x}} = 2\mathbf{x} + A^T \lambda = 0 \quad (10.83)$$

$$\frac{\partial L}{\partial \lambda} = A\mathbf{x} - \mathbf{y} = 0 \quad (10.84)$$

From Eq. (10.83),

$$\mathbf{x} = -\frac{A^T \lambda}{2} \quad (10.85)$$

Substitute Eq. (10.85) into Eq. (10.84),

$$\mathbf{y} = A\mathbf{x} = \frac{-AA^T \lambda}{2} \quad (10.86)$$

which leads to:

$$\lambda = -2(AA^T)^{-1}\mathbf{y} \quad (10.87)$$

Substitute Eq. (10.87) into Eq. (10.85),

$$\mathbf{x}_{ln} = \frac{-A^T(-2(AA^T)^{-1}\mathbf{y})}{2} = A^T(AA^T)^{-1}\mathbf{y} \quad (10.88)$$

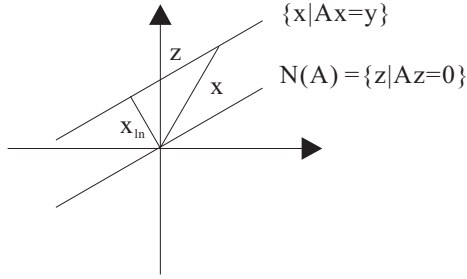


Figure 10.20: Least-norm solution \mathbf{x}_{ln} has smaller norm than any other solution.

Actually, the least-norm solution achieves the optimization by having $\mathbf{z}^T \mathbf{x}_{ln} = 0$ given $\mathbf{z} = \mathbf{x} - \mathbf{x}_{ln}$. Specifically, given any other solution \mathbf{x} to $A\mathbf{x} = \mathbf{y}$, with $A\mathbf{x}_{ln} = 0$, we have $A(\mathbf{x} - \mathbf{x}_{ln}) = A\mathbf{z} = 0$. Therefore,

$$\begin{aligned} \mathbf{z}^T \mathbf{x}_{ln} &= (\mathbf{x} - \mathbf{x}_{ln})^T \mathbf{x}_{ln} \\ &= (\mathbf{x} - \mathbf{x}_{ln})^T A^T (AA^T)^{-1} \mathbf{y} \\ &= [A(\mathbf{x} - \mathbf{x}_{ln})]^T (AA^T)^{-1} \mathbf{y} = 0 \end{aligned} \quad (10.89)$$

$\mathbf{z}^T \mathbf{x}_{ln} = 0$ suggests that $\mathbf{z} \perp \mathbf{x}_{ln}$, which leads to:

$$\|\mathbf{x}\|^2 = \|\mathbf{x}_{ln} + \mathbf{x} - \mathbf{x}_{ln}\|^2 = \|\mathbf{x}_{ln}\|^2 + \|\mathbf{x} - \mathbf{x}_{ln}\|^2 = \|\mathbf{x}_{ln}\|^2 + \|\mathbf{z}\|^2 \geq \|\mathbf{x}_{ln}\|^2 \quad (10.90)$$

As Eq. (10.90) (illustrated in Fig. 10.20), \mathbf{x}_{ln} has smaller norm than any other solution. \mathbf{x}_{ln} is the projection of 0 on solution set $\{x|A\mathbf{x} = \mathbf{y}\}$. In other word, $\mathbf{x}_{ln} \perp N(A)$.

Relate Least-norm Solution to Regularized Least-squares

The least-norm solution can be related to regularized least-square solution. Consider the problem of optimizing an under-determined linear system with two objectives. Define the two optimization objectives of $J_1 = \|A\mathbf{x} - \mathbf{y}\|$ and $J_2 = \|\mathbf{x}\|$. The least-norm solution will minimize J_2 with $J_1 = 0$. If the two optimization objectives are integrated into weighted-sum objective J as Eq. (10.91) and therefore are minimized as a whole,

$$J = J_1 + \mu J_2 = \|A\mathbf{x} - \mathbf{y}\| + \mu \|\mathbf{x}\| \quad (10.91)$$

The solution that minimizes J is \mathbf{x}_μ , as Eq. (10.92)

$$\mathbf{x}_\mu = (A^T A + \mu I)^{-1} A^T \mathbf{y} \quad (10.92)$$

$\mathbf{x}_\mu \rightarrow \mathbf{x}_{ln}$ as $\mu \rightarrow 0$.

10.3 Redundancy Resolution by Optimizing Manipulability

Redundancy resolution by pseudo-inverse of Jacobian implicitly minimize the norm of the joint space velocity. It is expected that the kinematical redundancy can be resolved by optimizing other performance indices, such as manipulability. Among the available manipulability performance indices, determinant of Jacobian and the condition number are commonly used.

10.3.1 Analytical derivation of manipulability performance indices

This section intends to analytically derive the manipulability performance indices, respectively for two-link, three-link and four link robotic manipulator in planar task.

Manipulability performance indices for two-link manipulator

For a two link manipulator with link length of $L_1 = L_2 = 1$, the Jacobian matrix is

$$\mathbf{J}_{2 \times 2} = \begin{bmatrix} -s_1 - s_{12} & -s_{12} \\ c_1 + c_{12} & c_{12} \end{bmatrix} \quad (10.93)$$

The transpose of Jacobian matrix is

$$\mathbf{J}_{2 \times 2}^T = \begin{bmatrix} -s_1 - s_{12} & c_1 + c_{12} \\ -s_{12} & c_{12} \end{bmatrix} \quad (10.94)$$

Thus,

$$\mathbf{J}\mathbf{J}^T = \begin{bmatrix} s_1^2 + 2s_1s_{12} + 2s_{12}^2 & -s_1c_1 - s_1c_{12} - s_{12}c_1 - 2s_{12}c_{12} \\ -s_1c_1 - s_1c_{12} - s_{12}c_1 - 2s_{12}c_{12} & c_1^2 + 2c_1c_{12} + 2c_{12}^2 \end{bmatrix} \quad (10.95)$$

$$\mathbf{J}^T\mathbf{J} = \begin{bmatrix} 2 + 2s_1s_{12} + 2c_1c_{12} & 1 + s_1s_{12} + c_1c_{12} \\ 1 + s_1s_{12} + c_1c_{12} & 1 \end{bmatrix} \quad (10.96)$$

$$\begin{aligned} \det(\mathbf{J}^T\mathbf{J} - \lambda\mathbf{I}) &= \begin{vmatrix} 2 + 2s_1s_{12} + 2c_1c_{12} - \lambda & 1 + s_1s_{12} + c_1c_{12} \\ 1 + s_1s_{12} + c_1c_{12} & 1 - \lambda \end{vmatrix} \\ &= -3\lambda - 2s_1s_{12}\lambda - 2c_1c_{12}\lambda + \lambda^2 + c_{12}^2 + c_1^2 - 2c_1^2c_{12}^2 - 2c_1c_{12}s_1s_{12} \\ &= \lambda^2 - (3 + 2s_1s_{12} + 2c_1c_{12})\lambda + c_{12}^2(1 - c_1^2) + c_1^2(1 - c_{12}^2) - 2c_1c_{12}s_1s_{12} \\ &= \lambda^2 - (3 + 2c_2)\lambda + c_{12}^2s_1^2 + c_1^2s_{12}^2 - 2c_1c_{12}s_1s_{12} \\ &= \lambda^2 - (3 + 2c_2)\lambda + (c_{12}s_1 - c_1s_{12})^2 \\ &= \lambda^2 - (3 + 2c_2)\lambda + s_2^2 = 0 \end{aligned} \quad (10.97)$$

which leads to,

$$\begin{aligned} \lambda_{1,2} &= \frac{(3 + 2c_2) \pm \sqrt{(3 + 2c_2)^2 - 4s_2^2}}{2} \\ &= \frac{(3 + 2c_2) \pm \sqrt{9 + 12c_2 + 4c_2^2 - 4s_2^2}}{2} \\ &= \frac{(3 + 2c_2) \pm \sqrt{9 + 12c_2 + 8c_2^2 - 4}}{2} \\ &= \frac{(3 + 2c_2) + \pm\sqrt{8c_2^2 + 12c_2 + 5}}{2} \\ &= \frac{(3 + 2c_2) \pm \sqrt{8(c_2^2 + 3/4c_2)^2 + 1/16}}{2} \end{aligned} \quad (10.98)$$

Therefore, the eigenvalue of Jacobian is

$$\Sigma_m = \begin{bmatrix} \sigma_1 & 0 \\ 0 & \sigma_2 \end{bmatrix} = \begin{bmatrix} \sqrt{\lambda_1} & 0 \\ 0 & \sqrt{\lambda_2} \end{bmatrix} \quad (10.99)$$

Furthermore, the manipulability performance indices are derived for two-link manipulator with various link length. Consider a two link manipulator with total link length of $L_1 + L_2 = l$. Define the link length ratio k as $k = \frac{L_1}{L_2}$. Hence, the link length L_1 and L_2 can be expressed with the link length ratio k and total link length l as:

$$L_1 = \frac{kl}{1+k} \quad (10.100)$$

$$L_2 = \frac{l}{1+k} \quad (10.101)$$

(10.102)

The Jacobian matrix of the two link manipulator becomes:

$$\begin{aligned} \mathbf{J}_{2 \times 2} &= \begin{bmatrix} -L_1 s_1 - L_2 s_{12} & -L_2 s_{12} \\ L_1 c_1 + L_2 c_{12} & L_2 c_{12} \end{bmatrix} \\ &= \frac{l}{1+k} \begin{bmatrix} -ks_1 - s_{12} & -s_{12} \\ kc_1 + c_{12} & c_{12} \end{bmatrix} \end{aligned} \quad (10.103)$$

$$\mathbf{J}^T \mathbf{J} = \frac{l}{1+k} \begin{bmatrix} -ks_1 - s_{12} & kc_1 + c_{12} \\ -s_{12} & c_{12} \end{bmatrix} \quad (10.104)$$

Thus,

$$\mathbf{J} \mathbf{J}^T = \frac{l^2}{(1+k)^2} \begin{bmatrix} k^2 s_1^2 + 2ks_1 s_{12} + 2s_{12}^2 & -k^2 s_1 c_1 - ks_1 c_{12} - ks_{12} c_1 - 2s_{12} c_{12} \\ -k^2 s_1 c_1 - ks_1 c_{12} - ks_{12} c_1 - 2s_{12} c_{12} & k^2 c_1^2 + 2kc_1 c_{12} + 2c_{12}^2 \end{bmatrix} \quad (10.105)$$

$$\mathbf{J}^T \mathbf{J} = \frac{l^2}{(1+k)^2} \begin{bmatrix} k^2 + 1 + 2ks_1 s_{12} + 2kc_1 c_{12} & ks_1 s_{12} + 1 + kc_1 c_{12} \\ ks_1 s_{12} + 1 + kc_1 c_{12} & 1 \end{bmatrix} \quad (10.106)$$

Let

$$\lambda = \frac{(1+k)^2}{l^2} \lambda_m \quad (10.107)$$

which leads to

$$\lambda_m = \frac{l^2}{(1+k)^2} \lambda \quad (10.108)$$

$$\begin{aligned}
& \det(\mathbf{J}^T \mathbf{J} - \lambda \mathbf{I}) \\
&= \frac{l^2}{(1+k)^2} \begin{vmatrix} k^2 + 1 + 2ks_1s_{12} + 2kc_1c_{12} - \frac{(1+k)^2}{l^2}\lambda_m & ks_1s_{12} + kc_1c_{12} + 1 \\ ks_1s_{12} + kc_1c_{12} + 1 & 1 - \frac{(1+k)^2}{l^2}\lambda_m \end{vmatrix} \\
&= \frac{l^2}{(1+k)^2} \begin{vmatrix} k^2 + 1 + 2ks_1s_{12} + 2kc_1c_{12} - \lambda & ks_1s_{12} + kc_1c_{12} + 1 \\ ks_1s_{12} + kc_1c_{12} + 1 & 1 - \lambda \end{vmatrix} \\
&= \frac{l^2}{(1+k)^2} [-k^2\lambda - 2ks_1s_{12}\lambda - 2\lambda - 2kc_1c_{12}\lambda + \lambda^2 + k^2c_{12}^2 + k^2c_1^2 - 2k^2c_1^2c_{12}^2 - 2k^2s_1s_{12}c_1c_{12}] \\
&= \frac{l^2}{(1+k)^2} [\lambda^2 - (k^2 + 2ks_1s_{12} + 2kc_1c_{12} + 2)\lambda + k^2c_{12}^2 + k^2c_1^2 - 2k^2c_1^2c_{12}^2 - 2k^2s_1s_{12}c_1c_{12}] \\
&= \frac{l^2}{(1+k)^2} [\lambda^2 - (k^2 + 2kc_2 + 2)\lambda + k^2c_{12}^2(1 - c_1^2) + k^2c_1^2(1 - c_{12}^2) - 2k^2s_1s_{12}c_1c_{12}] \\
&= \frac{l^2}{(1+k)^2} [\lambda^2 - (k^2 + 2kc_2 + 2)\lambda + k^2c_{12}^2s_1^2 + k^2c_1^2s_{12}^2 - 2k^2s_1s_{12}c_1c_{12}] \\
&= \frac{l^2}{(1+k)^2} [\lambda^2 - (k^2 + 2kc_2 + 2)\lambda + k^2(c_{12}s_1^2 + c_1^2s_{12}^2 - 2s_1s_{12}c_1c_{12})] \\
&= \frac{l^2}{(1+k)^2} [\lambda^2 - (k^2 + 2kc_2 + 2)\lambda + k^2(c_{12}s_1 - c_1s_{12})^2] \\
&= \frac{l^2}{(1+k)^2} [\lambda^2 - (k^2 + 2kc_2 + 2)\lambda + k^2s_2^2] = 0
\end{aligned} \tag{10.109}$$

which leads to,

$$\begin{aligned}
\lambda_{1,2} &= \frac{(k^2 + 2kc_2 + 2) \pm \sqrt{(k^2 + 2kc_2 + 2)^2 - 4k^2s_2^2}}{2} \\
&= \frac{(k^2 + 2kc_2 + 2) \pm \sqrt{k^4 + 4k^2c_2^2 + 4 + 4k^3c_2 + 4k^2 + 8kc_2 - 4k^2s_2^2}}{2} \\
&= \frac{(k^2 + 2kc_2 + 2) \pm \sqrt{k^4 + 4k^2c_2^2 + 4 + 4k^3c_2 + 8kc_2 + 4k^2c_2^2}}{2} \\
&= \frac{(k^2 + 2kc_2 + 2) \pm \sqrt{k^4 + 4k^3c_2 + 4k^2c_2^2 + 4k^2c_2^2 + 8kc_2 + 4}}{2} \\
&= \frac{(k^2 + 2kc_2 + 2) \pm \sqrt{k^2(k^2 + 4kc_2 + 4c_2^2) + 4(k^2c_2^2 + 2kc_2 + 1)}}{2} \\
&= \frac{(k^2 + 2kc_2 + 2) \pm \sqrt{k^2(k + 2c_2)^2 + 4(kc_2 + 1)^2}}{2}
\end{aligned} \tag{10.110}$$

As Eq. (10.110) shows, the Jacobian matrix can have two equal eigenvalues if and only if

$$k + 2c_2 = 0 \quad (10.111)$$

$$kc_2 + 1 = 0 \quad (10.112)$$

which implies:

$$-2c_2^2 + 1 = 0 \quad (10.113)$$

$$(10.114)$$

and therefore

$$k = -2c_2 \quad (10.115)$$

With $k > 0$, $c_2 = -\frac{\sqrt{2}}{2}$ and $k = \sqrt{2}$. In this case,

$$\lambda_{1,2} = \frac{k^2 + 2kc_2 + 2}{2} = \frac{2 + 2\sqrt{2}(-\frac{\sqrt{2}}{2}) + 2}{2} = 1 \quad (10.116)$$

Hence,

$$\lambda_m = \frac{l^2}{(1+k)^2} \lambda_{1,2} = \frac{l^2}{(1+\sqrt{2})^2} \quad (10.117)$$

The corresponding eigenvalue matrix of Jacobian is:

$$\Sigma_m = \begin{bmatrix} \sigma_m & 0 \\ 0 & \sigma_m \end{bmatrix} = \begin{bmatrix} \sqrt{\lambda_m} & 0 \\ 0 & \sqrt{\lambda_m} \end{bmatrix} = \frac{l}{1+\sqrt{2}} \begin{bmatrix} 1 & 0 \\ 0 & 1 \end{bmatrix} \quad (10.118)$$

When $k = \sqrt{2}$, the velocity ellipsoid becomes a circle, which implies the velocity transmission of the two-link manipulator is uniform in all the direction.

According to the simulation result, we have the following sub-conclusions:

(1) The flattening of the velocity (force) ellipsoid depends on the manipulator configuration (particularly the θ_2 for two-link manipulator), as well as the link length ratio k . Note that for an ellipsoid defined by

$$\frac{(x - x_c)^2}{a^2} + \frac{(y - y_c)^2}{b^2} = 1 \quad (10.119)$$

the flattening of an ellipsoid is

$$f = \frac{a - b}{a} \quad (10.120)$$

(2) For two-link manipulator, the velocity ellipsoid become a circle when $k = \sqrt{2}$. In this case, the velocity transmission of the two-link manipulator is uniform in all the direction.

Based on Eq. (10.107), the condition number of the two-link manipulator can be analytically expressed as:

$$C_n = \frac{\lambda_{m_1}}{\lambda_{m_2}} = \frac{\frac{l^2}{(1+k)^2} \lambda_1}{\frac{l^2}{(1+k)^2} \lambda_2} = \frac{\lambda_1}{\lambda_2} \quad (10.121)$$

With Eq. (10.110), C_n can be expressed as Eq. (10.122)

$$\begin{aligned} C_n = \frac{\lambda_1}{\lambda_2} &= \frac{\frac{(k^2 + 2kc_2 + 2) + \sqrt{k^2(k + 2c_2)^2 + 4(kc_2 + 1)^2}}{2}}{\frac{(k^2 + 2kc_2 + 2) - \sqrt{k^2(k + 2c_2)^2 + 4(kc_2 + 1)^2}}{2}} \\ &= \frac{(k^2 + 2kc_2 + 2) + \sqrt{k^2(k + 2c_2)^2 + 4(kc_2 + 1)^2}}{(k^2 + 2kc_2 + 2) - \sqrt{k^2(k + 2c_2)^2 + 4(kc_2 + 1)^2}} \\ &= 1 + \frac{2\sqrt{k^2(k + 2c_2)^2 + 4(kc_2 + 1)^2}}{(k^2 + 2kc_2 + 2) - \sqrt{k^2(k + 2c_2)^2 + 4(kc_2 + 1)^2}} \end{aligned} \quad (10.122)$$

Manipulability performance indices for three-link manipulator

This section conducts analytical derivation of the manipulability performance indices for three-link manipulator with various link length ratio.

Consider a three-link manipulator with total link length of $L_1 + L_2 + L_3 = l$. Define the link length ratios k_1 as $k_1 = \frac{L_1}{L_3}$, k_2 as $k_2 = \frac{L_2}{L_3}$. Hence, the link length L_1 , L_2 and L_3 can be expressed with the link length ratio k_1 , k_2 and total link length l as:

$$L_1 = \frac{k_1 l}{1 + k_1 + k_2} \quad (10.123)$$

$$L_2 = \frac{k_2 l}{1 + k_1 + k_2} \quad (10.124)$$

$$L_3 = \frac{l}{1 + k_1 + k_2} \quad (10.125)$$

$$(10.126)$$

The Jacobian matrix is:

$$\begin{aligned} \mathbf{J}_{2 \times 3} &= \begin{bmatrix} -L_1 s_1 - L_2 s_{12} - L_3 s_{123} & -L_2 s_{12} - L_3 s_{123} & -L_3 s_{123} \\ L_1 c_1 + L_2 c_{12} + L_3 c_{123} & L_2 c_{12} + L_3 c_{123} & L_3 c_{123} \end{bmatrix} \\ &= \frac{l}{1 + k_1 + k_2} \begin{bmatrix} -k_1 s_1 - k_2 s_{12} - s_{123} & -k_2 s_{12} - s_{123} & -s_{123} \\ -k_1 c_1 - k_2 c_{12} - c_{123} & -k_2 c_{12} - c_{123} & -c_{123} \end{bmatrix} \end{aligned} \quad (10.127)$$

$$\begin{aligned}
\mathbf{J}_{2 \times 3}^T &= \begin{bmatrix} -L_1 s_1 - L_2 s_{12} - L_3 s_{123} & L_1 s_1 + L_2 c_{12} + L_3 c_{123} \\ -L_2 s_{12} - L_3 s_{123} & L_2 c_{12} + L_3 c_{123} \\ -L_3 s_{123} & L_3 c_{123} \end{bmatrix} \\
&= \frac{l}{1+k_1+k_2} \begin{bmatrix} -k_1 s_1 - k_2 s_{12} - s_{123} & -k_1 c_1 - k_2 c_{12} - c_{123} \\ -k_2 s_{12} - s_{123} & -k_2 c_{12} - c_{123} \\ -s_{123} & -c_{123} \end{bmatrix} \tag{10.128}
\end{aligned}$$

Thus,

$$\mathbf{J}\mathbf{J}^T = \frac{l^2}{(1+k_1+k_2)^2} \begin{bmatrix} JJt_{11} & JJt_{12} \\ JJt_{21} & JJt_{22} \end{bmatrix} \tag{10.129}$$

where,

$$\begin{aligned}
JJt_{11} &= k_1^2 - k_1^2 c_1^2 + 2k_1 s_1 k_2 s_{12} + 2k_1 s_1 s_{123} + 2k_2^2 - 2k_2^2 c_{12}^2 + 4k_2 s_{12} s_{123} + 3 - 3c_{123}^2 \\
&= k_1^2 s_1^2 + 2k_1 s_1 k_2 s_{12} + 2k_1 s_1 s_{123} + 2k_2^2 s_{12}^2 + 4k_2 s_{12} s_{123} + 3s_{123}^2 \\
JJt_{12} &= JJt_{21} = \\
&- k_1^2 s_1 c_1 - k_1 s_1 k_2 c_{12} - k_1 s_1 c_{123} - k_2 s_{12} k_1 c_1 \\
&- 2k_2^2 s_{12} c_{12} - 2k_2 s_{12} c_{123} - s_{123} k_1 c_1 - 2s_{123} k_2 c_{12} - 3s_{123} c_{123} \\
JJt_{22} &= k_1^2 c_1^2 + 2k_1 c_1 k_2 c_{12} + 2k_1 c_1 c_{123} + 2k_2^2 c_{12}^2 + 4k_2 c_{12} c_{123} + 3c_{123}^2 \tag{10.130}
\end{aligned}$$

Let $\lambda = \frac{(1+k_1+k_2)^2}{l^2} \lambda_m$, i.e.

$$\lambda_m = \frac{l^2}{(1+k_1+k_2)^2} \lambda \tag{10.131}$$

$$\begin{aligned}
&\det(\mathbf{J}\mathbf{J}^T - \lambda \mathbf{I}) \\
&= \frac{l^2}{(1+k_1+k_2)^2} \begin{vmatrix} JJt_{11} - \frac{(1+k_1+k_2)^2}{l^2} \lambda_m & JJt_{12} \\ JJt_{21} & JJt_{22} - \frac{(1+k_1+k_2)^2}{l^2} \lambda_m \end{vmatrix} \\
&= \frac{l^2}{(1+k_1+k_2)^2} \begin{vmatrix} JJt_{11} - \lambda & JJt_{12} \\ JJt_{21} & JJt_{22} - \lambda \end{vmatrix} \\
&= \lambda^2 \\
&- [3 + 2k_1 s_1 k_2 s_{12} + 2k_1 c_1 k_2 c_{12} + k_1^2 + 2k_2^2 + 4k_2 s_{12} s_{123} + 2k_1 c_1 c_{123} + 4k_2 c_{12} c_{123} + 2k_1 s_1 s_{123}] \lambda \\
&- 2k_1^2 s_1 k_2 s_{12} c_1 c_{123} - 2k_1^2 c_1^2 k_2 c_{12} c_{123} + 2k_1^2 c_1^2 + 2k_2^2 c_{12}^2 + 2k_1 c_1 k_2 c_{12} \\
&+ 2k_1^2 c_{123}^2 + 2k_2^2 c_{123}^2 + k_1^2 k_2^2 c_{12}^2 - 4k_1^2 c_1^2 c_{123}^2 + k_2^2 k_1^2 c_1^2 \\
&- 4k_2^2 c_{12}^2 c_{123}^2 + 2k_1^2 k_2 c_{12} c_{123} - 2k_1^2 c_1^2 k_2^2 c_{12}^2 - 2k_1^2 s_1 k_2^2 s_{12} c_1 c_{12} \\
&+ 2k_1 s_1 k_2 s_{12} c_{123}^2 - 2k_1^2 s_1 s_{123} c_1 k_2 c_{12} - 4k_1^2 s_1 s_{123} c_1 c_{123} - 2k_1 s_1 s_{123} k_2 c_{12} c_{123} \\
&+ 2k_2 s_{12} s_{123} k_1^2 c_1^2 - 2k_2 s_{12} s_{123} k_1 c_1 c_{123} - 4k_2^2 s_{12} s_{123} c_{12} c_{123} - 2c_{123}^2 k_1 c_1 k_2 c_{12} \tag{10.132}
\end{aligned}$$

$$\begin{aligned}
& \det(\mathbf{JJ}^T - \lambda \mathbf{I}) \\
= & \lambda^2 \\
- & [3 + 2k_1 k_2 c_2 + k_1^2 + 2k_2^2 + 4k_2 c_3 + 2k_1 c_{23}] \lambda \\
- & 2k_1^2 k_2 s_1 s_{12} c_1 c_{123} - 2k_1^2 k_2 c_1^2 c_{12} c_{123} + 2k_1^2 c_1^2 + 2k_2^2 c_{12}^2 + 2k_1 k_2 c_1 c_{12} \\
+ & 2k_1^2 c_{123}^2 - 4k_1^2 c_1^2 c_{123}^2 + 2k_2^2 c_{123}^2 + k_1^2 k_2^2 c_{12}^2 + k_1^2 k_2^2 c_1^2 \\
- & 4k_2^2 c_{12}^2 c_{123}^2 + 2k_1^2 k_2 c_{12} c_{123} - 2k_1^2 k_2^2 c_1^2 c_{12}^2 - 2k_1^2 k_2^2 s_1 s_{12} c_1 c_{12} \\
+ & 2k_1 k_2 s_1 s_{12} c_{123}^2 - 2k_1^2 k_2 s_1 s_{123} c_1 c_{12} - 4k_1^2 s_1 s_{123} c_1 c_{123} - 2k_1 k_2 s_1 s_{123} c_{12} c_{123} \\
+ & 2k_1^2 k_2 s_{12} s_{123} c_1^2 - 2k_1 k_2 s_{12} s_{123} c_1 c_{123} - 4k_2^2 s_{12} s_{123} c_{12} c_{123} - 2k_1 k_2 c_{123}^2 c_1 c_{12}
\end{aligned} \tag{10.133}$$

$$\begin{aligned}
= & \lambda^2 \\
- & [3 + 2k_1 k_2 c_2 + k_1^2 + 2k_2^2 + 4k_2 c_3 + 2k_1 c_{23}] \lambda \\
+ & 2k_1^2 c_1^2 + 2k_1^2 c_{123}^2 - 4k_1^2 c_1^2 c_{123}^2 - 4k_1^2 s_1 s_{123} c_1 c_{123} \\
+ & 2k_2^2 c_{12}^2 + 2k_2^2 c_{123}^2 - 4k_2^2 c_{12}^2 c_{123}^2 - 4k_2^2 s_{12} s_{123} c_{12} c_{123} \\
+ & k_1^2 k_2^2 c_{12}^2 + k_1^2 k_2^2 c_1^2 - 2k_1^2 k_2^2 c_1^2 c_{12}^2 - 2k_1^2 k_2^2 s_1 s_{12} c_1 c_{12} \\
+ & 2k_1 k_2 s_1 s_{12} c_{123}^2 + (2k_1 k_2 c_1 c_{12} - 2k_1 k_2 c_{123}^2 c_1 c_{12}) - 2k_1 k_2 s_1 s_{123} c_{12} c_{123} - 2k_1 k_2 s_{12} s_{123} c_1 c_{123} \\
+ & 2k_1^2 k_2 s_{12} s_{123} c_1^2 + (2k_1^2 k_2 c_{12} c_{123} - 2k_1^2 k_2 c_1^2 c_{12} c_{123}) - 2k_1^2 k_2 s_1 s_{12} c_1 c_{123} - 2k_1^2 k_2 s_1 s_{123} c_1 c_{12} \\
= & \lambda^2 \\
- & [3 + 2k_1 k_2 c_2 + k_1^2 + 2k_2^2 + 4k_2 c_3 + 2k_1 c_{23}] \lambda \\
+ & 2k_1^2 (c_1^2 + c_{123}^2 - 2c_1^2 c_{123}^2 - 2s_1 s_{123} c_1 c_{123}) \\
+ & 2k_2^2 (c_{12}^2 + c_{123}^2 - 2c_{12}^2 c_{123}^2 - 2s_{12} s_{123} c_{12} c_{123}) \\
+ & k_1^2 k_2^2 (c_1^2 + c_1^2 - 2c_1^2 c_{12}^2 - 2s_1 s_{12} c_1 c_{12}) \\
+ & 2k_1 k_2 (s_1 s_{12} c_{123}^2 + s_{123}^2 c_1 c_{12} - s_1 s_{123} c_{12} c_{123} - s_{12} s_{123} c_1 c_{123}) \\
+ & 2k_1^2 k_2 (s_{12} s_{123} c_1^2 + s_1^2 c_{12} c_{123} - s_1 s_{12} c_1 c_{123} - s_1 s_{123} c_1 c_{12})
\end{aligned} \tag{10.134}$$

Hence, Eq. (10.132) can be further simplified as:

$$\begin{aligned}
& \det(\mathbf{J}\mathbf{J}^T - \lambda\mathbf{I}) \\
= & \lambda^2 \\
- & [3 + 2k_1 k_2 c_2 + k_1^2 + 2k_2^2 + 4k_2 c_3 + 2k_1 c_{23}] \lambda \\
+ & 2k_1^2(c_1^2 - c_1^2 c_{123}^2 + c_{123}^2 - c_1^2 c_{123}^2 - 2s_1 s_{123} c_1 c_{123}) \\
+ & 2k_2^2(c_{12}^2 - c_{12}^2 c_{123}^2 + c_{123}^2 - c_{12}^2 c_{123}^2 - 2s_{12} s_{123} c_{12} c_{123}) \\
+ & k_1^2 k_2^2(c_{12}^2 - c_1^2 c_{12}^2 + c_1^2 - c_1^2 c_{12}^2 - 2s_1 s_{12} c_1 c_{12}) \\
+ & 2k_1 k_2[s_1 c_{123}(s_{12} c_{123} - s_{123} c_{12}) + c_1 s_{123}(s_{123} c_{12} - s_{12} c_{123})] \\
+ & 2k_1^2 k_2[c_1 s_{12}(s_{123} c_1 - s_1 c_{123}) + s_1 c_{12}(s_1 c_{123} - c_1 s_{123})] \\
= & \lambda^2 \\
- & [3 + 2k_1 k_2 c_2 + k_1^2 + 2k_2^2 + 4k_2 c_3 + 2k_1 c_{23}] \lambda \\
+ & 2k_1^2(c_1^2 s_{123}^2 + s_1^2 c_{123}^2 - 2s_1 s_{123} c_1 c_{123}) \\
+ & 2k_2^2(c_{12}^2 s_{123}^2 + s_{12}^2 c_{123}^2 - 2s_{12} s_{123} c_{12} c_{123}) \\
+ & k_1^2 k_2^2(s_1^2 c_{12}^2 + c_1^2 s_{12}^2 - 2s_1 s_{12} c_1 c_{12}) \\
+ & 2k_1 k_2[-s_1 c_{123} s_3 + c_1 s_{123} s_3] \\
+ & 2k_1^2 k_2[c_1 s_{12} s_{23} - s_1 c_{12} s_{23}]
\end{aligned} \tag{10.135}$$

$$\begin{aligned}
& \det(\mathbf{J}\mathbf{J}^T - \lambda\mathbf{I}) \\
= & \lambda^2 \\
- & [3 + 2k_1 k_2 c_2 + k_1^2 + 2k_2^2 + 4k_2 c_3 + 2k_1 c_{23}] \lambda \\
+ & 2k_1^2(c_1 s_{123} - s_1 c_{123})^2 \\
+ & 2k_2^2(c_{12} s_{123} - s_{12} c_{123})^2 \\
+ & k_1^2 k_2^2(s_1 c_{12} - c_1 s_{12})^2 \\
+ & 2k_1 k_2(-s_1 c_{123} + c_1 s_{123}) s_3 \\
+ & 2k_1^2 k_2(c_1 s_{12} - s_1 c_{12}) s_{23} \\
= & \lambda^2 \\
- & [3 + 2k_1 k_2 c_2 + k_1^2 + 2k_2^2 + 4k_2 c_3 + 2k_1 c_{23}] \lambda \\
+ & 2k_1^2 s_{23}^2 + 2k_2^2 s_3^2 + k_1^2 k_2^2 s_2^2 + 2k_1 k_2 s_{23} s_3 + 2k_1^2 k_2 s_2 s_{23} \\
= & \lambda^2 \\
- & [3 + 2k_1 k_2 c_2 + k_1^2 + 2k_2^2 + 4k_2 c_3 + 2k_1 c_{23}] \lambda \\
+ & (k_1^2 k_2^2 s_2^2 + 2k_1^2 k_2 s_2 s_{23} + k_1^2 s_{23}^2) + (k_1^2 s_{23}^2 + 2k_1 k_2 s_{23} s_3 + k_2^2 s_3^2) + k_2^2 s_3^2 \\
= & \lambda^2 \\
- & [3 + 2k_1 k_2 c_2 + k_1^2 + 2k_2^2 + 4k_2 c_3 + 2k_1 c_{23}] \lambda \\
+ & (k_1 k_2 s_2 + k_1 s_{23})^2 + (k_1 s_{23} + k_2 s_3)^2 + (k_2 s_3)^2
\end{aligned} \tag{10.136}$$

Eq. (10.136) shows that the radius of the manipulability ellipsoids of a three-link

manipulator are determined only by the configuration of θ_2 and θ_3 , for given k_1 and k_2 .

Hence, the manipulability ω_n can be calculated as Eq. (10.138)

$$\omega_n^2 = \det(\mathbf{JJ}^T) = \frac{l^2}{(1+k_1+k_2)^2} \begin{vmatrix} JJ_{t11} & JJ_{t12} \\ JJ_{t21} & JJ_{t22} \end{vmatrix} \quad (10.137)$$

which equals to the terms without λ , in Eq. (10.132). Therefore,

$$\omega_n = \sqrt{\det(\mathbf{JJ}^T)} = \frac{l}{(1+k_1+k_2)} \sqrt{(k_1 k_2 s_2 + k_1 s_{23})^2 + (k_1 s_{23} + k_2 s_3)^2 + (k_2 s_3)^2} \quad (10.138)$$

The condition number can be analytically expressed as $C_n = \frac{\lambda_1}{\lambda_2}$.

Manipulability performance indices for four-link manipulator

This section conducts analytical singular value decomposition for a four-link manipulator on planar task, which will lead to the analytical representation of manipulability performance indices.

Consider a four-link manipulator with total link length of $L_1 + L_2 + L_3 + L_4 = l$. Define the link length ratio as $k_1 = \frac{L_1}{L_4}$, $k_2 = \frac{L_2}{L_4}$ and $k_3 = \frac{L_3}{L_4}$. Hence, the link lengths L_1, L_2, L_3 can be expressed with the link length ratio k_1, k_2, k_3 and total link length l as:

$$L_1 = \frac{k_1 l}{1 + k_1 + k_2 + k_3} \quad (10.139)$$

$$L_2 = \frac{k_2 l}{1 + k_1 + k_2 + k_3} \quad (10.140)$$

$$L_3 = \frac{k_3 l}{1 + k_1 + k_2 + k_3} \quad (10.141)$$

$$L_4 = \frac{l}{1 + k_1 + k_2 + k_3} \quad (10.142)$$

$$(10.143)$$

The Jacobian matrix is:

$$\begin{aligned}
\mathbf{J}_{2 \times 4} &= \begin{bmatrix} -L_1 s_1 - L_2 s_{12} - L_3 s_{123} - L_4 s_{1234} & -L_2 s_{12} - L_3 s_{123} - L_4 s_{1234} & -L_3 s_{123} - L_4 s_{1234} & -L_4 s_{1234} \\ L_1 c_1 + L_2 c_{12} + L_3 c_{123} + L_4 c_{1234} & L_2 c_{12} + L_3 c_{123} + L_4 c_{1234} & L_3 c_{123} + L_4 c_{1234} & L_4 c_{1234} \end{bmatrix} \\
&= \frac{l}{1 + k_1 + k_2 + k_3} \begin{bmatrix} -k_1 s_1 - k_2 s_{12} - k_3 s_{123} - s_{1234} & -k_2 s_{12} - k_3 s_{123} - s_{1234} & -k_3 s_{123} - s_{1234} & -s_{1234} \\ k_1 c_1 + k_2 c_{12} + k_3 c_{123} + c_{1234} & k_2 c_{12} + k_3 c_{123} + c_{1234} & k_3 c_{123} + c_{1234} & c_{1234} \end{bmatrix} \tag{10.144}
\end{aligned}$$

$$\begin{aligned}
\mathbf{J}_{2 \times 3} &= \begin{bmatrix} -L_1 s_1 - L_2 s_{12} - L_3 s_{123} - L_4 s_{1234} & L_1 c_1 + L_2 c_{12} + L_3 c_{123} + L_4 c_{1234} \\ -L_2 s_{12} - L_3 s_{123} - L_4 s_{1234} & L_2 c_{12} + L_3 c_{123} + L_4 c_{1234} \\ -L_3 s_{123} - L_4 s_{1234} & L_3 c_{123} + L_4 c_{1234} \\ -L_4 s_{1234} & L_4 c_{1234} \end{bmatrix} \\
&= \frac{l}{1 + k_1 + k_2 + k_3} \begin{bmatrix} -k_1 s_1 - k_2 s_{12} - k_3 s_{123} - s_{1234} & k_1 c_1 + k_2 c_{12} + k_3 c_{123} + c_{1234} \\ -k_2 s_{12} - k_3 s_{123} - s_{1234} & k_2 c_{12} + k_3 c_{123} + c_{1234} \\ -k_3 s_{123} - s_{1234} & k_3 c_{123} + c_{1234} \\ -s_{1234} & c_{1234} \end{bmatrix} \tag{10.145}
\end{aligned}$$

Thus,

$$\mathbf{J}\mathbf{J}^T = \frac{l^2}{(1 + k_1 + k_2 + k_3)^2} \begin{bmatrix} JJt_{11} & JJt_{12} \\ JJt_{21} & JJt_{22} \end{bmatrix} \tag{10.146}$$

where

$$\begin{aligned}
JJt_{11} &= k_1^2 s_1^2 + 2k_1 s_1 k_2 s_{12} + 2k_1 s_1 k_3 s_{123} + 2k_1 s_1 s_{1234} \\
&+ 2k_2^2 s_{12}^2 + 4k_2 s_{12} k_3 s_{123} + 4k_2 s_{12} s_{1234} \\
&+ 3k_3^2 s_{123}^2 + 6k_3 s_{123} s_{1234} \\
&+ 4s_{1234}^2 \\
JJt_{12} &= JJt_{21} = \\
&- 3s_{1234} k_3 c_{123} - s_{1234} k_1 c_1 - 3k_3 s_{123} c_{1234} - 2k_2^2 s_{12} c_{12} - 2s_{1234} k_2 c_{12} - 3k_3^2 s_{123} c_{123} \\
&- 2k_2 s_{12} c_{1234} - k_1^2 s_1 c_1 - k_1 s_1 k_2 c_{12} - k_1 s_1 k_3 c_{123} - k_2 s_{12} k_1 c_1 - 2k_2 s_{12} k_3 c_{123} \\
&- k_3 s_{123} k_1 c_1 - 2k_3 s_{123} k_2 c_{12} - k_1 s_1 c_{1234} - 4s_{1234} c_{1234} \\
JJt_{22} &= k_1^2 c_1^2 + 2k_1 c_1 k_2 c_{12} + 2k_1 c_1 k_3 c_{123} + 2k_1 c_1 c_{1234} \\
&+ 2k_2^2 c_{12}^2 + 4k_2 c_{12} k_3 c_{123} + 4k_2 c_{12} c_{1234} \\
&+ 3k_3^2 c_{123}^2 + 6k_3 c_{123} c_{1234} \\
&+ 4c_{1234}^2
\end{aligned} \tag{10.147}$$

Let $\lambda = \frac{(1+k_1+k_2+k_3)^2}{l^2} \lambda_m$, i.e.

$$\lambda_m = \frac{l^2}{(1+k_1+k_2+k_3)^2} \lambda \quad (10.148)$$

$$\begin{aligned} & \det(\mathbf{J}\mathbf{J}^T - \lambda\mathbf{I}) \\ &= \frac{l^2}{(1+k_1+k_2+k_3)^2} \begin{vmatrix} JJt_{11} - \frac{(1+k_1+k_2+k_3)^2}{l^2} \lambda_m & JJt_{12} \\ JJt_{21} & JJt_{22} - \frac{(1+k_1+k_2+k_3)^2}{l^2} \lambda_m \end{vmatrix} \\ &= \frac{l^2}{(1+k_1+k_2+k_3)^2} \begin{vmatrix} JJt_{11} - \lambda & JJt_{12} \\ JJt_{21} & JJt_{22} - \lambda \end{vmatrix} \end{aligned} \quad (10.149)$$

$$\begin{aligned} & \begin{vmatrix} JJt_{11} - \lambda & JJt_{12} \\ JJt_{21} & JJt_{22} - \lambda \end{vmatrix} \\ &= \lambda^2 \\ &- [2k_1k_3c_1c_{123} + 2k_1k_3s_1s_{123} + 4k_2k_3c_{12}c_{123} + 4 + 2k_1k_2s_1s_{12} + 2k_2^2 + 4k_2k_3s_{12}s_{123} \\ &+ 2k_1k_2c_1c_{12} + 4k_2s_{12}s_{1234} + 6k_3s_{123}s_{1234} + 2k_1c_1c_{1234} + 4k_2c_{12}c_{1234} \\ &+ 6k_3c_{123}c_{1234} + 2k_1s_1s_{1234} + k_3^2 + 3k_3^2] \lambda \\ &+ k_1^2(3c_{1234}^2 - 6c_1^2c_{1234}^2 - 6s_1s_{1234}c_1c_{1234} + 3c_1^2) \\ &+ k_2^2(4c_{1234}^2 + 4c_{12}^2 - 8c_{12}^2c_{1234}^2 - 8s_{12}s_{1234}c_{12}c_{1234}) \\ &+ k_3^2(3c_{123}^2 - 6c_{123}^2c_{1234}^2 + 3c_{1234}^2 - 6s_{123}s_{1234}c_{123}c_{1234}) \\ &+ k_1^2k_2^2(c_{12}^2 + c_1^2 - 2c_1^2c_{12}^2 - 2s_1s_{12}c_1c_{12}) \\ &+ k_2^2k_3^2(2c_{123}^2 + 2c_{12}^2 - 4c_{12}^2c_{123}^2 - 4s_{12}s_{123}c_{12}c_{123}) \\ &+ k_1^2k_3^2(2c_{123}^2 + 2c_1^2 - 4c_1^2c_{123}^2 - 4s_1s_{123}c_1c_{123}) \\ &+ k_1k_2(4s_1s_{12}c_{1234}^2 - 4s_1s_{1234}c_{12}c_{1234} - 4s_{12}s_{1234}c_1c_{1234} - 2s_{12}k_3^2s_{123}c_1c_{123} + 4c_1c_{12} - 4c_{1234}^2c_1c_{12}) \\ &+ k_2k_3(4c_{12}c_{123} + 4s_{12}s_{123}c_{1234}^2 - 4s_{12}s_{1234}c_{123}c_{1234} - 4s_{123}s_{1234}c_{12}c_{1234} - 4c_{1234}^2c_{12}c_{123}) \\ &+ k_1k_3(2s_1s_{123}c_{1234}^2 - 2s_{123}s_{1234}c_1c_{1234} + 2c_1c_{123} - 2c_{1234}^2c_1c_{123} - 2s_1s_{1234}c_{123}c_{1234}) \\ &+ k_2^2k_2(2c_{12}c_{1234} - 2c_1^2c_{12}c_{1234} - 2s_1s_{12}c_1c_{1234} - 2s_1s_{1234}c_1c_{12} + 2s_{12}s_{1234}c_1^2) \\ &+ k_1^2k_3(4c_{123}c_{1234} - 4c_1^2c_{123}c_{1234} - 4s_1s_{123}c_1c_{1234} - 4s_1s_{1234}c_1c_{123} + 4s_{123}s_{1234}c_1^2) \\ &+ k_2^2k_3(4c_{123}c_{1234} - 4c_{12}^2c_{123}c_{1234} - 4s_{12}s_{123}c_{12}c_{1234} - 4s_{12}s_{1234}c_{12}c_{123} + 4s_{123}s_{1234}c_{12}^2) \\ &+ k_1^2k_2k_3(2c_{12}c_{123} - 2c_1^2c_{12}c_{123} - 2s_1s_{12}c_1c_{123} - 2s_1s_{123}c_1c_{12} + 2s_{12}s_{123}c_1^2) \\ &+ k_1k_2k_3(2c_1c_{12} - 2c_{123}^2c_1c_{12} + 2s_1s_{12}c_{123}^2 - 2s_1s_{123}c_{12}c_{123}) \\ &- 2s_{12}s_{123}c_1c_{1234} - 2s_{12}s_{1234}c_1c_{123} + 4s_{123}s_{1234}c_1c_{123}) \end{aligned} \quad (10.150)$$

10.3.2 Manipulability performance measured by w_n

This section conducts simulations to find the manipulability performance measured by w_n , i.e., the determinant of Jacobian. The manipulability performance are compared

between manipulator configurations of different families, as well as the between the manipulators with different link length ratio.

w_n for different families of configurations

Manipulator configurations of different families demonstrate different manipulability performance, measured by determinant of Jacobian.

- w_n of Family 1, measured by determinant of Jacobian

The w_n of the configurations of Family 1 are shown in Fig. 10.21

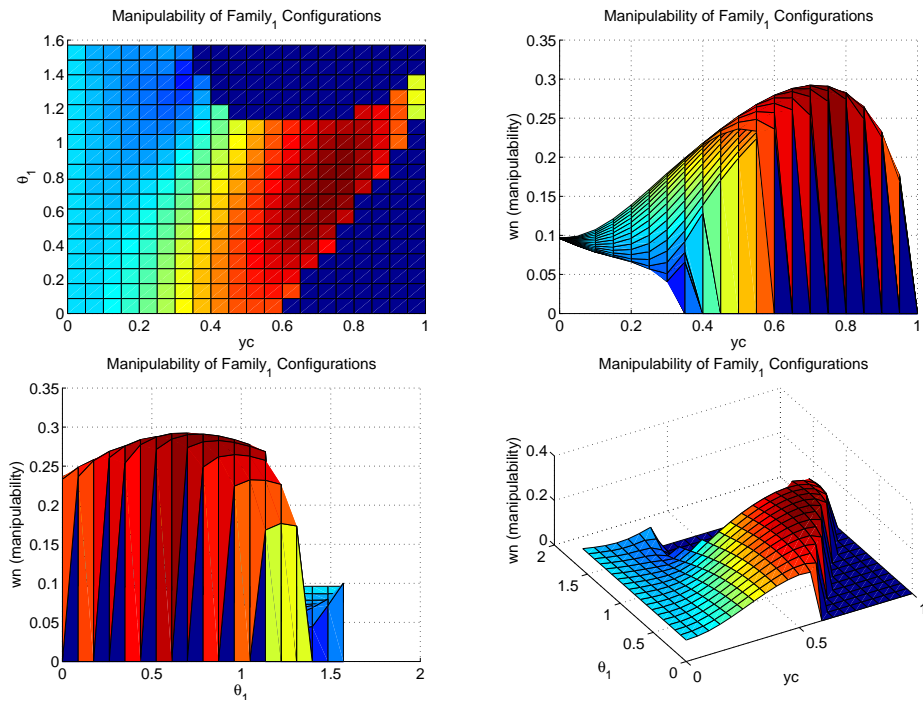


Figure 10.21: w_n of Family 1 Configurations.

- w_n of Family 2, measured by determinant of Jacobian

The manipulability of the configurations of Family 1 are shown in Fig. 10.22

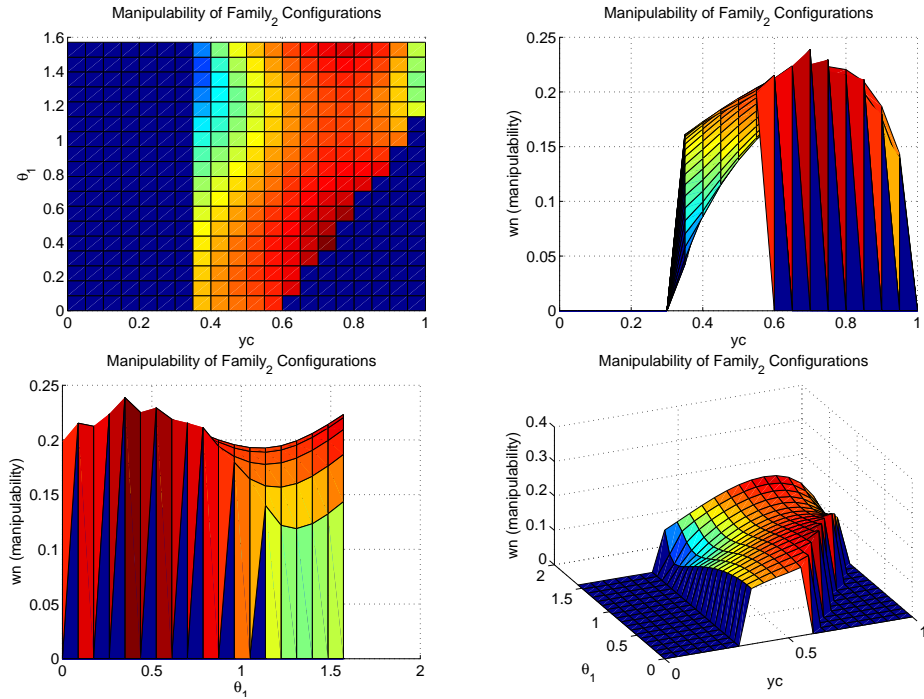


Figure 10.22: w_n of Family 2 Configurations.

- w_n of Family 3, measured by determinant of Jacobian

The w_n of the configurations of Family 3 are shown in Fig. 10.23

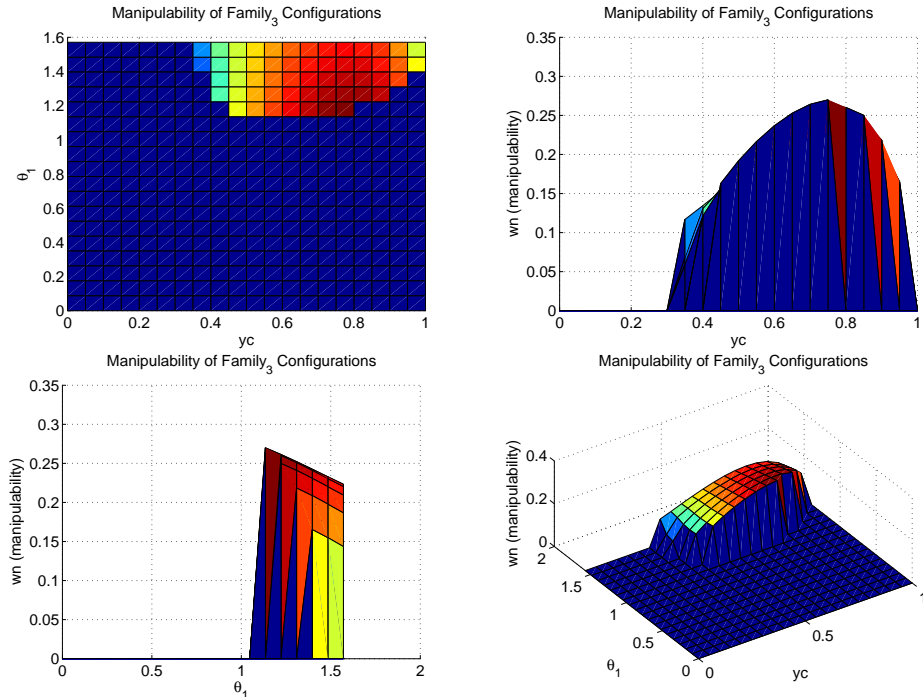


Figure 10.23: Manipulability of Family 3 Configurations.

Fig. 10.24 shows the achievable max manipulability along the designed trajectory, given the freedom to choose any θ_1 within $[0^\circ, 90^\circ]$. Note that Family 1 is always perform better than the other two families.

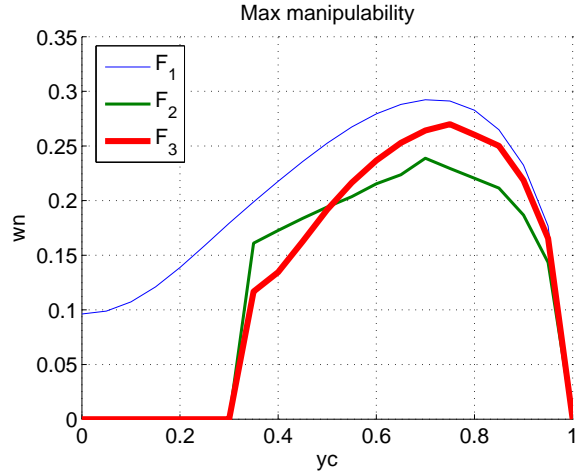


Figure 10.24: Max w_n along the designed trajectory.

w_n for two-link manipulator

Given a fixed total link length l (e.g. $l = L_1 + L_2 = 1$), w_n varies according to the link length ratio k as Fig. 10.25.

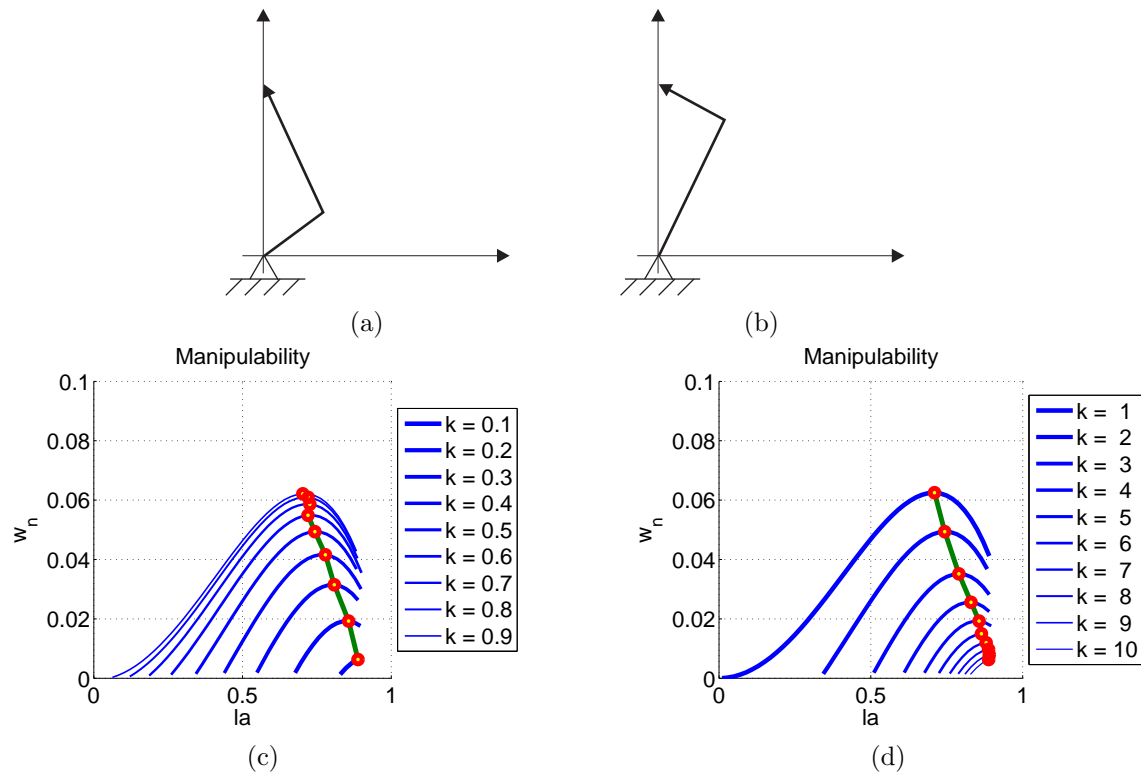


Figure 10.25: Two-link manipulator: w_n for Different Link Length Ratio. la is the end-effector position in task space

The w_n curve and condition number curve plotted with the population of θ_2 are as Fig. 10.26

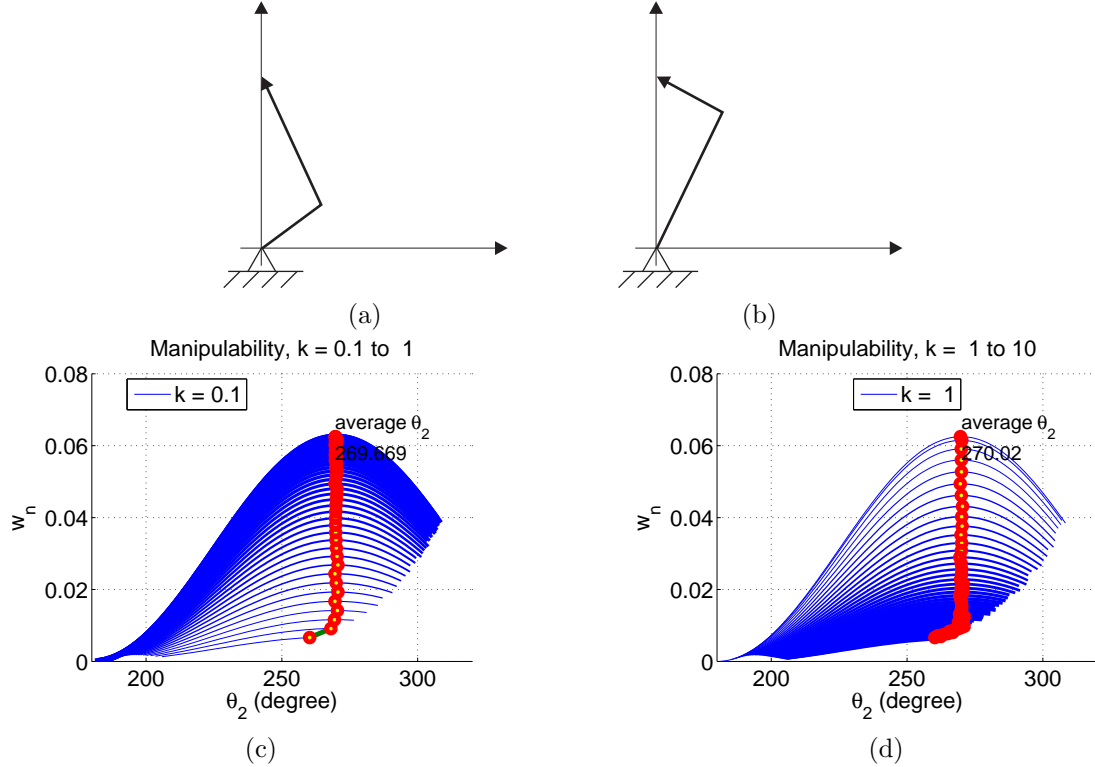


Figure 10.26: Two-link manipulator: w_n for Different Link Length Ratio, plotted by θ_2

It can be found that the best w_n happens for $k = 1$, i.e. equal link length will produce the best w_n performance for a two-link manipulator.

w_n for three-link manipulator

For three-link manipulator, the joint angle profile corresponding to the best w_n performance is (Fig. 10.27):

10.3.3 Manipulability performance measured by C_n

This section conducts simulations to find the manipulability performance measured by c_n , i.e., the condition number. The manipulability performance are compared between the manipulators with different link length ratio.

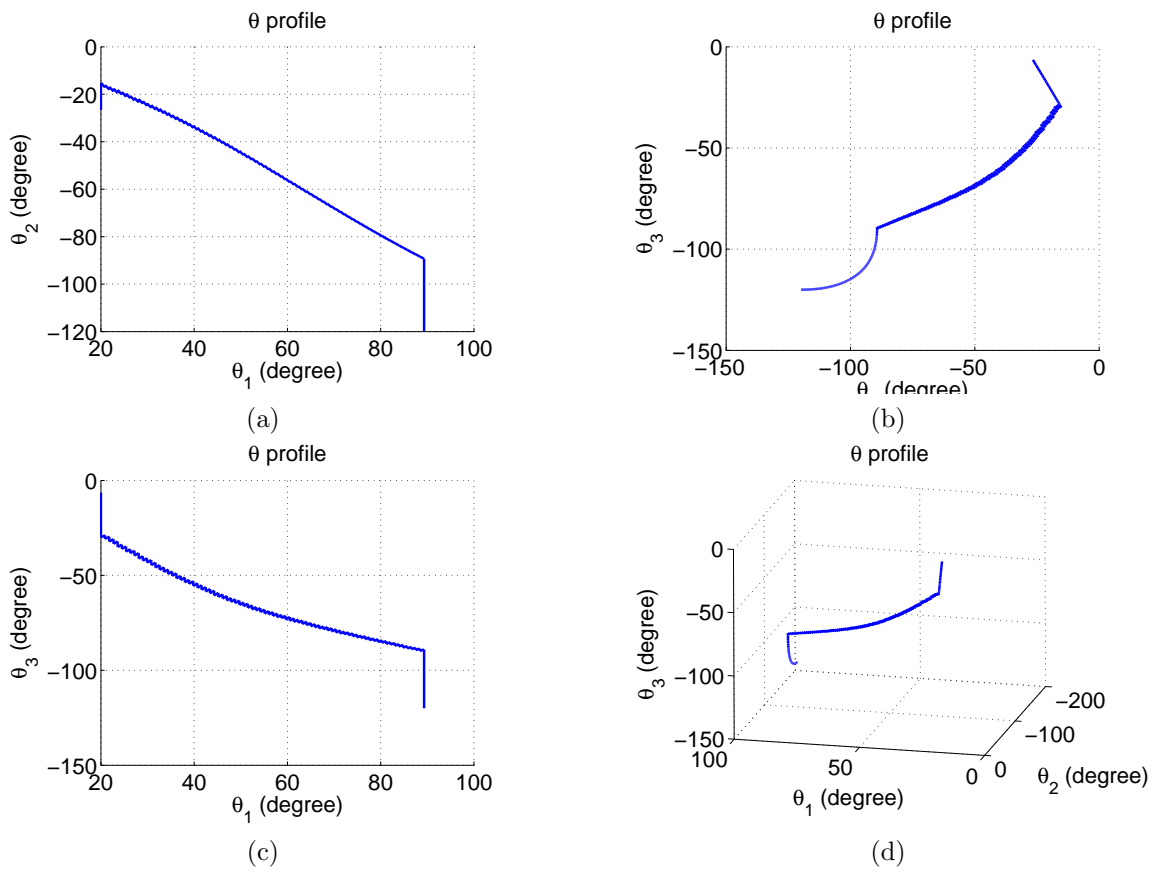


Figure 10.27: Best w_n profile, plotted by θ_1, θ_2 , and θ_3 .

C_n for two-link manipulator

Given a fixed total link length l (e.g. $l = L_1 + L_2 = 1$), the manipulability curve and condition number curve varies according to the link length ratio k as Fig. 10.28

The manipulability curve and condition number curve plotted with the population of θ_2 are as Fig. 10.29

It can be found that the best C_n happens for $k = 1$, i.e. equal link length will produce the best condition number performance for a two-link manipulator.

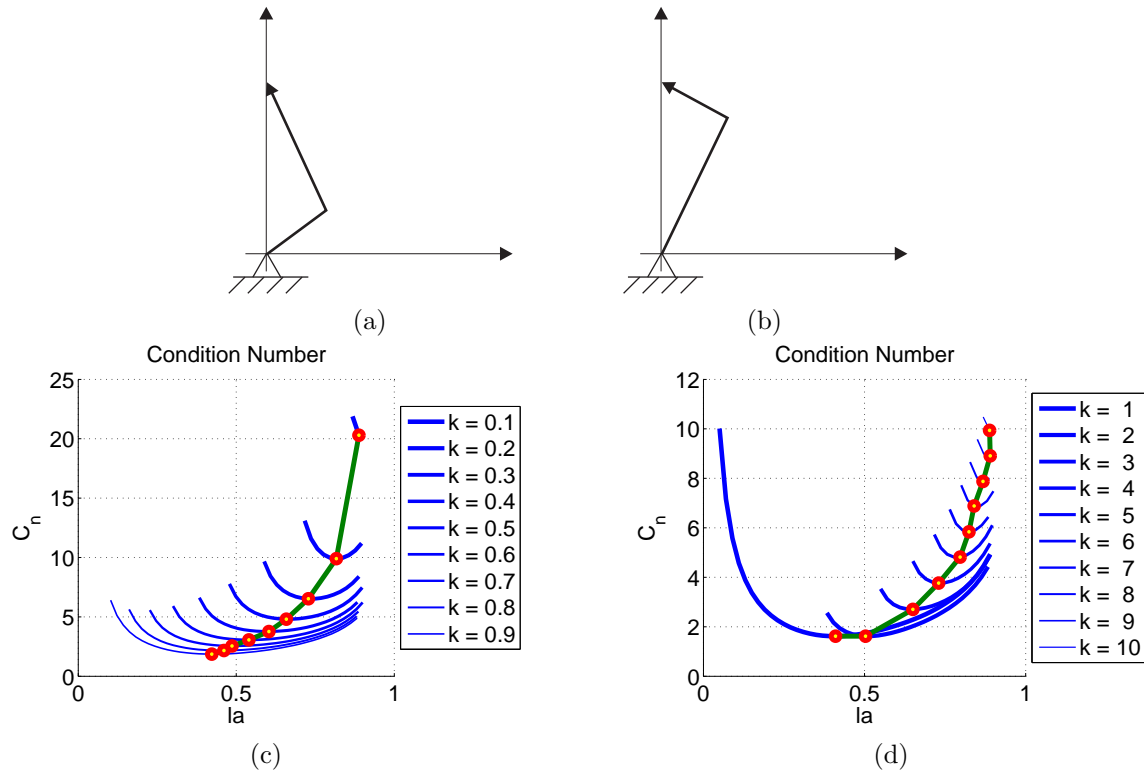


Figure 10.28: Two-link manipulator: C_n for Different Link Length Ratio. la is the end-effector position in task space

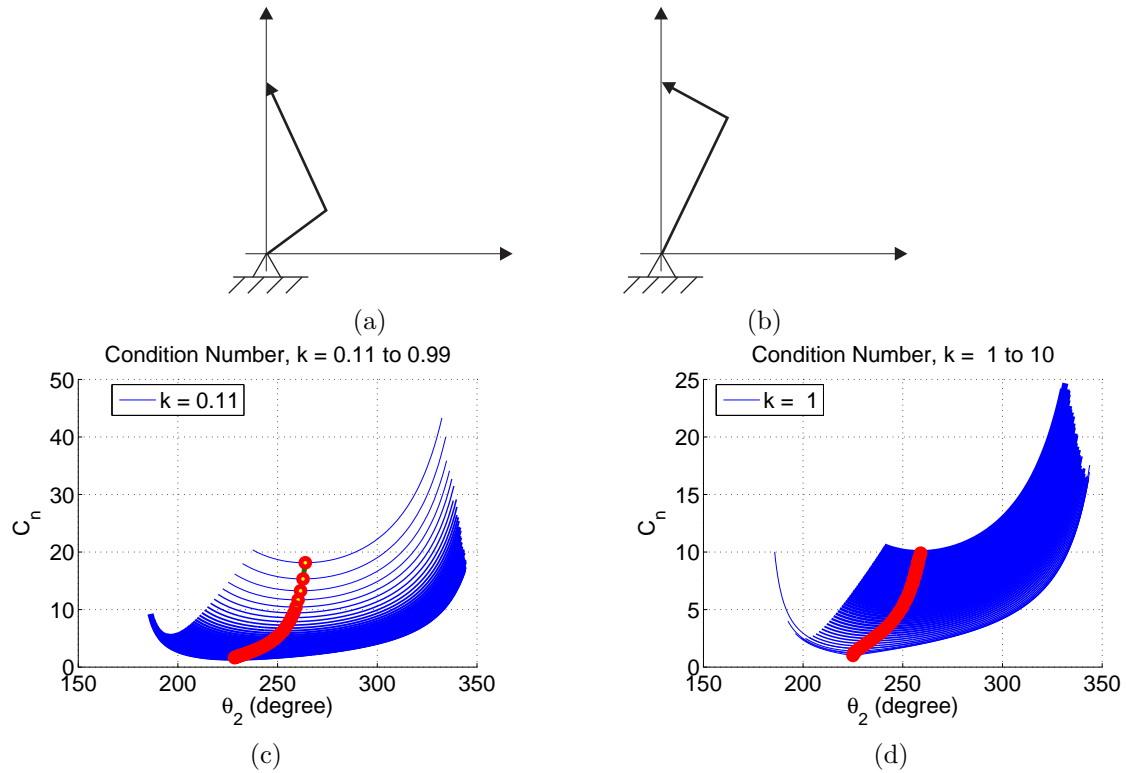


Figure 10.29: Two-link manipulator: C_n for Different Link Length Ratio, plotted by θ_2

C_n for three-link manipulator

The joint angle profile corresponding to the best condition performance is as Fig. 10.30:

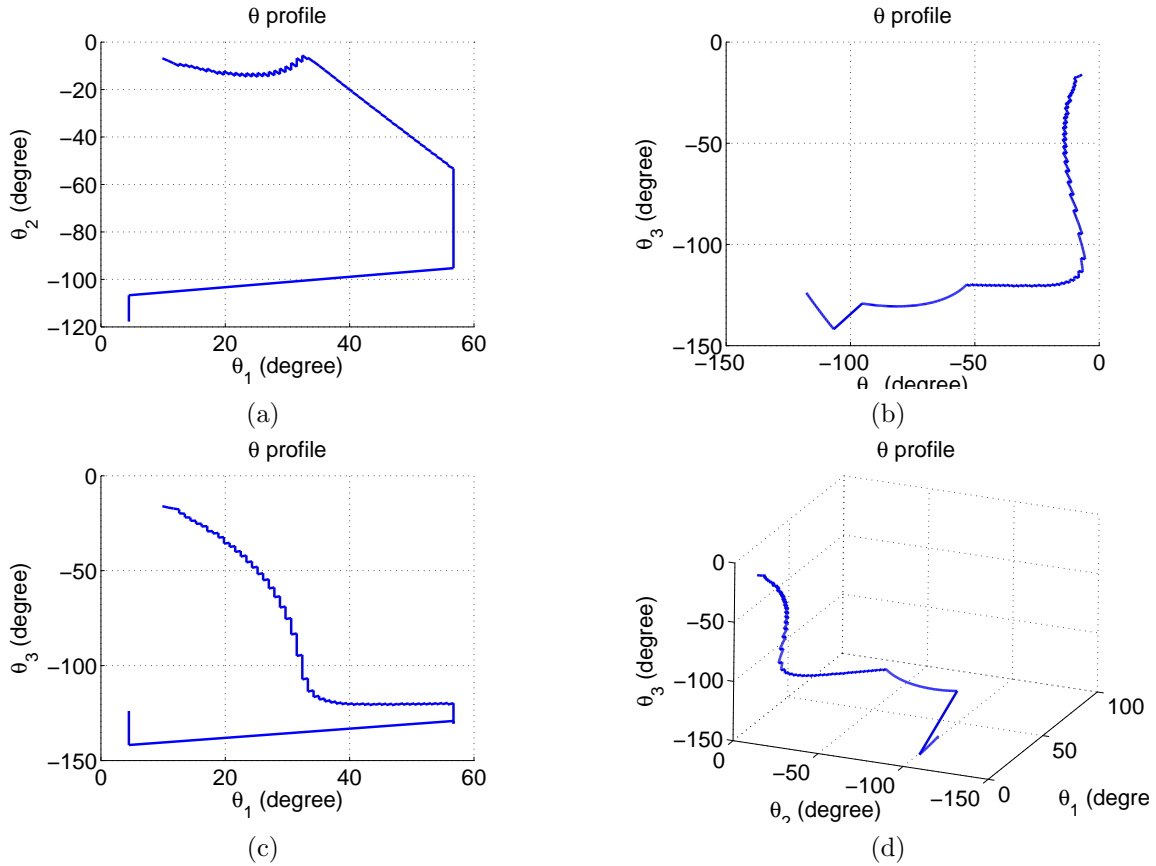


Figure 10.30: Best C_n profile, plotted by θ_1, θ_2 , and θ_3 .

10.3.4 Best manipulability performance by Link Length ratio

The link length ratio is defined as $k_1 = \frac{L_1}{L_3}$ and $k_2 = \frac{L_2}{L_3}$ with the restriction of $L_1 + L_2 + L_3 = l$. While the end-effector of a three link manipulator is moving along a straight line, the best manipulability performance varies for different k_1 and k_2 .

Keep $k_2 = 1$ (i.e. $L_2 = L_3$), $0.1 \leq k_1 \leq 5$ results in various performance of the best manipulability curve as Fig. 10.31, measured by w_n .

Keep $k_1 = 1$ (i.e. $L_1 = L_3$), $0.1 \leq k_2 \leq 5$ results in various performance of the best manipulability curve as Fig. 10.32, measured by w_n .

MAN	Upper Arm (UA)	Lower Arm (LA)	Hand (HA)	Total	k_1	k_2
99 percentile	312	274	213	800	1.465	1.286
50 percentile	279	257	190	726	1.468	1.353
1 percentile	216	234	168	648	1.286	1.393
WOMAN	Upper Arm (UA)	Lower Arm (LA)	Hand (HA)	Total	k_1	k_2
99 percentile	279	247	198	724	1.409	1.247
50 percentile	247	234	175	673	1.509	1.337
1 percentile	234	211	152	597	1.539	1.388

Table 10.3: Link Length Measurement (mm) and Link Length Ratio for Man and Woman.

Fig. 10.33 shows the best manipulability performance for the link length ratio of human arms (50 percentile), measured by w_n .

10.3.5 Analytical Derivation of Velocity & Force Ellipsoid

For robot with only one type of joints (i.e. prismatic or revolute joints) and for one type of tasks, the transformation of velocities (forces) can be characterized by a comparison of the end-effector velocity (wrench) produced by unit joint velocities (torques) [140]. The velocity (force) transmission between the joint space and the task space can be analytically represented by velocity (force) ellipsoid.

- Velocity Ellipsoid

Consider the joint velocities contained in the unit sphere of joint velocity space (n -dimensional), which correspond to a set of unit joint velocity of a mechanism. Given the joint velocity as $\dot{\theta}$ and end-effector velocity as $\dot{\mathbf{x}}$,

$$\dot{\theta}^T \dot{\theta} = \|\dot{\theta}\|^2 = \dot{\theta}_1^2 + \dot{\theta}_2^2 + \dots + \dot{\theta}_n^2 = 1 \quad (10.151)$$

Note that for a mechanism (non-redundant and redundant), the joint velocity $\dot{\theta}$ and the end-effector velocity $\dot{\mathbf{x}}$ can be related by pseudo-inverse as

$$\dot{\theta} = \mathbf{J}^\dagger \dot{\mathbf{x}} \quad (10.152)$$

where $\mathbf{J}_{m \times n}$ has $m \leq n$. In this case, $\text{rank}(\mathbf{J}) = m$ and the definition of \mathbf{J}^\dagger is

$$\mathbf{J}^\dagger = \mathbf{J}^T (\mathbf{J}\mathbf{J}^T)^{-1} \quad (10.153)$$

Let $\mathbf{J}\mathbf{J}^T = \mathbf{A}$, where \mathbf{A} is a square matrix of rank.

$$\mathbf{A}^\dagger = \mathbf{A}^{-1} = (\mathbf{J}\mathbf{J}^T)^\dagger = (\mathbf{J}\mathbf{J}^T)^{-1} \quad (10.154)$$

According to Equation A2.9 in [17],

$$(\mathbf{J}^\dagger)^T \mathbf{J}^\dagger = (\mathbf{J}\mathbf{J}^T)^\dagger \quad (10.155)$$

We have

$$(\mathbf{J}^\dagger)^T \mathbf{J}^\dagger = (\mathbf{J}\mathbf{J}^T)^{-1} \quad (10.156)$$

Therefore,

$$\begin{aligned} \|\dot{\theta}\|^2 &= \dot{\theta}^T \dot{\theta} \\ &= (\mathbf{J}^\dagger \dot{\mathbf{x}})^T (\mathbf{J}^\dagger \dot{\mathbf{x}}) \\ &= \dot{\mathbf{x}}^T [(\mathbf{J}^\dagger)^T (\mathbf{J}^\dagger)] \dot{\mathbf{x}} \\ &= \dot{\mathbf{x}}^T [(\mathbf{J}^\dagger)^T (\mathbf{J}^\dagger)] \dot{\mathbf{x}} \\ &= \dot{\mathbf{x}}^T [(\mathbf{J}\mathbf{J}^T)^{-1}] \dot{\mathbf{x}} \end{aligned} \quad (10.157)$$

By singular value decomposition (SVD),

$$\mathbf{J} = \mathbf{U} \boldsymbol{\Sigma}_m \mathbf{V}^T \quad (10.158)$$

Where \mathbf{U} and \mathbf{V} are orthogonal matrix such that

$$\begin{aligned} \mathbf{U}^T \mathbf{U} &= \mathbf{U} \mathbf{U}^T = \mathbf{I} \\ \mathbf{U}^T &= \mathbf{U}^{-1} \end{aligned} \quad (10.159)$$

and so it is with \mathbf{V} . $\boldsymbol{\Sigma}_m$ is a diagonal matrix, with diagonal elements σ_i ($i = 1, \dots, n$).

Thus,

$$\begin{aligned}
\|\dot{\theta}\|^2 &= \dot{\theta}^T \dot{\theta} \\
&= \dot{\mathbf{x}}^T [(\mathbf{U}\Sigma_m \mathbf{V}^T)(\mathbf{U}\Sigma_m \mathbf{V}^T)^T]^{-1} \dot{\mathbf{x}} \\
&= \dot{\mathbf{x}}^T [\mathbf{U}\Sigma_m (\mathbf{V}^T \mathbf{V}) \Sigma_m^T \mathbf{U}^T]^{-1} \dot{\mathbf{x}} \\
&= \dot{\mathbf{x}}^T [\mathbf{U}\Sigma_m^2 \mathbf{U}^T]^{-1} \dot{\mathbf{x}} \\
&= \dot{\mathbf{x}}^T [(\mathbf{U}^T)^{-1} \Sigma_m^{-2} (\mathbf{U}^{-1})] \dot{\mathbf{x}} \\
&= \dot{\mathbf{x}}^T [\mathbf{U}\Sigma_m^{-2} \mathbf{U}^T] \dot{\mathbf{x}} \\
&= (\mathbf{U}^T \dot{\mathbf{x}})^T \Sigma_m^{-2} (\mathbf{U}^T \dot{\mathbf{x}}) = 1
\end{aligned} \tag{10.160}$$

Let $\mathbf{U}^T \dot{\mathbf{x}} = \omega$,

$$\begin{aligned}
\|\dot{\theta}\|^2 &= (\mathbf{U}^T \dot{\mathbf{x}})^T \Sigma_m^{-2} (\mathbf{U}^T \dot{\mathbf{x}}) \\
&= \omega^T \Sigma_m^{-2} \omega \\
&= \sum \frac{\omega_i^2}{\sigma_i^2} = 1
\end{aligned} \tag{10.161}$$

Where ω_i^2 is the diagonal elements of $\omega^T \omega$.

Equations (10.160) and (10.161) represented the velocity transmission as velocity ellipsoid. The principle axes of the ellipsoid are defined by \mathbf{U} and the radiiuses of the ellipsoid are determined by the diagonal elements of Σ_m , i.e. σ_i .

- Force Ellipsoid

Consider the joint torques contained in the unit sphere of joint torque space (n -dimensional), which correspond to the unit joint torque of a mechanism. Given the joint torques as τ and end-effector wrench as \mathbf{F} ,

$$\tau^T \tau = \|\tau\|^2 = \tau_1^2 + \tau_2^2 + \dots + \tau_n^2 = 1 \tag{10.162}$$

Note that for a mechanism (non-redundant and redundant), the joint torques τ and the end-effector wrench \mathbf{F} can be related by \mathbf{J}^T as

$$\tau = \mathbf{J}^T \mathbf{F} \tag{10.163}$$

where $\mathbf{J}_{m \times n}$ has $m \leq n$. In this case, $\text{rank}(\mathbf{J}^T) = m$.

Therefore,

$$\begin{aligned}
\|\tau\|^2 &= \tau^T \tau \\
&= (\mathbf{J}^T \mathbf{F})^T (\mathbf{J}^T \mathbf{F}) \\
&= \mathbf{F}^T [\mathbf{J} \mathbf{J}^T] \mathbf{F}
\end{aligned} \tag{10.164}$$

By singular value decomposition (SVD) as Equations (10.158) and (10.159)

$$\begin{aligned}
\|\tau\|^2 &= \tau^T \tau \\
&= \mathbf{F}^T [(\mathbf{U} \boldsymbol{\Sigma}_m \mathbf{V}^T) (\mathbf{U} \boldsymbol{\Sigma}_m \mathbf{V}^T)^T] \mathbf{F} \\
&= (\mathbf{U}^T \mathbf{F})^T \boldsymbol{\Sigma}_m^2 (\mathbf{U}^T \mathbf{F}) = 1
\end{aligned} \tag{10.165}$$

Let $\mathbf{U}^T \mathbf{F} = \gamma$,

$$\begin{aligned}
\|\tau\|^2 &= (\mathbf{U}^T \mathbf{F}) \boldsymbol{\Sigma}_m^2 (\mathbf{U}^T \mathbf{F}) \\
&= \gamma^T \boldsymbol{\Sigma}_m^2 \gamma \\
&= \sum \frac{\gamma_i^2}{\sigma_i^{-2}} = 1
\end{aligned} \tag{10.166}$$

Where γ_i^2 is the diagonal elements of $\gamma^T \gamma$.

Eq. (10.166) represented the velocity transmission as velocity ellipsoid. The principle axes of the ellipsoid are defined by \mathbf{U} and the radiuses of the ellipsoid are determined by by the diagonal elements of $\boldsymbol{\Sigma}_m^{-1}$, i.e. $\frac{1}{\sigma_i}$.

- Relationship Between Velocity ellipsoid and Force ellipsoid

Decompose the end-effector velocity (wrench) vector by in the reference frame of \mathbf{U} , we can build up the velocity ellipsoid and force ellipsoid of the same mechanism in the same coordinate system, which explicitly demonstrates the relationship between their radiuses. Along the axis that the velocity ellipsoid has radius of σ_i , the corresponding force ellipsoid has radius of $\frac{1}{\sigma_i}$.

When the end-effector of a two link manipulator ($L_1 = L_2 = 1$) moving along a straight line (e.g. the x-axis), the velocity ellipsoid will populate as Fig. 10.34(as Yoshikawa's Fig4.3 of [17]).

Similarly, the force ellipsoids are generated from unit joint space as Fig. 10.35.

10.4 Entropy as the measurement of probabilistic reachability

A well-designed robotic manipulator are expected to have a workspace that adapt to the task requirement. The area that is frequently visited by task requirement should be easily reached by the end-effector of the robotic manipulator, without much control effort. To study the probabilistic reachability within the workspace, this section introduces the entropy as a performance index and conducts simulations to find out the probabilistic distribution of end-effector position for the planar manipulator with different degrees of redundancy.

From the perspective of statistical mechanics, the concept of entropy was originally proposed as measurement of uncertainty. The control effort introduced to a system intends to reduce the uncertainty in the probabilistic distribution of outputs. Particularly for a robotic manipulator, the control effort is imposed by the mechanical constraints, i.e., the kinematics and dynamics of the robotic manipulator. As a measurement of uncertainty, the entropy can evaluate the control effort imposed by the kinematics and dynamics of the mechanical constraints. To be specific, the control effort is measured as the entropy difference between the input space, i.e., the joint space, and the output space, i.e., the task space.

In addition to measuring the control effort imposed by mechanical constraint, the entropy can also measure the probabilistic distribution of end-effector, i.e., the probabilistic reachability in the workspace. Given a joint space with uniform distribution, the robotic manipulator with different degrees of redundancy will generate task space with different probabilistic distribution of the end-effector position. The preliminary study on the task space entropy intend to demonstrate the phenomenon.

10.4.1 Problem setup

The problem is setup for planar manipulators with different degrees of kinematical redundancy. To maintain the range of workspace, the total link length of the redundant manipulator is unified, i.e., $\sum L_i = 1$. For simplification, each of the planar manipulator has equal link length. Take the three link manipulator as example, the geometry of the manipulator is defined as:

$$\begin{aligned} L_1 + L_2 + L_3 &= 1 \\ L_1 = L_2 = L_3 \end{aligned} \tag{10.167}$$

The probabilistic distribution in joint space is uniform. In a simulation experiment, a set of joint angles, i.e., a manipulator configuration, are randomly pick up and end-effector position is generated by the planar manipulator accordingly. Given a end-effector position (x, y) , the number of manipulator configurations that generate the this end-effector position is denoted as N_{xy} , and the total number of manipulator configurations generated by all the simulation experiments is denoted as N . Therefore, the probability that the manipulator reach the position (x, y) , i.e., the probabilistic reachability of position (x, y) is:

$$P(x, y) = \frac{N_{xy}}{N} \tag{10.168}$$

The entropy of the task space can be computed as:

$$H = \sum P(x, y) \ln[P(x, y)] \tag{10.169}$$

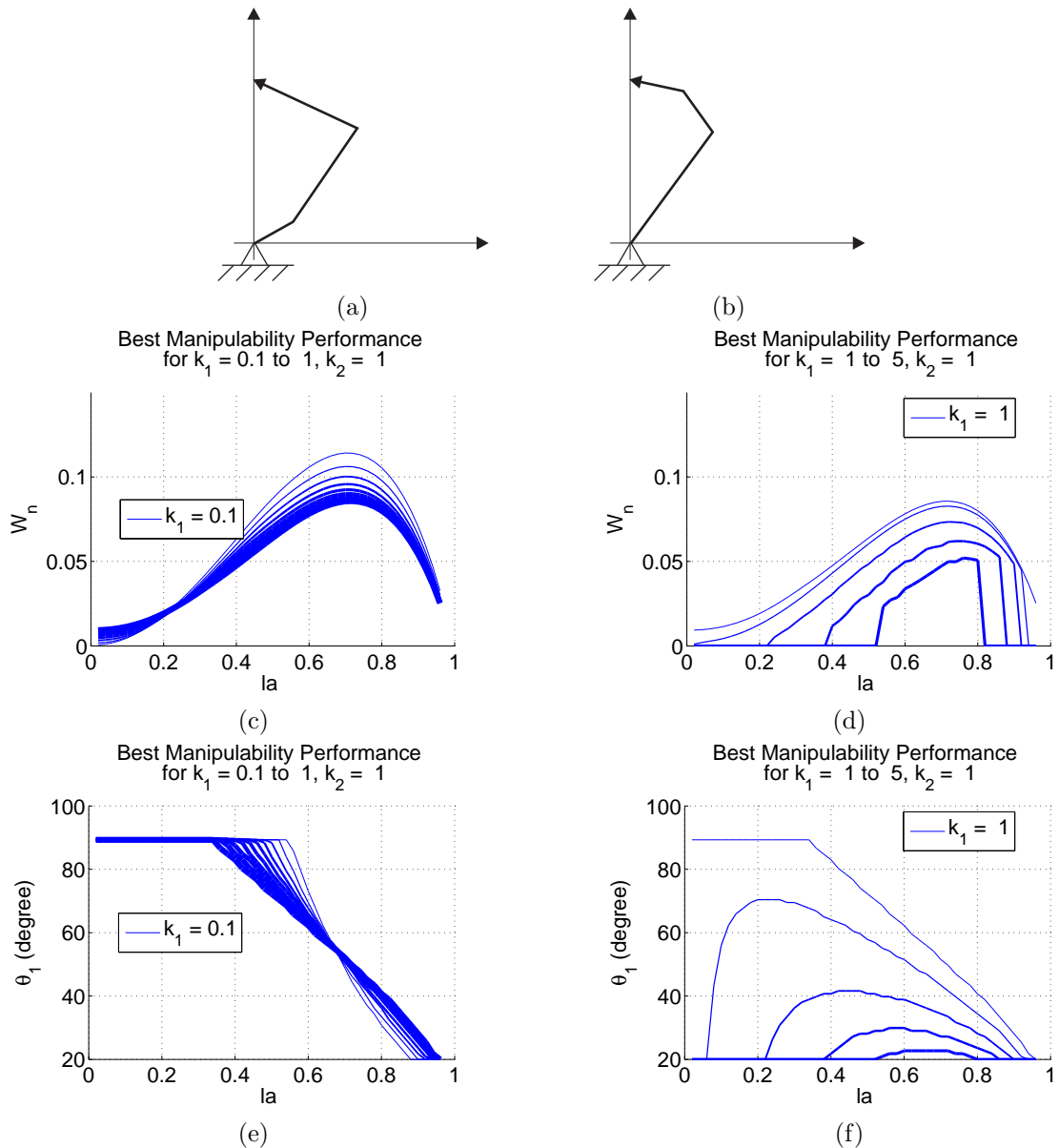


Figure 10.31: Best Manipulability Performance (measured by w_n) for Different $0.1 \leq k_1 \leq 5$ and $k_2 = 1$.

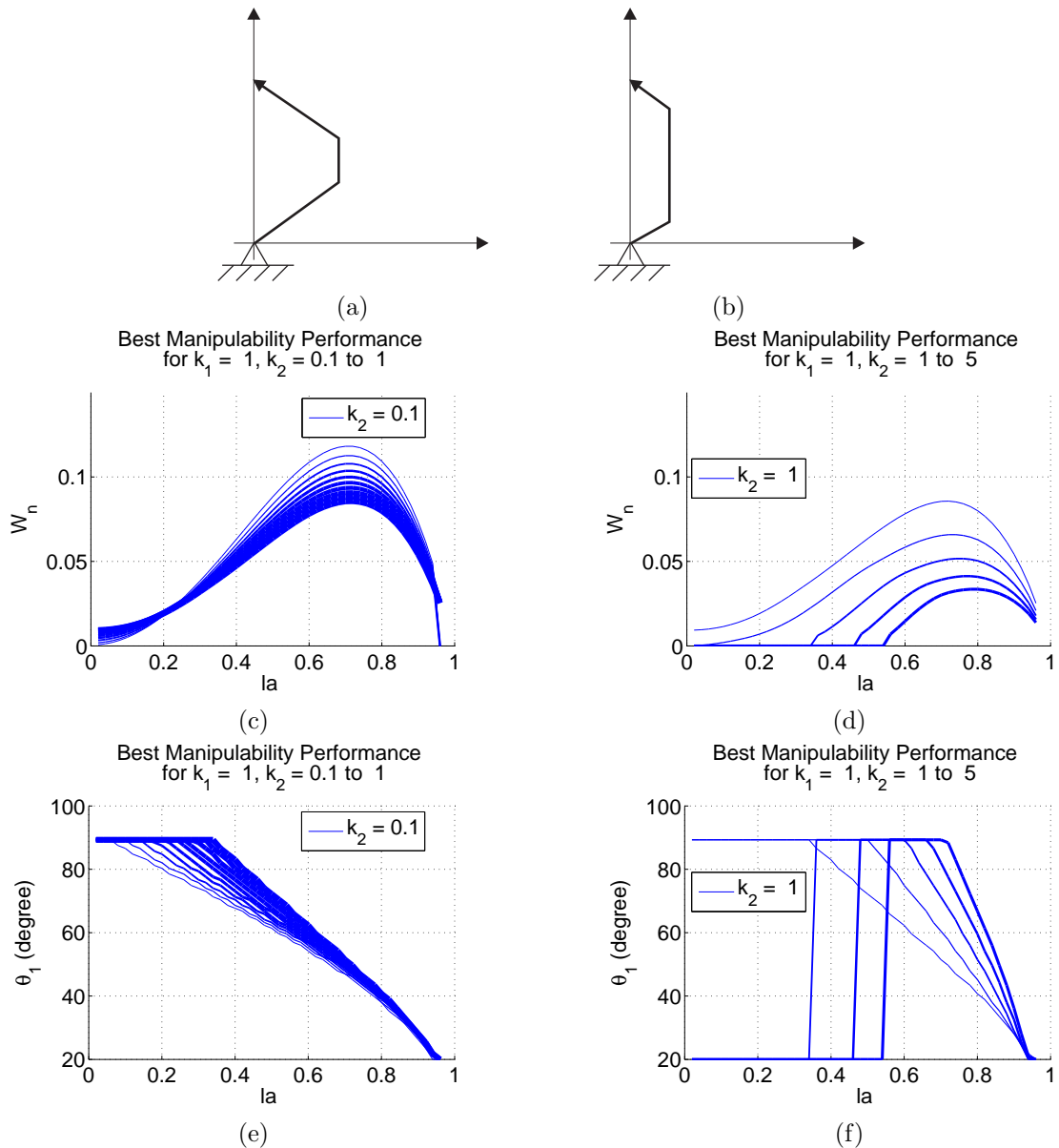


Figure 10.32: Best Manipulability Performance (measured by w_n) for Different $k_1 = 1$ and $0.1 \leq k_2 \leq 5$.

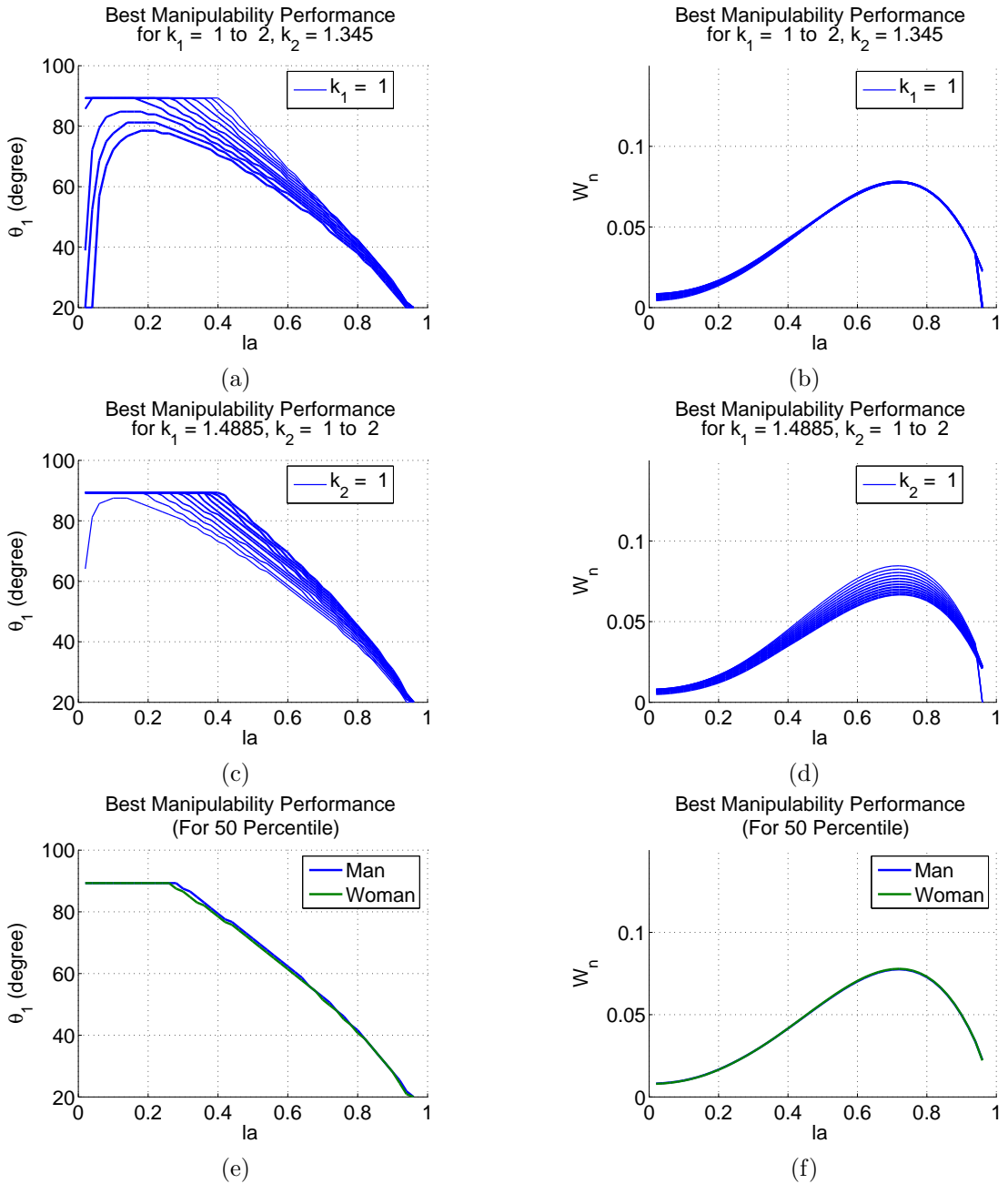


Figure 10.33: Best Manipulability Performance (measured by w_n) for Different k_1 and k_2 around the Measurements of Human Arms (50 percentile).

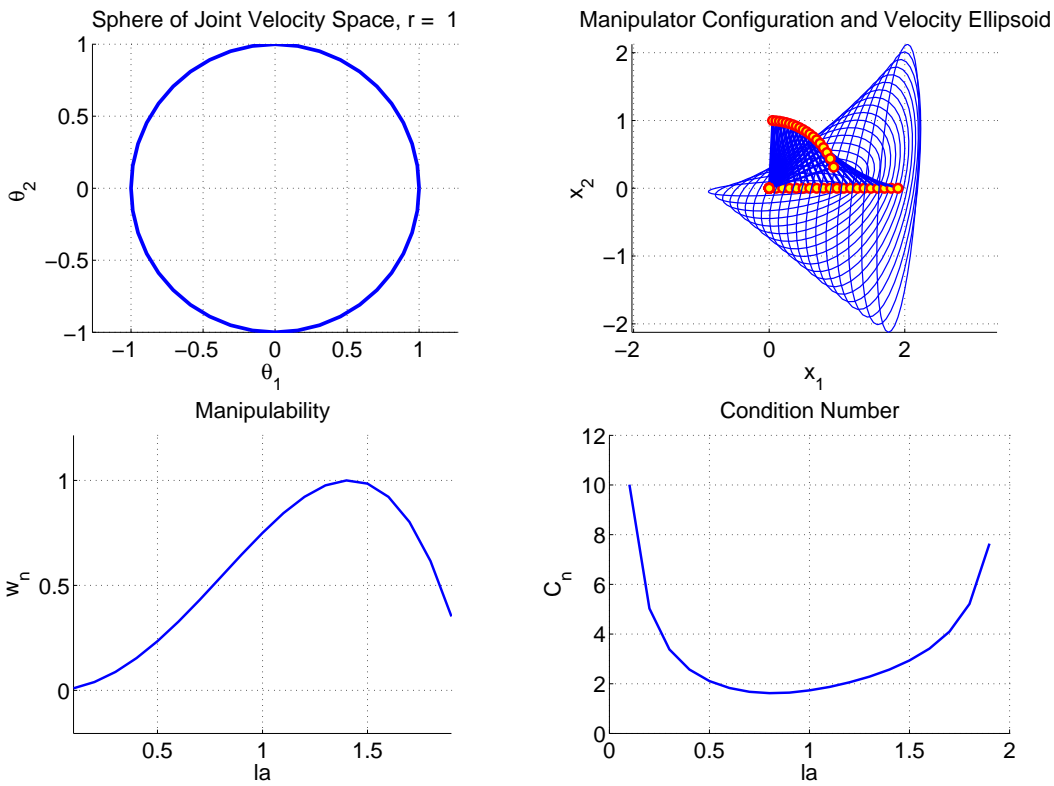


Figure 10.34: For a two-link Manipulator, generated from unit sphere $\dot{\theta}^T \dot{\theta} = 1$.

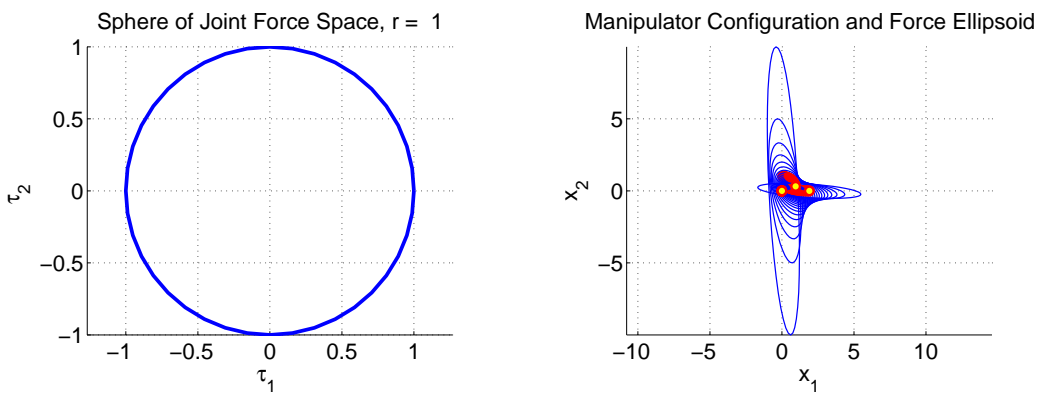


Figure 10.35: For a two-link Manipulator, generated from unit sphere $\tau^T \tau = 1$.

10.4.2 Simulation results

Simulation experiments are conducted for planar manipulator with different degrees of redundancy, shown in Fig. 10.36 to Fig. 10.41. The simulation results shows that as mechanical constraints, the manipulators with different degrees of redundancy impose different control effort. Given the joint space with uniform distribution, the manipulator that cover the same range of workspace requires demonstrates different probabilistic reachability. Without extra control effort in joint space, the manipulator tends to reach the task space points with higher probabilistic reachability. Note that in all the simulation experiments, the center of the workspace always have relatively higher probabilistic reachability, which implies that the center of the workspace is assigned with inherent importance in the geometric design of the manipulator. Considering the fact that the planar manipulator intends to model human arms by simplification, the center of the workspace at which the head resides is assigned with inherent importance by the morphology of human arms.

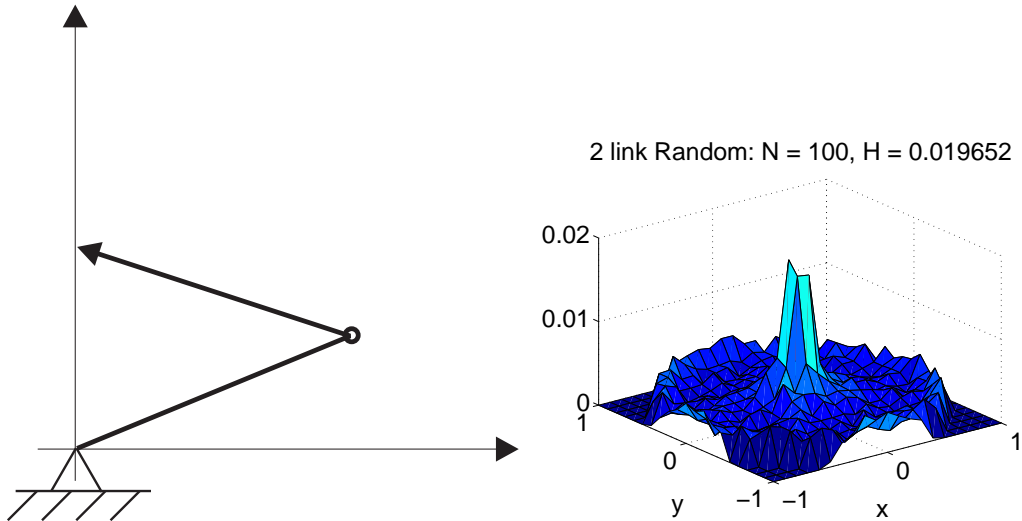


Figure 10.36: Relevant research.

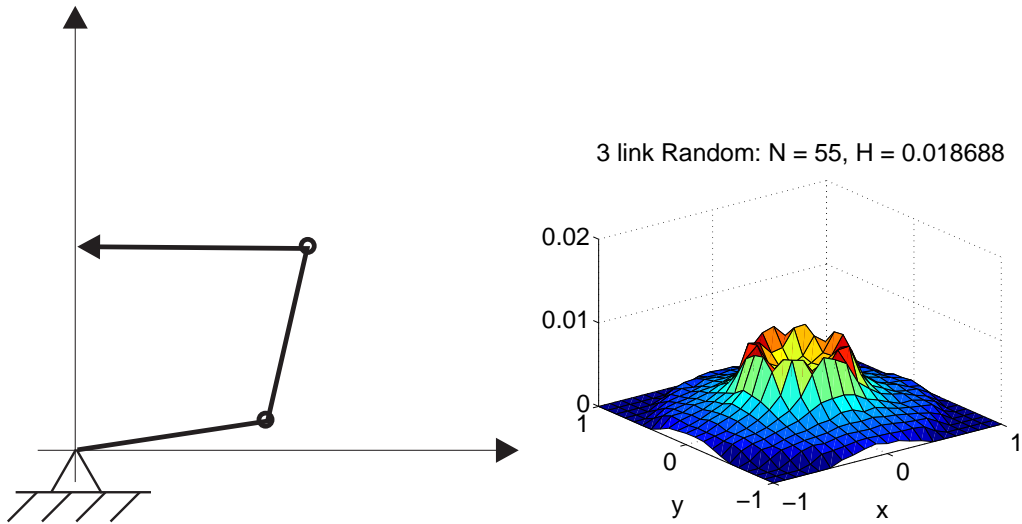


Figure 10.37: Relevant research.

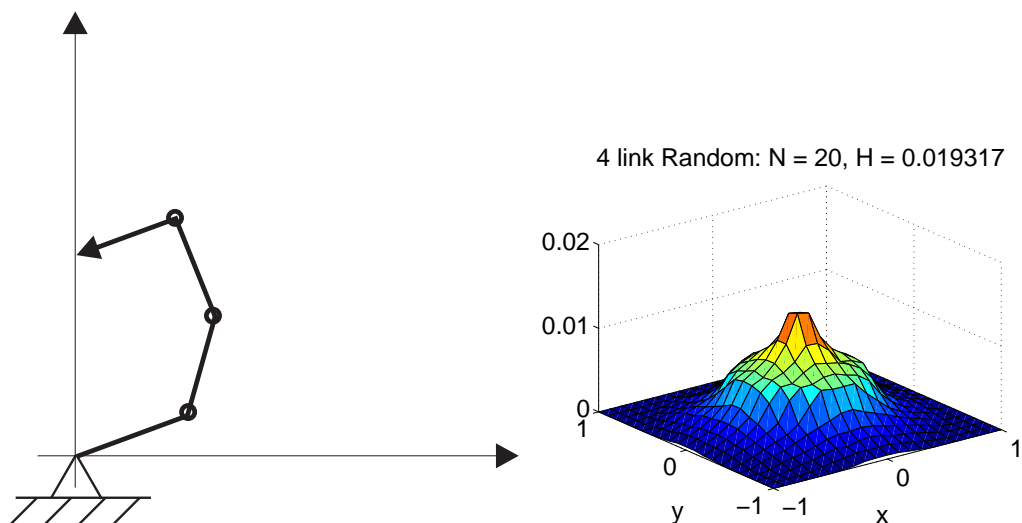


Figure 10.38: Relevant research.

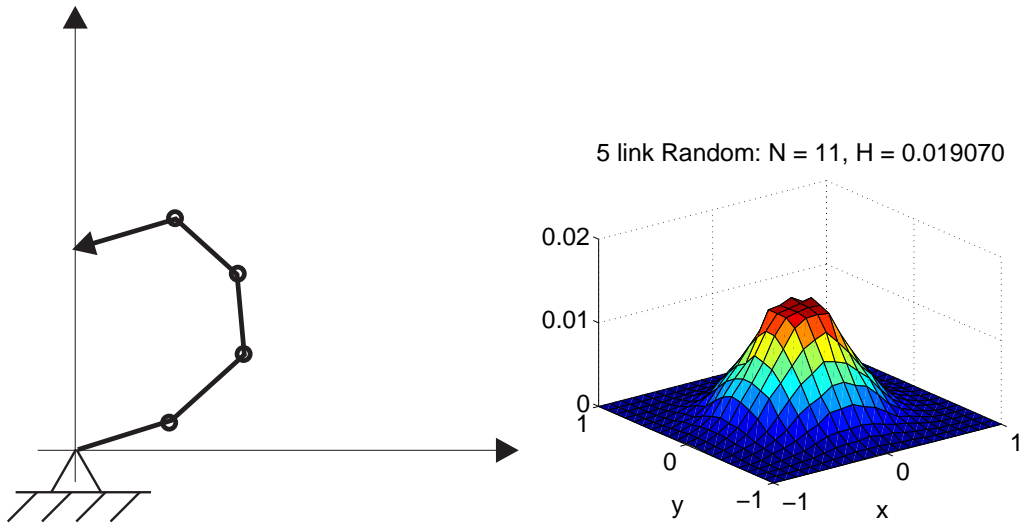


Figure 10.39: Relevant research.

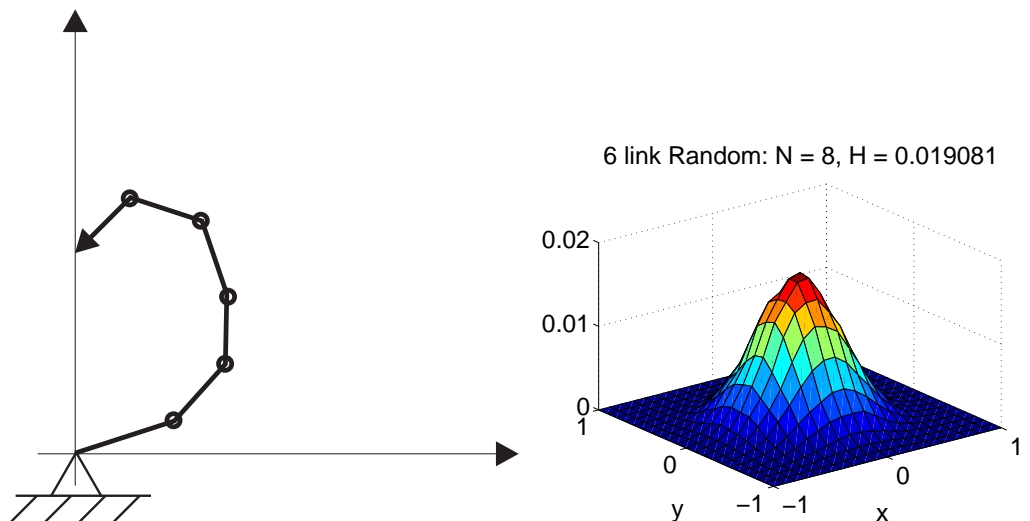


Figure 10.40: Relevant research.

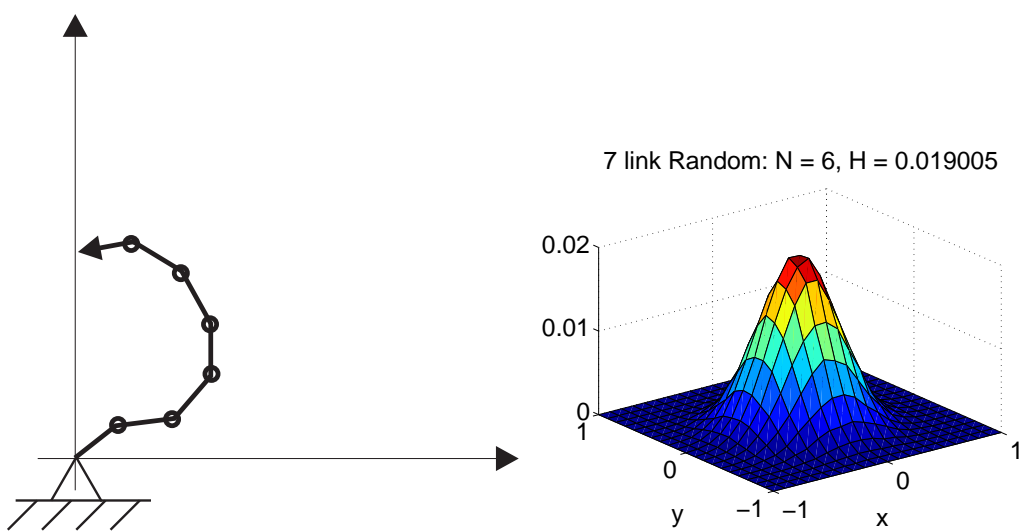


Figure 10.41: Relevant research.

Chapter 11

Appendix IV: Design Optimization of a Multi-Arms Surgical Robotic System for Manipulation Dexterity

The aim of this research is to optimize the geometry of four robotics arms and their relative position and orientation of their bases using a cost function that takes into account: (1) the size and the shape of the common workspace of all the arms (2) the mechanism isotropy (3) the mechanism stiffness. Given the generic nature of the surgical robotic configuration utilizing minimally invasive surgical (MIS) technique with tools with the same length as manual tools the optimization is not targeting a specific internal organ or anatomical structure but based on measurements conducted with patients and animal model for assessing the maximal reachable workspace as well as the operational workspace. Since the reposted study was conducted prior to the detailed design was completed. The results of the optimization process affected design parameters and therefore the mechanism design itself.

11.1 Introduction

Surgical procedures are traditionally performed by two or more surgeons along with staff nurses. One surgeon serves as the primary surgeon and the other serves as his/her assistant. Surgical robotics have redefined the dynamics in which the two surgeons interact with each other and with the surgical site. Raven IV is a new generation of the surgical robot system having four articulated robotic arms with a

spherical configuration, each holding an articulated surgical tool. The system allows two surgeons to tele-operate the Raven IV collaboratively from two remote sites. The current research effort aims to configure the link architecture of each robotic arm, along with the position and orientation of the four bases which dictates the port placement and configuration with respect to the patient body, a total of seven different parameters which led to 2.3×10^{10} system configurations, in order to optimize the common workspace reachable by all four robotic arms. Each parameter was studied individually and a brute force approach was used to optimize the cost function across the entire set of parameters. The simulation results indicate that tilting the base of the robotic arms in the range of -20 to 20 deg while moving the ports closer together up to 50 mm apart leads to a preferred circular shape of the common workspace with an isotropy value of 0.5. A carefully configured system with multiple surgical robotic arms will enhance the interactive performance of the two surgeons. The four arms surgical robotic setting regains access of two surgeons into the surgical sites a configuration which enables collaborative surgery between two surgeons or a surgeon and an artificial agent.

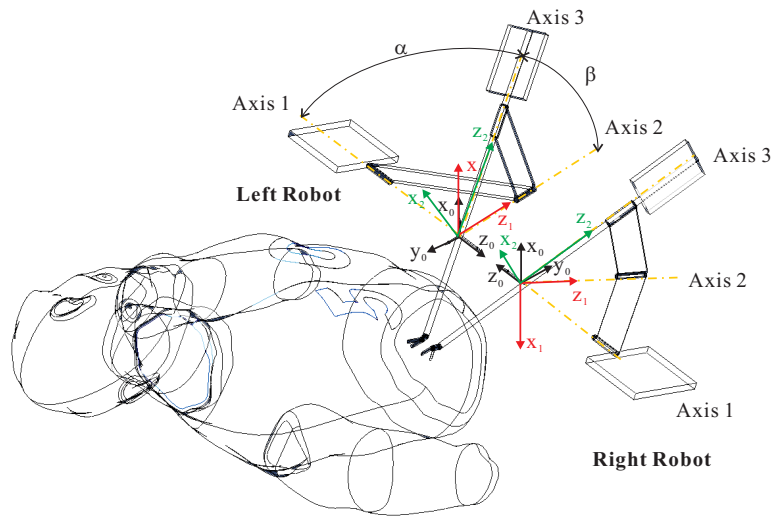
11.2 Methodology

The methodology of optimizing the design of the Raven IV mechanism is primary base kinematics parameters. This section defines the direct and inverse kinematics, The Jacobian matrix, as well as the cost function. The cost function for the optimizing the size and shape of the common workspace shared by four Raven arms was composed from link lengths, ports spacing, bases orientation, and isotropy.

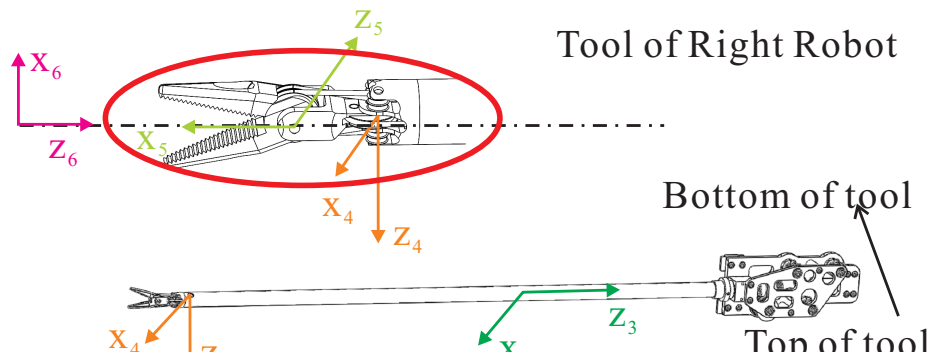
11.2.1 Direct Kinematics of the Raven IV Arms

The Raven IV surgical robot system consists of two pairs of surgical robotic arms. The pairs are mirror images of each other, which results in symmetric kinematics. Each arm has seven degrees of freedom (DOFs): six DOFs for positioning and orienting the end-effector and one for opening and closing the end-effector.

The base frame is located at the converging center of the spherical mechanism formed by the first three links of a Raven IV arm (Fig. 11.1a). The Denavit-Hartenberg (DH) Parameters (Table 11.1) are derived in the standard method defined by [212].



(a) Robot arm.



(b) Surgical tool.

Figure 11.1: Reference Frame of the Raven IV surgical robot system.

The direct kinematics can be derived from Table 11.1, for the left and right arms respectively. Note that $\sin \theta_i$ is denoted as s_i , $\cos \theta_i$ is denoted as c_i , $\sin \alpha_i$ is denoted as $s\alpha_i$, $\cos \alpha_i$ is denoted as $c\alpha_i$.

Table 11.1: Denavit-Hartenberg Parameters for Raven IV Arms (standard method).

Robot	$i - 1$	i	α_i	a_i	d_i	θ_i
Left Robot (1,3)	0	1	$\pi - \alpha$	0	0	$\theta_1(t)$
	1	2	$-\beta$	0	0	$-\theta_2(t)$
	2	3	0	0	0	$\pi/2 - \theta_3(t)$
	3	4	$-\pi/2$	0	$d_4(t)$	0
	4	5	$\pi/2$	a_5	0	$\pi/2 - \theta_5$
	5	6	$-\pi/2$	0	0	$\pi/2 + \theta_6$
Right Robot (2,4)	0	1	$\pi - \alpha$	0	0	$\pi - \theta_1(t)$
	1	2	$-\beta$	0	0	$\theta_2(t)$
	2	3	0	0	0	$\pi/2 + \pi + \theta_3(t)$
	3	4	$-\pi/2$	0	$d_4(t)$	0
	4	5	$-\pi/2$	a_5	0	$\pi/2 + \theta_5$
	5	6	$-\pi/2$	0	0	$\pi/2 - \theta_6$
Range	$\theta_1 \in [0^\circ, 90^\circ]$			$\theta_2 \in [20^\circ, 140^\circ]$		
	$\theta_3 \in [-86^\circ, 86^\circ]$			$d_4 \in [0, 250]$ mm		
	$\theta_5 \in [-86^\circ, 86^\circ]$			$\theta_6 \in [-86^\circ, 86^\circ]$		

The direct kinematics is defined as the position and the orientation of the end-effector with respect to the base frame given the joint angles:

$${}^0T = {}^0_1 T \cdot {}^1_2 T \cdot {}^2_3 T \cdot {}^3_4 T \cdot {}^4_5 T \cdot {}^5_6 T = \begin{bmatrix} r_{11} & r_{12} & r_{13} & P_x \\ r_{21} & r_{22} & r_{23} & P_y \\ r_{31} & r_{32} & r_{33} & P_z \\ 0 & 0 & 0 & 1 \end{bmatrix} \quad (11.1)$$

11.2.2 Inverse Kinematics of the Raven IV Arms

Given the position and orientation of the end-effector of a Raven IV arm, the six DOFs for positioning and orienting the end-effector can be determined by resolving the inverse kinematics analytically. In spite the seven DOF of each arm which will render it as a redundant mechanism with infinite solutions for the inverse kinematics, The two jaws of the tools effector that can move independently and form the second wrist as well as the grasping function were reduced to a single DOF defining the virtual

line between the two jaws at the center line of the grasper. With this approach the system as a whole was reduced mathematically to a six DOF system with a close form inverse kinematics solution. Physical joint limits defined by Table 11.1 were added to the analytical description to ensure the practical reachability of the arm to a specific point in space. Eq. (11.1) describes the homogeneous transformation of the Raven IV arm kinematics.

Hence, ${}_0^6T$ can be determined as the inverse of ${}_6^0T$ such that

$${}_0^6T = \begin{bmatrix} r'_{11} & r'_{12} & r'_{13} & P_{xinv} \\ r'_{21} & r'_{22} & r'_{23} & P_{yinv} \\ r'_{31} & r'_{32} & r'_{33} & P_{zinv} \\ 0 & 0 & 0 & 1 \end{bmatrix} \quad (11.2)$$

where for the left Robot,

$$\begin{aligned} P_{xinv} &= (-d_4c_5 + a_5)c_6 \\ P_{yinv} &= s_5d_4 \\ P_{zinv} &= (-d_4c_5 + a_5)s_6 \end{aligned} \quad (11.3)$$

and for the right robot,

$$\begin{aligned} P_{xinv} &= (d_4c_5 - a_5)c_6 \\ P_{yinv} &= s_5d_4 \\ P_{zinv} &= (-d_4c_5 + a_5)s_6 \end{aligned} \quad (11.4)$$

Let us define P_{inv} as:

$$\begin{aligned}
 P_{\text{inv}}^2 &= (P_{x\text{inv}}^2 + P_{y\text{inv}}^2 + P_{z\text{inv}}^2) \\
 &= (d_4 c_5 - a_5)^2 c_6^2 + s_5^2 d_4^2 + (-d_4 c_5 + a_5)^2 s_6^2 \\
 &= (a_5 - d_4 c_5)^2 + s_5^2 d_4^2 \\
 &= a_5^2 - 2a_5 d_4 c_5 + d_4^2 c_5^2 + s_5^2 d_4^2 \\
 &= a_5^2 - 2a_5 d_4 c_5 + d_4^2
 \end{aligned} \tag{11.5}$$

which gives:

$$c_5^2 = \left(\frac{a_5^2 + d_4^2 - P_{\text{inv}}^2}{2a_5 d_4} \right)^2 \tag{11.6}$$

Note that both (11.3) and (11.4) lead to

$$c_5^2 = 1 - s_5^2 = 1 - (P_{y\text{inv}}/d_4)^2 \tag{11.7}$$

Hence,

$$1 - \left(\frac{P_{y\text{inv}}}{d_4} \right)^2 = \left(\frac{a_5^2 + d_4^2 - P_{\text{inv}}^2}{2a_5 d_4} \right)^2 \tag{11.8}$$

Eq. (11.8) satisfies both the left robot and the right robot and therefore leads to four possible solutions to d_4 as:

$$d_{41} = \sqrt{a_5^2 + P_{\text{inv}}^2 + 2a_5 \sqrt{(P_{\text{inv}}^2 - P_{y\text{inv}}^2)}} \tag{11.9}$$

$$d_{42} = -\sqrt{a_5^2 + P_{\text{inv}}^2 + 2a_5 \sqrt{(P_{\text{inv}}^2 - P_{y\text{inv}}^2)}} \tag{11.10}$$

$$d_{43} = \sqrt{a_5^2 + P_{\text{inv}}^2 - 2a_5 \sqrt{(P_{\text{inv}}^2 - P_{y\text{inv}}^2)}} \tag{11.11}$$

$$d_{44} = -\sqrt{a_5^2 + P_{\text{inv}}^2 - 2a_5 \sqrt{(P_{\text{inv}}^2 - P_{y\text{inv}}^2)}} \tag{11.12}$$

out of which only (11.12) is acceptable for both the left and right arm given the constraints in Table 11.1.

θ_6 can be resolved as:

$$s_6 = P_{\text{zinv}} / (-d_4 c_5 + a_5) \quad (11.13)$$

for the left robot,

$$c_6 = P_{\text{xinv}} / (-d_4 c_5 + a_5) \quad (11.14)$$

and for the right robot,

$$c_6 = -P_{\text{xinv}} / (-d_4 c_5 + a_5) \quad (11.15)$$

$$\theta_6 = \text{Atan2}(s_6, c_6) \quad (11.16)$$

θ_5 can be resolved as:

$$s_5 = P_{\text{yinv}} / d_4 \quad (11.17)$$

$$c_5 = \sqrt{1 - s_5^2} \quad (11.18)$$

$$\theta_5 = \text{Atan2}(s_5, c_5) \quad (11.19)$$

Given the solution of d_4 , θ_5 and θ_6 , we can compute

$$\begin{aligned} {}_3^0T &= {}_1^0T \cdot {}_2^1T \cdot {}_3^2T = {}_6^0T \cdot [{}_4^3T \cdot {}_5^4T \cdot {}_6^5T]^{-1} \\ &= \begin{bmatrix} a_{11} & a_{12} & a_{13} & a_x \\ a_{21} & a_{22} & a_{23} & a_y \\ a_{31} & a_{32} & a_{33} & a_z \\ 0 & 0 & 0 & 1 \end{bmatrix} \end{aligned} \quad (11.20)$$

where

$$a_{32} = s_2 s_\alpha c_3 + (c_2 s_\alpha c_\beta + c_\alpha s_\beta) s_3 \quad (11.21)$$

$$a_{33} = c_2 s_\alpha s_\beta - c_\alpha c_\beta \quad (11.22)$$

θ_2 can be resolved as:

$$c_2 = \frac{c_\alpha c_\beta + a_{33}}{s_\alpha s_\beta} \quad (11.23)$$

$$s_2 = \sqrt{1 - c_2^2} \quad (11.24)$$

$$\theta_2 = \text{Atan2}(s_2, c_2) \quad (11.25)$$

Let us define $a = s_2 s_\alpha$ and $b = c_2 s_\alpha c_\beta + c_\alpha s_\beta$. Eq. (11.21) becomes

$$a_{32} = ac_3 + bs_3 \quad (11.26)$$

and a , b and a_{32} are known. Eq. (11.26) can be solved with the tangent-of-the-half-angle substitutions (see Section 4.5 of [?]):

$$\theta_3 = 2 \text{Atan} \left(\frac{b \pm \sqrt{a^2 + b^2 - a_{32}^2}}{a + a_{32}} \right) \quad (11.27)$$

Eq. (11.26) can also be solved as (see C.10 of [?]):

$$\theta_3 = \text{Atan2}(b, a) \pm \text{Atan2}(\sqrt{a^2 + b^2 - a_{32}^2}, a_{32}) \quad (11.28)$$

Note that solutions only exist when $a^2 + b^2 - a_{32}^2 \geq 0$. Additionally, (11.27) requires $a + a_{32} \neq 0$; (11.28) requires $a_{32} \neq 0$ and $a \neq 0$.

An algorithm to check a_{13} ((11.29) and (11.30)) in (11.20) can be used to choose between the two possible solutions of θ_3 .

For the left robot,

$$a_{13} = -s_2 s_\alpha s_3 + c_2 s_\alpha c_3 c_\beta + c_\alpha c_3 s_\beta \quad (11.29)$$

For the right robot,

$$a_{13} = s_2 s_\alpha s_3 - c_2 s_\alpha c_3 c_\beta - c_\alpha c_3 s_\beta \quad (11.30)$$

Given the solution for θ_2 and θ_3 , θ_1 can be determined by:

$$\begin{aligned} {}_1^0 T &= {}_6^0 T \cdot [{}^3_4 T \cdot {}^4_5 T \cdot {}^5_6 T]^{-1} [{}^1_2 T \cdot {}^2_3 T]^{-1} \\ &= \begin{bmatrix} b_{11} & b_{12} & b_{13} & b_x \\ b_{21} & b_{22} & b_{23} & b_y \\ b_{31} & b_{32} & b_{33} & b_z \\ 0 & 0 & 0 & 1 \end{bmatrix} \end{aligned} \quad (11.31)$$

with $s_1 = b_{11}$, $c_1 = b_{21}$ for the left robot, $s_1 = b_{11}$, $c_1 = b_{21}$ for the right robot and

$$\theta_1 = \text{Atan2}(s_1, c_1) \quad (11.32)$$

11.2.3 The Common Workspace and the Reference Plane

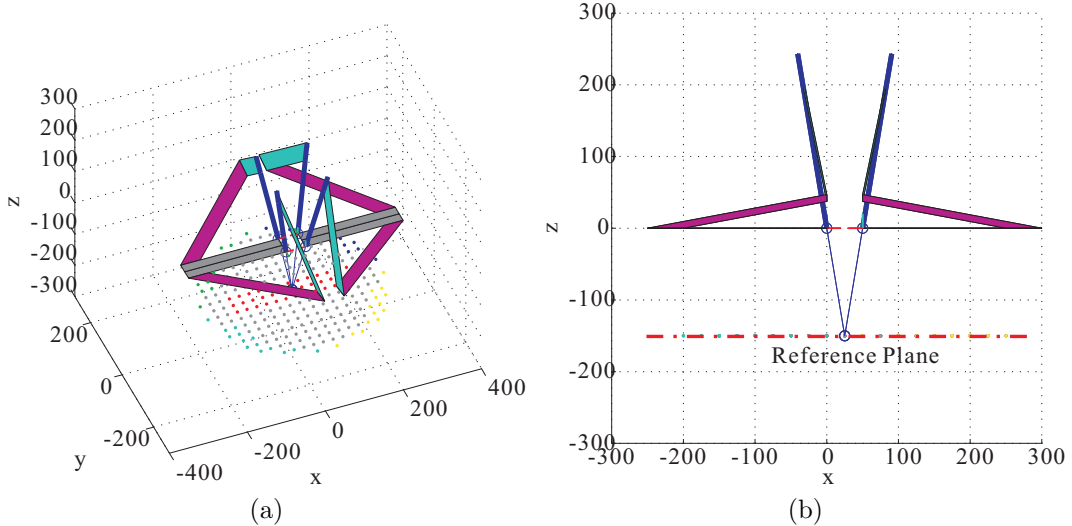


Figure 11.2: The common workspace projected onto the reference plane: (a) 3D view; (b) projection onto x-z plane. For each Raven IV arm, the gray bar represents its base. The magenta and the cyan bars represent the first and second link respectively.

The common workspace is a subset of each arm's workspace that is overlaps with

the workspaces of all the other three arms. As such it is the operational workspace shared by all four arms. The four Raven arms are arranged with respect to each other as depicted schematically in Fig. 11.2. The gray bars represents the bases of the arms while the magenta and the cyan bars represents the first and second links of each arm respectively. The four Raven IV arms can reach a common volume in a 3D space. For the purpose of optimizing the system, a reference 2D plane was defined inside the patient 150 mm below the plane which includes the ports of the four arms. This plane is a typical operational plan in which the tools are inserted half way into the patient.

11.2.4 Area-Circumference Ratio

Maximizing the common workspace is not the only consideration since the shape of the workspace plays an important role in how it can be functionally used. The optimized common workspace is expected to have the largest circular area possible as opposed to an elliptical area. Mathematically, the area and shape of the common workspace can be collectively evaluated by the ratio between the area and its circumference ς , which is defined as

$$\varsigma = \frac{\text{Area}}{\text{Circumference}} \quad (11.33)$$

According to the **isoperimetric inequality**, a circle has the largest possible area among all the shapes with the same circumference. The Area-Circumference ratio of a circle ς_c is proportional to its radius r :

$$\varsigma_c = \frac{\pi r^2}{2\pi r} = \frac{r}{2} \quad (11.34)$$

Practically, the common workspace has an amorphic shape that can not be expressed analytically. However, maximizing ς , i.e. $\max(\varsigma)$, will result in the common workspace that is as close as possible to a circle.

Fig. 11.3 presents two common workspaces of two Raven arms resulting from different link lengths. The common workspace depicted in Fig. 11.3b (with $\varsigma = 4.48$) is preferable compared to the workspace illustrated in Fig. 11.3a.

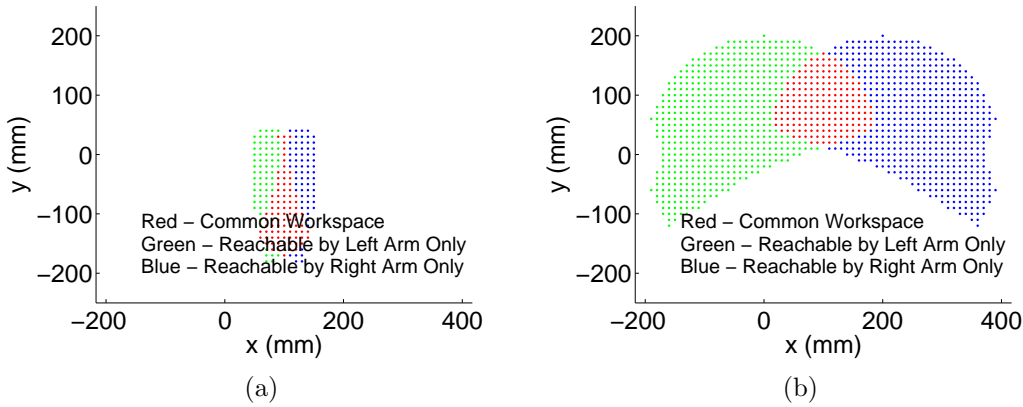


Figure 11.3: Example of two typical common workspaces of two Raven arms constructed from two different link lengths defined by α and β : (a) Two arm configuration defined by links length $\alpha = 65^\circ$, and $\beta = 15^\circ$, resulted with $\varsigma = 2.23$; (b) Two arm configuration defined by links length $\alpha = 65^\circ$, $\beta = 80^\circ$, resulted with $\varsigma = 4.48$.

11.2.5 Mechanism Isotropy

Isotropy is a kinematic performance measure with values in the range of [0, 1] where a value of 0 represents singular configuration in which the mechanism lose one or more DOF and is mechanically locked and value of 1 represents the mechanism's ability to move equally in all directions and therefore repeats the best mapping between the joint space and the end effector space. The isotropy is defined based on the Jacobian matrix \mathbf{J} as one over the condition number of the Jacobian matrix.

$$Iso = \frac{1}{\text{Condition number of } \mathbf{J}} \quad (11.35)$$

The Jacobian matrix is derived analytically by using the velocity propagation method in which the angular and the linear velocities are propagated iteratively from frame i to frame $i + 1$ as:

$${}^{i+1}\omega_{i+1} = {}^i_i R^i \omega_i + \dot{\theta}_{i+2} \hat{Z}_{i+1} \quad (11.36)$$

$${}^{i+1}\mathbf{v}_{i+1} = {}^{i+1}R({}^i\omega_i \times {}^iP_{i+1} + {}^i\mathbf{v}_i) + \dot{d}_{i+2}\hat{Z}_{i+1} \quad (11.37)$$

Note that for a prismatic joint, $\dot{\theta}_{i+1} = 0$ in (11.36); for a revolute joint, $\dot{d}_{i+1} = 0$ in (11.37).

The robot is structured such that the first 3 DOF determine the wrist position of the tool in space and the remaining four DOF dictates the orientation of the tool in space. Furthermore since the design of the robotic tool follows the same general geometry of a MIS tool the primary focus of the optimization methodology in terms of maximizing the robotic arm workspace under additional constraints is the geometry of the first two links and the relative positions of the bases of the 4 arms with respect to each other. As a result, the following analytical derivation of the Jacobian includes only the first three DOF (positioning of the wrist) of the arm, i.e., θ_1 , θ_2 and d_4 . Therefore, the DH parameters in Table 11.1 are modified to rule out the non-relevant DOFs: (1) $\theta_3 = 0$; (2) $\alpha_4 = 0$; (3) DH parameters relevant to joint 5 and joint 6 are not considered and therefore are all set to zero.

Using the velocity propagation method for expressing the Jacobian, the angular velocity of the tool's wrist for the left arm is defined as :

$${}^3\mathbf{v}_3 = \begin{bmatrix} c_2 c_\beta s_\alpha \dot{\theta}_1 + s_\beta c_\alpha \dot{\theta}_1 - s_\beta \dot{\theta}_2 \\ s_2 s_\alpha \dot{\theta}_1 \\ c_2 s_\beta s_\alpha \dot{\theta}_1 - c_\beta c_\alpha \dot{\theta}_1 + c_\beta \dot{\theta}_2 \end{bmatrix} \quad (11.38)$$

and for the right arm is defined as :

$${}^3\mathbf{v}_3 = \begin{bmatrix} -c_2 c_\beta s_\alpha \dot{\theta}_1 - s_\beta c_\alpha \dot{\theta}_1 + s_\beta \dot{\theta}_2 \\ s_2 s_\alpha \dot{\theta}_1 \\ c_2 s_\beta s_\alpha \dot{\theta}_1 - c_\beta c_\alpha \dot{\theta}_1 + c_\beta \dot{\theta}_2 \end{bmatrix} \quad (11.39)$$

The linear velocities of the tool's wrist are the same for both the left and the right arms, and expressed as:

$${}^3\mathbf{v}_3 = \begin{bmatrix} 0 \\ 0 \\ \dot{d}_4 \end{bmatrix} \quad (11.40)$$

Therefore, the Jacobian matrix expressed in coordinate system number 3 for the left robot is defined as :

$${}^3\mathbf{J} = \begin{bmatrix} c_2c_\beta s_\alpha + s_\beta c_\alpha & -s_\beta & 0 \\ s_2s_\alpha & 0 & 0 \\ c_2s_\beta s_\alpha - c_\beta c_\alpha & c_\beta & 1 \end{bmatrix} \quad (11.41)$$

and for the right robot is defined as:

$${}^3\mathbf{J} = \begin{bmatrix} -(c_2c_\beta s_\alpha + s_\beta c_\alpha) & s_\beta & 0 \\ s_2s_\alpha & 0 & 0 \\ c_2s_\beta s_\alpha - c_\beta c_\alpha & c_\beta & 1 \end{bmatrix} \quad (11.42)$$

The resulting Jacobian matrix has a unit vector corresponding to the prismatic joint along the z -axis of Frame 4. Therefore, the mechanism isotropy only depends on the 2×2 top left sub-matrix of the Jacobian, denoted as ${}^3\mathbf{J}_s$.

11.2.6 Cost Function

The common workspace is optimized based on a cost function which includes four parameters. The numerator of the cost function include multiplications of parameters that are maximized and the numerator of the cost function includes parameters that are minimize such that the whole cost function are maximized. The four parameters of the cost function are: (1) the Area-Circumference ratio (ς) is maximized given bounded isotropy values; (2) The sum of the isotropy across the entire common workspace ($\sum Iso$) is maximized; (3) the minimum isotropy (Iso_{min}) of the common workspace is maximized; and (4) the sum of the robotic arm first two joint angles cubed ($\alpha^3 + \beta^3$) is minimized. Since the stiffness of a contour lever beam is proportional to the length of the beam's cubed. Shorter link lengths resulted in a stiffer mechanism which in tern reduces end effector position and orientation error due to link deformation. Given the spherical geometry of the mechanism in which its first three axes intersect at a single point defining its remote center, the kinematics of the mechanism is independent of the radius of the sphere. As a result, the link lengths are defined here as angles. The radius of the mechanism was defined later on as part of the design process to provide sufficient space around the entry point of the tool into the body to include the MIS port. With the above considerations, the cost function

of the optimization of the common workspace is defined as:

$$C = \max_{(\alpha, \beta, \phi_x, \phi_y, \phi_z, b_x, b_y)} \left\{ \frac{\varsigma \cdot \sum Iso \cdot Iso_{min}}{\alpha^3 + \beta^3} \right\} \quad (11.43)$$

Where $\sum Iso$ denotes the sum of the actual isotropy of the points in the common workspace, Iso_{min} denotes the minimum isotropy required in the common workspace, and $\alpha^3 + \beta^3$ represents the stiffness of the structure, since the stiffness of the link is inversely proportional to the cubic power of the dimension.

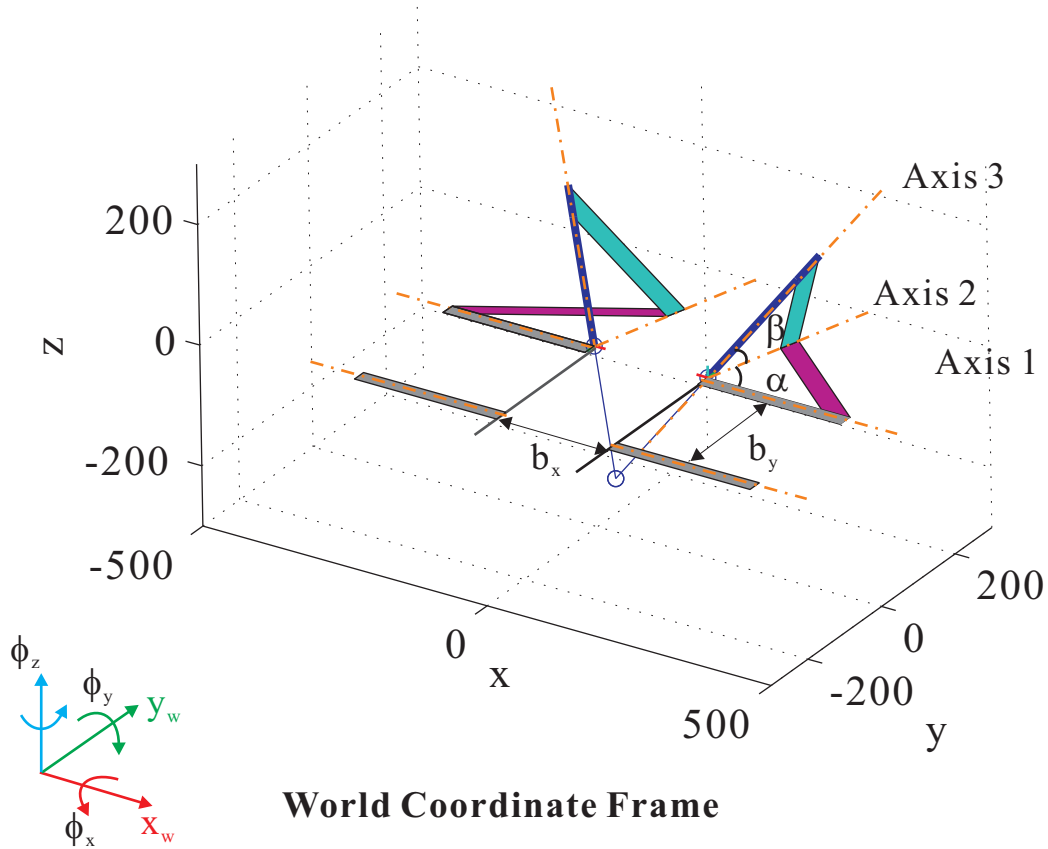


Figure 11.4: Parameters for the optimization of the common workspace.

Eq. (11.43) intends to maximize the cost function by choosing the link length of the first two links α and β , the distance between the ports, the base orientation of the arms, and the minimum isotropy required in the workspace: (1) the α between the Axis 1 and Axis 2, and the β between Axis 2 and Axis 3; (2) the base orientation are about X_w , Y_w and Z_w axes of the world coordinate frame respectively, i.e. ϕ_x ,

ϕ_y and ϕ_z ; and (3) the port spacing b_x and b_y is the horizontal distance between the bases of the Raven IV arms, measured along X_w and Y_w respectively; (4) Iso_{\min} is the minimum isotropy required in the common workspace.

11.3 Results

Following the definition of the combined cost function the effect of each parameter was studied individually showing various trends of the system performance as a function of the changes of its internal parameters. Once each parameter was studied individually the cost function was used to enforce all the constraints simultaneously and a numerical brute force search approach was utilized to study the entire parameters' space for selecting the optimal set of parameters which maximizes the cost function.

11.3.1 Isotropy Performance

Limiting the minimal acceptable value of the isotropy Iso_{\min} has a significant effect on the resulting optimized common workspace. Out of the three time dependent variable θ_1 (shoulder joint angle) θ_2 (elbow joint angle) and d_4 tool shaft displacement the Jacobian matrix is only a function of the elbow joint angle θ_2 as depicted in Fig. 11.6 in which the Isotropy is plotted as a function of θ_1 and θ_2 indicating the dependency of the Isotropy on θ_2 only. If a threshold is set for the minimal value of the Isotropy, as depicted in Fig. 11.5 for values of 0.1, 0.3, 0.5, 0.7, 0.9 (marked by the dashed vertical lines) the range of the values for θ_2 is decreased as the value of isotropy threshold is increased. This relationship is depicted in Fig. 11.5 for a specific link lengths in which $\alpha = 55^\circ$ and $\beta = 60^\circ$ however the same relationship between the θ_2 and the Iso_{\min} holds for any arm configuration with the range of link length under study .

Fig. 11.7 demonstrates the C_{\max} when different Iso_{\min} is required in the common workspace. The cost function is maximized when $Iso_{\min} = 0.5$. The expected benefit will be diminished by both higher and lower minimum isotropy requirement.

11.3.2 Robotic Mechanism Design - Link length

The lengths of the first two links, which are expressed as two angles α and β given the spherical nature of the mechanism, are two out of the seven parameters defining the cost function's set of constraints. Among all the seven parameters these two link

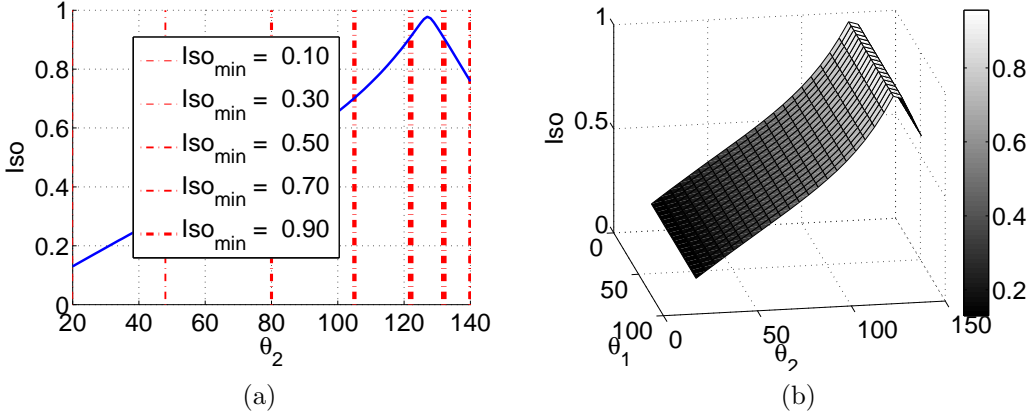


Figure 11.5: Isotropy as a function of the first two joint angles for a specific arm configuration ($\alpha = 55^\circ, \beta = 40^\circ$) (a) Range of θ_2 as it is affected by different Iso_{min} values marked by dashed vertical lines. (b) Isotropy Iso as a function of the time dependent variable θ_1 (shoulder joint angle) θ_2 (elbow joint angle).

lengths are defined during the design process whereas the rest of the parameters can be changed by positioning and originating the bases of the robot with respect to each other as part of setting up the system. If all the constraints are removed, by setting the two link lengths α and β to be 90 deg, the size of the workspace of a single arms is maximized.

Fig. 11.8 depicts the cost function values as a function of the link length α and β plotted with a resolution of 10 degrees in a range of [0,90]. In general, the value of the cost function is increased as the as the length of the links increase. With the introduction of the contains as defined by the cost function, it is maximized when $\alpha = 85^\circ$ and $\beta = 65^\circ$.

the length the demonstrates the effect of structure design, particularly for the link length α and β . According to the simulation results, the cost function is maximized by $\alpha = 85^\circ$ and $\beta = 65^\circ$. White color on the periphery of the plot indicates link lengths pairs that do not meeting the criteria as defined by the cost function.

11.3.3 Robot Base Orientation

The base orientation of each surgical robotic arm is determined by thee angles of the inertial (world) coordinate system i.e. rotation are about X_w , Y_w and Z_w axes by ϕ_x , ϕ_y and ϕ_z ; A mirror image axial symmetry was assumed for the rotations with respect

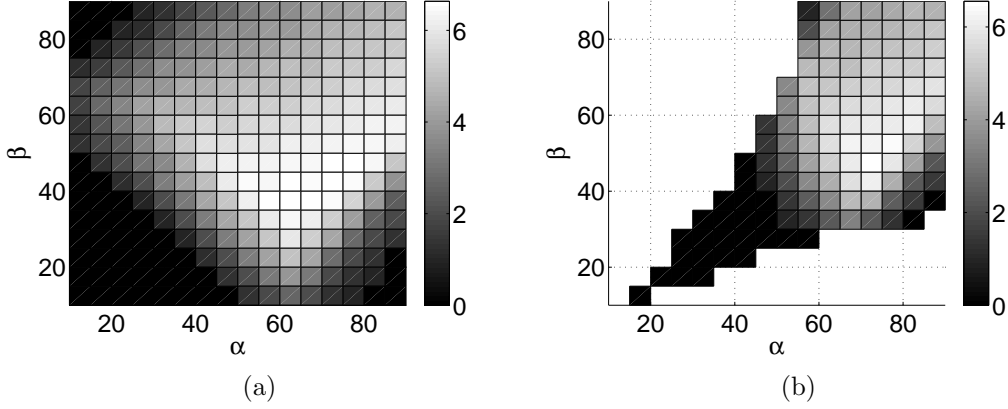


Figure 11.6: Distribution of ξ for different Iso_{min} . (a) For $Iso_{min} = 0$, $\xi_{max} = 6.64$ when $\alpha = 80^\circ$, $\beta = 40^\circ$; (b) For $Iso_{min} = 0.5$, $\xi_{max} = 6.55$ when $\alpha = 70^\circ$, $\beta = 35^\circ$.

to all the axes. The following refers to the top right mechanism (first quadrant in Fig. 11.4).

Fig. 11.9 demonstrates the base orientation effects of individual axes on the cost function value C_{max} in the angle range of $+/- 20$ deg. Only one axis was change at a time while the other two were kept at an angle equal to zero. The cost function value monotonously increases as the base orientation about the y -axis (i.e., ϕ_y) increases but reaches a peak value for $\phi_y = 10$ deg. The cost function is sensitive to changes in the rotating of the base along the x -axis (i.e. ϕ_x) as it is exponentially increases as a function of ϕ_x with a maximal value of $\phi_z = -20$ deg. The cost function value is the least sensitive to rotation along the z -axis (i.e. ϕ_z) as it monotonously decreases as the base angle increases as a function of ϕ_z and have a maximal value of $\phi_z = -20$ deg.

Following the individual effect of based orientation along each axis Fig. 11.10 depicts the cost function values as a function of various combinations of base orientations at three perpendicular planes. Relaying solely on based orientation the best performance is accomplished for base inclination of $\phi_x = 20^\circ$, $\phi_y = 10^\circ$, and $\phi_z = -20^\circ$.

11.3.4 Ports Spacing

Fig. 11.11 demonstrates the effect of port spacing. As the distance between the ports along the x -axis increases the performance criterion C_{max} decreases. However the performance crematoria C_{max} reaches its maximal value as the distance between the

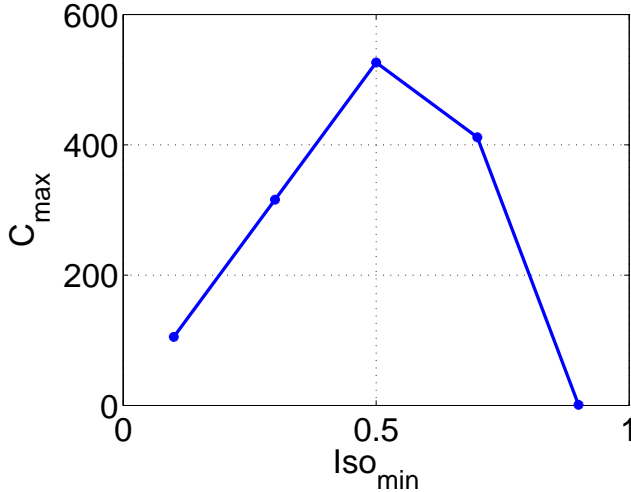


Figure 11.7: Best Performance of C_{\max} for different Iso_{\min} .

ports along the y -axis reaches a value of 100 mm. As a result the expected benefit is maximized by separating the ports location 100 mm along x -axis and 50 mm along y -axis. This result coincides with empirical data of port placement in minimally invasive surgical applications.

11.3.5 Full Optimization

A brute force search across the the bounded parameters with specific resolutions for each parameter was conducted for maximizing the preference criterion C_{\max} base on the previously defined cost function (11.43). A total of 2.304×10^{10} configurations were analyzed. This performance criterion is maximized for a set of seven parameters listed in Table 11.2. These parameters are translated to a specific configuration of the four robotic arms as depicted in Fig. 11.12a. This four arm arrangement led to the largest circular common workspace shared by the four arms as depicted in Fig. 11.12b) with an approximate radius of 150 mm .

Fig. 11.7, Fig. 11.8, Fig. 11.9 and Fig. 11.11 shows the trend of C_{\max} with respect to each optimization parameters. According to Fig. 11.9, the best C_{\max} happens at $\max \phi_x$ and $\min \phi_z$. For every other optimization parameter, best C_{\max} happens in the middle of its value range. To find an even better C_{\max} and its corresponding parameter values, we conduct another brute force search in the neighborhood of the optimal parameter value of α , β , ϕ_y , b_x , b_y and Iso_{\min} with refined resolutions. As

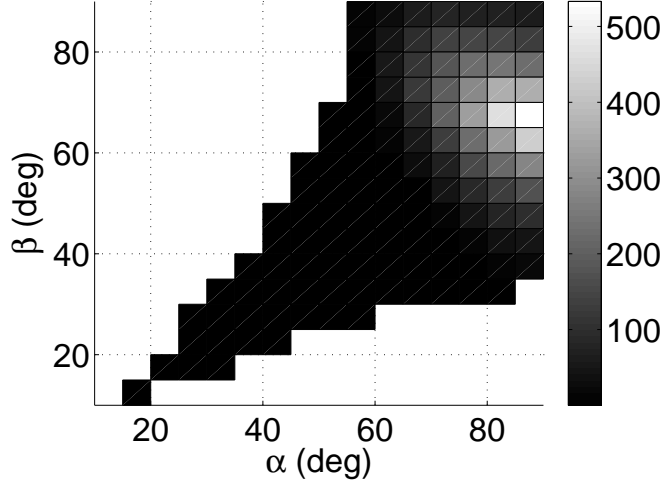


Figure 11.8: The cost function values C_{\max} as a function of the link length α and β plotted with a resolution of 10 degrees in a range of $[0,90]$. The cost function is maximized for $\alpha = 85^\circ$ and $\beta = 65^\circ$.

shown in Table ??, we have $C_{\max} = 533.01$ when $b_x = 90$ mm.

(Table 11.1)

11.4 Conclusion

Providing a group of two surgeons the level of access, manipulability, dexterity of the surgical site as well as the visual views of it via robotic technology requires at least four robotics arms and two stereo cameras rendering the surgical site. The core of this research was to optimize the design of four surgical robotics arms to maximize a shared workspace while maximizing the manipulatable factors, stiffness and minimizing its footprint. Given the generic nature of the surgical robotic system, its design did not target specific anatomical structures or surgical procedure.

The design parameters of the system can be divided into two groups: (i) design parameters that are fixed following the fabrication of the robotic arms i.e. angular link lengths, or (ii) design parameters that can be change at any point during the operation of the system i.e. position and orientations of the individual robotic arms as well as the relationship between them i.e. spacing between the bases as well as the relative orientation with each other and the surgical site.

The cost function for optimizing the design account for geometry kinematics and

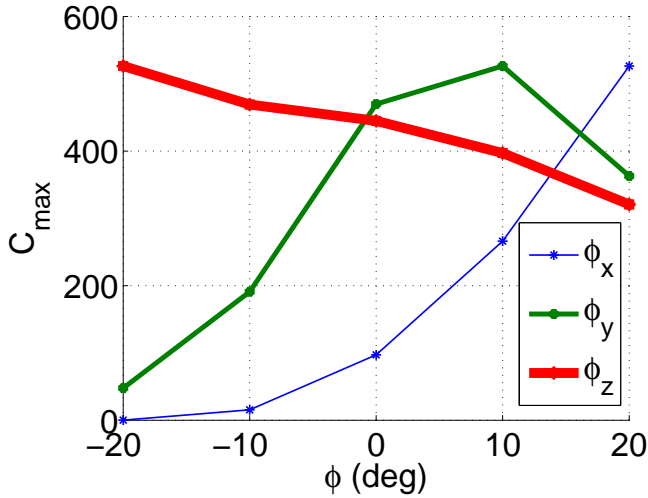


Figure 11.9: Effect of base orientation (ϕ_x , ϕ_y , and ϕ_z).

stiffness parameters. The effect of each parameter was studied individually followed by a brute force search across range of all the parameters. The effect of the individual parameters are as following (1) Isotropy - The analytical derivation of the system shows that the mechanism isotropy performance of a Raven arm depends on a 2×2 sub-matrix of the 3×3 Jacobian matrix for the end-effector positioning (i.e. θ_1 , θ_2 and d_4) once the Jacobian matrix is expressed in coordinate of the tool's shaft. Given the spherical nature of the mechanism the isotropy is a function of the elbow joint only. Its maximal and minimal values are a function of the two link lengths. Bounding the mechanism isotropy ensures high performance of entire system. An increase of the minimal acceptable value of the Isotropy leads to a decrease in the common workspace. However the overall performance criteria is maximized once the minimal isotropy is set to 0.5. (2) Link Lengths - The first two links of the mechanism were optimized. Given the spherical geometry of the mechanism, the link lengths are expressed as angles. The kinematics of the mechanism is independent of the sphere's radius. The radius set to provide sufficient space to encapsulate the MIS port. Setting the angles of the first two links to be 90 Deg each allows to position the end effector at the tip of the tool inserted along the radius anywhere in the sphere. However there are two major disadvantages in setting the link's angular length to these values. First, the longer the link the more flexible the mechanism is. Second, as the link angular length is longer potential collisions between the surgical robotic arms and the body of the patient are more prominent. Optimizing for the mechanism for link angular length

Table 11.2: Parameter Ranges and preferred values for the optimization of the Raven IV surgical robot system.

	Range	Optimal value	Resolution
α	$[5^\circ, 90^\circ]$	85°	20°
β	$[5^\circ, 90^\circ]$	65°	20°
ϕ_x	$[-20^\circ, 20^\circ]$	20°	10°
ϕ_y	$[-20^\circ, 20^\circ]$	10°	10°
ϕ_z	$[-20^\circ, 20^\circ]$	-20°	10°
b_x	$[50, 200]$ (mm)	100 (mm)	50 (mm)
b_y	$[50, 200]$ (mm)	50 (mm)	50 (mm)
Iso_{min}	$[0.1, 0.9]$	0.5	0.2
Result	$C_{max} = 526.3338$ for $Iso_{min} = 0.5$		

shows that as the link length increases the performance criterion improves however the best performance is accomplished when the link lengths are set to $\alpha = 85^\circ$ and $\beta = 65^\circ$. Setting the minimal isotropy to a value of 0.5 eliminates some combinations of link length angles. (3) Base Orientation - The base orientation is dictated by three angles. Among the three axis the cost function is highly sensitive to changes along the two angles which define the plane of the base and less sensitive to changes along the axis which is perpendicular to the base. The optimal solution of the base configuration is result in a configuration forming a shape of an X on the coronal plane, convex shape in the Axial plane, and concave shape in the Sagittal plane. It is interesting to note that the configuration of the bases will be similar to the orientation of the palms of two surgeons interacting with the surgical site while standing on two sides of the operating room table. (4) Port Spacing - Creating the shared workspace with a circular geometry is accomplished by spacing the bases 50 mm along the superior/inferior axis and 100 mm along the left / right axis. Analyzing clinical post placement in MIS indicates similar distances.

A brute force optimization followed the detailed study of the individual parameters. A set of parameters was identified for maximizing the cost function. This set of parameters define the structural geometry of the mechanism and its relative position and origination of the four surgical robotic arms with respect to each other in order to maximize a circular shape common workspace of the four arms. The introduction of multiple robotic arms into the surgical field facilitates several operational modes are

available in which each pair of arms can be under full human control or under semi autonomous mode (supervisory control). This collaboration efforts of at least two surgeons regain the lost of functionality that is lost with the introduction of surgical robotic system into the operating room. Furthermore, the present of multiple robotic arms in the surgical field allows to explore supervisory control of semi autonomous operation. Although the primary focus of the current study is surgical robotic system design, the proposed design methodology can be generalized and applied to a wide spectrum of robotic arms that are aimed to share a common workspace with additional kinematic constrains.

Following the system optimization, detailed design, system fabrication, and system integration the system was initially tested using a collaboration mode. Two surgeons located at at the University of Washington campus in Seattle tele-operated the system collaboratively each controlling a pair of Raven arms while completing Fundamental Laparoscopic skill (FLS) tasks using commercial internet connection. The preliminary results indicates the feasibility of two surgeons to either interact with each other while performing collaborative effort assisting each other to complete the same task or conduct two parallel sub tasks that will eventually merged to complete the over arching task faster.

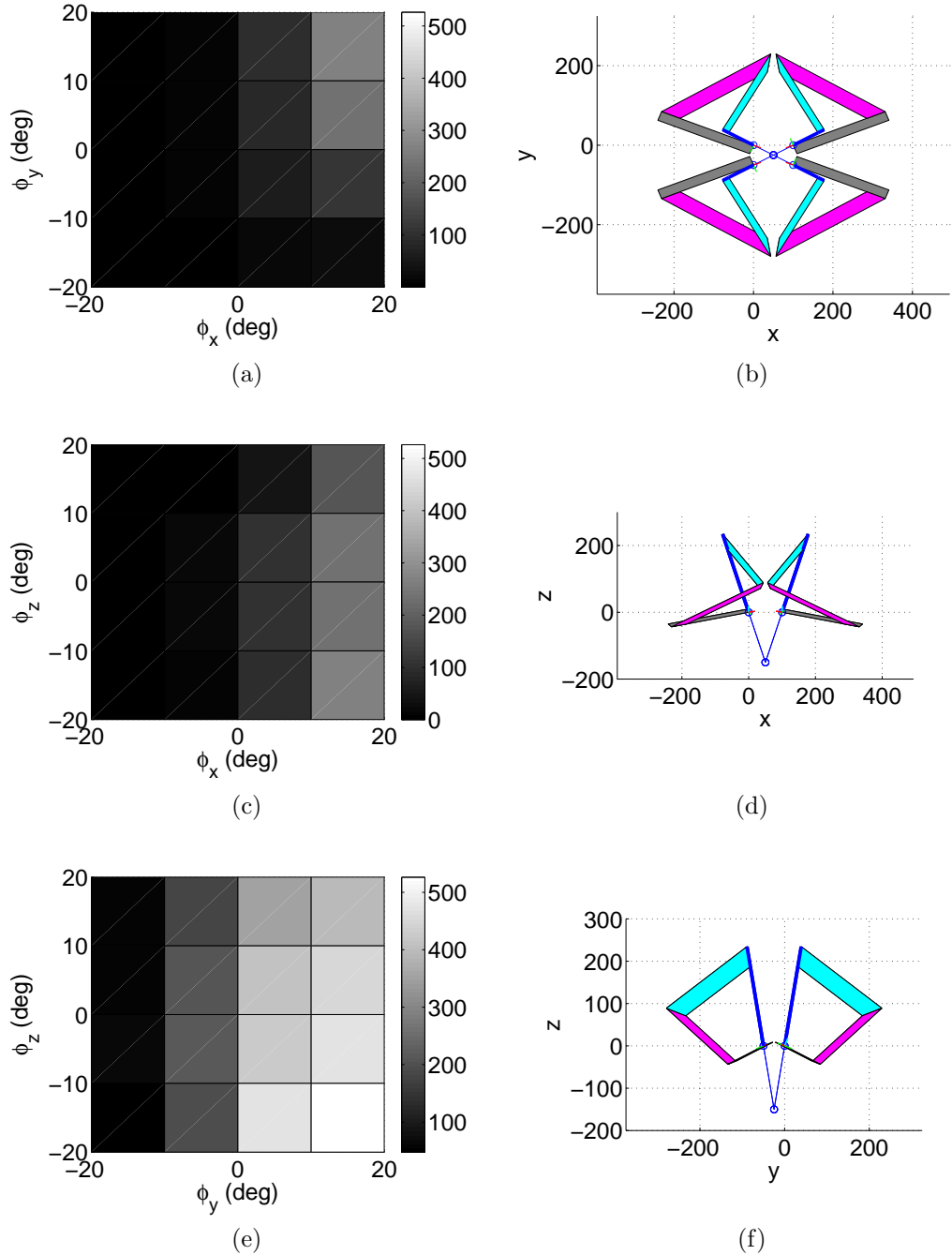


Figure 11.10: Performance criterion C_{\max} is plotted as a function of various base orientation (ϕ_x , ϕ_y , and ϕ_z). In (a), (c) and (e), a color map is depicting the value of Performance criterion C_{\max} in pairs of two coordinates and the corresponding projection of the arms in two planes are depicted in (b) x-y plane, (d) x-z plane and (f) y-z plane of the world coordinate system. The gray bar represents the base of a Raven IV arm.

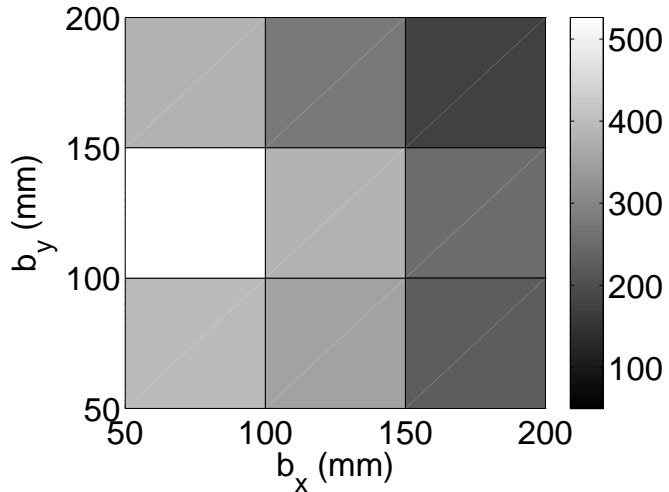


Figure 11.11: Performance criteria C_{\max} as a function of port spacing along two orthogonal directions b_x and b_y .

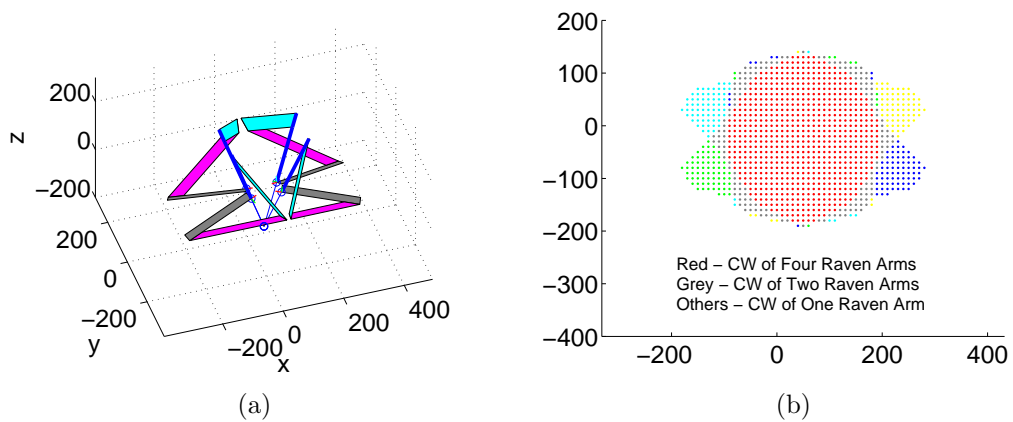


Figure 11.12: Optimal configuration of the Raven IV surgical robot four arms following a brute force search (a) Relative position and orientation of the system bases (b) optimized workspace.

Bibliography

- [1] S. L. Roberts and S. K. Falkenberg, *Biomechanics: Problem Solving for Functional Activity*. St. Louis: Mosby, United States, 1992.
- [2] J. C. Perry, J. Rosen, and S. Burns, “Upper-limb powered exoskeleton design,” *Mechatronics*, vol. 12, no. 4, pp. 408–417, 2007.
- [3] J. C. Perry and J. Rosen, “Design of a 7 degree-of-freedom upper-limb powered exoskeleton,” in *IEEE/RAS-EMBS International Conference on Biomedical Robotics and Biomechatronics*, (Pisa, Italy), Feb 2006.
- [4] L. M. Miller and J. Rosen, “Comparison of multi-sensor admittance control in joint space and task space for a seven degree of freedom upper limb exoskeleton,” in *Proceedings of the 3rd IEEE RAS & EMBS International Conference on Biomedical Robotics and Biomechatronics*, (Tokyo, Japan), pp. 26–29, Sept. 2010.
- [5] E. R. Kandel, J. H. Schwartz, T. M. Jessell, S. A. Siegelbaum, and A. J. Hudspeth, *Principles of Neural Science*. McGraw-Hill Professional; 5th edition, 2012.
- [6] D. Purves, G. J. Augustine, D. Fitzpatrick, W. C. Hall, A.-S. LaMantia, and L. E. White, *Neuroscience*. Sinauer Associates, Inc., 2011. 5th edition.
- [7] J. Soechting, C. Buneo, U. Herrmann, and M. Flanders, “Moving effortlessly in three dimensions: does donders’ law apply to arm movement?”, *J. Neuroscience*, vol. 15, no. 9, pp. 6271–6280, 1995.
- [8] M. Latash, “Motor synergies and the equilibrium-point hypothesis,” *Motor Control*, vol. 14, no. 3, p. 294C322, 2010.

- [9] M. H. Raibert and J. K. Hodgins, “Legged robots,” in *Biological Neural Networks in Invertebrate Neuroethology and Robotics* (R. D. Beer, T. McKenna, and R. Ritzmann, eds.), pp. 319–354, Elsevier Science & Technology Books, 1993.
- [10] M. Turvey and S. Fonseca, “Nature of motor control: perspectives and issues.,” *Adv Exp Med Biol.*, vol. 629, pp. 93–123, 2009.
- [11] M. Kawato, “Internal models for motor control and trajectory planning.,” *Curr Opin Neurobiol.*, vol. 9, no. 6, pp. 718–727, 1999.
- [12] D. Wolpert and Z. Ghahramani, “Computational principles of movement neuroscience.,” *Nat Neurosci.*, vol. Suppl., pp. 1212–1217, 2000.
- [13] L. Sciavicco, “A dynamic solution to the inverse kinematic problem for redundant manipulators,” in *ICRA 1987*, vol. 4, (Raleigh, NC, USA), pp. 1081–1087, Mar. 1987.
- [14] L. Sciavicco, “A solution algorithm to the inverse kinematic problem for redundant manipulators,” *IEEE Trans. Robot. Automat.*, vol. 4, no. 4, pp. 403–410, 1988.
- [15] H. Asada and J. Granito, “Kinematic and static characterization of wrist joints and their optimal design,” in *ICRA 1985*, (St. Louis, Missouri), pp. 244–250, Mar. 1985.
- [16] T. Yoshikawa, “Dynamic manipulability of robot manipulators,” in *ICRA 1985*, (St. Louis, Missouri), pp. 1033–1038, Mar. 1985.
- [17] T. Yoshikawa, *Foundations of Robotics: Analysis and Control*. The MIT Press, 1990.
- [18] H. Kim, L. Miller, and J. Rosen, “Redundancy resolution of a human arm for controlling a seven dof wearable robotic system,” in *EMBC 2011*, (Boston, USA), Aug. 2011.
- [19] T. Kang, J. He, and S. I. H. Tillery, “Determining natural arm configuration along a reaching trajectory,” *Exp Brain Res*, vol. 167, pp. 352–361, 2005.

- [20] N. Hogan, “An organizing principle for a class of voluntary movements,” *J. of Neuroscience*, vol. 4, no. 2, pp. 2745–2754, 1984.
- [21] T. Flash and N. Hogan, “The coordination of arm movements: an experimentally confirmed mathematical model,” *J. of Neurophysiology*, vol. 5, pp. 1688–1703, 1985.
- [22] Y. Uno, M. Kawato, and R. Suzuki, “Formation and control of optimal trajectory in human multijoint arm movement - minimum torque-change model,” *Biology Cybernetics*, vol. 61, pp. 89–101, 1989.
- [23] E. Nakano, H. Imamizu, R. Osu, Y. Uno, H. Gomi, T. Yoshioka, and M. Kawato, “Quantitative examinations of internal representations for arm trajectory planning: Minimum commanded torque change model,” *The Journal of Neurophysiology*, vol. 81, no. 5, pp. 2140–2155, 1999.
- [24] C. M. Harris and D. M. Wolpert, “Signal-dependent noise determines motor planning,” *Nature*, vol. 194, pp. 780–784, 1998.
- [25] E. Todorov and M. I. Jordan, “Optimal feedback control as a theory of motor coordination,” *Nature Neuroscience*, vol. 5, pp. 1226–1235, 2002.
- [26] H. Miyamoto and M. Kawato, “Tops (task optimization in the presence of signal-dependent noise) model,” *Sys. and Comp. in Japan.*, vol. 35, pp. 48–58, 2004.
- [27] A. Biess, D. Liebermann, and T. Flash, “A computational model for redundant human three-dimensional pointing movements: integration of independent spatial and temporal motor plans simplifies movement dynamics.,” *J. of Neurosci.*, vol. 27, pp. 13045–64, 2007.
- [28] H. Kim, Z. Li, D. Milutinovic, and J. Rosen, “Resolving the redundancy of a seven dof wearable robotic system based on kinematic and dynamic constraint,” in *ICRA 2012*, (St. Paul, Minnesota, USA), 2012.
- [29] B. Kashi, I. Avrahami, J. Rosen, and M. Brand, “A bi-criterion model for human arm posture prediction.,” in *2012 World Congress on Medical Physics and Biomedical Engineering*, (Beijing, China), pp. 1–4, May 2012.

- [30] A. Frisoli, C. Loconsole, R. Bartalucci, and M. Bergamasco, “A new bounded jerk on-line trajectory planning for mimicking human movements in robot-aided neurorehabilitation,” *Robotics and Autonomous Systems*, vol. 61, no. 4, pp. 404–415, 2012.
- [31] J. Hollerbach and K. Suh, “Redundancy resolution of manipulators through torque optimization,” *IEEE Trans. Robot. Automat.*, vol. 3, pp. 308–316, Aug. 1987.
- [32] S. Tillery, T. Ebner, and J. Soechting, “Task dependence of primate arm postures,” *Experimental. Brain Researchy*, vol. 104, no. 1, pp. 1–11, 1995.
- [33] J. Soechting and M. Flanders, “Parallel, interdependent channels for location and orientation in sensorimotor transformations for reaching and grasping,” *J. of Neurophysiology*, vol. 70, no. 3, pp. 1137–1150, 1993.
- [34] M. Jeannerod, “The timing of natural prehension movements.,” *J. Neurophysiology*, vol. 16, no. 3, pp. 235–254, 1984.
- [35] M. Mon-Williams and J. Tresilian, “A simple rule of thumb for elegant prehension.,” *Curr. Biol.*, vol. 11, no. 13, pp. 1058–61, 2001.
- [36] P. Haggard and A. Wing, “On the hand transport component of prehensile movements.,” *Curr. Biol.*, vol. 29, no. 3, pp. 282–7, 2001.
- [37] J. Smeets and E. Brenner, “A new view on grasping,” *Motor Control*, vol. 3, pp. 237–271, 1999.
- [38] J. Fan, J. He, and S. Tillery, “Control of hand orientation and arm movement during reach and grasp.,” *Exp. Brain Res.*, vol. 171, no. 3, pp. 283–96, 2006.
- [39] E. Todorov, “Optimality principles in sensorimotor control,” *Nature neuroscience*, vol. 7, pp. 907–915, 2004.
- [40] J. P. Scholz and G. Schoner, “The uncontrolled manifold concept: identifying control variables for a functional task,” *Experimental brain research*, vol. 126, no. 3, pp. 289–306, 1999.
- [41] M. Latash, *Synergy*. Oxford University Press, USA, 1 edition, 2008.

- [42] J. Kelso, K. Holt, P. Rubin, and P. Kugler, “Patterns of human interlimb coordination emerge from the properties of non-linear, limit cycle oscillatory processes: theory and data.,” *J Mot Behav.*, vol. 13, no. 4, pp. 226–61, 1981.
- [43] W. Byblow, J. Summers, A. Semjen, I. Wuyts, and R. Carson, “Spontaneous and intentional pattern switching in a multisegmental bimanual coordination task,” *Motor Control*, vol. 3, pp. 372–393, Oct. 1999.
- [44] R. Carson, “The dynamics of isometric bimanual coordination.,” *Exp Brain Res.*, vol. 105, no. 3, pp. 465–76, 1995.
- [45] J. Kelso, “Phase transitions and critical behavior in human bimanual coordination,” *American Journal of Physiology*, vol. 246, pp. R1000–R1004, 1984.
- [46] J. Kelso, D. Southard, and D. Goodman, “On the coordination of two-handed movements,” *J. of Experimental Psychology*, vol. 5, pp. 229–238, 1979.
- [47] R. Marteniuk and C. MacKenzie, “A preliminary theory of two-hand coordinated control,” *Advances in Psychology*, vol. 1, pp. 185–197, 1980.
- [48] A. Semjen, J. Summers, and D. Cattaert, “Hand coordination in bimanual circle drawing.,” *J. Experimental Psychology*, vol. 21, pp. 1139–1157, Oct. 1995.
- [49] S. Swinnen, K. Jardin, R. Meulenbroek, N. Dounskoia, D. Hofkens-Van, and M. Brandt, “Egocentric and allocentric constraints in the expression of patterns of interlimb coordination,” *Arch Phys Med Rehabil*, vol. 9, pp. 348–377, May 1997.
- [50] S. Swinnen, K. Jardin, S. Verschueren, R. Meulenbroek, L. Franz, N. Dounskoia, and C. Walter, “Exploring interlimb constraints during bimanual graphic performance: effects of muscle grouping and direction.,” *Arch Phys Med Rehabil*, vol. 90, no. 1, pp. 79–87, 1998.
- [51] L. Cohen, “Synchronous bimanual movements performed by homologous and non-homologous muscles,” *Perceptual and Motor Skills*, vol. 32, pp. 639–644, 1971.
- [52] A. Ridderikhoff, C. E. Peper, and P. J. Beek, “Unraveling interlimb interactions underlying bimanual coordination,” *J. of Neurophysiology*, vol. 94, pp. 3112–3125, 2005.

- [53] S. P. Swinnen, “Intermanual coordination: from behavioural principles to neural-network interactions,” *Nature Reviews Neuroscience*, vol. 3, pp. 350–361, 2002.
- [54] C. Peper, P. Beek, and P. van Wieringen, “Frequency-induced phase transitions in bimanual tapping.,” *Biol Cybern.*, vol. 73, no. 4, pp. 301–9, 1995.
- [55] J. Summers, D. Rosenbaum, B. Burns, and S. Ford, “Production of polyrhythms.,” *J Exp Psychol Hum Percept Perform.*, vol. 19, pp. 416–28, 1993.
- [56] S. Messier, D. Bourbonnais, J. Desrosiers, and Y. Roy, “Kinematic analysis of upper limbs and trunk movement during bilateral movement after stroke,” *Arch Phys Med Rehabil.*, vol. 87, pp. 1463–70, 2006.
- [57] C. Wu, S. Chou, C. Chen, M. Kuo, T. Lu, and Y. Fu, “Kinematic analysis of a functional and sequential bimanual task in patients with left hemiparesis: intra-limb and interlimb coordination,” *Disabil Rehabil.*, vol. 31, pp. 958–66, 2009.
- [58] M. Barnes, “Management of spasticity,” *Age and Ageing*, vol. 27, pp. 239–245, 1998.
- [59] C. Walter, S. Swinnen, and N. Dounskoia, “Generation of bimanual trajectories of disparate eccentricity: levels of interference and spontaneous changes over practice.,” *J Mot Behav.*, vol. 34, pp. 183–95, June 2002.
- [60] P. Zanone and J. Kelso, “Evolution of behavioral attractors with learning: nonequilibrium phase transitions.,” *J Exp Psychol Hum Percept Perform.*, vol. 18, no. 2, pp. 403–21, 1992.
- [61] N. Dounskoia, K. Nogueira, S. Swinnen, and E. Drummond, “Limitations on coupling of bimanual movements caused by arm dominance: when the muscle homology principle fails.,” *J. Neurophysiol.*, vol. 103, pp. 2027–38, Apr. 2010.
- [62] R. Sainburg and D. Kalakanis, “Differences in control of limb dynamics during dominant and nondominant arm reaching.,” *J Neurophysiol.*, vol. 83, no. 5, pp. 2661–75, 2000.
- [63] R. Sainburg, “Handedness: differential specializations for control of trajectory and position.,” *Exerc Sport Sci Rev.*, vol. 33, pp. 206–13, 2005.

- [64] L. Bagesteiro and R. Sainburg, “Handedness: dominant arm advantages in control of limb dynamics.,” *J Neurophysiol.*, vol. 88, pp. 2408–21, 2002.
- [65] K. Haaland, J. Prestopnik, R. Knight, and R. Lee, “Hemispheric asymmetries for kinematic and positional aspects of reaching.,” *Brain*, vol. 127, pp. 1145–58, 2004.
- [66] H. Heuer, “Control of the dominant and nondominant hand: exploitation and taming of nonmuscular forces.,” *Exp Brain Res.*, vol. 178, no. 3, pp. 363–73, 2007.
- [67] R. Sainburg, “Evidence for a dynamic-dominance hypothesis of handedness.,” *Exp Brain Res.*, vol. 142, pp. 241–58, 2002.
- [68] C. Peper and P. Beek, “Modeling rhythmic interlimb coordination: The roles of movement amplitude and time delays,” *Human Movement Science*, vol. 18, pp. 263–280, June 1999.
- [69] D. Serrien and S. Swinnen, “Load compensation during homologous and non-homologous coordination.,” *Exp Brain Res.*, vol. 121, pp. 223–9, 1998.
- [70] S. Swinnen, N. Dounskaia, S. Verschueren, D. Serrien, and A. Daelman, “Relative phase destabilization during interlimb coordination: the disruptive role of kinesthetic afferences induced by passive movement.,” *Exp Brain Res.*, vol. 105, no. 3, pp. 439–54, 1995.
- [71] J. Brinkman and H. G. J. M. Kuypers, “Splitbrain monkeys: Cerebral control of ipsilateral and contralateral arm, hand, and finger movements,” *Science*, vol. 176, no. 4034, pp. 536–539, 1972.
- [72] H. Heuer, W. Spijkers, T. Kleinsorge, H. van der Loo, and C. Steglich, “The time course of cross-talk during the simultaneous specification of bimanual movement amplitudes.,” *Exp Brain Res.*, vol. 118, pp. 381–92, 1998.
- [73] R. Marteniuk, M. CL, and B. DM., “Bimanual movement control: information processing and interaction effects.,” *J Exp Psychol*, vol. 36, no. 2, pp. 335–365, 1984.
- [74] D. J. Serrien, “Coordination constraints during bimanual versus unimanual performance conditions,” *Neuropsychologia*, vol. 46, pp. 419–425, 2008.

- [75] F. Debaere, N. Wenderoth, S. Sunaert, P. V. Hecke, and S. Swinnen, “Cerebellar and premotor function in bimanual coordination: Parametric neural responses to spatiotemporal complexity and cycling frequency,” *Neuroimage*, vol. 21, pp. 1416–1427, 2004.
- [76] G. Goldberg, “Supplementary motor area structure and function: Review and hypotheses,” *Behavioral and Brain Sciences*, vol. 8, pp. 567–616, 1985.
- [77] L. Jancke, M. Peters, M. Himmelbach, T. Nosselt, J. Shah, and H. Steinmetz, “FMRI study of bimanual coordination,” *Neuropsychologia*, vol. 38, pp. 164–174, 2000.
- [78] P. Nachev, C. Kennard, and M. Husain, “Functional role of the supplementary and pre-supplementary motor areas,” *Exp Brain Res.*, vol. 9, no. 2008, pp. 856–869, 2008.
- [79] S. Swinnen and N. Wenderoth, “Two hands, one brain: Cognitive neuroscience of bimanual skill,” *Trends in Cognitive Science*, vol. 8, no. 2004, pp. 18–25, 2004.
- [80] L. Bagesteiro and R. Sainburg, “Nondominant arm advantages in load compensation during rapid elbow joint movements.,” *J Neurophysiol.*, vol. 90, pp. 1503–13, 2003.
- [81] S. Duff and R. Sainburg, “Nondominant arm advantages in load compensation during rapid elbow joint movements.,” *Exp Brain Res.*, vol. 179, pp. 551–61, 2007.
- [82] C. Schabowsky, J. Hidler, and P. Lum, “Greater reliance on impedance control in the nondominant arm compared with the dominant arm when adapting to a novel dynamic environment.,” *Exp Brain Res.*, vol. 182, pp. 567–77, 2007.
- [83] M. Rice and K. Newell, “Upper-extremity interlimb coupling in persons with left hemiplegia due to stroke,” *Arch Phys Med Rehabil.*, vol. 85, no. 4, pp. 629–34, 2004.
- [84] M. Harris-Love, S. McCombe-Waller, and J. Whitall, “Exploiting interlimb coupling to improve paretic arm reaching performance in people with chronic stroke,” *Arch Phys Med Rehabil*, vol. 86, no. 11, pp. 2131–7, 2005.

- [85] D. Rose and C. Winstein, “The co-ordination of bimanual rapid aiming movements following stroke.,” *Clin Rehabil*, vol. 19, no. 4, pp. 42–62, 2005.
- [86] B. Bobath, *Adult hemiplegia: evaluation and treatment. 3rd ed.* Oxford: Butterworth-Heinemann, 1990.
- [87] M. Mudie and T. Matyas, “Can simultaneous bilateral movement involve the undamaged hemisphere in reconstruction of neural networks damaged by stroke?,” *Disabil. Rehabil.*, vol. 22, no. 1/2, pp. 23–37, 2000.
- [88] J. Whitall, S. McCombe Waller, K. Silver, and R. Macko, “Repetitive bilateral arm training with rhythmic auditory cueing improves motor function in chronic hemiparetic stroke,” *Stroke*, vol. 31, no. 10, pp. 2390–5, 2000.
- [89] J. Cauraugh and S. Kim, “Two coupled motor recovery protocols are better than one: electromyogram-triggered neuromuscular stimulation and bilateral movements,” *Stroke*, vol. 33, no. 6, pp. 1589–94, 2002.
- [90] J. Cauraugh and S. Kim, “Progress toward motor recovery with active neuromuscular stimulation: muscle activation pattern evidence after a stroke,” *J. Neurol. Sci.*, vol. 207, no. 1-2, pp. 25–9, 2003.
- [91] G. Lewis and W. Byblow, “Neurophysiological and behavioural adaptations to a bilateral training intervention in individuals following stroke,” *Clin Rehabil*, vol. 18, no. 1, pp. 48–59, 2004.
- [92] J. Desrosiers, D. Bourbonnais, H. Corriveau, S. Gosselin, and G. Bravo, “Effectiveness of unilateral and symmetrical bilateral task training for arm during the subacute phase after stroke: a randomized controlled trial,” *Clin Rehabil*, vol. 19, no. 6, pp. 581–93, 2005.
- [93] O. Khatib, “Inertial properties in robotic manipulation: An object-level framework,” *IJRR*, vol. 5, pp. 19–36, 1995.
- [94] J. Huang, M. Hara, and T. Yabuta, “Controlling a finger-arm robot to emulate the motion of the human upper limb by regulating finger manipulability,” in *Motion Control* (F. Casolo, ed.), pp. 773–792, INTECH, 2010.

- [95] H. Kazerooni, “Exoskeletons for human performance augmentation,” in *A handbook of Robotics* (B. Siciliano and O. Khatib, eds.), pp. 773–792, pringer Handbook of Robotics, 1st edition, 2008.
- [96] H. Kazerooni, T. Sheridan, and P. Houpt, “Robust compliant motion for manipulators, part i: The fundamental concepts of compliant motion,” *IEEE Trans. Robot. Autom.*, vol. 2, pp. 83–92, 1986.
- [97] H. Kazerooni, “On the robot compliant motion control,” *ASME Journal of Dynamic Systems, Measurement, and Control*, vol. 111.
- [98] H. Kazerooni, B. Waibel, and S. Kim, “On the stability of robot compliant motion control : theory and experiments,” *ASME Journal of Dynamic Systems, Measurement, and Control*, vol. 112, pp. 417–426, 1990.
- [99] B. Waibel and H. Kazerooni, “Theory and experiments on the stability of robot compliance control,” *IEEE Trans. Robot. Autom.*, vol. 7, pp. 95–104, 1991.
- [100] T. Snyder and H. Kazerooni, “Dynamics and control of robotic systems worn by humans,” in *ICRA 1996*, vol. 2, (Minneapolis, MN, USA), pp. 1147–1152, 1996.
- [101] H. Kazerooni and J. Guo, “Human extenders,” *ASME Journal of Dynamic Systems, Measurement, and Control*, vol. 115, pp. 281–290, 1995.
- [102] H. I. Krebs, M. Ferraro, S. P. Buerger, M. J. Newbery, A. Makiyama, M. Sandmann, D. Lynch, B. T. Volpe, and N. Hogan, “Rehabilitation robotics: pilot trial of a spatial extension for mit-manus,” *J. NeuroEngineering and Rehabilitation*, vol. 1, Oct 2004.
- [103] H. I. Krebs, N. Hogan, M. L. Aisen, and B. T. Volpe, “Robot-aided neurorehabilitation: a robot for wrist rehabilitation.,” *IEEE Trans Neural Syst Rehabil Eng.*, no. 3, pp. 327–35, 2007.
- [104] D. Reinkensmeyer, E. Wolbrecht, and J. Bobrow, “A computational model of human-robot load sharing during robot-assisted arm movement training after stroke,” in *Conf Proc IEEE Eng Med Biol Soc*, (Lyon, France), pp. 4019–4023, Aug. 2007.

- [105] S. Majumdar, *Pneumatic System: Principles and Maintenance*. New Delhi: Tata McGraw-Hill, 1995.
- [106] J. He, E.J.Koeneman, R.S.Schultz, H.Huang, J. Wanberg, D.E.Herring, T.Sugar, R.Herman, and J.B.Koeneman, “Design of a robotic upper extremity repetitive therapy device,” in *ICORR 2005*, (Chicago, IL), 2005.
- [107] J. He, E.J.Koeneman, R.S.Schultz, D.E.Herring, J. Wanberg, H.Huang, T.Sugar, R.Herman, and J.B.Koeneman, “Rupert: a device for robotic upper extremity repetitive therapy,” in *EMBS 2005*, (Shanghai, China), Sep 2005.
- [108] H. Kim, L. Miller, I. Fedulow, M. Simkins, G. Abrams, N. Byl, and J. Rosen, “Kinematic data analysis for post-stroke patients following bilateral versus unilateral rehabilitation with an upper limb wearable robotic system.,” *IEEE Trans Neural Syst Rehabil Eng*, vol. 21, no. 2, pp. 153–64, 2013.
- [109] J. Perry, J. Powell, and J. Rosen, “Isotropy of an upper limb exoskeleton and the kinematics and dynamics of the human arm,” *J. of Applied Bionics and Biomechanics*, vol. 6, no. 2, pp. 175–191, 2009.
- [110] J. Rosen and J. Perry, “Upper limb powered exoskeleton,” *J. of Humanoid Robotics*, vol. 4, no. 3, pp. 1–20, 2007.
- [111] S. Selha, P. Dupont, R. Howe, and D. Torchiana, “Dexterity optimization by port placement in robot-assisted minimally invasive surgery,” in *2001 SPIE Int. Sym. on Intelligent Systems & Advanced Manufacturing*, (Newton, MA, USA), Oct. 2001.
- [112] J. Cannon, J. Stoll, S. Selha, P. Dupont, R. Howe, and D. Torchiana, “Port placement planning in robot-assisted coronary artery bypass,” *IEEE Transactions on Robotics & Automation*, vol. 19, pp. 912–917, Oct. 2003.
- [113] A. Trejos and R. Patel, “Port placement for endoscopic cardiac surgery based on robot dexterity optimization,” in *Proc. of the 2005 IEEE Int. Conf. on Robotics & Automation*, (Barcelona, Spain), pp. 912–917, May 2005.
- [114] R. Bauernschmitt, M. Feuerstein, J. Traub, E. Schirmbeck, G. Klinker, and R. Lange, “Optimal port placement and enhanced guidance in robotically assisted cardiac surgery,” *Surg Endosc*, vol. 21, pp. 684–687, 2007.

- [115] J. Li, S. Wang, X. Wang, and C. He, “Optimization of a novel mechanism for a minimally invasive surgery robot,” *Int. Journal Medicine Robotics Computer Assist Surgery*, vol. 6, pp. 83–90, 2010.
- [116] A. Maciejewski and C. Klein, “Obstacle avoidance for kinematically redundant manipulators in dynamically varying environments,” *IJRR*, vol. 4, pp. 109–117, 1985.
- [117] B. Christensen, W. Drotning, and S. Thunborg, “Model-based, sensordirected remediation of underground storage tanks,” *J. Robot. Syst.*, vol. 9, no. 2, pp. 145–159, 1992.
- [118] R. Colbaugh and M. Jamshidi, “Robot manipulator control for hazardous waste-handling applications,” *J. Robot. Syst.*, vol. 9, no. 2, pp. 215–250, 1992.
- [119] E. Wu, J. Hwang, and J. Chladek, “Fault tolerant joint development for the space shuttle remote manipulator system: Analysis and experiment,” in *Proc. 4th Int. Symp. Robot. Manufact. (ISRAM92)*, (Sante Fe, NM), pp. 505–510, Nov. 1992.
- [120] A. Maciejewski, “Fault tolerant properties of kinematically redundant manipulators,” in *ICRA 1990*, (Cincinnati, OH), pp. 638–642, Nov. 1990.
- [121] C. Lewis and A. A. Maciejewski, “Fault tolerant operation of kinematically redundant manipulators for locked joint failures,” *IEEE Trans. Robot. Automat.*, vol. 13, pp. 622–629, 1997.
- [122] R. G. Roberts and A. A. Maciejewski, “A local measure of fault tolerance for kinematically redundant manipulators,” *IEEE Trans. Robot. Automat.*, vol. 12, pp. 543–552, Aug. 1996.
- [123] J. Baillieul, “Avoiding obstacles and resolving kinematic redundancy,” in *ICRA*, (San Francisco, CA), pp. 1698–1704, Apr. 1986.
- [124] R. Colbaugh, H. Seraji, and K. Glass, “Obstacle avoidance of redundant robots using configuration control,” *Int. J. of Robotics Research*, vol. 6, pp. 721–744, July 1989.
- [125] S. L. Chi, “Task compatibility of manipulator postures,” *Int. J. of Robotics Research*, vol. 7, pp. 13–21, Oct. 1988.

- [126] Z. C. Lin, R. V. Patel, and C. A. Balafoutis, “Impact reduction for redundant manipulators using augmented impedance control,” *J. Robot. Syst.*, vol. 12, pp. 301–313, May 1995.
- [127] H. Seraji, “Task options for redundancy resolution using configuration control,” in *30th Annual International Conference of the IEEE Engineering in Medicine and Biology Society EMBS*, (Pasadena, USA), pp. 2793–2798, Dec. 1991.
- [128] V. V. Anderson and R. Horn, “Tensor-arm manipulator design,” *ASME Trans.*, vol. 67-DE-57, no. 3, pp. 1–12, 1967.
- [129] G. Chirikjian and J. Burdick, “A modal approach to hyper-redundant manipulator kinematics,” *IEEE Transactions on Robotics and Automation*, vol. 10, pp. 343–354, June 1994.
- [130] A. Hayashi, J. Park, and B. Kuipers;, “Toward planning and control of highly redundant manipulators,” in *Proc. of IEEE International Symposium on Intelligent Control*, vol. 2, (Philadelphia, PA), pp. 683–688, Sept. 1990.
- [131] D. Tesar and M. Bulter, “a generalized modular architecture for robot structure,” *ASME Manufacturing Review*, vol. 2, pp. 91–118, June 1989.
- [132] A. Morecki, K. Jaworker, W. Pogorzelski, T. Zielinska, and J. Fraczek, “Robotics system - elephant trunk type elastic manipulator combined with a quadruped walking machine,” in *Proc. of the Second International Conference on Robotics and Factories of the Future*, (San Diego, CA), pp. 649–656, July 1987.
- [133] M. Ivanescu, “Position dynamic control for a tentacle manipulator,” in *Proc. of IEEE International Conference on Robotics and Automation*, vol. 2, (Washington, DC), pp. 1531–1538, May 2002.
- [134] A. Hamilton and D. Wolpert, “Controlling the statistics of action: obstacle avoidance,” *J. of Neurophysiology*, vol. 87.
- [135] W. Li, E. Todorov, and X. Pan, “Hierarchical optimal control of redundant biomechanical systems,” in *EMBS 2004*, pp. 4618–4621, 2004.
- [136] H. Seraji and R. Colbaugh, “Improved configuration control for redundant robots,” *J. of Robotic Systems*, vol. 7, pp. 897–928, 1990.

- [137] T. L. Boullion and P. L. Odell, *Generalized inverse matrices*. Wiley-Interscience, 1971.
- [138] J. Angeles and F. Park, “Performance evaluation and design criteria,” in *A handbook of Robotics* (B. Siciliano and O. Khatib, eds.), pp. 229–244, pringer Handbook of Robotics, 1st edition, 2008.
- [139] A. Bicchi, “On the mobility and manipulability of general multiple limb robots,” *IEEE Journal of Robotics and Automation*, vol. 11, no. 2, pp. 215–228, 1995.
- [140] S. Saha, *Introduction to Robotics*. Tata McGraw-Hill Publishing Company Limited, 2008.
- [141] J. K. Salisbury and J. J. Craig, “Articulated hands: force control and kinematic issues,” *Int. J. of Robotics Research*, vol. 1, no. 1, pp. 4–17, 1982.
- [142] J. Angeles and C. Lopez-Cajun, “Kinematic isotropy and the conditioning index of serial robotic manipulators,” *Int. J. Robotics Research*, vol. 11, no. 6, pp. 560–571, 1992.
- [143] J. Angeles and A. Rojas, “Manipulator inverse kinematics via condition-number minimization and continuation,” *Int. J. Robotics Automation*, vol. 2, no. 2, pp. 61–69, 1987.
- [144] J. Angeles, “The design of isotropic manipulator architectures in the presence of redundancies,” *Int. J. Robotics Research*, vol. 11, no. 3, pp. 560–571, 1992.
- [145] A. Fattah and A. Hasan Ghasemi, “Isotropic design of spatial parallel manipulators,” *Int. J. Robotics Research*, vol. 21, no. 9, pp. 811–824, 2002.
- [146] T. Graettinger and B. Krogh, “The acceleration radius: a global performance measure for robotic manipulators,” *IEEE Trans. Robot. Automat.*, vol. 4, pp. 60–69, 1988.
- [147] A. Bowling and O. Khatib, “The dynamic capability equations: a new tool for analyzing robotic manipulator performance,” *IEEE Trans. Robot.*, vol. 21, pp. 115–123, Feb. 2005.
- [148] A. Liegeois, “Automatic supervisory control of the configuration and behavior of multibody mechanisms,” *IEEE Transactions on Systems, Man, and Cybernetics.*, vol. 7, pp. 868–871, 1977.

- [149] C. A. Klein and C. Huang, “Review of pseudoinverse control for use with kinematically redundant manipulators,” *IEEE Transactions on Systems, Man, and Cybernetics.*, vol. SMC, pp. 245–250, 1983.
- [150] M. Spong, “Remarks on robot dynamics: canonical transformations and riemannian geometry,” in *Proceedings of 1992 IEEE International Conference on Robotics and Automation*, vol. 1, (Nice, France), pp. 554–559, 1992.
- [151] C. Gosselin and J. Angeles, “A new performance index for the kinematic optimization of robotic manipulator,” in *Proc. ASME Mec. Conf.*, (Kissimmee, FL), pp. 441–447, 1988.
- [152] R. Dubey and J. Y. S. Luh, “Redundant robot control using task based performance measures,” *J. Robot. Syst.*, vol. 5, pp. 409–432, Mar. 1988.
- [153] W. P. Medendorp, J. D. Crawford, D. Henriques, J. V. Gisbergen, and C. Gielen, “Kinematic strategies for upper arm-forearm coordination in three dimensions,” *J. Neurophysiology*, vol. 84, no. 5, pp. 2302–2316, 2000.
- [154] B. Garner and M. Pandy, “Final posture of the upper limb depends on the initial position of the hand during prehension movements,” *Comput Methods Biomed Engin.*, vol. 2, no. 2, pp. 107–124, 1999.
- [155] P. M. Fitts, “The information capacity of the human motor system in controlling the amplitude of movement,” *J. Experimental Psychology*, vol. 47, 1954.
- [156] I. S. Mackenzie and W. Buxton, “Extending fitts’ law to two-dimensional tasks,” in *Proc. of ACM CHI’92 Conference*, pp. 219–226, 1992.
- [157] C. Terzuolo and P. Viviania, “Determinants and characteristics of motor patterns used for typing,” *J. of Neuroscience*, vol. 5, pp. 431–437, 1982.
- [158] P. Viviani and C. Terzuolo, “Trajectory determines movement dynamics,” *J. of Neuroscience*, vol. 7, pp. 431–437, 1982.
- [159] S. Schaal and D. Sternad, “Origins and violations of the 2/3 power law in rhythmic 3d movements,” *Experimental Brain Research*, vol. 136, pp. 60–72, 2001.

- [160] D. Rosenbaum, R. Meulenbroek, J. Vaughan, and C. Jansen, “Posture-based motion planning: applications to grasping,” *Psychological Review*, vol. 108, no. 4, pp. 709–734, 2001.
- [161] F. Hermens and S. Gielen, “Posture-based or trajectory-based movement planning: a comparison of direct and indirect pointing movements.,” *Experimental brain research*, vol. 159, no. 3, pp. 340–348, 2004.
- [162] M. Kawato, “Bidirectional theory approach to integration,” in *Attention and Performance XVI: Information Integration in Perception and Communication* (T. Inui and J. L. McClelland, eds.), pp. 335–367, Cambridge, MA: The MIT Press, 1996.
- [163] D. Vaillancourt and K. Newell, “movement variability and theories of motor control,” in *Classics in Movement Science* (M. Latash and V. Zatsiorsky, eds.), pp. 409–435, Human Kinetics, 2001.
- [164] R. S. Woodworth, *The Accuracy of Voluntary Movement*. The Macmillan Company, 1899.
- [165] N. Bernstein, *The coordination and regulation of movements*. Oxford, New York: Pergamon Press, 1967.
- [166] H. Muller and D. Sternad, “Motor learning: changes in the structure of variability in a redundant task,” *Advances in experimental medicine and biology, Progress in Motor Control*, vol. 629, pp. 439–456, 2009.
- [167] J. Gordon, M. F. Ghilardi, and C. Ghez, “Accuracy of planar reaching movements,” *Experimental Brain Research*, vol. 99, no. 1, pp. 97–111, 1994.
- [168] J. Messier and J. Kalaska, “Comparison of variability of initial kinematics and endpoints of reaching movements,” *Experimental Brain Research*, vol. 125, no. 2, pp. 139–152, 1999.
- [169] Z. Li, D. Glozman, D. Milutinovic, and J. Rosen, “Maximizing dexterous workspace and optimal port placement of a multi-arm surgical robot,” in *ICRA 2011*, (Shanghai, China), pp. 3394–3399, May 2011.
- [170] W. Nelson, “Physical principles for economies of skilled movements.,” *Biological cybernetics*, vol. 46, pp. 135–147, 1983.

- [171] M. Harwood, L. Mezey, and C. Harris, “The spectral main sequence of human saccades,” *J. of Neurophysiology*, vol. 19, pp. 9098–9106, 1999.
- [172] M. Pandy, B. Garner, and F. Anderson, “Optimal control of non-ballistic muscular movements: a constraint-based performance criterion for rising from a chair,” *J. of Neurophysiology*, vol. 117, pp. 9098–9106, 1995.
- [173] E. Todorov and M. Jordan, “Smoothness maximization along a predefined path accurately predicts the speed profiles of complex arm movements,” *J. of Neuroscience*, vol. 880, pp. 696–714, 1998.
- [174] G. Sutton and K. Sykes, “The variation of hand tremor with force in healthy subjects.,” *J. of physiology*, vol. 191, pp. 699–711, 1967.
- [175] R. Schmidt, H. Zelaznik, B. Hawkins, J. Frank, and J. Quinn, “Motor-output variability: a theory for the accuracy of rapid motor acts,” *Psychology review*, vol. 47, pp. 415–541, 1979.
- [176] P. N. Sabes, M. Jordan, and D. M. Wolpert, “The role of inertial sensitivity in motor planning,” *J. of Neuroscience*, vol. 18.
- [177] J. Scholz, G. Schoner, and M. Latash, “Identifying the control structure of multijoint coordination during pistol shooting,” *Experimental brain research*, vol. 135, no. 3, pp. 382–404, 2000.
- [178] Z. Li, M. L. Latash, and V. M. Zatsiorsky, “Force sharing among fingers as a model of the redundancy problem,” *Experimental brain research*, vol. 119, pp. 276–286, 1998.
- [179] D. Rosenbaum, *Human Motor Control*. Academic Press, 1990.
- [180] A. Wing and S. Lederman, “Points for precision grip,” in *Sensorimotor control of grasping* (D. Nowak and J. Hermsdorfer, eds.), pp. 194–203, Cambridge University Press, 2009.
- [181] B. Tyldesley and J. Grieve, *Muscles, Nerves and Movement: In Human Occupation, 3rd Edition*. Wiley-Blackwell, 2002.
- [182] B. Vollmer and H. Forssberg, “Development of grasping and object manipulation,” in *Sensorimotor Control of Grasping: Physiology and Pathophysiology*

(D. A. Nowak and J. Hermsdorfer, eds.), pp. 178–192, Cambridge University Press, 2009.

- [183] A. M. Smith, “The neurohaptic control of the hand,” in *Sensorimotor Control of Grasping: Physiology and Pathophysiology* (D. A. Nowak and J. Hermsdorfer, eds.), pp. 178–192, Cambridge University Press, 2009.
- [184] K. Nagai and T. Yoshikawa, “Impedance control of redundant macro-micro manipulators,” in *IROS 1994*, vol. 2, (Munich, Germany), pp. 1438–1445, 1994.
- [185] T. Yoshikawa, K. Hosoda, T. Doi, and H. Murakami, “Quasi-static trajectory tracking control of flexible manipulator by macro-micro manipulator system,” in *ICRA 1993*, vol. 3, (Munich, Germany), pp. 210–215, 1993.
- [186] Y. Nakamura and H. Hanafusa, “Inverse kinematic solutions with singularity robustness for robot manipulator control,” *ASME Journal of Dynamic Systems, Measurement, and Control*, vol. 108, pp. 163–171, 1986.
- [187] J. Furusho and H. Usui, “A control method for manipulator with redundant,” *Trans. JSME*, vol. 55, pp. 1391–1398, 1989.
- [188] O. Khatib, “Real-time obstacle avoidance for manipulators and mobile robots,” *IJRR*, vol. 5, pp. 90–98, 1986.
- [189] L. Loeff and A. Soni, “An algorithm for computer guidance of a manipulator in between obstacles,” *Trans. ASME J. of Engineering for Industry*, vol. 97, pp. 836–842, 1975.
- [190] Z. Guo and T. Hsia, “Joint trajectory generation for redundant robots in an environment with obstacles,” *J. of Robotic Systems*, vol. 10, pp. 199–215, 1993.
- [191] K. Glass, R. Colbaugh, D. Lim, and H. Seraji, “Real-time collision avoidance for redundant manipulators,” *IEEE J. Robot. Autom.*, vol. 11, pp. 448–457, 1995.
- [192] J. Vannoy and J. Xiao, “Real-time adaptive and trajectory-optimized manipulator motion planning,” in *Proceedings. 2004 IEEE/RSJ International Conference on Intelligent Robots and Systems*, vol. 1, pp. 497–502, 2004.

- [193] J. Kim and P. Khosla, “Real-time obstacle avoidance using harmonic potential functions,” in *ICRA 1991*, vol. 1, (Sacramento, CA , USA), pp. 790–796, 1991.
- [194] J. Salisbury and C. Melchiorri, *Exploiting the Redundancy of a Hand-Arm Robotic System*. MIT A.I. Memo No.1261, 1990.
- [195] B. T. Quan, J. Huang, M. Harada, and T. Yabuta, “Control of a macro-micro robot system using manipulability of the micro robot,” *JSME International Journal Series C,Special Issue on Advanced Technology of Vibration and Sound*, vol. 49, pp. 897–904, 2006.
- [196] J. Huang, D. Yamada, T. Hori, M. Hara, and T. Yabuta, “Emulating the motion of a human upper limb: Controlling a finger-arm robot by using the manipulability of its finger,” in *ROBIO 2006*, (Kunming, China), pp. 607–612, 2006.
- [197] J. Huang, D. Yamada, T. Hori, M. Hara, and T. Yabuta, “Integration of impedance control and manipulability regulation for a finger-arm robot,” in *ICRA 2009*, address =.
- [198] M. Stoykov and D. Corcos, “A review of bilateral training for upper extremity hemiparesis.,” *Occup Ther Int.*, vol. 16, no. 3-4, pp. 190–203, 2009.
- [199] J. Cauraugh and J. Summers, “Neural plasticity and bilateral movements: A rehabilitation approach for chronic stroke.,” *Prog Neurobiol.*, vol. 75, pp. 309–20, 2005.
- [200] J. Netz, T. Lammers, and V. Homberg, “Reorganization of motor output in the non-affected hemisphere after stroke.,” *Brain*, no. Pt9, pp. 1579–86.
- [201] M. Staudt, W. Grodd, C. Gerloff, M. Erb, J. Stitz, and I. Krageloh-Mann, “Two types of ipsilateral reorganization in congenital hemiparesis: a tms and fmri study.,” *Brain*, vol. 125, no. Pt 10, pp. 2222–37, 2002.
- [202] S. Cramer, “Repairing the human brain after stroke: I. mechanisms of spontaneous recovery.,” *Ann Neurol.*, vol. 63, no. 3, pp. 272–87, 2008.
- [203] C. Stinear, P. Barber, J. Coxon, M. Fleming, and W. Byblow, “Priming the motor system enhances the effects of upper limb therapy in chronic stroke,” *Brain*, vol. 131, no. 5, pp. 1381–90, 2008.

- [204] N. Murase, J. Duque, R. Mazzocchio, and L. Cohen, “Influence of interhemispheric interactions on motor function in chronic stroke.,” *Ann Neurol.*, vol. 55, no. 3, pp. 400–9, 2004.
- [205] S. McCombe Waller and J. Whitall, “Bilateral arm training: why and who benefits?,” *NeuroRehabilitation*, vol. 23, no. 1, pp. 29–41, 2008.
- [206] S. Cardoso de Oliveira, “The neuronal basis of bimanual coordination: recent neurophysiological evidence and functional models.,” *Acta Psychol (Amst)*, vol. 110, no. 2-3, pp. 139–59, 2002.
- [207] A. Smith and W. Staines, “Cortical adaptations and motor performance improvements associated with short-term bimanual training.,” *Brain Res.*, vol. 1071, pp. 165–74, 2006.
- [208] A. van Delden, C. Peper, G. Kwakkel, and P. Beek, “A systematic review of bilateral upper limb training devices for poststroke rehabilitation,” *Stroke Res Treat.*, vol. 2012, pp. 1–17, 2012.
- [209] J. Stevens and M. Stoykov, “Simulation of bilateral movement training through mirror reflection: a case report demonstrating an occupational therapy technique for hemiparesis,” *Top Stroke Rehabil.*, vol. 11, pp. 59–66, 2004.
- [210] G. Yavuzer, R. Selles, N. Sezer, S. Sutbeyaz, J. Bussmann, F. Koseoglu, M. Atay, and H. Stam, “Mirror therapy improves hand function in subacute stroke: A randomized controlled trial,” *Biol Cybern.*, vol. 89, pp. 393–8, 2008.
- [211] J. Perry and J. Rosen, “Design of a 7 degree-of-freedom upper-limb powered exoskeleton,” in *Proceedings of the 3rd IEEE RAS & EMBS International Conference on Biomedical Robotics and Biomechatronics*, (Pisa, Italy), pp. 805–810, Feb. 2006.
- [212] J. Craig, *Introduction to Robotics: Mechanics and Control*, 3rd edition, ch. 1. Prentice Hall, 2003.
- [213] Z. Li, H. Kim, D. Milutinovic, and J. Rosen, “Synthesizing redundancy resolution criteria of the human arm posture in reaching movements.,” *Redundancy in Robot Manipulators and Multi-robot systems*, vol. 57, pp. 201–240, 2013.

- [214] N. I. Badler and D. Tolani, “Real-time inverse kinematics of the human arm,” *Presence*, vol. 5, no. 4, pp. 393–401, 1996.
- [215] Unknown, “Motion genesis.” Previously Autolev. Accessed: May 13, 2014.
- [216] T. Kane and D. Levinson, *Dynamics: Theory and Applications*. New York: McGraw-Hill, 1985.
- [217] Aerospace medical research laboratory, “Investigation of inertial properties of human body,” tech. rep., Mar 1975.
- [218] Z. Li, J. Roldan, D. Milutinovic, and J. Rosen, “The rotational axis approach for resolving the kinematic redundancy of the human arm in reaching movements.,” in *EMBC 2013*, (Osaka, Japan), pp. 2507–2510, July 2013.
- [219] Y. Wada, Y. Kaneko, E. Nakano, R. Osu, and M. Kawato, “Quantitative examinations for multi joint arm trajectory planning using a robust calculation algorithm of the minimum commanded torque change trajectory,” *J. of Neural Networks*, vol. 14, pp. 381–393, 2001.
- [220] R. P. Duma and P. L. Strick, “Motor areas in the frontal lobe of the primate,” *Physiol Behav*, vol. 77, pp. 677–682, 2002.
- [221] M. Graziano, C. Tylor, and T. Moore, “Complex movements evoked by micro stimulation of precentral cortex,” *Neuron*, vol. 34, pp. 841–851, 2002.
- [222] F. E. Mount, M. Whitmore, and S. L. Stealey, “Evaluation of neutral body posture on shuttle mission sts-57 (spacehab-1),” tech. rep., Feb 2003.
- [223] E. T. Jaynes, “Information theory and statistical mechanics,” *Phys. Rev.*, vol. 106, pp. 620–630, 1957.
- [224] Y. Nakamura, H. Hanafusa, and T. Yoshikawa, “Task-priority based redundancy control of robot manipulators,” *IJRR*, vol. 6, pp. 3–15, 1987.
- [225] I. A. Kapandji, L. Honore, and R. Tubiana, *Physiology of the Joints*. Elsevier - Health Sciences Division, 2007.
- [226] W. H. DuMouchel and F. L. O’Brien, “Integrating a robust option into a multiple regression computing environment.,” in *Computer Science and Statistics: Proc. 21st Symposium on the Interface*, (Alexandria, VA), pp. 41–48, Mar. 1989.

- [227] W. Khalil and E. Dombre, *Modeling, Identification and Control of Robots*. Kogan Page Science, 2004.